GEOLOGIC HISTORY OF ISIDIS PLANITIA ON MARS

M.A. Ivanov[1,2], H. Hiesinger[2], G. Erkeling[2], and D. Reiss[2], *[1]Vernadsky Inst., RAS, Moscow, Russia, mikhail_ivanov@brown.edu; [2]Inst. für Planetologie, Univ. of Muenster, Muenster, Germany*

Introduction: Isidis Planitia occupies one of the largest (~1800 km) impact basins on Mars. In this region, landforms of volcanic, fluvial, and glacial origin are abundant [1-5] and the floor of the basin is one of the most important sites of thumbprint terrain (TPT) on Mars [e.g., 2,6]. In order to assess the evolution of the Isidis basin and understand the place and role of different processes in its geologic history, we have mapped in detail an extensive area (between 75- 103°E and 1-27°N) that includes Isidis Planitia (floor of the basin) and its surroundings (rim of the basin) using all available imagery and topographic data sets. Here we describe the morphology of the material units, interpret their nature, give age estimates for the units, and, finally, outline the major steps in the geologic history of the region.

Large-scale topographic configuration of the Isidis basin: The regional break in slopes and distribution of elevations on the floor and the rim of the basin divide the whole region into topographic provinces of lowlands (< -3.5 km, floor of the basin), midlands (from -3,5 to -2,4 km, lower rim), and uplands (> -2.4 km, higher rim). This large-scale topographic configuration of the basin probably governed the spatial distribution of materials emplaced, removed, and redeposited in this region.

Description, interpretation, and age assessment of units: We have defined the units that compose the Isidis Planitia region in a traditional photogeological way: if the surface of a terrain has a specific morphology (within some limits), which is distinctly different from the other terrains, this morphology defines a rock unit [7]. This definition has pure empirical character and does not include an interpretative component. The relative ages of the units were derived from both the stratigraphic relationships and the results of crater counts.

Mountainous materials (Nm) form the uplands and occur preferentially in Libya Montes. The surface of the unit displays high (up to a few km) peaks with lower mounds and ridges. The unit has a specific morphology, occurs in many regions of Mars, and is interpreted as materials formed by large and small impact events [8-10]. The principal constituents of the unit of mountainous materials are thought to be impact breccias. The size-frequency distribution (SFD) of craters on the surface of unit Nm shows at least two isochrones corresponding to the model ages of ~3.97 ($^{+0.04}/_{-0.06}$) Ga (formation) and ~3.85 ($^{+0.02}/_{-0.03}$) Ga (modification).

Subdued mountains materials (Nms) have lower topography and often surround massifs of unit Nm. The surface of unit Nms is rugged, but lacks the high peaks and its materials overlap/embay structures of the higher mountain peaks of unit Nm. We interpret materials of unit Nms as a mixture of the impact breccias and clastic materials eroded and deposited within intermountain basins. The SFD of craters indicate two model ages of the unit, ~3.86 ($^{+0.05}/_{-0.1}$) and ~3.76 ($^{+0.03}/_{-0.03}$) Ga.

Unit of upland plains (NHpu) has a flattened surface and embays units Nm and Nms. In places, structures resembling wrinkle ridges complicate the surface of the unit. Graben of Nili and Amenthes Fossae cut upland plains and expose their layered structure. The layers are similar to those that characterize volcanic plateaus elsewhere on Mars (e.g., Lunae Planum) [11,12]. The layered structure of upland plains and possible presence of wrinkle ridges suggest that unit Npu has a volcanic origin. The SFD of craters on the surface of the unit suggests two model ages, ~3.75 ($^{+0.03}/_{-0.04}$) and ~3.55 ($^{+0.02}/_{-0.02}$) Ga.

Ridged plains (Hpr) have a smooth and flat surface and cover broad areas within the midlands. Several specific features characterize ridged plains: (1) wrinkle ridges, (2) internal layered structure of the plains (3) straight and sharp-crested ridges similar to exhumed volcanic dikes [13]. These features collectively suggest a volcanic origin of ridged plains. The SFD of craters on the surface of ridged plains is fitted by two isochrones, ~3.66 ($^{+0.04}/_{-0.05}$) (formation) and ~3.53 ($^{+0.02}/_{-0.03}$) Ga (modification).

Plains of *Syrtis Major* (HpSM) demonstrate large calderas, wrinkle ridges, and lava flows/tubes. All these features indicate a volcanic origin of the Syrtis Major plateau [e.g., 14,15]. The high scarps at the eastern edges of Syrtis Major expose its layered structure, which is similar to that seen in units NHpu and Hpr. In the eastern portion of Syrtis Major, the SFD of the craters suggests that the unit was emplaced ~3.49 ($^{+0.08}/_{-0.19}$) Ga ago, although the entire plateau was estimated to be of lower Hesperian age [5].

Knobby materials (Hmk) are seen in the transition from the midlands to the lowlands and form a broad zone around the floor of the Isidis basin. Occurrences of the unit

*) All the abstracts are the original authors' versions

2MS³-PS-01

represent clusters of small and low mesa- and peak-like mounds. The mesas preferentially occur in association with areas of ridged plains (unit Hpr) and represent their erosional remnants. Disintegrated occurrences of the unit preclude reliable crater counting on the surface of the unit.

Etched upland materials (NHue) occur within the uplands in large areas around Nili Fossae. Heavily degraded craters, low ridges, and scarps with sharp and jagged edges are typical features of the unit. The abundance of the eroded craters implies that the unit was formed due to effective erosion of older materials. The SFD of craters on the surface of unit NHue suggests two model ages, ~3.78 ($^{+0.04}/_{-0.07}$) (emplacement of original materials) and ~3.49 ($^{+0.03}/_{-0.04}$) Ga (erosion).

Channeled materials (Hmch) occur in the NW (Arena Colles region, HmchAC) and S (Libya Montes, HmchLM) portions of the Isidis basin. The characteristic features of the unit (fluvial channels/valleys) in both regions suggest its formation during episodes of fluvial activity. The SFD of craters on the surface of unit HmchAC corresponds to a model age of ~3.51 ($^{+0.04}/_{-0.07}$) Ga and the surface of unit HmchLM is estimated to be ~3.37 ($^{+0.05}/_{-0.09}$) Ga old.

Smooth plains (Hps) have a homogenous surface that usually lacks characteristic morphologic details. The plains form a broad zone that encircles the floor of the Isidis basin. The largest area of Hps is associated with knobby unit; materials of smooth plains embay the knobs. Characteristic features of smooth plains are narrow and very sinuous ridges. The morphology of them is inconsistent with many types of ridge-forming processes (tectonic, volcanic, fluvial, etc.) but closely resembles the morphology of eskers [e.g., 16]. This interpretation suggests that the smooth plains represent materials related to extensive glaciation within the Isidis Planitia region. The SFD of craters suggests a model age of formation of the unit of ~3.33 ($^{+0.1}/_{-0.23}$) Ga.

Plains with cones (HAcp) occur within the lowlands and occupy the floor of the Isidis basin. The surface of the plains is smooth, homogenous, and features thousands of small cone-like mounds [17,18]. The mounds or their chains often form long curved lines that in the images of low resolution appear as nested ridges of the thumbprint terrain [1,2]. The mounds occur exclusively within unit HApc and are absent in any other unit. The SFD of impact craters on the surface of unit HApc suggests a model age of its formation of ~3.26 ($^{+0.13}/_{-0.4}$) Ga. Impact craters with lobate ejecta that overlap the mounds provide the upper stratigraphic limit of TPT, ~2.8 ($^{+0.46}/_{-0.87}$) Ga [19].

Sequence and nature of major events in the Isidis Planitia region: The definition of the units, interpretation of their nature, and assessment of the ages of their formation and modification allow outlining of a model of evolution of the Isidis Planitia region since its formation by the major impact perhaps in the beginning of the Noachian [20]. The presence of the large (Noachian) craters on the rim implies that the actual topographic configuration of the Isidis Planitia region is its long-lasted feature.

Four principal episodes compose the geologic history of the Isidis Planitia region. ***(1) Impact-dominated episode (Noachian):*** Impacts and slope mass-wasting processes dominated formation of the oldest materials (Nm and Nms) and likely were the most important contributors to the initial filling of the Isidis basin. ***(2) Volcanically dominated episode (early Hesperian):*** Volcanism appears as the most important process in the Isidis Planitia region since the end of Noachian (emplacement of unit NHpu). Ridged plains (Hpr) and plains in Syrtis Major (HpSM) continued volcanic activity on the rim of the basin and mostly completed formation of the circum-Isidis volcanic province by the middle of Hesperian. Volcanic materials probably represent the major portion of the fill of the basin. They almost completely buried the previous crater record and were deformed into broad and low topographic ridges, i.e. wrinkle ridges. ***(3) Glacial/fluvial episode (late Hesperian):*** By the end of formation of the circum-Isidis volcanic province, predominantly glacial (NHue, Hmk, Hsp, HAcp) and some fluvial (Hmch) processes dominated the geological evolution and were responsible for the widespread resurfacing in the Isidis Planitia region. Although the ice/water-related units are widespread, the net effect of their formation was apparently negligible. The estimates of the total volume of materials eroded from the rim and deposited on the floor by the glacial and fluvial activity suggest that the maximum thickness of materials on the floor of the basin is less than a few hundred meters. The composite layer of these deposits had buried the broad ridges on the floor of the basin but was not able to erase their topographic characteristics. ***(4) Wind-dominated episode:*** The wind activity dominated during the final episode of the geologic history of the Isidis Planitia region that continues since the beginning of Amazonian. Modification of the surface in this during this time appears to be minor.

References: 1) Greeley, R. and J.E. Guest, USGS Map I-1802-B, 1987; 2) Grizzaffi, P. and P.H. Schultz, Icarus, 77, 358, 1989; 3) Ivanov, M.A. and J.W. Head, JGR, 108, 5063, 10.1029/2002JE001994, 2003; 4) Hiesinger, H. and J.W. Head, LPSC-35, #1167, 2004a; 5) Hiesinger, H. and J.W. Head, JGR, 109, E01004, 10.1029/2003JE002143, 2004b; 6) Lockwood, J.F., et al., LPSC-23, 795, 1992; 7) Wilhelms, D. E. in: Planetary Mapping, CUP, 208, 1990; 8) Tanaka, K.L., and D.H. Scott, USGS Map I-1802-C, 1987; 9) Leonard, G.J. and K.L., USGS Map I-2694, 2001; 10) Mest, S.C., and D.A. Crown, Icarus, 153, 89, 2001; 11) Ivanov, M.A., et al., JGR, 115, E03001, 10.1029/2008JE003256, 2010; 12) Tormanen, T., et al., LPSC-41, #1310, 2010; 13) Head, J.W., et al., Geology, 34, 285, 2006; 14) Greeley, R. and P. Spudis, RGSP, 19, 13, 1981; 15) Schaber, G.G., JGR, 87, 9852, 1982; 16) Kargel, J.S., et al., JGR, 100, 5351, 1995; 17) Hiesinger, H., et al., EGU GA, 11, EGU2009-7812, 2009; 18) Hielscher, F.J., et al., LPSC-41, #2394, 2010; 19) Sturm, S., BchSci Th., - Wilhelms-Universität Münster, p. 51, 2008; 20) Schultz, R.A. and H.V. Frey, JGR. 95, 14175, 1990

OPEN-BASIN LAKES ON MARS: A GLOBAL ANALYSIS OF ASSOCIATED LACUSTRINE AND POST-FLUVIAL DEPOSITS.

T. A. Goudge[1], J.W. Head[1], J.F. Mustard[1], C.I. Fassett[1], [1]*Department of Geological Sciences, Brown University, Box 1846, Providence, RI, USA. Contact: Tim_Goudge@brown.edu*

Introduction: Paleolake basins have long been observed on Mars [1,2], and several workers have compiled extensive and thorough catalogues of these features [e.g. 2,3], commonly dividing martian paleolakes into two major categories: closed-basin lakes and open-basin lakes [e.g. 2,3]. The major distinction between the two is that closed-basin lakes have only a visible inlet valley [2], while open-basin lakes (OBLs) have both an observable inlet and outlet valley [2,3]. The presence of both an inlet and outlet valley means that water within the OBLs must have ponded to at least the level of the outlet valley before breaching and overflowing the basin, requiring a period of sustained fluvial activity on the surface of Mars [3].

Over 200 OBLs have been mapped in the ancient Noachian and Hesperian highlands across much of the planet [3], and recent work has shown that the majority of fluvial activity within the valley networks that feed these paleolakes ceased at or near the Noachian-Hesperian boundary [4]. Therefore, the OBL deposits currently present on the surface of Mars have had a ~3.7 Gyr [4,5] history that has been largely devoid of fluvial activity, during which a variety of geologic processes have acted to resurface, bury and exhume them. This study is presented as a comprehensive analysis of the morphologies associated with the entire catalogue of OBLs from [3] to help understand both the post-fluvial-activity history of these basins as well as the distribution of exposed lacustrine deposits within these paleolakes.

Datasets Used and Analysis: In order to examine the morphology of the OBLs, a combination of ~6 m/pixel imagery from the Context Camera (CTX) instrument aboard the Mars Reconnaissance Orbiter spacecraft [6], ~19 m/pixel imagery from the visible imager portion of the Thermal Emission Imaging System (THEMIS) instrument aboard the Mars Odyssey spacecraft [7] and ~50 m/pixel imagery from the High Resolution Stereo Camera (HRSC) instrument aboard the Mars Express spacecraft [8] were used. Each OBL in the catalogue from [3] was classified based on: (1) whether the OBL contains exposed deposits that appear to be lacustrine in nature; and (2) what, if any, type of process appears to have been the most recent cause of resurfacing. It should be noted that the classification of being resurfaced and having exposed lacustrine deposits are not mutually exclusive, as an OBL can be partially resurfaced while still containing exposed lacustrine deposits.

Three types of lacustrine deposits were identified in this survey, which include: (1) delta and fan deposits at OBL inlets (**Fig. 1A**); (2) layered deposits that are topographically below the OBL outlet and are completely confined to their host OBL (**Fig. 1B**); and (3) exposed, light-toned floor deposits that have a morphology consistent with other observed sedimentary deposits on Mars [9] (**Fig. 1C**).

In addition to indentifying the presence or absence of exposed lacustrine deposits, each OBL was classified on whether or not there appears to have been resurfacing subsequent to the lacustrine activity within the basin. Identified resurfacing units include volcanic, glacial and unknown in origin. Volcanically resurfaced OBLs are characterized by smooth plains deposits on their floors with high crater retention, wrinkle ridges and lobate margins that embay pre-existing deposits and topography (**Fig. 2A**). Glacially resurfaced OBLs are characterized by lobate floor texture and lobate ridges [10] and ring mold craters [11] (**Fig. 2B**), both typical of ice-related deposits. Finally, several basins appear to be resurfaced based on the presence of heavily eroded inlet and outlet valleys, a consistent surface texture both inside and outside the basin, and partially filled impact craters (**Fig. 2C**); however, there is no easily identifiable source for this resurfacing.

Results: From the 226 OBLs examined [3], 81 (35.8%) contain exposed lacustrine deposits, while 145 (64.2%) have no discernable evidence for lacustrine deposits. Additionally, all of the classified OBLs appear at least partially resurfaced. The most prominent identifiable resurfacing unit is volcanic, with 96 OBLs (42.5%) being identified as volcanically resurfaced, while only 19 (8.4%) are glacially resurfaced and 111 (49.1%) do not have a clear solitary source for resurfacing.

Discussion and Implications: Two primary observations arise from the global distribution of the classification presented here (**Fig. 3**). First, it is clear that there is a higher density of OBLs with lacustrine deposits in two distinct areas: Nili Fossae and northern

2MS^3-PS-02

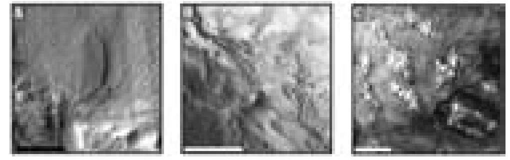

Fig. 1. Examples of exposed lacustrine deposits observed in open-basin lakes. Scale bars are 2 km. (A) Partially erored delta at 22.38^{0}S, 23.68^{0}W. (B) Layered deposit at 26.98^{0}N, 74.17^{0}E. (C) Exposed floor deposits at 4.37^{0}S, 1.171^{0}W.

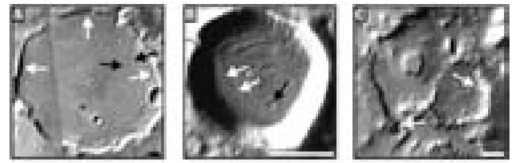

Fig. 2. Exampeles of the three identified resurfacing processes. Scale bars are 2 km. (A) Volcanically resurfaced open-basin lake at 12.45^{0}S, 157.11^{0}E. Note the smooth plains appearance and high crater retention. Black arrows indicate wrinkle ridges and white arrows indicate embayment of basin perimeter (crater rims). (B) Glacially resurfaced open-basin lake at 36.24^{0}S, 124.42^{0}W. Black arrows indicate ring-mold craters and white arrows indicate lobate debres apon deposits. (C) Resurfaced open-basin lake with unknown source of resurfacing at 0.61^{0}N, 91.28^{0}E. Note the consistent texture both inside and outside the basin. White arriws indicate partially buried impact craters.

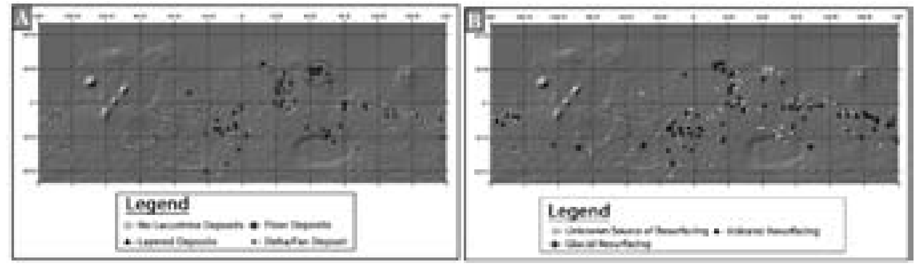

Fig. 3. Global distribution of the results. Background is MOLA hillshade [15] (A) Exposed lacustrine deposits classification. Areas with high concentrations of exposed lacustrine deposits (Nili Fossae and nothern Arabia Terra) are uotlined in dotted black lake resurfacing classification.

Arabia Terra (**Fig. 3A**, outlined areas), which is likely explained by either recent exhumation of lacustrine deposits within the OBLs in these areas and/or a higher sediment load during OBL lacustrine activity, which would have created thicker lacustrine deposits that have been preferentially preserved. Secondly, it is clear that while many of the volcanically resurfaced OBLs tend to cluster around clear volcanic sources such as Syrtis Major, Hesperia Planum and Apollinaris Mons (**Fig. 3B**), there also appears to be a clustering of volcanically resurfaced OBLs in areas such as Arabia Terra and Margaritifer Terra, which don't have as obvious a source of volcanism. This lack of an obvious volcanic vent requires a more localized source, perhaps in the form of large feeder dikes, which have been observed in Terra Tyrrhena and are thought to have emplaced regional expanses of Hesperian ridged plains [12].

While all of the examined OBLs do appear resurfaced to some degree, approximately one third of the investigated OBLs contain exposed lacustrine deposits, which may display primary sedimentary minerals. Although recent work has show that several of these paleo-lacustrine deposits contain a large variety of aqueous alteration minerals [e.g. 13,14], there appear to be far more OBLs with exposed lacustrine deposits (81) than there are OBLs with observed aqueous alteration minerals (16). This disparity is very striking and represents three possible scenarios: (1) thin resurfacing units, such as aeolian dust cover, are spectrally obscuring aqueous minerals within the lacustrine deposits; (2) currently analyzed spectral data over these exposed lacustrine deposits is at an inadequate resolution to detect any aqueous alteration minerals present; or (3) many exposed lacustrine deposits have a lithology that is primarily composed of non-aqueous alteration minerals, such as unaltered crustal material. While the first two mechanisms are certainly contributing to the observed disparity, determining the role played by unaltered crustal material in the makeup of exposed lacustrine deposits is very important for understanding the water chemistry associated with this early period of martian fluvial activity and will help to understand past martian climates.

References: [1] Goldspiel, J. and Squyres, S. (1991) *Icarus*. **89**:392. [2] Cabrol, N. and Grin, E. (1999) *Icarus*. **142**:160. [3] Fassett, C. and Head, J. (2008) *Icarus*. **198**:37. [4] Fassett, C. and Head, J. (2008) *Icarus*. **195**:61. [5] Hartmann, W. and Neukum, G. (2001) *Space Sci. Reviews*. **96**:165 [6] Malin, M., *et al*. (2007) *JGR*. **112**:E05S04. [7] Christensen, P., *et al*. (2004) *Space Sci. Reviews*. **110**:85. [8] Neukum, G. *et al*. (2004) *ESA Spec. Pub*. **1240**:17. [9] Malin, M. and Edgett, K. (2000) *Science*. **290**:1927. [10] Head, J. *et al*. (2008) *PNAS*. **105**:13258. [11] Kress, A. and Head, J. (2008) *GRL*. **35**:L23206. [12] Head, J. *et al*. (2006) *Geology*. **34**:285. [13] Ehlmann, B. *et al*. (2008) *Nature Geosci*. **1**:355. [14] Mustard, J. *et al*. (2008) *Nature*. **454**:305. [15] Smith, D. *et al*. (2001) *JGR*. **106**:23,689.

SURVIVAL OF HALOPHILES AT PRESENCE OF SULFATES AND PERCHLORATES

A.V. Bryanskaya[1], A.A. Berezhnoy[2], A.S. Rozanov[1], S.E. Peltek[1], A.K. Pavlov[3],
[1]Institute of Cytology and Genetics, SB RAS, Novosibirsk, Russia;[2] Sternberg Astronomical Institute, Moscow State University, Russia; [3] Ioffe Physical-Technical Institute, St. Petersburg, Russia. Contact: bal412003@mail.ru

Introduction: Earth's microorganisms can be delivered to Mars by impacts of meteoroids of Earth's origin and modern mission to Mars. To study of the possibility of survival of Earth's microorganisms on Mars, we need to select the most suitable types of them. Halophiles are one of the most interesting types of microorganisms, because salt solutions on Mars could be more widely distributed through subsurface Martian soil in comparison with pure liquid water. The existence of salt solutions that could serve as media for organisms analogous to halophilic archea at -23 °C and high salt concentrations on Mars has been widely discussed [1]. Study of the elemental composition of the Martian soils shows high concentrations of Cl [2], perchlorates [3], and solubable sulfates [4]. At Viking landing sites the content of perchlorates and organic carbon is estimated to be < 0.1% and 0.7 – 6.5 ppm, respectively [3]. High abundance of perchlorates around 1% was discovered at Phoenix landing site [5].

The aim of this study was to select bacterial and archeal strains most adapted to Martian conditions for the next step of our experiment about the possibility of the active growth of these microorganisms at dryness, low atmospheric pressure and other extreme conditions.

Methods: Bacterial (*Halomonas* sp. H8b, *Halomonas* sp. H12b, *Salicola* sp. H9b) and archeal (*Halorubrum* sp. H3a, *Halorubrum* sp. H13a) strains were isolated from different salt lakes of Altai region. Strains were grown in medium, which contained per liter 0-300 g NaCl, 5 g $MgCl_2$, 1 g KCl, 1 g $CaCl_2$, 4 g tryptone, 2 g yeast extract, and 10 ml of a trace metal solution, at 37 °C. For exposure experiments cells were plated on solidified growth medium with different concentrations (0, 1, 7, 30, 50%, where NaCl at 200 g/L was taken for 100%) of $NaClO_4$, Na_2SO_4, $MgSO_4$, respectively, and incubated at 37°C for 7 days. Cell numbers were estimated from CFU. At least three exposure experiments were performed.

Results: Results of a previous experiment on halophiles survival at various NaCl concentrations, various temperature and freezing conditions allowed us to discover strains that were the most resistant to NaCl and low temperature. For the present study, we took 5 of these 9 strains [6].

Perchlorates. Halomonas sp. H12b и *Halorubrum* sp. H13a were found to be the most resistant to various concentration of perchlorates (see Fig. 1). They could survive at up to 7% $NaClO_4$ with constant CFU/ml, ranging from 0 to 7%. At 50% $NaClO_4$ no growth of any strain was observed.

Sulfates. At 50% of sodium sulfate growth medium didn't polymerize due to disruption of interactions between gel-forming molecules [7], so we accepted 30% Na_2SO_4 concentration which enabled polymerization. *Halomonas* sp. H12b was the most resistant to sulfates, its CFU increase with increasing Na_2SO_4 concentration.

The same was observed for the *Halorubrum* sp. H3a strain; however, it failed to grow at 30% Na_2SO_4. CFU of all strains increased when sodium chloride was replaced by 1% sodium sulfate; at increased concentration; number of bacteria declined. Replacement of sodium chloride by magnesium sulfate was tolerated by all strains (see Fig. 1). For *Halomonas* sp. H12b strain, the addition of 1% magnesium sulfate resulted in increase of CFU, and for *Halomonas* sp. H8b и *Halorubrum* sp. H3a stains led to its reduction. For archeal strains (*Halorubrum* sp. H3a и *Halorubrum* sp. H13a), 7% magnesium sulfate stimulated microorganism growth, while 50% magnesium sulfate suppressed it.

Discussion: In previous experiment [6] with survival of halophiles at different salt concentrations and freezing cycles we found out that halotolerant bacteria belonging to the *Halomonas* genus had the widest growth ranges. Growth optimums of bacterial strains were shifted towards smaller NaCl concentrations (100, 200 g/L). Obligatory halophilic archeal strains had smaller growth ranges and had growth optimum at 200-300 g/L NaCl. Bacterial strains were more tolerant to different incubation temperatures. Archeal strains were less tolerant to freezing; the most significant mortality was detected at -70 °C, which was earlier demonstrated for the halophilic archeobacterium *Natronorubrum* sp. [8]. Best behavior at high content of sulfates is detected for *Halomonas* sp. H12b and *Salicola* sp. H9b, probably, due to the fact that molar concentration of salts decreases with increasing content of sulfates while *Halomonas* sp. H12b and *Salicola* sp. H9b have optimal growth at lowest NaCl content (100 g/L) in comparison with other microorganisms.

2MS^3-PS-03

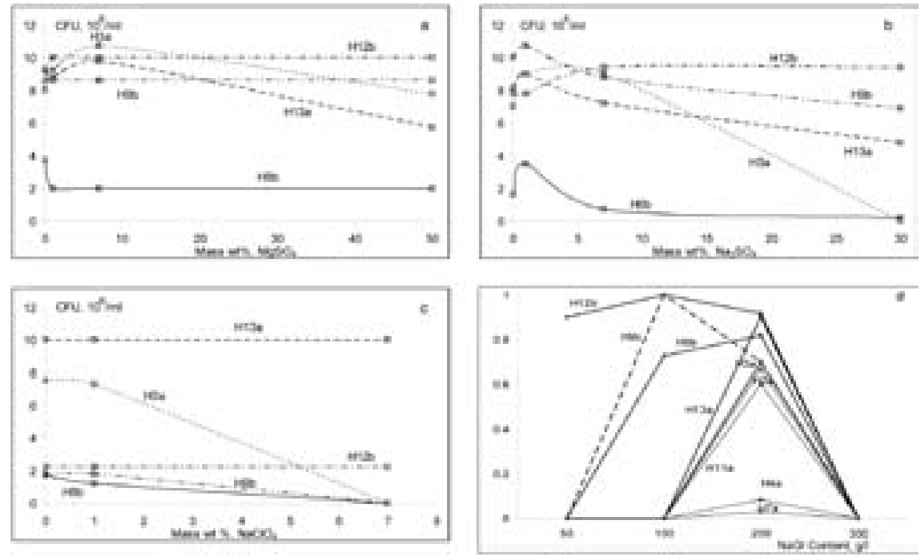

Fig. 1. Survival of microorganisms after freezing at -70 °C at different content of NaCl and $MgSO_4$ (a), Na_2SO_4 (b), $NaClO_4$ (c). Total salt content is 200 g/L. Survival of microorganisms after freezing at -70 °C at different content of NaCl (d).

As the result of these experiments, we determined the strains most resistant to wide range of extreme factor, the Halomonas sp. H12b и Halorubrum sp. H13a strains. The strains Salicola sp. H9b, Halomonas sp. H8b и Halorubrum sp. H3a were less resistant (in ascending order). In this case, archela strains were more tolerant to various salt concentrations, but less resistant to oscillations of various environmental parameters, while bacteria have can survive and reproduce in a very wide range of concentrations of various salts.

Judging from the results of our experiments, we can suggest that halophilic archea and halotolerant bacteria could be the analogs of Martian organisms, since they can survive wide mineralization ranges and low temperatures with the lowest decline of viability. There are two other main harmful factors of martian subsurface environments limiting survival of terrestrial bacteria. The first is a low atmospheric pressure and the second is high level of ionizing radiation producing by cosmic rays. In previos experiments have been demonstrated that the wild strain of Vibrio sp are able to reproduce under very low atmospheric pressure even lower of modern martian atmospheric pressure [9]. Also there are several types of high radiotolerant bacteria such as well known *Deinococcus radiodurance*. We are planning to study the impact both factors on halophilic bacteria. For future experiments on survival of microorganisms we are going to use *Halomonas* sp. H12b and *Halorubrum* sp. H13a.

Acknowledgements. The financial support by Integration Projects 10 and 131 of the Siberian Branch of RAS, RFBR 11-05-00717 is gratefully acknowledged.

References: 1. Litchfield C.D. Meteoritics and Planetary Science, Vol. 33, Is. 4, p. 813-819, 1998
2. Taylor G. J., Boynton W. V., McLennan S. M. et al. Geophys. Res. Lett., Vol. 37, Is. 12, CiteID L12204, 2010
3. Navarro-González R., Vargas E., de la Rosa J. et al. J. Geophys. Res., Vol. 115, Is. E12, CiteID E12010, 2010
4. Kounaves S. P., Hecht, M. H., Kapit J. et al. Geophys. Res. Lett., Vol. 37, Is. 9, CiteID L09201, 2010
5. Hecht, M.H., Kounaves, S.P., Quinn, R.C., West, S.J., Young,S.M.M., Ming, D.W., Catling, D.C., Clark, B.C., Boynton,
W.V., Hoffman, J., DeFlores, L.P., Gospodinova, K., Kapit, J. and Smith, P.H. Science, Vol. 325, p. 64–67, 2009
6. Bryanskaya A.V., Berezhnoy A.A., Rozanov A.S. et al. III International conference Biosphere, Origin, and Evolution, Rithymno, Crete, Greece, October 16 - 20, 2011, in press
7. Kevbrin V.V. Proceedings of Winogradsky Institute of Microbiology, Vol. 14, p. 374-392, 2007
8. Peeters Z., Vos, D., ten Kate I. L. et al. Advances in Space Research, Vol. 46, Is. 9, p. 1149-1155, 2010
9. A.K. Pavlov, V.N. Shelegedin, M.A. Vdovina and A.A. Pavlov International Journal of Astrobiology, Vol. 9 (1), p. 51–58, 2010

2MS³-PS-04

LASER BASED METHODS OF SURFACE COMPOSITION ANALYSIS FOR IN SITU PLANETARY EXPLORATION

C. d'Uston, *Institut de Recherche enAstrophysique et Planetologie , 9 Avenue du Colonel Roche , 31400 Toulouse, France. Contact: lionel.duston@cesr.fr*

Introduction:

True exploration field geology of the solar system planetary bodies has already begun in the past recent yearsOn Mars we have now done robotic geologic transects on the surface and reconnaissance geologic mapping. To characterise the encountered geologic units, various instruments have been developed which provide morphologic and spectroscopic data in order to get information on the composition of the surface materials and henceforth a glimpse at the history of the planetary body. Recently new methods of observations have been proposed and are developed to investigate details of the Martian geochemistry for the analysis of the chemical and mineral composition; they resulted from the investment in developing laser devices which make them miniaturised and ruggedized in order to fit the space travels conditions and to sustain the planetary surface environment. In this presentation, two methods recently made possible, will be described as they are part of selected set of instruments for the next missions of exploration: Laser Induced Breakdown Spectroscopy (LIBS), and Raman spectroscopy.

LIBS method:

The LIBS technique involves firing a focused, pulsed laser beam at targets to excite a light-emitting plasma. Spectral analysis identifies elements present and provides semi-quantitative elemental analyses (Figure 1). Typical spot size on a target is ~50micron in diameter. In combination with a co-aligned high resolution micro-imager (RMI), the knowledge of the exact position of this spot allows identifying the mineral context of the measurement.

Repeated laser pulses can be used to remove dust and to study and remove weathering coatings from rock samples in their field settings.

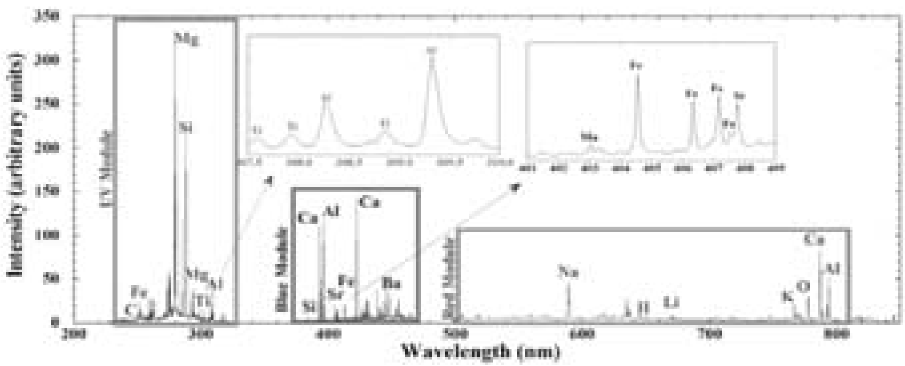

Fig. 1. LIBS spectrum obtained with CHEMCAM

LIBS analyses yield elemental compositions typically for H, Li, Be, B, C, N, O, F, Na, Mg, Al, Si, P, Cl, K, Ca, Ti, V, Cr, Fe, Ni, Zr, Rb, Sr, As, Ba, and Pb. In Martian environment, Carbon, N, and O abundances have interferences from atmospheric constituents, raising the C detection limit to ~2% wt. LIBS is particularly sensitive to the alkali and alkali earth elements, with some detection limits down to ~1 ppm at close range. On the other hand, LIBS is insensitive to halogens, with detection limits for F, Cl, S, and P in the range of several wt. %.

CHEMCAM is such an instrument ready to fly on board the rover Curiosity of Mars Science Laboratory mission. It uses a laser wavelength of 1064nanometer, and provide an energy of 16mJ per pulse at the exit; this allows to inject >1GW.cm^{-2} per pulse at a frequency of 15Hz, in the target at distance between 2m and 7m. It has been developed under responsibility of Dr. R. Wiens (LANL, PI) and Dr. S. Maurice (IRAP, Co-PI).

Raman spectroscopy method:

Raman Spectroscopy is used to analyse the vibrational modes of a substance either in the solid, liquid or gas state. It relies on the inelastic scattering (Raman Scattering) of monochromatic light produced by atoms and molecules. The radiation-matter interaction results in the energy of the exciting photons to be shifted up or down. The shift in energy gives information about the vibrational states in the system which appears as a spectral distribution or Raman spectrum. This spectrum therefore provides an unique fingerprint by which the substances can be identified and structurally analyzed.

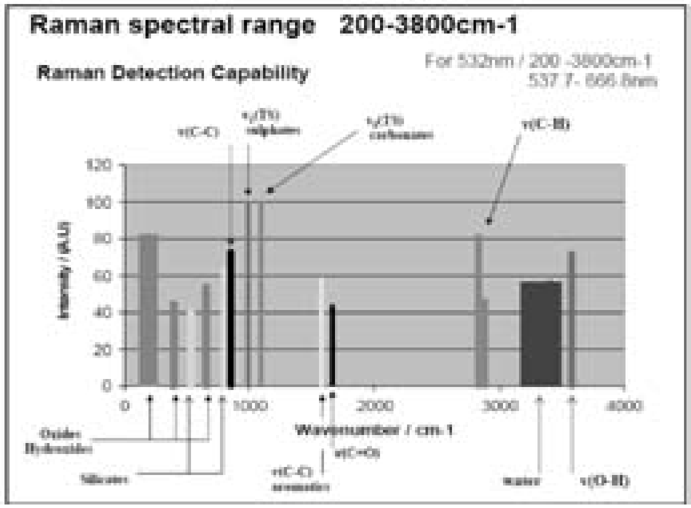

Fig. 2. Main wavelength domains in a Raman spectrum with identification of elements of interest.

From this, we determine molecular structure and composition. The energy difference between the laser and Raman shifted photon on longer wavelengths are called the "Stokes-Raman shift" or simply the "Raman Shifts" and the positions of Raman lines are given in wavenumbers (Figure 2). This makes Raman shifts independent of laser wavelength.

Minerals and organic functional groups have fingerprint Raman spectra suitable for their unambiguous identification. Compared to VIS-NIR and mid-IR emission or reflectance spectra, Raman peaks are sharp, non-overlapping, and nearly free of overtones and combinations. Peak positions and widths are maintained for grain sizes down to tens of nanometers. Minerals and organic species can be readily identified even in raw spectra of mixtures. Peak positions, not peak intensities, are used for both identification and quantification; deconvolution of spectra is in general unnecessary. Compare with XRD, species in the forms of gas, liquid, crystal and glass can all be characterized by Raman spectroscopy, there is no need for sample to be crystalline for detection.

The Raman Laser Spectrometer (RLS) is one of the Pasteur Payload instruments onboard ExoMars 2018. It will perform Raman spectroscopy on crushed powdered samples inside the Rover's ALD (Analytical Laboratory Drawer). It uses a continuous laser with an excitation wavelength of 533 nanometres of which the produced irradiance on the sample is 0.6kW.cm^{-2} with a spot size of 50 microns.

Future developments:

Other opportunities are under study with the goal of adapting the laser device to larger ranges of operating temperatures as could be necessary for a long duration exploration of the moon surface, or to implement complementary functionalities such as laser induced X-ray fluorescence spectroscopy (LIXS). The main advantage of these methods is that they are fast and very flexible. As a consequence, they will probably become a standard element of the scientific payload of in situ planetary exploration missions.

THE MESSENGER MISSION TO MERCURY: AN OVERVIEW OF RESULTS FROM THE ORBITAL PHASE.

James W. Head, III[1], Sean C. Solomon[2], and the MESSENGER Team, *[1]Department of Geological Sciences, Brown University, Providence, RI 02912, USA, [2]Department of Terrestrial Magnetism, Carnegie Institution of Washington, Washington, DC 20015, USA. Contact: James_Head@brown.edu*

The MErcury Surface, Space ENvironment, GEochemistry, and Ranging (MESSENGER) mission [1], a part of NASA's Discovery Program, was designed to answer six questions [2-6]: (1) What planetary formational processes led to Mercury's high ratio of metal to silicate? (2) What is the geological history of Mercury? (3) What are the nature and origin of Mercury's magnetic field? (4) What are the structure and state of Mercury's core? (5) What are the radar-reflective materials at Mercury's poles? (6) What are the important volatile species and their sources and sinks near Mercury? MESSENGER [7] has completed a complex interplanetary cruise phase [8] that involved three flybys of Mercury and successfully entered Mercury orbit on March 18, 2011 with its complement of instruments and experiments [9-16]. A summary of the mission and recent results is available online at http://messenger.jhuapl.edu/. A synthesis of results from the flybys and the orbital phase will be presented.

References: [1] S. C. Solomon et al. (2007) *Space Sci. Rev., 131,* 3-39. [2] J. W. Head et al. (2007) *Space Sci. Rev., 131,* 41-84. [3] W. V. Boynton et al. (2007) *Space Sci. Rev., 131,* 85-104. [4] M. T. Zuber et al. (2007) *Space Sci. Rev., 131,* 105-132. [5] J. A. Slavin et al. (2007) *Space Sci. Rev., 131,* 133-160. [6] D. L. Domingue et al. (2007) *Space Sci. Rev., 131,* 161-186. [7] J. C. Leary et al. (2007) *Space Sci. Rev., 131,* 187-217. [8] J. V. McAdams et al. (2007) *Space Sci. Rev., 131,* 219-246. [9] S. E. Hawkins, III, et al. (2007) *Space Sci. Rev., 131,* 247-338. [10] J. O. Goldsten et al. (2007) *Space Sci. Rev., 131,* 339-391. [11] C. E. Schlemm et al. (2007) *Space Sci. Rev., 131,* 393-415. [12] B. J. Anderson et al. (2007) *Space Sci. Rev., 131,* 417-450. [13] J. F. Cavanaugh et al. (2007) *Space Sci. Rev.*, *131*, 451-479. [14] W. E. McClintock and M. R. Lankton (2007) *Space Sci. Rev.*, *131*, 481-521. [15] G. B. Andrews et al. (2007) *Space Sci. Rev., 131,* 523-556. [16] D. K. Srinivasan et al. (2007) *Space Sci. Rev., 131,* 557-571.

EXPLORING MERCURY BY MEANS OF MIR SPECTROSCOPY: MERCURY RADIOMETER AND THERMAL INFRARED SPECTROMETER (MERTIS) FOR BEPICOLOMBO

G. Arnold, *German Aerospace Center, Rutherfordstr.2, 12489 Berlin.Contact: Gabriele.arnold@dlr.de*

MERTIS (Mercury Radiometer and Thermal Infrared Spectrometer) is an imaging mid infrared spectrometer to explore Mercury onboard ESA's cornerstone mission BepiColombo. The instrument is designed to study the surface composition, and surface temperature of Mercury. It combines a push-broom IR grating spectrometer (TIS) for the 7-14 (TIR) µm range with a radiometer for the 7-40 µm regions. TIS and TIR share the same optics and they use a uncooled microbolometer detector array. The paper summarizes the scientific goals and actual development status of the experiment.

TITAN IONOSPHERIC'S CAVITY AS EXPLORED BY THE PWA-HASI INSTRUMENT ON HUYGENS.

M. Hamelin, *LATMOS-IPSL-Université de Versailles, UPMC, T45, 4 pl. Jussieu, 75252 Paris, France, Contact: michel.hamelin@latmos.ipsl.fr*

Abstract: In January 14th, 2005, the Huygens probe performed a successful entry and descent in the atmosphere of Titan. The permittivity, waves and altimetry (PWA) instrument, a subsystem of the Huygens atmospheric structure instrument (HASI) measured in situ electrical conductivity of the atmosphere and electromagnetic waves in the ELF and VLF ranges from about 140 km down to the surface and continued to provide measurements on the ground during 30 additionnal minutes before the Cassini-Huygens loss of visibility and telemetry link cut. The Cassini Saturn orbiter completed these measurenents on the topside during close Titan flybys, the 140-1000 km altitude range remaining not covered by in situ measurements.

We present a review of published PWA results with some additionnal comments. Atmospheric conductivity profiles were measured by concurrent techniques (Mutual Impedance and Relaxation probes) revealing a low altitude ionized layer around 60 km caused by galactic cosmic radiation. Current models and measurements are in relatively good agrement up to about 90 km, but not above, where the measured conductivity vanishes possibly due to aerosol electron capture. Relaxation Probe measurements show either bubbles or layers without free electrons crossed along the descending trajectory. Electromagnetic waves were recorded in both ELF and VLF ranges with dedicated on board processing due to telemetry limitations. Relatively high amplitude emission for a Schumann resonance was detected around 36 Hz and was found natural after detailed investigation of possible artefacts. After several steps of investigation a credible model was built for both the strong wave generation through Titan interaction with Saturn's rotating magnetosphere, and for the resonant cavity boundaries. The model of a low conductivity upper Titan ground layer as suggested by the Cassini radar and PWA measurements, allowed to deduce the depth of the presumed buried H2O and NH3 ocean as about 45±15 km. In the VLF range some continuous emissions and low energy bursts were observed without clear identification of the involved processes. Finally a comment will be raised on papers that used the public PWA data with fully erroneous procedures, claiming the evidence of lightning activity on Titan.

COUPLING AEROSOL MICROPHYSICS AND ATMOSPHERIC DYNAMICS IN THE 3D MODEL OF TITAN ATMOSPHERE.

A. V. Rodin[1,2], I.V. Mingalev[3], K.G.Orlov[3], Yu.V.Skorov[4], A.V.Burlakov[2]. *[1]Moscow Institute of Physics and Technology, Russia, [2]Space Research Institute, Russia, [3]Polar Geophysical Institute, Russia, [4]Technical University of Braunschweig, Germany. Contact: Alexander.Rodin@phystech.edu*

Introduction: Titan presents an example of rich and unusual climate system, including the complex 'carbohydrological' cycle, which in some aspects resembles the Earth' water cycle with hydrocarbons replacing H_2O molecule. On the other hand, due to relatively slow rotation, the dynamics of its dense and optically thick atmosphere has many similarities with that of Venus, such as zonal superrotation. Like on Venus, the dynamics of Titan atmosphere is deeply coupled with aerosols, which affect radiative forcing. Deep, optically thick tholin haze layer in the Titan atmosphere is a result of complex organic chemistry and microphysical processes, including charging, coagulation and condensation of hydrocarbons [1]. The specific feature of the Titan atmosphere is its exceptional vertical extent compared to relatively small size of the satellite. This implies the possibility of strong contribution of non-hydrostatic effects to the atmospheric circulation.

The dynamics of Titan atmosphere has been of great interest for numerical modeling long ago[2]. We present the first non-hydrostatic model based on the full gas dynamics equation system[3]. The model predicts zonal superrotation driven by the diurnal thermal tide, as well as circumpolar vortices. The model includes tholin aerosols treated as passive tracers, with microphysical transformation rates calculated offline. The goal of simulations is the comparison with Cassini/Huygens data.

General circulation model: The model is based on the non-hydrostatic dynamical core on the grid including 512 nodes with fixed step of 500 m in altitude and optionally, either non-uniform triangular grid or uniform grid with 128 nodes in longitude and 64 nodes in latitude. Radiative forcing is replaced by a simple relaxation scheme with mean time constant of 20h and relaxation thermal profile derived from observations. Equator-to-pole and pole-to-pole thermal contrasts are control parameters of the model. No topographical forcing is included. Up to 40 passive tracers are included in the model to represent different size categories of tholin aerosols.

Microphysical model: The model includes charging due to photoelectric effect and accretion of ions and electrons from the atmosphere and coagulation, driven primarily by the Brownian motion and Coulomb forces. Coagulation equation is solved on the logarithmic size grid with a range from 10 nm to 10 μm. Spatial redistribution of particles is controlled by advection in the atmospheric flows, sedimentation and eddy diffusion. To mimic the subgrid effects of eddy mixing and wave transport, the formalism of fractional diffusion implemented in the vertical domain.

Results: The model reproduces zonal superrotation with the maximal velocity in the core of the equatorial jet reaching 200-240 m/sec in the altitude range 200-300 km. Mesoscale circumolar vortices are formed in the latitude range 60°-70°. Vortices are centered in the antipodal points 5°-10° off the poles, with the vortex in the summer hemisphere located near the morning terminator. The model develops circulation pattern with quantitative parameters in agreement with observations. Wide midlatitude superrotation core with the amplitude 200-240 m/sec appears in the altitude range 200-300 km. Zonal wind speed decreases above these altitudes and increases again above 400 km. Wind velocity field reveals modulation with zonal wavenumbers 2 and 4 features, which may explain the diurnal variations of the Titan surface temperature retrieved from CIRS observations [5]. Wind field discontinuity near the tropopause observed by the Huygens probe is reproduced as a result of tidal wave propagating in the medium with discontinuous static stability. Distribution of tholins is consistent with 1D simulations and reveals wave-2 and wave-4 zonal modulation.

Acknowledgements: The work has been supported by RFBR grant 10-02-01260-a

References:

1. Del Genio A. D., Zhou W. Simulations of superrotation on slowly rotating planets: sensitivity to rotation and initial conditions. // Icarus, 1996. V. 120, 332–343.
2. Krasnopolsky, V.A. A photochemical model of Titan's atmosphere and ionosphere. Icarus 2008, DOI: 10.1016/j.icarus.2008.12.038.
3. Mingalev I.V., Mingalev V.S., Mingalev O.V., Kazeminejad B., Lammer H., Birnat H.K., Lihteneger H.I.M., Schvingenschu K., Ruker H.O. Numerical simulation of circulation of the Titan's atmosphere: Interpretation of measurements of the Huygens probe // Cosmic Research. 2009. V.47. P.114–125.

POSSIBLE MECHANISMS OF SATURN'S AURORA GENERATION.

E. S. Belenkaya[1], S. W. H. Cowley[2], J. D. Nichols[2], V. V. Kalegaev[1], M. S. Blokhina[1], *[1]Institute of Nuclear Physics, Moscow State University, Vorob'evy Gory, 119992 Moscow, Russia, [2]Department of Physics & Astronomy, University of Leicester, Leicester LE1 7RH, UK. Contact: elena@dec1.sinp.msu.ru*

Abstract: Mapping of Saturn's auroras into the magnetosphere is fulfilled using UV images of the southern dayside oval obtained by the Hubble Space Telescope (HST) and a paraboloid model of the magnetospheric magnetic field. The model simulates prevailing conditions in the interplanetary medium, corresponding to high solar wind dynamic pressure and variable interplanetary magnetic field (IMF) strength and direction determined from suitably lagged field data observed just upstream of Saturn's dayside bow shock by the Cassini spacecraft. Two out of four images obtained in February 2008 when such simultaneous data are available are examined in detail, exemplifying conditions for northward and southward IMF. The model field structure in the outer magnetosphere and tail is found to be very different in these cases. Nevertheless, the dayside UV oval is found to have a consistent location relative to the field structure in each case. The poleward boundary of the oval is located close to the open-closed field boundary and thus maps to the vicinity of the magnetopause. The equatorward boundary of the oval then maps typically near the outer boundary of the equatorial ring current. Similar results are also found for related images from the January 2004 HST data set. These new results show that if the radial plasma transport is dominated by centrifugally driven flux tube interchange motions, leading to creation of the primary source of precipitating auroral particles at the outer dayside boundary of the plasma sheet and equatorial ring current, an aurora generation at the equatorward UV oval edge could arise. On the poleward UV auroral oval edge located near the boundary between open and closed field lines a ring of upward-directed currents should flow due to the velocity shift existing between open and closed field lines.

NEW METHODS FOR THE DETECTION OF PLASMA LAYERS IN THE IONOSPHERE DURING RADIO OCCULTATION.

A. L. Gavrik, Y. A. Gavrik, T. F. Kopnina, *Kotel'nikov Institute of Radio Engineering and Electronics of RAS, Fryazino, Russia, alg248@ire216.msk.su*

Introduction: The explorations of Venus with spacecraft began 40 years ago. By now, several spacecrafts have conducted more than 800 radio occultations of the Venusian ionosphere. Twenty-five percent of these probings were performed with the use of the "Venera-15" and "Venera-16" orbiters. A theoretical analysis showed that the possibilities of the radio occultation method can be extended. New methods make it possible to reliably separate the effects of the noise, ionospheric plasma, and neutral atmosphere on the occultation results, thus allowing detection and investigation of the fine structure of ionosphere. To test the new method, we used the recorded data on the field intensity of the coherent signals (wave length 32 and 8 cm) from the "Venera-15" and "Venera-16" orbiters. The uniqueness of these experimental data lies in the fact that the recorded effects of the ionospheric plasma are six times stronger than the effects observed during Venus missions accomplished by other countries (wave length 13 and 3 cm). It means that more accurate profiles of the electron concentration in the ionosphere can be obtained, a circumstance that is of special importance in detecting and studying low density plasma layers at low altitudes and in the nighttime ionosphere.

The objective of the present study is to obtain new information on the Venusian ionosphere through the use of more sophisticated methods for analyzing the results of the radio occultation performed by the "Venera-15" and "Venera-16" orbiters.

Procedure for detecting the layered structures: Precise determination of the power and phase of the two coherent signals not only provides verification of theoretical relationship, but also allows reliable separation of the effects of plasma, atmosphere, and noise on the radio probing results. To perform the analysis, it is necessary to determine, from the experimental data, the refraction attenuations of the two signals $X_{DM}(t)$ (L-band 32 cm) and $X_{CM}(t)$ (8 cm) as functions of time and find the reduced frequency difference $\delta f(t)$ from the signal phase measurements. From variations $\delta f(t)$, frequency variations of the L-band signal $\Delta f(t)$ can be recovered and, with the use of relationship $X_{\Delta f}(t)=1+k\cdot d/dt[\Delta f(t)]$, predicted refraction attenuation of the L-band signal $X_{\Delta f}(t)$ can be determined.

Obtaining of frequency variation $\Delta f(t)$ from reduced frequency difference $\delta f(t)$ allows us to investigate solely the effect of the plasma and eliminate the effects of the neutral atmosphere, instabilities of the on-board oscillator, and trajectory data errors. Coincidence between variations of refraction attenuation of the radio signal $X_{DM}(t)$ and variations $X_{\Delta f}(t)$ will be indicative of the influence of the regular structures of the ionosphere under investigation, an indication that follows from obtained relationship: the variations in the probing signal frequency during ionosphere probing will be in one-to-one correspondence with the refraction attenuation. The absence of this correspondence is an indication of the influence of the noise or other factors that are not taken into account.

Conclusions: The processing of the experimental data ("Venera-15" and "Venera-16") has resulted in the discovery of a new region of ionospheric plasma in the daytime Venusian ionosphere at altitudes from 80 to 120 km. The detection of layers with low concentration of ionospheric plasma was possible owing to the establishment of the linear relationship between the variations of the independent radio signal parameters and to the precision determination of the power and phase of the coherent signals. This circumstance considerably increased the sensitivity of the radio probing method to refractive index variations.

It is shown that a considerable ratio between plasma influence in the L-band signal parameters and equipment noises provides high precision of determination of Venus ionosphere parameters. Presented new method of plasma layers detection makes possible to detect small variations in electron density and reveals wave phenomena in the planets ionosphere during occultation. It is shown that new radio physical experiments in which the on-board equipment of orbital spacecrafts receives coherent radio waves transmitted from the ground-based station and measures the power and phase of these waves are needed to increase the sensitivity of radio occultation observations. These experiments will enable one to increase the capacity of the radio link by a factor of about 10 compared with that of traditional experiments, thus increasing the accuracy of the results and the space-time resolution of radio occultation of the ionosphere and the atmosphere of a planet.

Acknowlegements: This work has been partly supported by program of Russian Academy of Science № VI.15.

NON-HYDROSTATIC GENERAL CIRCULATION MODEL OF THE VENUS ATMOSPHERE.

A. V. Rodin[1,2], I.V. Mingalev[3], K.G.Orlov[3]. *[1]IMoscow Institute of Physics and Technology, Russia, [2]Space Research Institute, Russia, [3]Polar Geophysical Institute, Russia. Contact: Alexander.Rodin@phystech.edu*

Introduction:

The dynamics of the Venus atmosphere has long been a challenge for general circulation models. Recent developments [1,2] resulted in successful simulation of zonal superrotation, which appear in good agreement with observations. There are numerous indications, such as mesoscale vortices, strong vertical motions, the importance of centrifugial forces and others, suggesting that non-hydrostatic effects may play an important role in the atmospheric dynamics. We present a new generation gas dynamical general circulation model of the Venus atmosphere. The goal of simulation was to study the mechanisms of the initial phase of superrotation development, and to explore sensitivity to initial conditions and external parameters.

The model:

The general circulation model is based on the numerical solution to the full equation set describing viscous, elastic gas dynamics on the rotating sphere. It uses a uniform grid with 128 nodes in longitude, 64 in latitude and 512 in the vertical, with a fixed vertical step of 200 m. High vertical density and corresponding time step imply serious limitations to the model performance. However, taking advantage of hybrid calculations using CUDA technology, the model is able to run over time period comparable with few Venusian sols. With realistic initial conditions, this period is sufficient to achieve quasi-steady state of the circulation.

The model has two options of the energy balance description. In the first case, a simple relaxation approximation is used. In the second case, atmospheric radiation fluxes are calculated using line-by-line algorithm. In order to increase performance, radiative transfer calculations are repeated with variable time step depending on altitude. Wind field with retrograde zonal direction and linear increase from the surface to cloud level was adopted as the initial condition.

Results:

The model reproduces zonal superrotation with the maximal velocity in the midlatitude jet reaching 80-100 m/sec in the altitude about 70 km. Mesoscale circumolar vortices are formed at the morning terminator above 60°-70° in latitude. Depending on thermal forcing, vertical structure of the Hadley cell and midlatitude jets may split in two independent cells, with the retrograde cell in between. In this case a strong downward motion appears near 60° latitude, and mean meridional flow converges at these latitudes. Above 60 km, circumpolar vortex reveals variable structure with zonal wavenumbers up to 3, consistent with observations[3].

Acknowledgements: The work has been supported by RFBR grant 10-02-01260-a

References:

1.[1] Lebonnois,,S., Hourdin,,F., Eymet,,V., Crespin,A., Fournier,,R.,Forget,,F. Superrotation of Venus atmosphere analysed with a full General Circulation Model. J. Geophys. Res., 2010. V.115:E06006, DOI 10.1029/2009JE003458

[2] Lee,,C., Lewis,S.,R., Read,,P.,L. Superrotation in a Venus general circulation model. J. Geophys. Res., 2007. V.,112:E04S11, DOI 10.1029/2006JE002874

[3] Piccioni, G., Drossart, P., Sanchez-Lavega, A., et al. South-polar features on Venus similar to those near the north pole. Nature, 2007. V. 450. No 7170. P. 637-640

COMET'S, AS A HUGE FRIABLE DUST PARTICLE – A GOOD PLACE FOR FORMATION OF MOLECULES OF THE TERRESTRIAL LIFE. "LIFE", AS PARAMETER OF COMPLEX SYSTEMS.

I. A. Maslov[1,2], [1]*Space Research Institute RAS, ul. Profsouznaya 84/32, Moskow, GSP-7, 117997 , Russia;* [2]*Sternberg Astronomical Institute, Moscow State University, Universitetsky pr. 13, Moscow 119992, Russia. Contact: imaslov@iki.rssi.ru*

Observations:

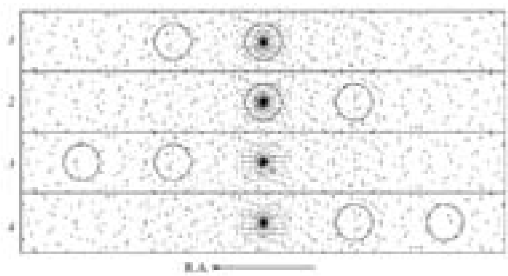

Fig. 1. Photometric observations of the comet C/2004 Q2 (Machholz) were spent from December 2004 to April 2005 on 1.25-m telescope at Crimean Laboratory of Moscow Sternberg Astronomical Institute (Crimea, Ukraine) in five standard infrared bands: JHKLM. The measurements were spent at four positions of a diaphragm (diameter 12 arc sec) of a photometer concerning the center of a comet. Two zones of sensitivity at distance 20-40 arc sec arise because of internal modulation in a photometer. The result is difference of signals from these zones.

Data:

The presented data [1] show, that: (1) the coma in the central part can have smaller brightness than on periphery. (2) Correlation between signals in zones with delay day and more from the center to periphery is observed.

Approximations:

We approximated our data by the sum of the scattered and thermal radiations:

$$B_\lambda = E_{\lambda o} / \pi * A_{1.65} (1.65/\lambda)^\alpha + P_\lambda(\lambda, T_\#) * Q_{4.7} (4.7/\lambda)^\beta,$$

where B_λ – spectral brightness, $E_{\lambda o}$ – solar illumination near the comet, $A_{1.65}$ – coefficient of brightness (albedo) at 1.65 μ, λ – wavelength, $P_\lambda(\lambda, T_\#)$ – Planck's function, $Q_{4.7}$ – optical thickness at 4.7 μ, α, β – constants. Dust particles heat up to equilibrium temperature $T_\#$: $4 * T_\#^{4+\beta} R_\#^2 = T_o^{4+\beta} R_o^2$,

where T_o=5770 K – effective temperature of the Sun, $R_\#$ – distance of a comet from the Sun, R_o – radius of solar photosphere.

Results:

The comet lost substance in the form of cold large fragments (α=0.17±0.20) which were divided into gas and a small dust particles (β=0.99±0.19) for a day and longer. Speed of fragments exceeded 0.3 km/s. It show that the comet has friable structure.

Hypothesis:

Self-reproduction molecules have arisen on a surface of comets, and have been protected by new external layers. Basis for this hypothesis: (1) the structure of comets surface at epoch of its forming is friable; (2) stochastic formation of molecules on cold particles of the complex form is very effective; (3) terrestrial oceans are forming of due to falling the comets. Probably, at the first stage of occurrence of a life, liquid water is harmful. This stage passes at the low temperatures and during long time scale of 10^9 years. On the Earth were suitable conditions for the self-reproduction molecules and their number was multiplied up to such degree that natural selection has begun at the time-scale of 10^6 years.

Scheme:

Deep Impact experiment and our astronomical observations [1] have shown that external layers of comets have very friable structure. Calculations show that stochastic formation of organic molecules on cold particles of the complex form is very effective [2]. It is possible that terrestrial oceans are forming of due to falling the comets [3]. Deep Impact and Stardust experiments have shown the big abundance of organic molecules in substance of comets. It allows us to draw the following scheme of occurrence of a life on the Earth.

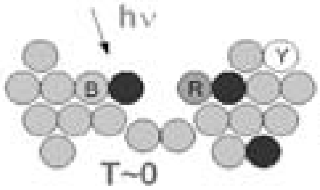

Fig. 2. During the formation of a comet, complex molecules form on its surface. Favourable conditions!!!: a porous surface, almost zero temperature and presence of external radiation.

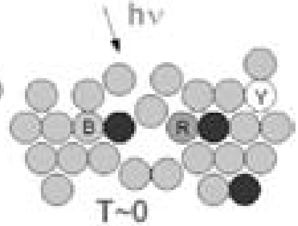

Fig. 3. These molecules are protected from further disintegration by an accumulating external layer of material. There have arisen self-reproducing molecules but the time of their reproduction due to such low temperatures is very large.

Fig. 4. Some comets which are passing close to the Jupiter, are thrown in an internal part of Solar system and are falling on the Earth surface.

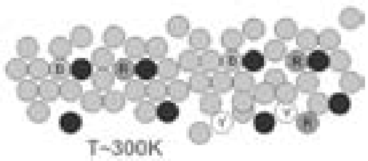

Fig.5. After comets impact on the surface of the Earth they release water (forming puddles), organic material and self-reproducing molecules. Temperatures of approximately 300 K result in a sudden increase in the rate of reproduction.

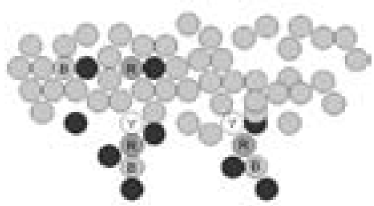

Fig. 6. Once the organic material in these puddles diminishes, natural selection among the self-reproducing molecules begins. Forms, which can change their structure to protect itself in the future, using an available external information, appear and survive. Life is born.

But what is the Life?:

May be it is possible to measure its presence in the complex system by using mathematical parameter?

(1) Occurrence of a life is improbable event; (2) if the life arises, its disappearance is improbable, too. These two probabilities define life-parameter of structure or the phenomenon:

«Life» ~ - log(Po · Pd),

were Po << 1 — probability of the occurrence, Pd << 1 — probability of the disappearance.

References: [1] Maslov I.A. et al. (2008). Astromomy Letters, 34, 353.
[2] Stantceva T., Shematovich V. I., Herbst E. (2002) . Astronomy and astrophysics, 391, 1069.
[3] Morbidelli A. et al. (2000). Meteoritics & Planet. Sci., 35, 1309.

RUSSIAN PLANS FOR SOLAR SYSTEM INVESTIGATION AND EXPLORATION

L.M. Zelenyi, *Space Research Institute (IKI), Moscow. Contact: lzelenyi@iki.rssi.ru*

The report presents an overview of the Russian mission to planets, their moons and small bodies of the Solar system which have been supported by the Russian Space Agency for the launch during the current decade or considered as a Phase A studies for the flight in the next decade.

In particular, the earliest missions are Luna-Glob and Luna-Resource, an orbiter and two landers, which are prepared now for operations in 2013 and 2014. Other important missions which are planned for this decade (or beginning of the next one) are mission to the Moon (stager 2) landers for Mars and Venus and very interesting and challenging expeditions to the Moons of Jupiter and one of Near Earth asteroids.

SEIS: A POSSIBLE VBB SEISMOMETER FOR THE FUTURE MARS-NET RUSSIAN MISSION

P. Schibler[1,2,3], P. Lognonne[1,2,3], T. Nébut[1,2,3], [1]*Institut de Physique du Globe de Paris, 4 avenue de Neptune, 94100 Saint-Maur, France;* [2]*CNRS;* [3]*Université Paris Diderot. Contact: schibler@ipgp.fr*

Introduction: Following the invitation from IKI for participating to the future Russian Mars-Net mission, our objective is to realize a preliminary study for the deployment of a seismometers network, on the surface of Mars. This experiment would be realized thanks to the "basic brick" of the planetary seismometer developed by IPGP: a Very Broad Band (VBB) axis/pendulum adapted to the Mars-Net mission but analog to the one already proposed for other missions (Humboldt-ExoMars, Selene 2, Discovery GEMS). In order to respect, as much as possible, the mass and power budgets of the Mars96/OPTIMISM seismometer, we plan to propose only one axis/pendulum modified to become vertical. This adaptation could be, for instance, simply realized by adding an additional mass and modifying the axis tilt. Compared to the seismic sensor proposed for GEMS, there would be a deployment on Mars without any uncoupling from the lander. So, we estimate that the performances of the Mars-Net seismometer (< 0.1 ng/Hz$^{1/2}$) will be halfway between OPTIMISM (1 ng/Hz$^{1/2}$) and GEMS (< 0.05 ng/Hz$^{1/2}$) seismometers.

Scientific objectives: Since the projects Mesur/InterMarsNet in 1990 years then NetLander in 2000 years, our knowledge of interior of Mars has progressed. A network mission about 2018-2020 has to take into account these evolutions. However a lot of questions are still open without any answer. Which is the seismic activity of the planet? Which is the average thickness of the crust? Which is the detailed mineralogy of the mantle? Is there thermical heterogeneities inside mantle associated to a remaining of contemporary mantlellic convection? Which is the fine structure of the core?

Therefore one of the first objectives of a network mission is the seismic discovery of Mars. That means, in particularly, to obtain for the first time the quantification of the contemporary seismic activity of the planet and the determination of the absolute thickness of the crust. That will be possible with the first station. But, of course, with the deployment of other stations it will be possible to inverse more elaborated models of the internal structure of Mars by using

- seismic data exploitable by one station: differential arrival times of known meteorites impacts, Love number extracted from the signal of solid tide (stacked on one year), modal frequencies extracted from analysis of normal modes (excited by a few quakes of magnitude greater than 5), data from Martian atmosphere due to meteorological network;
- seismic data exploitable by two stations: times of surface waves propagation obtained by cross-correlation between two stations, principal and secondary phases of impacts data;
- then all other data from seismic network, exploitable by three stations and more;

Instrument description: The heritage, at IPGP, of planetary seismometers was often presented. Our accommodation study will be, obviously, based on this heritage. The idea is to reuse our "basic brick", that means the recurrent pendulum of ExoMars mission by aiming the same performances in terms of resolution. On the other hand, we will aim the OPTIMISM-Mars96 specifications in terms of mass, volume and power budgets.

Fig. 1. OPTIMISM Flight Model 3 (vertical axis)

Figure 2: NetLander, ExoMars Phase B breadboard of VBB oblique axis

OPTIMISM seismometer specifications:

- Bandwidth: 0.02 – 2 Hz
- Volume: 9x9x9.5 cm
- Power: 67.5 mW under 15 V
- Sampling rates: 4, 1, ¼ sps
- Mass: 405 g
- Data: 1 Mbits/day expected

Concept proposed for Mars-Net network: Taking in account the preliminary lander mass budget, we will propose only one axis, by using an oblique VBB axis and by tilting it until its sensibility axis became vertical. We would bring back the gravity center of the whole on the sensibility axis by adding a 50g mass on OG axis (become horizontal). The figure below is showing an explanatory plan. We already used a counterweight for ExoMars mock-up: pendulum is equilibrated for Martian gravity, so for terrestrial tests we have to add a counterweight.

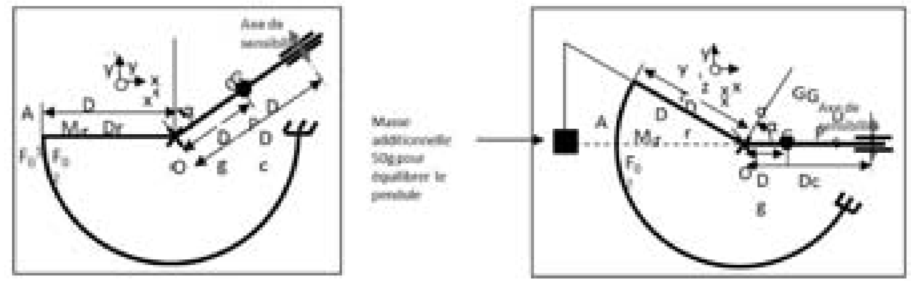

Fig. 3.

	VBB – ExoMars version	'vertical' VBB
Mobil mass (kg)	0,102	0,152
Modal frequency (Hz)	0,68	0,95
Moment of inertia (kg.m²)	2,53e^{-4}	4,74e^{-4}
Mechanical gain (s²)	0,05	0,008

Parameter differences between the two models: ExoMars and Mars-Net

Technical points to study: During the preliminary study, several points will be particularly examined, without waiting for the phase A of the mission.

At instrument level:

- Mechanical sturdiness of the whole to take in account hard landing specifications
- Mechanical simulation of the tilting and of the pivot to obtain a vertical pendulum
- Leveling by gravity (as for OPTIMISM concept)
- New definition of the sphere containing the pendulum

At system level:

- Mechanical interfaces, mass budget, coupling with ground
- Electrical interfaces, harness definition, power budget
- Data budget, data acquisition

References: [1] B.Banerdt, Chicarro A.F., M. Coradini, F. Federico, R. Greeley, M. Hechler, J.M. Knudsen, C. Leovy, P.Lognonné, L. Lowry, D. Mc Cleese, C. McKay, R. Pellinen, R. Philipps, G.E.N. Scoon, T. Spohn S. Squyres, F. Taylor and H. Wänke. InterMarsnet, Phase A study report, ESA Pub, SCI(96)2, 1996. [2] P. Lognonné, V.N. Zharkov, J.F. Karczewski, B. Romanowicz, M. Menvielle, G. Poupinet, B. Brient, C. Cavoit, A. Desautez, B. Dole, D. Franqueville, J. Gagnepain-Beyneix, H. Richard, P. Schibler, N. Striebig, The Seismic Optimism Experiment, Planetary Space Sciences, 46, 739-747, ,doi : 10.1016/S0032-0633(98)00009-9, 1998. [3] Linkin, V., A.M. Harri, A. Lipatov, K. Belostotskaja, B. Derbunovich, A. Ekonomov, L. Khloustova, R. Krmenev, V. Makarov, B. Martinov, D. Nenarokov, M. Prostov, A. Pustovalov, G. Shustko, I. Jarvine,, H. Kivilinna, S. Korpela, K. Kumpulainen, R. Pellinen, R. Pirjola, P. Riihela, A. Salminen, W. Schmidt, T. Siili, J. Blamont, T. Carpentier, A. Debus, C.T. Hua, J.F. Karczewski, H. Laplace, P. Levacher, P. Lognonné, C. Malique, M. Menvielle, G. Mouli, J.P. Pommereau, K. Quotb, J. Runavot, D. Vienne, F. Grunthaner, F. Kuhnke, G. Mussman, R. Rieder, H. Wanke, T. Economou, M. Herring, A. Lane, C. McKay, A sophisticated lander for scientific exploration of Mars: Scientific objectives and Implementation of the Mars96 Small Station, *Planetary Space Sciences*, **46**, 717-737, doi:10.1016/S0032-0633(98)00008-7, 1998. [4] Gudkova, T., Lognonné, P. , Gagnepain-Beyneix, J., Seismic source inversion for Large impacts detected by the Apollo seismometers, Planet. Space. Science, in press, 2010

A PLANETARY BROAD BAND SEISMOMETER ON SELENE-2 / GEMS2 MISSIONS: FOCUS ON VBB TECHNICAL IMPROVEMENTS

T.Nébut[1], J.Gagnepain-Beyneix[1], P.Lognonné[1], N.Kobayashi[2], D.Giardini[4], U.Christensen[5], S. de Raucourt[1], D.Mimoun[6], M.Bierwirth[5], P.Zweifel[4], S.Tillier[1], O.Robert[1], N.Escande[1], T.Gabsi[1], B.Lecomte[1], O.Pot[1], D.Mance[4], R.Roll[5], H.Shiraisi[2], R.Garcia[7], R.Yamada[2], A.Mocquet[8], B.Banerdt[3], S.Tanaka[2],
[1]IPGP, Paris, France, [2]ISAS/JAXA, Sagamihara, Japan, [3]JPL, Pasadena, USA, [4]ETHZ,Zurich, Switzerland, [5]MPS, Lindau, Germany, [6]ISAE, Toulouse, France, [7]IRAP, Toulouse, France, [8]LPGN, Nantes, France. Contact : nebut@ipgp.fr

The Moon will be explored during the next decade by a series of missions, especially from Japan,

China, India and USA. We present here the status of the development of space qualified Very Broad Band seismometer in Europe. This instrument, completed by Japanese Short Period Seismometers, is called Lunar Broad Band Seismometer (LBBS). It is considered for the Japanese project SELENE-2 and US project GEMS2. The main scientific goals of SELENE 2 are to determine the internal structure of the whole Moon and more specifically the composition and size of the lunar core.

The LBBS instrument is the result of an international consortium:

- A 3-axis short period (SP) seismometer (ISAS/JAXA)
- A 3-axis very broad band (VBB) seismometer (IPGP)
- A deployment system (DPL) (MPS)
- A data acquisition system (SEIS-AC) (ETHZ)

Both SP and VBB development rely on technical heritage of cancelled space missions (LUNAR-A for the SP, Netlander & Humboldt/ExoMars for the VBB).

This technical development lead VBB to reach a Technical Readiness Level (TRL) above 5 (ESA ExoMars PDR), and we aim at TRL 6 within the next few months.

The adaptation of the VBB from Mars to Moon conditions and environment is challenging. The resolution has to be improved by a factor of ten and should be inferior to 2.10^{-11}m/s²/sqrt(Hz) @ 0.1 Hz while the Instrument are supporting very large temperature variations (several 10s of degrees) compared to those of typical VBB seismometers.

Two technical axis have been considered to reach the scientific goals : on one hand take advantage of Netlander's development and studies and achieve the work already done, on the other hand new developments are presently tested at IPGP.

For Netlander development, an analytic theoretical noise study of every subsystem has been realized and corroborated with field experimental measurements. It appeared that a trade-off between resolution and VBB thermal sensibility was possible. A passive thermal compensation device was designed and tested at IPGP reducing VBB thermal sensitivity by a factor of 12, and we aim at a factor of 20. It will be possible to improve the resolution consequently if thermal sensitivity is reduced.

For Moon missions VBB developments, efforts have been made both on mechanical design and Displacement Capacitive Sensor (DCS). The mechanical part of VBB is an inverted pendulum; the theoretical study we made shows that the mechanical gain can be improved by a factor of 3 to 5. The DCS geometry has been modified : By improving the size and reducing the gap of the electrodes, the Signal to Noise Ratio will be improved; we also designed a DCS prototype with selectable active or passive electronics on the sensor head. The aim is to enlighten the role of power dissipation on the long-term global VBB noise.

All these technical modifications have been realized on two VBB breadboards. The tests are undergoing this autumn in the urban seismic vault of the IPGP observatory in Saint Maur. Then all LBBS subsystems will be assembled and a field measurement campaign in low noise seismic site is foreseen, probably in BFO (Black Forest Observatory). Once the whole LBBS breadboard has been tested in relevant environment, the TRL will be close to 6.

SCIENTIFIC ASPECTS OF THE MEIGA PAYLOAD FOR MARS METNET MISSION

Luis Vázquez[1], [1]*Departamento de Matemática Aplicada, Facultad de Informática, Universidad Complutense de Madrid / 28040-Madrid (Spain). Contact: lvazquez@fdi.ucm.es, www.fdi.ucm.es/profesor/lvazquez, www.meiga-metnet.org*

We present a summary of the Spanish scientific payload associated to the Mars MetNet Precursor Mission of Russia, Finland and Spain. Also we present a summary of the development studies in progress.

SMALL MAGNETIC SENSORS FOR LUNAR & MARTIAN EXPLORATION

M. Díaz Michelena, *INTA, Ctra. Torrejón-Ajalvir km 4.2 28850 Torrejón de Ardoz, Spain. Contact: diazma@inta.es*

Abstract: The magnetic characterization of the planetary soils is of great importance in the search for evidence of past life of the planets. In the particular case of Mars, there have been many missions carrying experiments for the magnetic characterization of the soil of the Red planet. Mars has a diverse set of magnetic minerals including prominently the iron oxides (titanomagnetites and titanohematites). Other magnetic minerals include paramagnetic olivine, and antiferromagnetic pyroxene, goethite, lepidocrite, akaganeite, schwertmanite, jarosite and ferrihydrite. The Viking 1 and 2 and Mars Pathfinder experiments consisted in several configurations of ring magnets with different strengths for capturing all the magnetic materials expected to be found on Mars.. The amount of material adhering to the magnets was recorded by optical cameras. These basic experiments concluded that the composition of the Martian soil and dust in the atmosphere were similar. The magnetization was estimated to be ~ 4 Am2/kg. The ferrous mineral content in the soil was inferred to be between 7 - 11 %. In 2003, combined magnetic collection and Mössbauer spectroscopy experiments on board the Mars Exploration Rovers (MER), Spirit and Opportunity were used to refine these measurements. The two rovers found that hematite is not a dominant mineral on Mars and most of the rocks were of a basaltic origin, like magnetite and titanomagnetite. There have since been many experiments designed for developing magnetometry on the surface of Mars using a combination of observations. Examples include the use of a fluxgate magnetometer for the Long Lived Martian Geoscience Observatory (ML-2SP, 2005) and an Anisotropic Magnetoresistance (AMR) gradiometer designed for the 2011 MetNet Precursor mission. A goal of future missions is to place an instrument on the surface of Mars capable of measuring the magnetic moment and hysteresis loops of minerals in the soil. The severe restrictions on mass in space missions (it can cost ~ $20K to place 1 kg of mass in a Low Earth Orbit – LEO) make it impossible to carry a Vibrating Sample Magnetometer (VSM) to Mars. Instead an experiment based on a micromechanical system is under development at INTA to achieve this objective. The system relies, which relies on the principle of Alternating Gradient Magnetometry (AGM) where a permanent magnet is vibrated to avoid the need of repeatedly locating the sample in a vibrating plate. The vibrational frequency and amplitutde of the magnet changes as a magnetic material is approached with the change proportional to the magnetic moment of the portion of soil approached. Additionally, the system will use an Optical (infrared) Wireless Link for intra-Spacecraft communication (OWLS) to facilitate communication between the instrument and the On Board Computer (OBC). We report on the development of a prototype instrument which is a 50 mm by 40 mm device consisting of a sensor head and an optoelectronic detector. The sensor head has a 5-8 mm per side square silicon membrane with a cylindrical SmCo permanent magnet with a ~0.8 T radial remanent magnetization. The 1.5 mm high, 3 mm OD permanent magnet is glued on the membrane. 4 coils, 9 mm in height and 12.5 mm diameter, are used to vibrate the magnet and generate an alternating magnetic field gradient of ~30 mT/m). The detection system relies on the different reflections that takes place depending on the relative position of the magnet when it vibrates. This system has a bundle of optical fibres in a daisy configuration: one of which is connected to a LED and the other to a photodiode. The novel aspect of this work is the effort made to grow the permanent magnet directly on the membrane with the dual objective of miniaturizing the sensor and increasing the repeatability of the sensor head preparation. The idea is to replace the bulk magnet with thin film sputtered magnet with out-of-plane anisotropy. The immediate challenge is to overcome the demagnetising fields associated with this geometry which limit strong magnetic fields to the edges of the films. The solution to the demagnetization problem consists of growing a homogeneous film with a chessboard pattern. In this configuration, the average surface magnetization can be substantially increased by ~2 orders of magnitude to achieve values of ~0.2 -0.3 T for materials with remanent magnetization values of 1.4 T. Further this pattern greatly reduces the risk of membrane fracture due to stress in the film. We report on several rough films deposited at 650°C .using a ~100 nm Ta buffer layer and a ~200 nm capping layer. Thin film samples were subsequently magnetized in a 3 T field perpendicular to the film. A second problem addressed is the a trade-off between the growth surface and the magnetic moment of the film. ANSYS simulations demonstrate that vibrational efficiency is improved the smaller the magnet area. However, a threshold magnetic moment is necessary and limited by the film geometry. In this work we present the results obtained for the system and contemplated future work.

DEVELOPMENT OF MINIATURIZED INSTRUMENTATION FOR MARS EXPLORATION

Héctor Guerrero, Ignacio Arruego and MEIGA / MetNet Precursor Team, *Instituto Nacional de Técnica Aeroespacial – INTA. Contact: guerreroph@inta.es*

The main lines of action of INTA to address the development of miniaturized space instruments for Mars exploration are presented. The final goal is to develop enabling technologies to achieve and to demonstrate small enough instruments, with ultra-low power consumption and high functionality. These are intended as payload 'building blocks' for very small missions to provide a quick access to planetary exploration, as are penetrators in the range of 15 kg of total mass. This is done in the framework of the MetNet Mars Precursor Mission (MMPM), leaded by Finland (FMI), Russia (IKI and Lavochkin Association and Production) and Spain (INTA, UCM, UC3M, US, UPC). MetNet looks to deploy on Mars meteorological stations to allow in situ observation and to improve the understanding of atmosphere and climate.

In particular, we present a magnetometer with resolution below 10 nT and mass in the range of 45 g; a sun irradiance spectral sensor with 10 bands (UV-VIS-near IR) and a mass in the range of 100 g. The magnetometer (at present at FM level) has two triaxial magnetometers (based on commercial AMR technologies) that operate in gradiometer configuration. Moreover has inside the box there a triaxial accelerometer to get the gravitational orientation of the magnetometer after its deployment. This unit is being designed to operate under the Mars severe conditions (at night) without any thermal conditioning.

The sun irradiance spectral irradiance sensor is composed by individual silicon and CSi photodiodes with interference filters on each, and flat non-imaging optics to prevent wavelength shifts due to oblique incidence. In order allow discrimination between direct and diffuse ambient light, the photodiodes are deployed on the top and lateral sides of this unit. The instrument is being optimized for deep UV detection, dust optical depth, O_3, among others capabilities under study.

Besides, INTA is developing optical wireless link technologies modules for operating on Mars at distances over 1 m, to minimize harness, reduce weight and improve Assembly Integration and Test (AIT) tasks. Actual emitter/receiver modules are below 10 g allowing data transmission rates over 1 Mbps.

2MS^3-FM-07

ADVANCES IN MINIATURIZATION TECHNOLOGIES FOR NEXT GENERATION INSTRUMENTS

[1]**D. Fernandez,** [1]**F. Gutierrez,** [2]**J.M Lautier,** [2]**R. Jansen,** [1]*ARQUIMEA, Spain;* [2]*ESA-ESTEC, Netherlands, Contact: dfernandez@arquimea.com*

Introduction:

In the last decade, planetary exploration has been fostered through international collaboration, and the main technical driver for spaceflight instruments development under scientist requirement has become a trade-off between Mass, Volume, and Power, the MVP figure of merit. Also, since scientific exploration is mainly financed by Government funds and launch windows are in many cases limited, Budget and Planning are key parameters regarding Project Risk Management, the BP figure of merit.

The Principal Investigator, PI, has confirmed to be the most important institution to guarantee a successful, flown and productive instrument. During the life of the instrument from conceptual scratch to an in operation flight model the PI has to cope with negotiations regarding MVP (typically never large enough), with both industrial partners and other co-PIs. Also the PI must lead important technical decisions in early stages of the design which will affect the BP in future phases of the development. And most important, the PI must fight for the instrument. The PI will indeed need to deal with industrial partners, other scientists, and politicians in order to get at the end a flight, a ticket for a journey to other celestial object, and the opportunity to contribute to a major historical goal, the exploration of the Universe.

In this paper, we give Principal Investigators, currently thinking about future exploration instruments, a flavour of emerging space technologies that shall be available in the near future. These technologies are not specific to measure one or another parameter, but generic Sensors, Actuators and Microelectronics technologies specifically designed for space instruments developers, and easily adapted to meet PI requirements. Such technologies are right know in the process of qualification and testing in the frame of several ESA, and MICINN technology programs, and can be considered critical to obtain better MVP and BP figures of merit in future exploration instruments. The added value of the technologies presented herein is miniaturization. In the last decade, miniaturization has become the real revolution in order to reduce MVP and BP figures in Consumer Electronics enabling devices that where scientific fiction only five years before.

We claim the next revolution in spaceflight equipment both for payload and platform will come through miniaturization technologies.

Actuators:

Electromagnetic actuators and pyroactuators for deployment of booms, antennas or solar pannels, removing protecting covers or cleaning dust sensors are started to be replaced by a new generation of Shape Memory Alloy actuators called SMARQ. The basis for this technology is a metallic alloy that contracts in response to either an electric current or a change in temperature. The operating temperature for these materials ranges from -180ºC up to 200ºC, enabling the use of these actuators for operation in Mars or other planets. The actuator material is designed to fit a certain deformation pattern, (rotary actuator, lineal, hold down and release, pinpuller, thermal switch ….). The benefits in terms of MVP (Mass Volume and Power) are 10 times lighter than traditional electromagnetic or pyroshock technologies, 5 times smaller, and 50% higher Power peak consumption. Also, its inherent redundancy (several fibers operating in parallel, much like Human Muscles) makes it an excellent technology for space use.

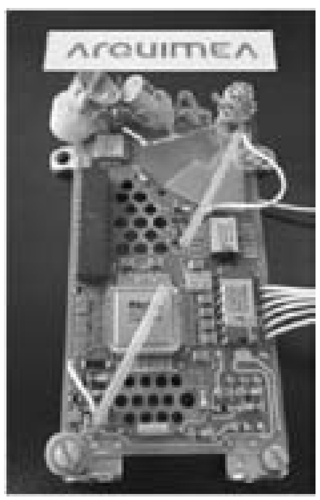

Fig. 1.

The SMARQ material, and several actuators (pinpuller, rotary, hold down and release actuators) are being, qualified for use in space in the frame of several contracts with the European Space Agency. Also, actuators for commercial satellites are being developed.

The technology is already available for instruments. In the frame of METNET Precursor mission, one of the instruments, the Dust Sensor, selected a SMARQ rotary actuator to deploy the black body during in flight calibration operation.

Microelectronics:

In the frame of several contracts with the European Space Agency, a new generation of Rad-Hard Analog Libraries are being developed, and it is already available for Custom Instrument ASICs. Rad Hard Mixed signal ASICs can reduce Instrument electronics MVP by a factor of 10 (both in terms of Mass, Volume and Power consumption). Very much like modern Consumer electronics, new generation of radhard mixed signal ASICs obtain better performance than old fashioned hi-rel discrete componentes, and all can be integrated in a single chip with better noise performance than traditional PCB electronics. (16 bits ADC, Low voltage Reference, low noise amplifiers, front electronics for arrays detectors….). Also, commercial satellite manufacturers such as Astrium or Thales are taking advantage of this technology in order to increase complexity and performance of their RadioFrequency Systems, Active Antennas or General OBDH Equipment.

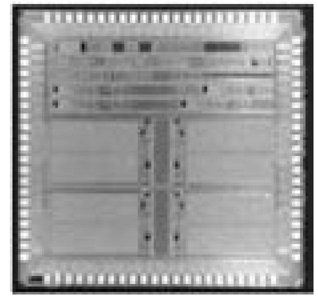

Fig. 2. Hi-Rel mixed signal ASIC including power amplifiers, ADC, References, Current Switchers and UART.

Sensors:

In a very early stage of development new materials sensible and selective to gasses are being developed. Combined with a mixed signal ASIC, this technology can provide an Instrument on a Chip approach to common exploration goals such as atmospheric composition detection, soil composition detection, or even protein detection (astrobiology). The technology is right now working at laboratory level, and will start space qualification by the end of the year, but several gasses (such as NO2, O2, H2), substances (acetone, ammonia) and proteins detection have been achieved. The technology is being used to detect bacteria, virus and parasites as well, therefore security applications such as NBQE early detection are also considered.

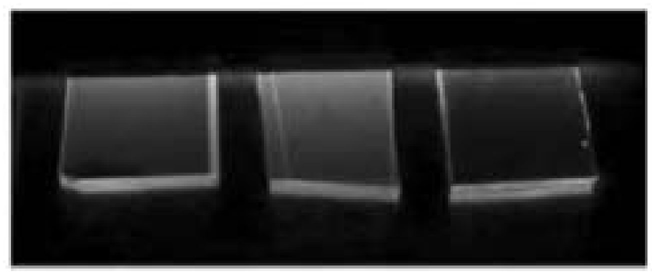

Fig. 3. New generation of detection materials.

Conclusions:

PI facing the development of a new instrument may now choose between a new range of space qualified technologies in terms of spaceflight Microsensors, Microactuators, and Microelectronics, that allow miniaturization of Instrument subsystem, and a better MVP and BP figure of merit.

ON CHEMICAL ANALYSIS OF SOLIDS BY A MINIATURE LASER -ABLATION MASS ANALYSER DESIGNED FOR SPACE RESEARCH

M. Tulej[1], A. Riedo[1], M. Iakovleva[1], and P. Wurz[1], [1]*Institute of Physics, Space Research and Planetary Sciences, Sidlerstrasse 5, 3012 Bern, Switzerland. Contact: marek.tulej@space.unibe.ch*

Introduction: Analyses of extraterrestrial materials onboard of landers or planetary rovers are of considerable interest for the future planetary missions. So far, the spectroscopic methods (α-particle X-ray spectrometers, γ-ray spectrometer) are used predominately for investigation of the chemical composition of solid state materials. Due to limited sensitivity, these methods offer mostly only analyses of major elements and their most abundant isotopes, whereas trace elements typically escape detection by these instruments [McSween et al., 2011]. Although the microscopic mineral grains or non-altered material can be identified from the major element abundances and nature of rocks or sedimentary deposits can be revealed from these studies a more deep understanding of the processes building the rock can only be achieved from analyses of abundances of trace elements. These can yield the nature of planetary differentiation and geological origin. The age dating of the material can be determined from isotopic patterns of radiogenic elements. Also, the isotopic composition of bio-relevant elements is of considerable interest to astrobiology. Bio-related isotopic anomalies have been well investigated in various terrestrial environments and their measurements on surfaces of other planets can provide important clues for past and present live activities. Apart to other candidates considered so far (e.g., laser induced break down spectroscopy, LIBS) to be useful for these studies, the laser ablation mass spectrometry (LA-MS) is one of the most promising techniques for *in situ* application on solar body surfaces. The mass analysers can be used for a rapid analysis of the entire elemental and isotopic composition of surface without its further preparation. Both lateral and vertical resolution can be achieved providing possibility for in-depth profiling and microanalysis. Last decade witnessed considerable progress in miniaturisation of laboratory instruments and their adaptation for flight on spacecraft missions has also been achieved [Brinckerhoff et al. 2000; Rohner et al., 2003, 2004]. The LASMA instrument is now a part of spacecraft payload for Russian missions to Phobos and the Moon. [Managadze et al., 2010; Wurz et al. 2011] The performance of miniaturised LA-TOF analysers is comparable to that of large laboratory systems and present developments aim to enhance detection sensitivity, mass resolution and find the experimental conditions for the preparation of the quantitative measurements.

Our group develops a laser ablation time-of-flight mass spectrometer (LMS) with a different concept for the ion confinement and detection to that applied in the LASMA instrument. [Rohner et al., 2003] Initial performance tests by applying IR laser radiation of Nd:YAG laser have shown a high performance in terms of mass resolution ($m/\Delta m \sim 600$) and sensitivity (~ppm). Nevertheless, the efficiency of element detection has been found to vary between elements with particular low detection efficiency of elements with high ionisation potential [Tulej at al., 2011]. The high dynamic range of our LMS instrument ($\sim 10^7$) can be still improved and more sensitive measurements are expected in further development of the instrument. Present studies are conducted with other laser sources and the computer control has been achieved over several important parameters for reproducible experimental conditions.

LMS Instrument: The LMS instrument is a small size reflectron-type time-of-flight mass spectrometer (length: 120 mm x diameter: 60 mm) specifically developed for the application to space research [Rohner et al., 2003]. The anticipated weight of the flight unit is about 500 g including all electronics. The instrument design has been optimised by taking into account the results achieved from detailed simulation of ion trajectories. The mass analyser can be easily coupled with various laser sources. A focused laser beam is used to melt, vaporise, atomise and ionise the solid sample and can be introduced through the window placed on the top of the reflectron after being focused by the lens (Fig. 1). The ions generated in plasma are introduced to the interior of mass analyser, confined, focused and detected according to their masses by ion detector. The LMS instrument was optimised for high sensitivity to detect trace elements at the level of ppm and below. This sensitivity is achieved without special sample treatment, allowing for easy application of the LMS instrument on a space platform. The mass spectrometric measurements can be prepared with a high resolution exceeding $m/\Delta m = 800$ (see Figure 2 for lead isotopes). The intensity and mass resolution can be also optimised using computer procedure.

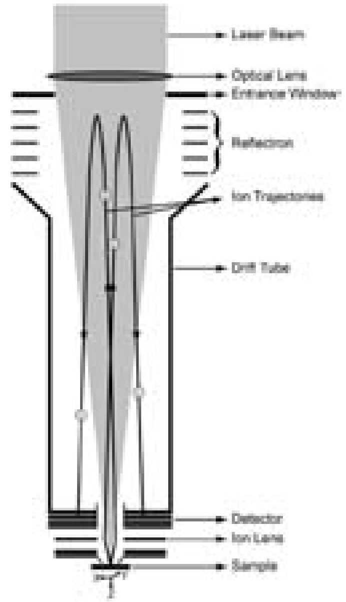

Fig. 1. Schematics of the laser ablation mass spectrometer used in this study. The laser beam enters from the top and is focussed on the sample placed on a translational stage at the bottom. Positive ions leaving an ablation plume enter the interior of the analyser through the nose-piece and are mass-selectively detected by the ion detector.

The mass spectra can be acquired from well defined spatial location and the sampled spot by the laser beam is 10–20 μm in diameter. Our studies show that the reproducible results can only be observed when some thousandths of waveforms can be acquired from one sample location. A statistically averaged spectrum, high mass resolution and measurements of intense and stable ion beam enables for sensitive measurements.

From the measurements of elemental and isotopic composition of the NIST standard reference samples (SRM) the detection limit of ~100 ppb was determined. LMS can be considered quasi-quantitative for the measurements for most elements when ns-second resolved lasers are used for ablation by using relative sensitivity coefficients (RSCs) for each species that have been established in prior calibrations. The quantitative detection of the lighter elements (e.g., C, P, S) is less accurate since the RSCs are larger. Considerable improvement of the detection efficiency of these elements is observed when UV laser radiation instead IR ones is applied. Figure 3 shows the typical correlation plot between the abundances of the elements quoted by NIST and measured by our instrument using IR and UV laser. The abundances of metallic elements such as Ti, V, Fe, Mn and Cr correlate closely to the quoted values whereas the abundances of non-metallic elements including C, Si, S and P can be even 100 times lower than the values quoted by NIST.

The isotopic fractionation effects are found to be negligible and the error in their determination is generally smaller than 1 %. Figure 4 displays the portion of a mass spectrum containing the elements B and C, recorded in studies of the SRM 661 sample, with an abundance of these elements quoted by NIST of 5 ppm and 0.39%, respectively. These elements are usually difficult to detect, nevertheless, we can observe the isotopic components of ^{10}B, ^{11}B, ^{12}C and ^{13}C with a large signal to nose ratio. The effective dynamic range of the full spectrum covers nearly seven decades. The isotopic ratios determined from the spectra are 21.0 % and 79.0 % for ^{10}B and ^{11}B isotopic component and 99.27 % and 0.73 % for ^{12}C and ^{13}C isotopes, respectively. These ratios are within 1% of the values quoted from the standard isotopic distribution for these elements. Similarly, the isotopic pattern of clusters and oxides can be reproduced within 2 % of their calculated values providing means for their identification in spectra and possible deconvolution from the spectra of elements. Clusters are generated via plasma chemistry and sometimes clusters can interfere with heavier elements in the mass spectra (isobaric interferences).

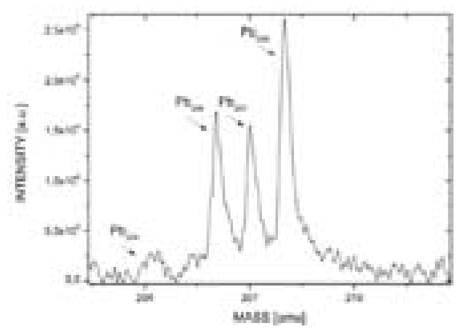

Fig. 2. Isotopic components of Lead measured in NIST standard for steel SRM 664

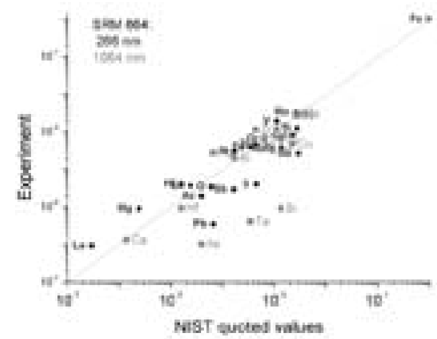

Fig. 3. The correlation diagram between the elemental abundances determined from the experiment and quoted by NIST for SRM 664.

Similarly to studies of NIST standard materials, measurements of minerals and meteoritic materials yield the elemental composition of major, minor and trace elements can be obtained together with their isotopic pattern proving that this approach can be powerful in the investigation of the composition of airless surfaces of asteroids, planets, and their moons on *in situ* and sample return missions.

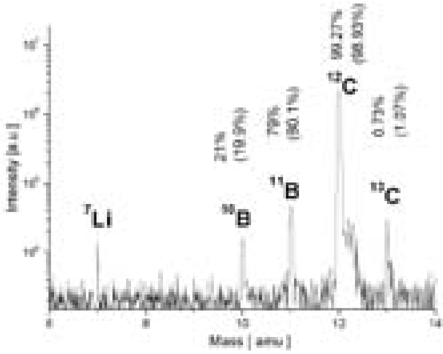

Fig. 4. Part of the mass spectrum recorded in the studies of the SRM 661 standard for steel. The isotopic components of B and C can be recorded with a high precision in spite of low abundances of the elements.

References: McSween, Jr., H.J., R.L. McNutt, Jr., T.H. Prettyman, Spacecraft instrument technology and cosmochemistry, PNAS, early edition, p. 1-6, 2011.
Brinckerhoff, W. B., G. G. Managadze, R. W. McEntire, A. F. Cheng and W. J. Green, Laser time-of-flight mass spectrometry for space, Rev. Sci. Instr., 71(2), 536–545, 2000.
Rohner, U., J.A. Whitby, P. Wurz, A miniature laser ablation time of flight mass spectrometer for in situ planetary exploration. Meas. Sci. Tech., 14, 2159-2164, 2003.
Rohner, U., J. Whitby, P. Wurz, and S. Barabash, A highly miniaturised laser ablation time-of-flight mass spectrometer for planetary rover, Rev. Sci. Instr., 75(5), 1314–1322, 2004.
Managadze, G. G., P. Wurz, R. Z. Sagdeev, A. E. Chumikov, M. Tuley, M. Yakovleva, N. G. Managadze and
A. L. Bodarenko, Sol. Sys. Res. 44, 376-384, 2010.
P. Wurz, D. Abplanalp, M. Tulej, M. Iakovleva, V.A. Fernandez, A. Chumikov, and G. Managadze, “In Situ Mass Spectrometric Analysis in Planetary Science,” Sol. Sys. Res. (2011) submitted.
Tulej, M , M. Iakovleva, I. Leya, and P. Wurz, “A miniature mass analyser for in situ elemental analysis of planetary material: performance studies,” Anal. Bioanal. Chem., 399, 2185–2200, 2010.

STATUS OF THE PLANETARY RADIO INTERFEROMETRY AND DOPPLER EXPERIMENT (PRIDE): APPLICATIONS FOR THE PHOBOS-SOIL AND OTHER PLANETARY MISSIONS

D.A. Duev[1,2], S.V. Pogrebenko[2], L.I. Gurvits[2,3], G. Cimò[2], T. Bocanegra Bahamon[2,3,4], G. Molera Calvés[5], L.L.A. Vermeersen[3], P. Rosenblatt[6], V. Dehant[6], V.M. Gotlib[7], A.S. Kosov[7], V.M. Linkin[7], *[1]Moscow State University, Moscow, Russia; [2]Joint Institute for VLBI in Europe, Dwingeloo, The Netherlands, [3]Delft University of Technology, Delft, The Netherlands; [4]Shanghai Astronomical Observatory, Shanghai, P.R. China; [5] Aalto University, Helsinki, Finland; [6] Royal Observatory of Belgium, Brussels, Belgium; [7] Space Research Institute, Moscow, Russia. Contact: lgurvits@jive.nl*

The Planetary Radio Interferometry and Doppler Experiment (PRIDE) with the Phobos-Soil mission is designed as a multi-disciplinary enhancement of the mission science return by means of precise estimates of the spacecraft state vectors. In particular, these estimates will be fed-in into the studies of the gravitational field of Mars and Phobos. Their applications and interpretation are discussed, in particular, by Rosenblatt et al. at this conference.

PRIDE measurements will be conducted using a network of Earth-based VLBI radio telescopes which will receive a signal from the Phobos-Soil spacecraft 8.4 GHz transmitter locked to the on-board Ultra-Stable Oscillator (USO). The measurements will begin during the cruise phase of the mission and continue through the areocentric and after-landing phases. After the departure of the Phobos-Soil return vehicle from Phobos, the transmittter on landing module will remain operational on the Phobos surface for at least a year.

During the last two years, as a preparatory stage for PRIDE-Phobos, several operational planetary spacecraft have been observed with the radio telescopes in Metsähovi (Finland), Yebes (Spain), Wettzell (Germany), Onsala (Sweden), Matera, Medicina and Noto (Italy), Svetloe, Zelenchukskaya and Pushchino (Russia). The Doppler and VLBI spacecraft tracking experiments have been successfully conducted by our team with a number of deep space missions, such as the ESA's Huygens Titan Probe, the Smart-1 Lunar probe, Venus Express (VEX) and Mars Express (MEX) during the Phobos-flyby (Molera Calvés et al. 2010 and references therein). The PRIDE group has been developing a suite of software tools for measurements of the Doppler shift of the spacecraft carrier signal and accurate estimates of the spacecraft state vectors using the VLBI phase referencing technique. PRIDE observing sessions with the VEX spacecraft were used as a test bench for optimizing the technique and reducing the lag of data processing from weeks down to several hours. Rapid results are crucial for the upcoming deep space missions in view of their potential applicability for mission operations.

The accuracy of the state vector estimates depends on several parameters, of which the most important ones are the stability of the on-board oscillator and the power of the carrier signal. The SNR level of the Doppler and VLBI fringe detections depends on these parameters. Based on the recent experiments with the VEX and MEX spacecraft, we expect to achieve the accuracy of better than a few cm/s for the radial velocity and better than 50 m for the lateral position in the case of the Phobos-Soil spacecraft.

In this presentation, we report the latest results of PRIDE observations of the VEX and MEX orbiters with the European VLBI Network (EVN) radio telescopes. In these experiments we have achieved a milli-Hz level of the radio signal spectral resolution and extracted the phase of the spacecraft carrier signal with the accuracy of 0.1 radian. As a scientifically attractive by-product of these observations, we also present an example of characterisation of the interplanetary plasma along the signal propagation line on various spatial and temporal scales at different solar elongation angles based on the analysis of the phases of the spacecraft carrier signal fluctuations. These fluctuations are well represented by a near-Kolmogorov spectrum. Results obtained from the PRIDE observations of the VEX spacecraft so far will be used as a bench-mark for the future PRIDE-Phobos observations and other potential applications of PRIDE for planetary science missions.

References: Molera Calvés G. et al. 2011, Proceedings of the 8th International Planetary Probes Workshop
Rosenblatt P. et al. 2011, this conference

DETECTION OF CYANOBACTERIA AND METHANOGENES IN MARS ANALOGUE MATERIAL BY RAMAN SPECTROSCOPY

U. Böttger[1], J.-P. de Vera[1], J. Fritz[2], I. Weber[3], J. Malaszkiewicz[4], J. Meessen[5], D. Wagner[4], H.-W. Hübers[1, 6]; *[1]Institute of Planetary Research/DLR, Rutherfordstr. 2, Berlin Germany; [2] Museum für Naturkunde, Berlin. Germany; [3] Institut für Planetologie, WWU Münster, Germany; [4]Alfred Wegener Institute for Polar and Marine Research,Potsdam. Germany; [5] Institute of Botany, Heinrich-Heine-University Düsseldorf, Germany; [6] Technische Universität Berlin, Institut für Optik und Atomare Physik, Berlin. Contact: ute.boettger@dlr.de*

Abstract: RLS (Raman Laser Spectrometer – one of the Pasteur Payload Instruments onboard ExoMars 2018) will perform Raman measurements on Mars to identify organic compounds and mineral products as an indication of biological activity. The measurements will be performed on crushed powdered samples inside the Rover's ALD (Analytical Laboratory Drawer).

Raman analytics with the same specifications as those onboard the future ExoMars mission are conducted to test their potential of identifying biological material on martian analogue material. Appropriate measurement parameters (e.g. integration time and number of repetitions) for the detection of biological material as well as for the determination of the mineral composition will be derived. In addition, we report on problems using Raman spectroscopy to discriminate cells of microorganisms from the mineral background.

Two organisms are chosen as test candidates for potential life on Mars: cyanobacteria and methane producing archaea. Prokaryotes like archaea and bacteria appeared on early Earth at least 3.8 to 3.5 billion years ago (Gya). At this time on Mars the climate was more temperate and wet compared to the present day as inferred from geological evidence for liquid water on the ancient martian surface. Thus life might have developed under similar conditions as on Earth or might have been transferred from Earth (or vice versa). Methane is known to be present on Mars, although a source is still unknown. Methane might originate from geothermal or biological activities nearby the surface of the red planet.

Cyanobacteria and prokaryotes using photosystem I belong to the oldest microbes on Earth. These organisms use pigments such as scytonemin and beta-carotene as UV protection. Especially beta - carotene emits a strong Raman signal. Raman analytics are used for detection of coccid, chain and biofilm forming cyanobacteria Nostoc commune strain 231-06 (Fraunhofer IMBT CCCryo) on the below described Mars analogue mineral mixtures. Nostoc commune is known to be resistant to desiccation, UV B radiation and low temperatures, and thus suitable as a candidate for a potential life form on Mars.

Furthermore the Raman technique is applied on samples of the methane producing archaea candidatus Methanosarcina gelisolum (strain SMA 21) isolated from Siberian permafrost affected soils. These archaea are embedded in the martian analogue material for further analysis.

Two different Mars analogue materials prepared from mineral and rock mixtures are used in this investigation. The (1) Phyllosilicatic Mars Regolith Simulant (P-MRS) and (2) Sulfatic Mars Regolith Simulant (S-MRS) reflect the current understanding regarding environmental changes on Mars. Weathering or hydrothermal alteration of crustal rocks and of secondary mineralization during part of the Noachian and Hesperian epoch followed by the prevailing cold and dry oxidising condition with formation of anhydrous iron oxides. The use of two different mixtures accounts for the observations that phyllosilicate deposits do not occur together with sulphate deposits. P-MRS and S-MRS serve as the surrounding geomaterials in which the cells of cyanobacteria and of methanogenes are embedded.

Varying periods of measurement time and number of repetitions are performed to get optimal Raman spectra for cyanobacteria and methanogenes. A measurement regime is proposed for mineral mixtures with cyanobacteria on the basis of the RLS instrument characteristics. Raman analytics are capable to identify biosignatures like beta – carotene on a multi-mineral mixture similar to those expected to be encountered during the ExoMars mission.

MONTE-CARLO 3D SIMULATION OF PLANETARY SURFACE IMAGING THROUGH THE OPTICALLY DENSE ATMOSPHERE (VENUS AS AN EXAMPLE)

A. Ekonomov, *Space Research Institute (IKI), Russia, Contact: alekonomo@yandex.ru*

Introduction:

The problem of imaging of the planet surfaces is a priority for space exploration, since the surface is crucial to study the origin mechanisms. However, if for other planets in the solar system conducted hundreds of experiments in this direction, for Venus there are only a few. This is due to an optically dense cloud cover in the upper atmosphere of Venus. Until now, the global picture is obtained only in radio wavelengths. First spacecraft to the board which was carried out large-scale location of Venus was on the Pioneer Venus Orbiter (1978), which carried out radar mapping of the surface. AMS Venus 15/16 (1978) have got on board the DBR with a resolution of 1-2 km, and Magellan (1989) had a DBR with a resolution of 100 m.

During 1975-1982 Soviet landers, being on a surface, have taken a number of panoramas with the high resolution of the order of shares of meter. Thus, there is a gap between the resolution of 100 m and shares of meter and it should be filled. Such experiment could be imaging from undercloud layer in a transparency window of 1 micron. Idea is not new, but technical study was not conducted.

Our own optical in-situ experiment1978-1982(VENERA 9,10,11,12,13,14 – Venus landers) on measurements of the radiation field in the atmosphere of Venus, CA 9 / 10 (Ekonomov et al, 1979) and 13/14 (Moshkin et al 1983) gave information from the clouds to the surface in 0.5-1.15 mkm.[1] They were the base of V.I. Moroz analytical estimates in the article [2].Estimates have confirmed an imaging experiment realizability.

3D Monte-Carlo simulation:

In turn to verify these analytical estimates we have executed 3D numerical simulation with Monte-Carlo method to check up an imaging experiment realizability.

Optical model: Optical 3D model consists of an 2D image- B/W picture that simulates the surface of Venus, the adjacent planeparallel layer(AL), simulating the atmosphere of Venus, in which the bulk scattering and absorption are taking place and the lens building an image of the surface of Venus in the focal plane of TV-camera. Scattering is consistent with basic model .of Venus atmosphere -Rayleigh scattering lower main cloud deck,

The Venus surface radiates upwards, towards an TV-lens. The part of radiation undergoes scattering in atmosphere and after scattering gets into lenses together with radiation not exposed to scattering. Besides the sunlight impinges in the day time on a AL and after scattering in it gets on lenses from below. All it reduces contrast of the image in a focal plane.

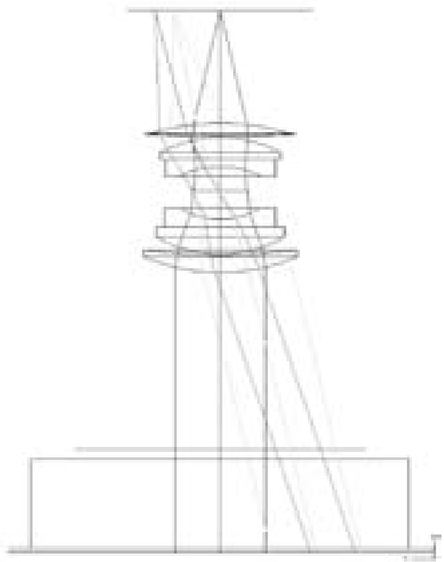

Fig. 1. Optical model.

Results of simulation:

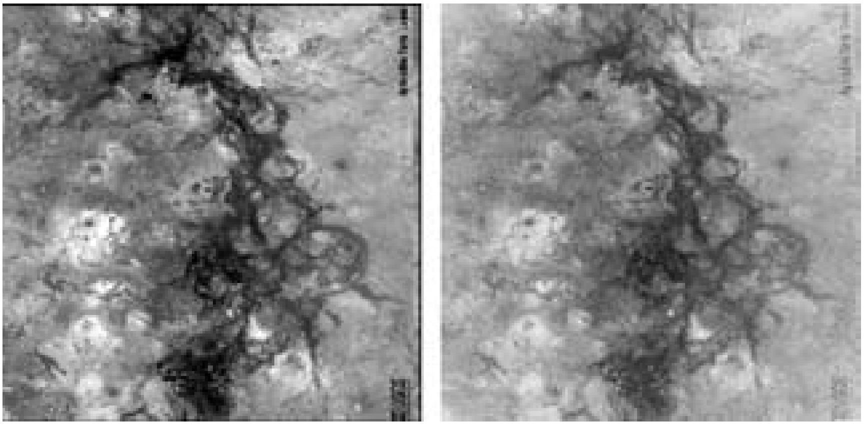

Fig. 2. Without scattering/with bulk scattering

Summary and Conclusions:

As a result of parametric calculations dependence of contrast on height is gained. The imaging experiment realizability is confirmed. Also the animation movie simulating descent to a surface may be synthesized.

References: [1] Ekonomov A.P., Moshkin, B.E., Golovin, Yu.M., Parfentjev, N.A.,Sanko, N.F.: Spectrophotometric experiments on descent probes “Venera-11” and “Venera-12”.1. Methods, results and a tentative interpretation. Kosmich. Issled. 17, 714–726 1979. (in Russian; English translation of “Kosmicheskie issledovaniya” is available as “Cosmic Research”).

[2] Moroz V.I.: Estimates of visibility of the surface of Venus from descent probes and balloons *Planetary and Space Science 50 (2002) 287 – 29

VENUS: IN SITU MINI MISSION.

A. Ekonomov, V.M. Gotlib ,V.M. Linkin, A.N.Lipatov, *Institute of Space Research, Moscow, Russian Federation. Contact: alekonomo@yandex.ru ,+7 495 333 21 44*

Abstract: A low cost, low mass (20-30 kg) for Venus lower atmosphere ***in situ*** investigation is proposed. ***In situ*** Venus investigation is necessary because Venus atmosphere is opaque in optical range and remote sensing from the orbit is impossible. The most part of the atmosphere's mass, its boundary layer above the surface and the surface itself are closed by the dense cloud layers. The sounders with the instrumentation should penetrate deep into the atmosphere. There are two alternatives for the sounder philosophy corresponding to two scientific goals:

1.the Venus atmospheric probe (*VAP*) for investigations of atmospheric parameters or

2.the Venus lander (*VL*) for a study of properties near the surface. Because of a heating protection and the thermal insulation problems their design concepts are quite different (table 1):

	Venus atmospheric probe (VAP)	**Venus lander (VL)**
Duration of the descent time 55-0 km	50 min/70 min	30 min / 40 min
Active time on the surface	15 min(not guaranteed) /0	60 min /50 min
Science	Atmospheric Optional: imaging	Atmospheric, Seismic Optional: imaging, chemistry
Stabilization	parachute	tail-plane
Ballistic coefficient M / Cd * A	minimum	maximum
Terminal speed at surface	<10 m/s	>15 m/s
Thermal control	Two stage passive, Melting PCM	Two stage passive, Melting PCM

Numerical SIMULINK model for dynamics and thermodynamics for Venus descender was created.

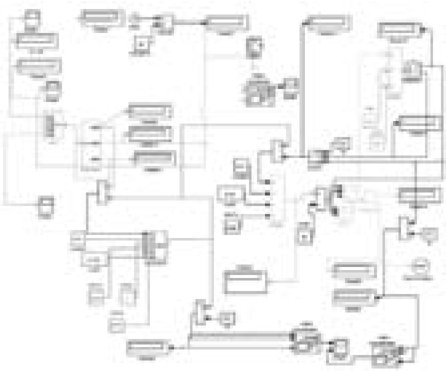

Fig. 1

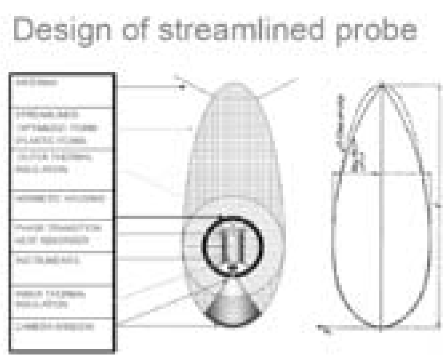

Fig. 2

A lot of calculations for a descent for the most suitable shapes of the sounder have been made including the stabilization and thermal design. Possible scientific instrumentation for both versions is discussed.

References: [1] Ekonomov, A., Korablev, O., Zasova, L.: Technology development for long-lived Venus landers .EPSC abstracts vol. 2,2007, EPSC2007-A-00387.
[2] Ekonomov, A.: How and why to survive at Venus surface. EPSC abstracts vol. 3,2008, EPSC2008-A-00207.
3] Ekonomov, A., Gotlib,V.,and Lipatov,A. Microprobe experiment in frame of future Russian mission Venera–D. EPSC abstracts volume 4,2009, EPSC2009-276.

2MS^3-MM-01

ORIGIN OF GROOVES ON PHOBOS: NEW OBSERVATIONS AND COMPARISONS TO THE MOON.

James W. Head[1] **and Lionel Wilson**[2], [1]*Department of Geological Sciences, Brown University, Providence, RI 02912 USA. Environmental Sciences Division, Lancaster University, Lancaster LA14YQ, UK.*
Contact: james_head@brown.edu.

Summary: Numerous theories have been proposed for the formation of grooves on Phobos, and no single explanation is likely to account completely for the wide variety of morphologies and orientations observed. One set of grooves is geographically associated with the impact crater Stickney. As a possible explanation for the characteristics of this type of groove set, we tested the hypothesis that these grooves were formed by ejecta clasts which left Stickney at velocities such that they were able to slide, roll, and/or bounce to distances comparable to observed groove lengths (of the order of one-quarter of the circumference of Phobos), partly crushing the regolith and partly pushing it aside as they moved (Fig. 1). This mechanism is physically possible and is consistent with the sizes, shapes, lengths, linearity and distribution of some of the grooves for plausible values of the material properties of both the regolith and the ejecta clasts. Because the escape velocity from Phobos varies by more than a factor of two over the surface of the satellite, it is possible for ejecta clasts to leave the surface again after generating grooves. The characteristics of tracks left by lunar rolling and bouncing boulders permit a comparison to the predictions (Figs. 2,3).

Discussion and Analysis: Two factors caused us to reassess theories for the origin of grooves on Phobos: 1) continuing analysis of high resolution images of linear tracks on the Moon formed by rolling and bouncing boulders (Figs. 2, 3) has shown that these features show many similarities to grooves on Phobos; 2) continued study of the formation of impact craters on very small bodies such as asteroids and the satellites of Mars underlines the unusual and often counterintuitive nature of the cratering process and the resulting ejecta emplacement patterns. Ejection velocities associated with the vast majority of the material forming crater deposits on the Moon are sufficient to cause this material to exceed escape velocity on asteroids and Phobos and Deimos, and thus to leave the impacted body. The only ejecta remaining on the impacted body in these cases is likely to be the least shocked and latest material excavated at very low velocities (e.g., below escape velocity); ejecta from Stickney-sized craters on Phobos will look and behave much differently, with emphasis on the low-velocity emplacement of ejecta blocks, perhaps similar to the tracks from rolling and bouncing blocks observed on the Moon.

We explored the consequences (Fig. 1) of assuming that these grooves were formed by ejecta clasts with diameters of the order of 100 m which left Stickney at velocities such that they were able to roll or bounce to distances of the order of one quarter the circumference of Phobos, partly crushing the regolith and partly pushing it aside as they moved. Using basic soil mechanics relationships and estimates of regolith material properties, we calculated the range of sizes of the boulders that would be responsible for the observed grooves. We then considered the motions of clasts ejected from the 10 km diameter crater Stickney which just fail to reach escape velocity in the Phobos environment. We show that groove formation by these clasts is physically possible and that the sizes, shapes, lengths, linearity and distribution of some grooves are consistent with plausible values of the material properties of both the regolith and the ejecta clasts. We also show that there are several possibilities for the fate of these clasts. Some of the clasts will be abraded and diminished in size during their traverse before coming to rest. Because the escape velocity from Phobos varies by more than a factor of two over the surface of the satellite, it is also possible for some of the clasts to leave the surface again after generating grooves. The paths of all primary crater ejecta clasts produced on Phobos must be considered in terms of the total gravity field of both Phobos and Mars. We thus draw a distinction between *super-orbital*, *orbital* and *sub-orbital* ejecta.

Sub-orbital clasts are those having an ejection velocity less than the escape velocity from Phobos alone. Such clasts are projected from near the edge of the crater cavity. They are excavated by stress waves having small stress amplitudes and stress gradients, and so will tend to be relatively coarse, relatively more coherent, and to be ejected at low speeds and at low elevation angles. There are expected to be very strong correlations between the sizes and the horizontal and vertical velocity components of such ejecta clasts. Of particular interest are sub-orbital ejecta clasts leaving the crater cavity at speeds of 3 to 8 m/s (i.e., just below, or essentially at, the local escape velocity) and at elevation angles close to zero. These clasts will travel out of the crater, over the crater rim crest and onto the crater rim in the terminal stages of the cratering event and may slide, roll, or bounce along the surface, producing a groove-like disturbance of the pre-existing surface with a width smaller than, or similar to, their own diameter.

Summary of Predictions and Tests from the Analysis: To provide a basis for comparison with new data from spacecraft missions we summarize some of the key predictions and tests from our model in reference to the morphology and structure of the grooves and compare these to lunar boulder tracks (Figs. 2, 3): Groove widths: The widths of grooves should be comparable to the size range of blocks shown to be capable of producing grooves on Phobos by this mechanism. The radii of the ejecta clasts required to produce grooves 100 m wide would lie in the range ~80 to 140 m, with larger grooves requiring proportionally larger clasts. Groove width-to-depth ratios: Consideration of the vertical forces acting on clasts shows that groove-like depressions with depth-to-width ratios in the range 0.05 to 0.17 are expected if the regolith cohesive strength is similar to or, more likely, a factor of 10 smaller than, that of the lunar regolith. Groove lengths: Ejecta clasts with radii in excess of ~100 m launched at speeds in the range 3 to 6 m/s are able to travel to distances of 10 to 30 km even if the regolith strength is near the upper end of the range implied by the groove shapes and is thus comparable with the strength of the lunar regolith. Groove morphology: Rolling and bouncing boulders could produce linear grooves (if the boulder is relatively rounded and rolling), chains of isolated craters (if the boulder is bouncing and leaving the ground between bounces), chains of connected craters (if the boulder is bouncing and not leaving the ground between bounces), or linear grooves with associated pits (if the boulder is rolling and bouncing and not leaving the surface). Change in groove morphology with distance: Monotonic decrease in velocity of rolling boulders, and any change in the size and morphology of the boulder will result in variations in groove morphology with range.

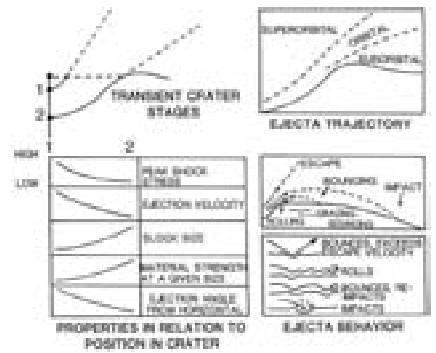

Fig. 1.

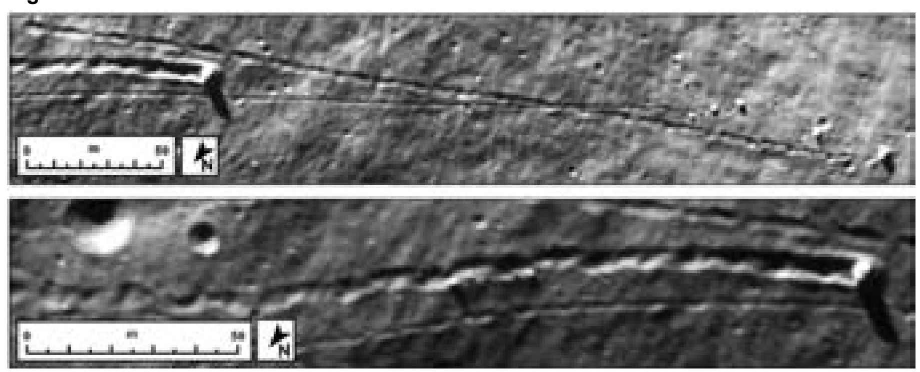

Fig. 2 and 3. LROC images of lunar boulder tracks.

THE ORIGIN OF PHOBOS GROOVES FROM EJECTA LAUNCHED FROM IMPACT CRATERS ON MARS – TESTS OF THE HYPOTHESIS.

K.R. Ramsley[1], J.W. Head[2], [1]*School of Engineering, Brown University, Box D, Providence, RI, USA.* [2]*Department of Geological Sciences, Brown University, Box 1846, Providence, RI, USA. Contact: Kenneth_Ramsley@brown.edu*

Introduction:

The surface of the martian moon Phobos is characterized by parallel and intersecting rows of pits (grooves) that bear resemblance to secondary crater chains on planetary surfaces. Murray [1] has hypothesized that the main groove-forming process on Phobos is the intersection of Phobos with ejecta from impact crater events on Mars to produce chains of secondary craters. The hypothesis infers a pattern of parallel jets of ejecta, either fluidized or solidified, that breaks into uniformly-spaced fragments and disperses uniformly along trajectory during the flight from Mars to Phobos. At the impact with Phobos the dispersed fragments emplace pits that are aligned along strike corresponding to the flight pattern of ejecta along trajectory. The aspects of the characteristics of grooves on Phobos cited by this hypothesis that might be explained by secondary ejecta include: their linearity, their parallelism, their planar orientation, their pitted nature, their change in character along strike, and a "zone of avoidance" where ejecta from Mars is predicted not to impact [1].

To test the hypothesis we plot Keplerian trajectories (true orbits and hyperbolic trajectories with periapsis and perifocal points located below the surface of Mars). From these trajectories we (1) set the fragment dispersion limits of ejecta patterns required to emplace the more typically well-organized parallel grooves observed in returned images from Phobos; (2) plot ranges of the ejecta flight durations from Mars to Phobos and map contours of exposure; (3) utilize the same contour map to observe trajectory-defined ejecta exposure shadows; (4) observe hemispheric exposure in response to shorter and longer durations of ejecta flight; (5) assess the viability of ejecta emplacing the large family of grooves covering most of the northern hemisphere of Phobos; and (6) plot the arrival of parallel lines of ejecta emplacing chains of pits at oblique incident angles.

Datasets Used and Analysis:

We have compiled a data set of approximately 5,000 trajectory solutions covering a comprehensive range of viable trajectories from Mars to Phobos in its current orbit. The present day orbit of Phobos represents the greatest historical extent of exposure to martian ejecta. Therefore our dataset inherently includes all surfaces of Phobos exposed to martian ejecta since the moon established its current tidal lock. From this dataset we plot the centers of hemispheric exposure for trajectories in the dataset up to 180 minutes of flight durations.

Hemispheric exposure centers are mapped onto a three dimensional model of Phobos for durations of flight of 0 to 45 minutes, 5 to 90 minutes and 5 to 180 minutes (**Fig. 1A**). From these centers, we observe the extent to which flight durations are associated with longitudinal exposure. For these three ranges of flight duration we further plot contours defining total exposure to ejecta to these ranges and inversely define exposure shadows (**Fig. 1B**).

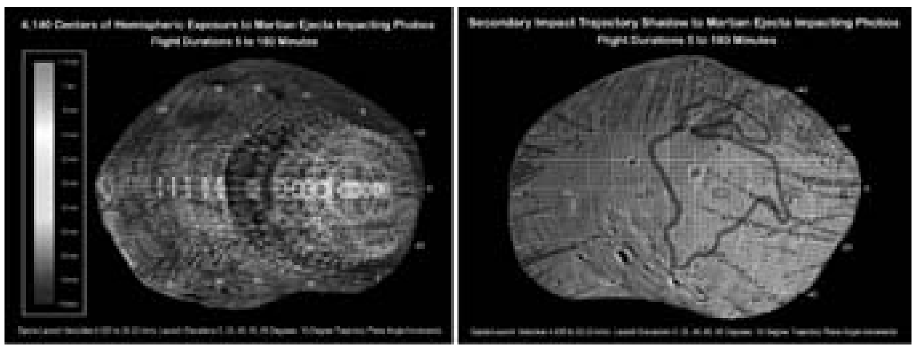

Fig. 1. (A) Centers of hemispheric exposure are mapped for 4,140 ejecta trajectories with flight durations of 5 to 180 minutes from Mars to Phobos. **(B)** A corresponding contour map is plotted revealing the exposure shadowing. Grooves mapped by Murray [1] are applied to a three dimensional model of Phobos derived from the shape model of Thomas [3]. For a color version of this abstract, please download from: http://www.engin.brown.edu/ddv/ramsley-2ms3.pdf

2MS^3-MM-02

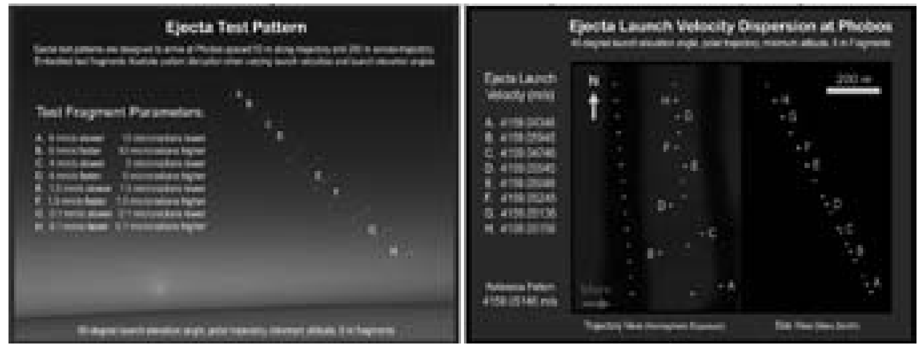

Fig. 2. (A) An ideal pattern of fragments is launched from the surface of Mars that is designed to emplace pits on Phobos with spacing of 50 m along strike. Eight test fragments of 8 meters in diameter in this array are altered by launch velocity dispersion rates of 0.1 to 8.0 mm/s. **(B)** Test fragments (cyan) are shown after a flight of 86 minutes just prior to impact with Phobos. Particles G and H are launched with 0.1 mm/s of added and reduced velocity and remain along trajectory with sufficient linearity to emplace grooves without observable defects. Due to variations of Keplerian elements, particles E and F (1.0 mm/s of launch velocity added and reduced) disperse across trajectory in excess of ~ 10 m and would be observed as a linear defect when emplacing a groove of up to 100 m in width. Particles A and B correspond to the typical velocity dispersion rate of 8.0 mm/s required to separate fragments from a fluidized or monolithic ejecta jet and would disrupted any ejecta pattern beyond recognition at the distance of Mars to Phobos. For a color version of this abstract, please download from: http://www.engin.brown.edu/ddv/ramsley-2ms3.pdf

To test the mechanism of dispersion of ejecta patterns during flight we vary the initial launch parameters of selected fragments and observe the disruption within the ideal pattern **(Fig 2A)**. Arriving at Phobos we examine the misalignment of impactors and assess limits on the extent of allowable initial launch variations **(Fig 2B)**. Many grooves on Phobos reveal no apparent deviations along strike. We therefore set the limit on the maximum along-strike dispersion at Phobos at not more than 10% (e.g. 10 meters misaligned when emplacing a 100-meter wide groove).

To test the viability of the northern family of grooves we select exposure hemispheres that reveal the most northerly centers of exposure. The emplacement duration to form this northern family is predicted to be no more than nine seconds and therefore the entire family must fit within one complete hemisphere of exposure. Our tests examine a 45-degree ejecta launch elevation. We also examine an extreme test case in order to model the greatest northerly exposure possible.

To test the emplacement of oblique impacts of parallel ejecta columns, we simulate a set of parallel trajectories that arrive at Phobos in a range of ~30 to ~60 degrees from the vertical. In order to locate the impact pits along strike we plot the intersection of trajectory lines onto a three dimensional model of Phobos in equal time units. We then observe the resulting pit pattern from the nadir angle to assess the extent to which the pit pattern is affected by the irregularity of the local terrain and the small-body radius of Phobos.

Results and Discussion:

The Murray hypothesis infers individual fragments separating from monolithic or fluidized jets. Yet the required rate of along-trajectory dispersion exceeds the allowable dispersion rate by a factor of eight for a typical trajectory. For this reason, the ejecta pattern must instead exit the primary crater with along- and across-trajectory spacing pre-set and each fragment in the flight pattern must adhere to its original grid position within the allowable dispersion limit (1.0 mm/s of launch velocity and 1.0 microradians of launch elevation for typical trajectories). Each fragment must further remain at its grid position within dispersion limits for up to three hours. There is no known natural or human-made mechanism able to organize flight with this extent of precision.

An ejecta exposure shadow aligns to the trailing orbital apex of Phobos if the motion of Phobos supplies the entirety of velocity vectors. Yet, ejecta would arrive at Phobos to supply a *second vector* that is similar to the velocity of Phobos in its orbit. The combined velocity of Phobos and ejecta generally shifts the longitude of exposure and exposure shadowing to the east (**Fig 1A and 1B**). As a consequence, the observed "zone of avoidance" is ~50% exposed to martian ejecta trajectories. Within contours that define ejecta shadows we also observe groove pits. Therefore the "zone of exclusion" is unrelated to the exposure of Phobos to martian ejecta.

Flights to the anti-Mars side of Phobos are proportionately fewer and longer in duration. We would expect evidence of this in the form of more widely spaced pits with far less organization east to west. We would also expect a trend toward lower pit population densities east to west. This is not observed.

In an extreme test providing the most northerly exposure conceivable, we assume a major basin-forming event [2] that inserts ejecta into a Phobos-crossing orbit with periapsis of 100km. The large northern hemisphere family of grooves does not fit entirely within this or any other valid hemisphere of exposure.

Due to the irregularities of the local terrain of Phobos and the small-body radius of the moon, almost all lines of parallel ejecta would arrive at Phobos at oblique angles across strike. The modification of emplaced grooves by local terrain should be extensive. In returned images we observe only infrequent examples.

Conclusions and Implications:

1. To emplace a family of grooves with virtually no defects, families of martian ejecta (often thousands of fragments) must launch into pre-spaced grid patterns with essentially no observable disruption of the pattern during flights of up to three hours. Fragments must further be nearly identical in diameter. This is implausible by any mechanism due to disruptions associated with varied Keplerian elements.
2. The observed “zone of avoidance” is not the result of martian ejecta since ~50% of this zone is exposed to martian ejecta.
3. The trajectory-derived exposure shadow contour for flight durations of 5 to 180 minutes reveals groove pits in violation of this shadow contour zone. This invalidates the related families of these groove pits.
4. Centers of hemispheric exposure clearly trend east to west with longer flight durations and should instigate lower pit densities and reduced groove organization. Yet this is not observed.
5. The northern family of grooves can not be emplaced by any valid trajectory. Further, this northern family leaks into the trajectory-defined exposure shadows for all flight durations of 5 to 180 minutes.
6. The vast majority of parallel columns of impactors would emplace lines of pits at oblique impact incident angles. These lines should be disrupted by the irregular topography and small-body radius of Phobos. Grooves observed on Phobos rarely respond to local terrain and are far too linear.

References: [1] Murray, J. (2010) The First Moscow Solar System Symposium. [2] Schultz, P. & Crawford, D. (1990) Abstracts of the Lunar and Planetary Science Conference 18:888. [3] Thomas, P. (1997) NASA Planetary Data System.

PHOBOS GROOVES, A LUNAR ANALOGY

Thomas Duxbury[1], Mark Robinson[2] , Carolyn Van DerBogert[3] , Peter C. Thomas[4], NewYork, USA GerhardNeukum[5], Harald Hiesinger[6], *[1]George Mason University, Fairfax, USA, [2]Arizona State University, Tempe, Arizona, USA, [3]Westfaelische Wilhelms-Universitat Muenster, Muenster, Germany, [4]Center for Radiophysics and Space Research, Cornell University, Ithaca, [5]Freie Universitaet, Berlin, Germany, [6]University of Muenster, Muenster, Germany. Contact: tduxbury@gmu.edu, mark.s.robinson@asu.edu, vanderbogert@uni-muenster.de, ,gneukum@zedat.fu-berlin.de, hiesinger@uni-muenster.de.*

The global network of grooves on Phobos was partially seen in the Mariner 9 images, at the limit of camera spatial resolution. The Viking Orbiters had many close flybys of Phobos, most occurring naturally as the orbit evolved. However, the closest Viking flybys of less than a few hundred km were targeted. The groove network was seen early in the Viking mission, but observing their extent took over a year to accumulate the global, high-resolution coverage. By the end of the Viking mission, the grooves were well mapped (Thomas, et al., 1978) and a majority appeared to be related to the formation of the large crater Stickney. Possible origins of the grooves might be related to surface fractures from the interior generated by Mars tidal forces while undergoing large impacts, tidal stresses during capture into Mars orbit (if Phobos was an asteroid), secondary craters chains from Phobos crater ejecta, crater ejecta rolling on the surface, or from secondary crater chains from Mars crater ejecta (Head, et al., 1978, Thomas, et al., 1979, Murchie, et al., 1989, Wilson,et al.,1989, and Murray, et al., 2006).

The study of the grooves continued during the Soviet Phobos 88 mission and continues today with the ESA Mars Express (MEX) and US Mars Reconnaissance Orbiter (MRO) missions. Mars Express has many close encounters naturally, as its orbit extends beyond the orbit of Phobos that is over 6,000 km from the Martian surface, as well as targeted closer flybys. Even though the MRO orbit is only a few hundred km from the surface of Mars, its high-resolution HiRISE and CRISM instruments easily resolve the Phobos surface at better than 10 m/pixel for HiRISE. The highest spatial resolution images of the grooves have come from the HRSC camera during the targeted MEX close flybys, near the 5-meter level.

With all of these direct observations of the Phobos grooves by spacecraft at Mars, it may be that our own moon will provide insight into the possible origin of some of these grooves. Recent Lunar Reconnaissance Orbiter Camera (LROC) images of our moon show linear features similar to the Phobos grooves. On lunar crater walls and central peaks, many boulder tracks, formed by rolling blocks of ejecta and mass-wasting of steep crater walls and peaks, areobserved. These boulder tracks follow the local surface topography, leaving long trails, sometimes crossing and sometimes with a braided appearance due to the irregular shapes of the boulders, similar to the morphology of Phobos grooves. They tend not to hop but stay in contact with the surface, unless encountering major topographic boundaries. The main difference between the trails on our moon and some of the Phobos grooves is that the boulders remain at the end of the lunar trails. Since very few boulders are seen on Phobos, they must have left the surface when the gravitational/frictional forces with the Phobos regolith became less than the radial velocity component of the rolling boulders, allowing the boulders to escape the surface. The LROC images give direct information on groove morphology to boulder size and shape within the lunar gravitational and topographic environment for comparative studies. Also relating the tremendous amount of grooves on Phobos to boulders, mostly from one crater, may reflect on the origin of Phobos being an accretion of Mars ejecta, providing a large inventory of boulders to be ejected during the largest of crater impacts.

2MS^3-MM-04

GROOVES OF PHOBOS AS SEEN ON THE MEX HRSC RECTIFIED IMAGES AND COMPARISONS WITH PLANETERY ANALOGS.

A.T. Basilevsky[1,2], J. Oberst[3,4], K. Willner[3], M. Waehlisch[4], G. Neukum[2], *[1]Vernadsky Institute, Moscow, Russia, [2]Free University Berlin, Germany, [4]TU Berlin Germany, [4]DLR Berlin, Germany. Contact: atbas@geokhi.ru*

Introduction: Here we analyze the HRSC images of Phobos revisiting a problem of origin of grooves, numerous linear features, often turning to chains of small craters (Fig. 1). They were originally assumed to be fractures resulted of the large impacts or from tidal stresses [e.g., 1,2]. Also were suggested other hypotheses, the most discussed of which are a suggestion that the grooves were formed by rolling blocks of Phobos crater ejecta [3,4,5] or they are chains of coalescing secondary craters formed by ejecta from large craters of Mars [6,7].

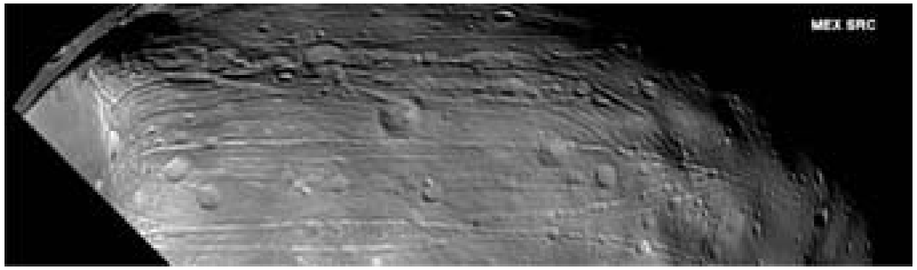

Fig. 1. Grooves on Phobos. Fragment of SRC image, DLR/FU.

The images under analysis: The used HRSC images have been reduced to resolution 10 m/px and reprojected into stereographic projection with central longitudes 31 and 103° E. This eliminated significant part of geometric distortions which made more difficult photogeologic analysis of the unprocessed images.

Photogeologic consideration: Grooves of Phobos indeed look very much as fractures and their turning to crater chains was explained by the drainage of regolith into the fractures or by blowing it out by the gas released from the Phobos interior [e.g., 1,2]. But the suggestion that Phobos grooves are fractures (faults) has difficulty because fractures typically show lateral offset of the younger fracture when it meets the older fracture while the Phobos grooves whose systems are believed to be of different age [e.g., 7] show no such offsets (Fig. 3).

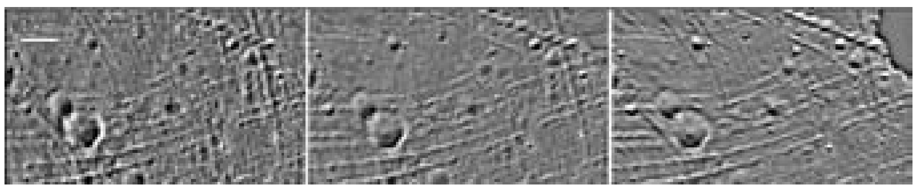

Fig. 2. Intersection of grooves of different orientations/ages. High-pass filtered fragments of HRSC images.

However, not always the later fracture shows offset when crossing the older one. Figure 3 shows Martian graben having obviously two different ages with no offsets at the younger /older graben intersections.

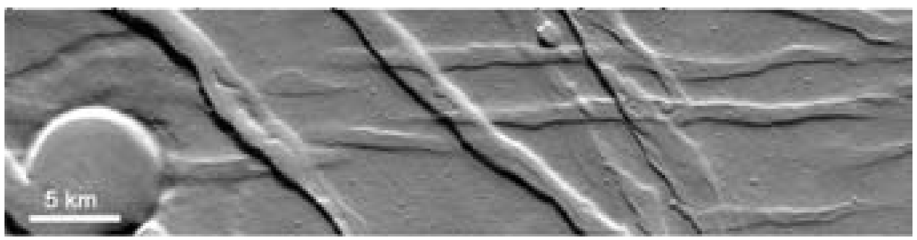

Fig. 3. Graben in Alba Patera area Mars. Fragment of Themis image, NASA.

The suggestion that Phobos grooves were formed by rolling boulders of Phobos crater ejecta is strongly supported by similarity (Figure 4) in general morphologies between them and tracks of rolling and bouncing boulders on slopes of lunar landforms [4,5].

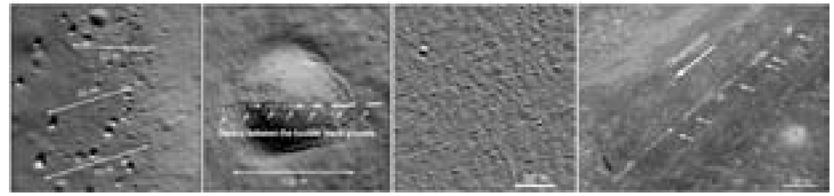

Fig. 4. Grooves formed by rolling boulders on the craters slopes. Fragments of LROC NAC images, NASA.

However if Phobos grooves were formed by this way, one may expect that at least some grooves should have blocks at their ends and this is not observed. This suggestion also implies that the blocks should have enough kinetic energy, otherwise they would not produce long grooves. But if so, the blocks should fly behind the positive bends of the topography like rims of prominent craters and there the groove should be interrupted. Figure 5 shows grooves entering in and leaving craters Drunlo and Clustril with no such interruptions.

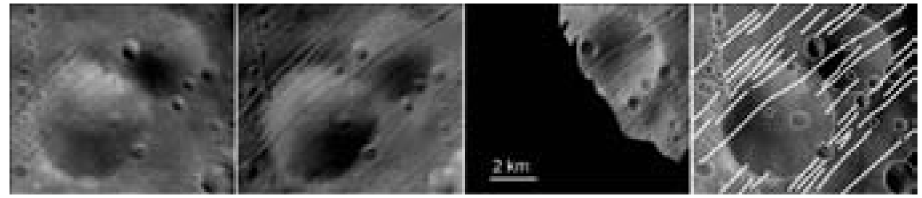

Fig. 5. Grooves crossing crater rims without interruptions on them. Fragments of HRSC images, DLR/FU.

The suggestion that Phobos grooves are chains of coalescing secondary craters formed by ejecta from large craters of Mars is strongly supported by general similarity of the grooves and the secondaries' chains. This mechanism could also explain formation of several families of parallel grooves [6,7]. But it meets difficulty if to look in Figure 6 which shows a family of parallel grooves along 90° of angular difference (from image left to the right). If these groves would be formed by ejecta from the same impact event on Mars the impact angles for the craters forming the left (on the image) grooves should differ by 90° from the impact angles forming the right grooves. In that case their morphologies should be rather different, that seems to be not the case.

Fig. 6. Fragment of HRSC image which covers 90 deg long area on Phobos.

Another problem for the secondary craters hypothesis is a discovery of grooves (at least two systems) very similar for the Phobos ones on asteroids Lutetia and Vesta (Figure 7) which have no close neighbors able to provide chains of secondaries.

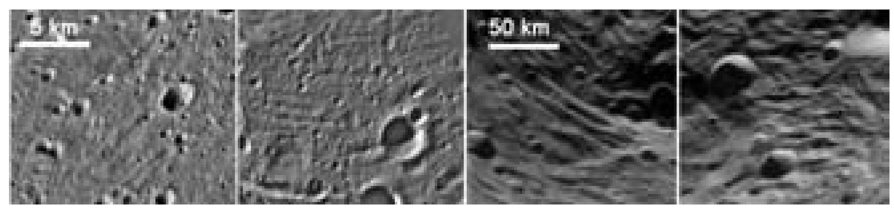

Fig. 7. Grooves on asteroids Lutetia (left images, Rosetta, ESA) and Vesta (right images, Dawn, NASA)

Conclusions: All suggested hypotheses of formation of grooves on Phobos have their strong and weak sides. Further analysis of images of Phobos may help to resolve the problem of the groove formation.

References: [1] Thomas P, et al. (1978) *Nature*, 273, 282-284. [2] Morrison S.J. (2009) *Icarus*, 2004, 262-270. [3] Wilson L. & Head J.W. (1989) *LPSC-20*, 1212. [4] Wilson L. & Head J.W. (2010) *1MSSS-2-3*, http://ms2010.cosmos. ru/pres.htm. [5] Duxbury T. et al. (2010) *1MSSS-2-4*. [6] Murray J, et al., (2006) *LPSC-37*, 2195. [7] Murray J. (2010) *1MSSS-2-5*.

ELONGATED CRATERS ON MARS REVISITED: TEST OF THE DECAYING MOONLETS HYPOTHESIS?

B. Buchenberger[1], O. Witasse[2], D. Loizeau[2], A. Chicarro[2], P. Rosenblatt[3],
[1]KU Leuven, Belgium, [2]Research and Scientific Support Department of ESA, ESTEC, Noordwijk, The Netherlands, [3]Observatoire Royal de Belgique, Brussels, Belgium, (bernd(at)buchenberger.eu, owitasse(at)rssd.esa.int)

Abstract: Elongated craters on Mars have been addressed in a number of articles. Subsequently, three datasets were estab¬lished in 1982, 1988 and 2000 respectively, using Viking images [1,2,3]. A new and improved set of data with 258 craters based on these previous datasets, and a database including up¬to¬date images taken by the High Resolution Stereo Camera (HRSC) onboard ESA's Mars Express were compiled. An analysis of the database shows amongst other information a change in impact direction with respect to crater age and an increase of maximum crater diameter as well as an increase of eccentricity with increasing crater age.

Introduction: Thanks to space exploration, impact cratering has been revealed as a fundamental process in shaping the surface of terrestrial planets. One common characteristic of most impact structures is their circular shape. However, a small fraction of elongated craters formed by oblique impacts can be observed. Detailed surveys of those elon¬gated craters have been performed for some of the inner planets. Especially for Mars, target of many planetary missions, three datasets were compiled based on Viking images.

Motivation for the study: One factor in the revision of elongated craters on Mars is the availability of high-resolution images in colour and 3D taken by the HRSC imager onboard Mars Express. Since the existing investigations are all based on Viking data, the advanced imaging capacity of Mars Express means a major step forward in the re-appraisal of elon¬gated craters on Mars. Another important aspect is the ongoing discussion on the decaying moonlets hypothesis, which might be an explanation for at least some of these craters, as well as the unsolved origin of the Martian moons, Phobos and Deimos [4]. The improvement of the existing datasets, the development of a database with HRSC images and the analysis of this database are expected to contribute to this discussion and might also serve as a foundation for further studies.

Database of elongated craters: The established database includes 258 elongated craters that are divided into three age groups according to their relative state of preservation. Furthermore the database is composed of 15 attributes including amongst others crater eccentricity, crater depth, crater age, terrain age or further comments and the resulting spreadsheet makes Mars Express images directly accessible via hyperlinks.

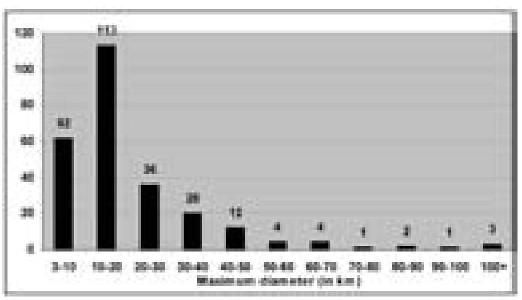

Fig. 1. Crater number related to maximum diameter

Summary and conclusion: The focus of this study was the development of a new database of the elongated crater population on Mars with up-to-date satellite imagery from ESA's Mars Express. In order to achieve this objective the existing datasets from 1982, 1988 and 2000 were analysed and an improved dataset was established. The result is a database with 258 elongated craters and 15 database attributes including high-resolution images mostly in colour and in 3D. The discussion of the decaying moonlet hypothesis shows that it is still a controversial topic. When evaluating the results of this study and other investigations, it seems probable that at least some of the elongated craters on Mars resulted from the impact of former satellites [5]. Future exploration of the Red Planet and its moons will deliver more data that might eventually lead to a definite answer to this open question. With respect to future planetary endeavours that might contribute to answering the origin of the Martian moons, the decaying moonlets hypothesis and therefore also the origin of the elongated craters, the Russian Phobos-Grunt mission and the ESA-NASA programme of Mars Exploration are of the utmost importance.

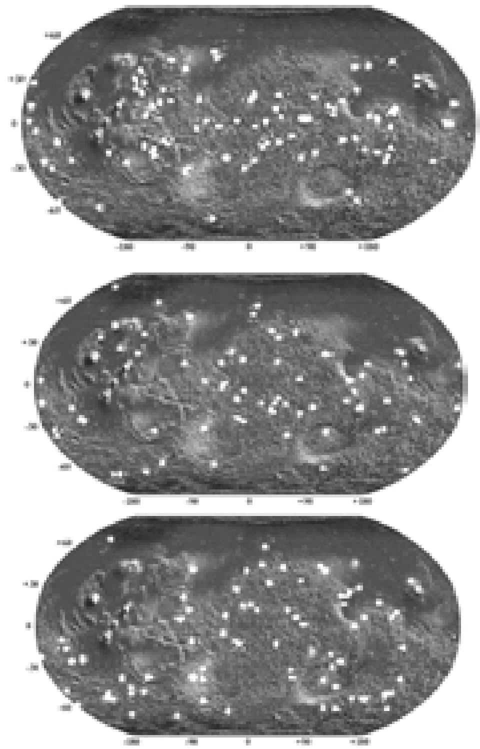

Fig. 2. Global crater distribution according to crater age (red = youngest, yellow=middle, green = oldest)

Table 1. Crater age with respect to crater size and crater eccentricity (group 1 = youngest, group 2 = middle, group 3 = oldest)

Age group 1	Age group 2	Age group 3
Average max. diam. 16 km	Average max. diam. 27 km	Average max. diam. 50 km
Average min. diam. 11 km	Average min. diam. 16 km	Average min. diam. 32 km
Average eccentricity 1.45	Average eccentricity 1.63	Average eccentricity 1.78

Table 2. Crater age related to impact direction

Age group 1		
Direction (°)	# of craters	%
0 to 67	42	43.8
68 to 109	15	15.6
110 to 177	39	40.6
Total	**96**	**100**

Age group 2		
Direction (°)	# of craters	%
4 to 86	58	78.4
97 to 170	16	21.6
Total	**74**	**100**

Age group 3		
Direction (°)	# of craters	%
0 to 90	26	29.5
91 to 168	57	64.8
Erosion	5	5.7
Total	**88**	**100**

Acknowledgements: B. Buchenberger sincerely thanks O. Witasse for his suggestion to undertake this study, and for his advises. B.B. also would like to thank A. Chicarro, D. Loizeau and P. Rosenblatt for their advices and encouragement. B.B. acknowledges the support from the faculty of the Research and Scientific Support Department of ESA.

References: [1] Schultz, P. H. and Lutz-Garihan, A. B.: Grazing Impacts on Mars: A Record of Lost Satellites, Journal of Geophysical Research, Vol. 87, pp. 84-96, 1982.
[2] Barlow, N. G.: Crater Size-Frequency Distributions and a Revised Martian Relative Chronology, Icarus, Vol. 75, pp.285-305, 1988.
[3] Bottke, W. F., Love, S. G. and Tytell, D.: Interpreting the Elliptical Crater Populations on Mars, Venus and the Moon, Icarus, Vol. 145, pp. 108-121, 2000.
[4] Craddock, R.A., Are Phobos and Deimos the result of a giant impact? Icarus, Vol. 211, Iss. 2, p. 1150, 2011
[5] Rosenblatt, P., and Charnoz, S., Formation of the Martian Moons from a circum-Mars accretion disk, this session, 2011

2MS³-MM-05

DIURNAL TEMPERATURE REGIME OF THE SURFICIAL REGOLITH OF PHOBOS IN THE LANDING SITE REGION OF THE PHOBOS-GRUNT LANDER FOR DIFFERENT SEASONS: THE MODEL PREDICTION.

R.O. Kuzmin[1,2], E.V. Zabalueva[1], [1] *Vernadsky Institute of Geochemistry and Analytical Chemistry, Russian Academy of Sciences, 19 Kosygin str., Moscow 119991, Russia (rok@geokhi.ru);* [2] *Space Research Institute, Russian Academy of Sciences, Profsoyuznaya str. 84/32, Moscow, 117810, Russia.*

Introduction: Because of the absence of the atmosphere, the short duration of the Phobos day (7.7 hours), and the presence of a highly porous and fine-grained soil on the Phobos surface, all components of the Russian *Phobos–Grunt* Lander will operate under frequent and sharp temperature changes: from positive to extremely low negative temperatures. As a consequence, information about the temperature regime directly on the surface of the Martian satellite and within the surficial regolith layer appears to be extremely important. The first analysis of the temperature regime of the Phobos's surface in the proposed before landing site (15°S, 310°W) on the initial stage of the *Phobos–Grunt* Mission development has been conducted based on the numerical model [1]. During the completing stage of the *Phobos–Grunt* Mission development the landing site was finally selected in other area of the Phobos [2,3] with both the surface albedo and thermal properties of the regolith somewhat different than in the case of the former landing site. The suggested new landing area is between 7°N to 21°N and 214° to 233°W [3]. Here we present the results of the numerical modeling of the thermal regime of the surface regolith layer (on diurnal and seasonal time scales) in the new area of the potential *Phobos–Grunt* landing site (figure 1). The new landing site is located on the hemisphere opposite to Mars and it not undergone to both the effect of the eclipse of Phobos by Mars and influence of the reflected and thermal radiation of Mars. We performed this modeling by taking into account all seasons on Mars and without the effects of the eclipse of Phobos by Mars.

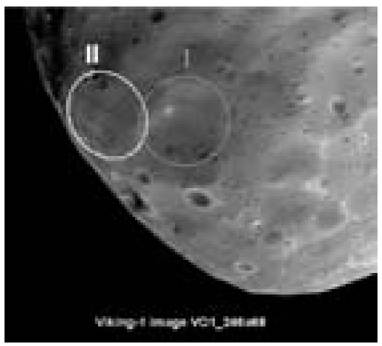

Fig. 1: New potential landing site for the *Phobos–Grunt Lander* (option I and option II).

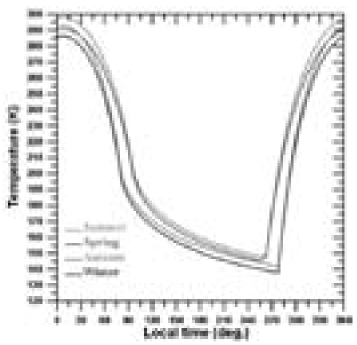

Fig.2: The diurnal cycle of the surface temperature on the Phobos for different seasons (in the northern hemisphere of Mars) in new potential landing site. The local time on Phobos is given in degrees and counted from local noon (0°).

Thermal model of the Phobos's surface: So far as Phobos represents an atmospereless body and the density of its surface regolith is close to the lunar one, we can suggest that the physical properties of the surficial material on Phobos and the Moon are quite similar. In the thermal model of Phobos, we also take into account the dependence of the thermal parameters (thermal conductivity and the specific heat) on temperature and depth that was confirmed early for Moon [4]. In developing the computer code for the estimation of the diurnal and seasonal temperature variations in the surface regolith layer at the potential landing site, we used as a basis the thermal model of the surface layer of Phobos [5], which takes into account (1) the ellipsoidal shape of the Phobos figure,(2) the eclipses of Phobos by Mars, (3) the reflected and thermal radiation of Mars, (4) the variable thermal conductivity and the specific heat of the material, and (5) the absence of internal heat sources. The thermal regime in the surface layer in the new potential *Phobos–Grunt* landing site has been described by the one-dimensional nonlinear thermal conductivity equation with the boundary conditions and the initial condition likewise it was described in our first paper [1].

Results of the thermal regime computation: As a result of the numerical modeling we estimated the variations of the diurnal temperatures on the surface itself and in the upper surficial layer (up to first centimeters) of Phobos during the different seasons at a point with coordinates 15° N, 230° W. At computation were used the albedo value 0.07 (typical for the area) and the regolith density 1100 kg/m^3. The diurnal course of the Phobos surface temperature in the potential landing site for different seasons is presented on the figure 2. Each curve was obtained for a definite orbital position of Mars (winter, Ls= 316°; spring, Ls=45.7°; summer, *L*s=136°; autumn, Ls=224°). The highest surface temperature varies from 286 to 298 K and the lowest one, from 137 to 148 K. In the figure 3 the diurnal distribution of temperature with depth is shown also for 4 seasons. The figure 4 shows the diurnal distribution of the temperature on the surface and with depth on the moment of the predicted date of landing of the *Phobos–Grunt* Lander in the proposed landing site (~14-15 February of 2013 yr., Ls=267°). It is clearly seen from the figure 3 and 4 that the diurnal temperature variations in proposed landing site have large amplitude on the satellite surface (149°-151°) and these variations damp very swiftly with depth, beginning from a small depth (in several millimeters). Thus, the amplitude of diurnal temperature variations damps by a factor of *e* at a depth of ~0.3 cm, and the decrease of temperature variations down to 1° occurs at a depth of 1.0–1.3 cm, depending on a season. The results of conducted numerical modeling maybe useful at analysis of the measurements data from the Thermophob instrument [6], which will work underneath of one of the Lander's legs.

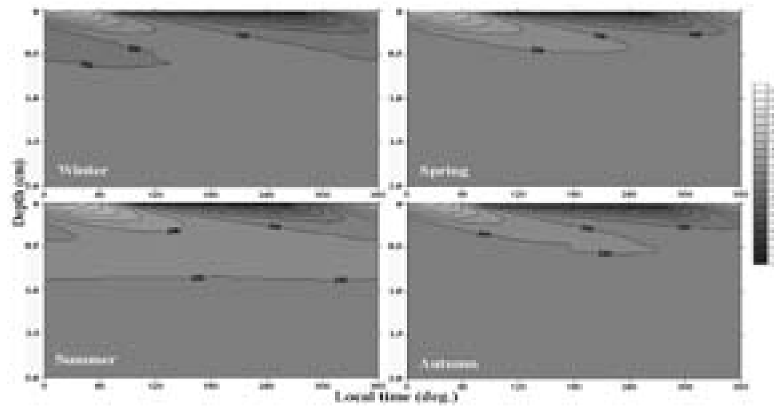

Fig.3: The diurnal variation of the temperature in the upper surficial layer of the Phobos regolith for different seasons. Local noon on Phobos corresponds 0°.

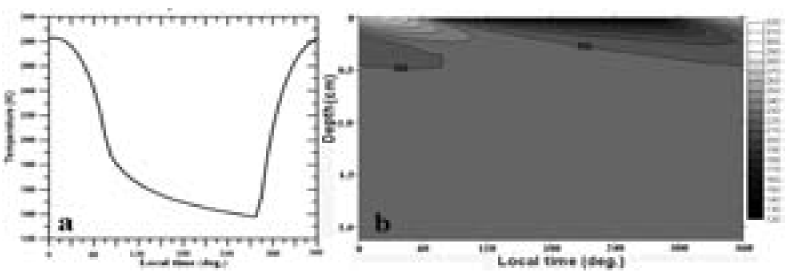

Fig.4: The diurnal cycle of the temperature on the surface of the Phobos (a) and its variations with depth (b) on the moment of the predicted date of landing of the *Fobos–Grunt* Lander within the proposed landing site.

References: [1] Kuzmin, R.O. and Zabalueva, E.V., , *Astron. Vestn.,* 2003, vol. 37, no. 6, pp. 526–535.
[2] A. T. Bazilevsky and T. V. Shingareva, *Solar System Research, 2010, Vol. 44, No. 1, pp.* 38–43. [3] A.T. Basilevsky et al., *Brown-Vernadsky Micro-symposium* 48, abstract µ48_05. [4] Langset, M.S., Jr. and Keihm, S.J. in *Kosmokhimiya Luny i Planet* (Cosmochemistry of the Moon and Planets), *Trudy Sovetsko-Amerikanskoi konferentsii po kosmokhimii Luny i planet* (Proc. Soviet–American Conf. on Cosmochemistry of the Moon and Planets), Moscow: Nauka, 1975, pp. 200–209. [5] Kuhrt, E. and Giese, B., *Icarus*, 1989, vol. 81, pp. 102–112. [6] M. Ya. Marov, A. V. Kolesnichenko, K. K. Manuilov, and V. P. Osipov, *Solar System Research,* 2010, Vol. 44, No. 5, pp. *393–402.*

2MS³-MM-07

PHOBOS GEODESY EXPERIMENT USING RADIO-TRACKING DATA OF THE PHOBOS-SOIL SPACECRAFT: CONSTRAINTS ON THE INTERIOR AND ORIGIN OF PHOBOS.

P. Rosenblatt[1], S. Le Maistre[1], A. Rivoldini[1], N. Rambaux[2,3], V. Lainey[3], J. Castillo-Rogez[4], C. Le Poncin-Lafitte[5], L.I. Gurvits[6,7], V. Dehant[1], and J.C. Marty[8]. *[1]Royal Observatory of Belgium, Brussels, Belgium; [2] Université Pierre et Marie Curie, Paris, France; [3]Institut de Mécanique Céleste et de Calcul des Ephémérides/Observatoire de Paris, Paris, France; [4]Jet Propulsion Laboratory, California Institute of Technology, Pasadena, USA; [5]Système de Référence Temps et Espace/Observatoire de Paris, Paris, France; [6]Joint Institute for VLBI in Europe, Dwingeloo, The Netherlands; [7]Department of Astrodynamics and Space Systems, Delft University of Technology, Delft, The Netherlands; [8]CNES/GRGS, Toulouse, France. Contact: rosenb@oma.be*

Introduction:

The Phobos-Soil mission, due to launch in October-November 2011, aims primarily to perform *in-situ* analyses of the soil of Phobos and bring samples back to Earth for further investigation. The main scientific objective of this mission is to determine the origin of this small celestial body, still an open question. Key constraints on the physical processes prevailing at the origin come from a better knowledge of the bulk properties and deep internal structure. Here, we propose a geodesy experiment which consists of precise measurements of the gravity field and rotation of Phobos, which are direct constraints on these properties. The proposed experiment will also contribute to improving our knowledge of the Martian system and of fundamental physics. The Phobos-Soil radio-tracking facilities will be used in order to precisely reconstruct the trajectory of the spacecraft when orbiting Mars at close distances to Phobos, as well as the rotation variations and the orbit of Phobos once the spacecraft has landed on its surface. This Phobos Geodesy Experiment (PGE) is proposed in the context of the Guest Investigator Program call, released by the Space Research Institute of the Russian Academy of Sciences (IKI) and the European Space Agency (ESA). The proposed experiment aims to support and to extend the synergies with and objectives of the PRIDE-Phobos experiment (probing Phobos' interior and testing fundamental physics [1]) and presented at this conference [7].

Scientific rationale:

The origin of the Martian moons, Phobos and Deimos, is still an open issue: they may be (a) asteroids captured by Mars, (b) remnants left over from Mars' formation, or (c) formed *in-situ* from a circum-Mars debris disk [e.g. 2]. The capture scenario mainly relies on optical remote sensing observations of their surface, which suggest that their material is similar to that suggested for outer-main belt asteroids. However, the dynamical evolution of an asteroid captured from a heliocentric orbit that can explain the current orbits of the moons remain to be properly modeled. On the other hand, *in-situ* formation is more prone to account for the current moon orbits and is not in contradiction with the surface composition inferred from remote sensing data. Some of the data collected recently by the Mars Express (MEX) spacecraft emphasize the importance of exploring the internal structure and origin in a self-consistent manner, opening new paths of investigation. In particular, the MEX data have allowed a precise determination of the density of Phobos, reviving the interest in obtaining a better understanding of its interior [2]. On the one hand, Phobos' interior can demonstrate a high porosity fraction, which raises a renewed interest for the *in-situ* formation scenarios. On the other hand, the density can also be explained with a water-rich Phobos' interior, which calls for a fresh look at the capture scenario [3]. Indeed, water ice is expected to increase significantly the rate of tidal dissipation inside Phobos, promoting faster orbital evolution than previously considered. However, a detailed modeling remains to be carried out in order to assess the modalities of capture and post-capture evolution. Density alone cannot provide tight constraints on Phobos' interior because the water ice content also depends on the porosity content [2]. More data about the interior are thus needed in order to constrain the fractions of porosity and water ice and their relative distribution inside Phobos.

The Mars Express images of Phobos have also been used to determine the amplitude of the forced libration in longitude (or periodic variations of the spin rate) as 1.24° +/- 0.15° [4]. Since the error bar includes the expected value of 1.1° obtained from the shape of Phobos in the case of homogeneous mass distribution [4], this measurement is not accurate enough to highlight departures from homogeneity across the satellite. Still, this value within its error bar indicates a slightly heterogeneous interior, as suggested by recent models of internal mass distribution [5]. The same models also show that the values of the principal moments of inertia of Phobos are sensitive to the amount and distribution of porosity and water ice in its interior. This implies that precise measurement of these moments of inertia may provide tighter constraints on the interior structure of Phobos (i.e. porosity versus water-ice content) [5]. As the moments of inertia are related to the forced libration amplitude and to the second-order coefficients of the non-spherical part of the gravity field of Phobos [6], precise measurements of these parameters will lead to a precise determination of the moments of inertia of Phobos.

In the context of the Phobos-Soil mission, we propose an additional geodetic experiment using the radio-tracking data of the spacecraft in order to get a precise view on the bulk internal structure of Phobos.

Measurements and goals of the Phobos Geodesy Experiment

The proposed geodesy experiment relies on the ranging and Doppler tracking data performed with the onboard coherent transponder (2-way ranging and Doppler) and the onboard Ultra-Stable-Oscillator (USO, 1-way Doppler) [7]. These measurements will provide radial distance and velocity along the line-of-sight between the spacecraft and Earth-based deep space tracking or VLBI (Very Long Baseline Interferometry) stations. The USO also offers the opportunity to perform VLBI tracking of the spacecraft, affording additional spacecraft position measurements in the plane-of-sky [8].

Determining the gravity field of Phobos: Before landing on Phobos, the Phobos-Soil spacecraft will orbit Mars in a Quasi-Synchronous-Orbit (QuSyO) with Phobos. During this mission phase, scheduled to last one month, the spacecraft will remain at very close distances to Phobos (45-55 km), and will serve as a sensor of its gravity field. Radio-tracking data will enable precise reconstruction of the orbital perturbations of the spacecraft. This Precise Orbit Determination (POD) process consists of fitting a dynamical model of the spacecraft motion to the available tracking data in order to estimate the gravity field coefficients, in particular the second-order ones, which will be used for a precise determination of the principal moments of inertia of Phobos. All deep space and VLBI tracking data will be used in order to separate robustly the gravity field signal from the perturbations induced by the maneuvers required to maintain the QuSyO. The tracking data will be processed with the dedicated orbitography software called GINS [13].

Monitoring the rotational motion of Phobos: Once landed on Phobos, the radio-tracking data of the spacecraft will be used to monitor the rotational motion of Phobos. A complete model of Phobos' rotational motion will then be fit to these tracking measurements in order to determine the amplitudes of the physical librations in longitude and in latitude at short and long periods [9, 10]. Preliminary simulations, using the GINS software, have shown that the radio-tracking data will allow determining the amplitude of the short-period librations with a precision of 0.1% after a few weeks of data acquisition (and better than 0.01% after a few months) [9]. Merging the radio tracking data with the star-tracker data will improve the determination of the librations as foreseen by the celestial mechanics experiment [11]. Along with the gravity field, the libration amplitudes will allow measuring the principal moments of inertia of Phobos at the single-digit percent level, which is required to constrain tightly the internal mass distribution inside the moon [3].

Monitoring the orbital motion of Phobos: The radio-tracking data of the landed spacecraft also contain information on the fine variations of the orbital motion of Phobos. The Doppler measurements are well suited to detect these variations, which could not be measured precisely with astrometry data so far. The gain of precision expected on the reconstructed orbit of Phobos will allow sensing the fine variations of the gravity field of Mars (e.g. due to the seasonal CO_2 mass exchange between the atmosphere and polar caps). It will allow determining the time variations of Mars' even zonal harmonics with a precision of a few percent [12], which have been poorly constrained so far by tracking data of spacecraft orbiting Mars on low-altitude polar orbits [e.g. 13]. It will also lead to an improved determination of the relativistic parameter β by a factor of 2.5 for tracking data acquired over one year. It will enable new tests of fundamental physics along with the detection of potential variations of the universal gravitational constant, as proposed by the PRIDE-Phobos experiment [1]. As the radio-tracking data contain information on the full motion of Phobos, the star-tracker measurements will be helpful to decouple the orbital motion from the rotational one. The tracking data will be processed with the NOE software dedicated to precise computation of natural satellite ephemerides.

An "integrated" geodesy experiment: Another important part of the proposed experiment will be based on the merging of the radio-tracking data of both QuSyO and landing phases of the mission. The goal of this global inversion of the tracking data is to improve the determination of physical parameters, like the gravity field of Phobos, which influence both spacecraft's and Phobos' orbital motions. This inversion scheme will follow the one using the natural satellite astrometry data together with the spacecraft tracking data proposed in the context of the European project ESPaCE [14]. The Phobos Geodesy Experiment will also provide a preview of what a space mission dedicated to the Mars geodesy, like the GETEMME mission [15], would be able to deliver.

The results of the Phobos Geodesy Experiment will support the interpretation of other experiments targeting the interior (e.g. using the seismometer, MUSS) and will complement surface observations, helping to answer the question of the origin of this small body.

References: [1] Linkin et al., 2009, EPSC2009-376; [2] Rosenblatt P., 2011, submitted to A&A Rev.; [3] Castillo-Rogez et al., 2011, EPSC-DPS2011-1673; [4] Willner et al., 2010, EPSL 294, 541-546; [5] Rosenblatt et al., 2010, 1st Moscow Solar system Symp., 29; [6] Borderies and Yoder, 1990, A&A 233, 235-521; [7] Duev et al., this meeting; [8] Gurvits et al., 2010, 1st Moscow Sol. Syst. Symp., 73; [9] Rambaux et al., EPSC-DPS2011-818; [10] Le Maistre et al., EPSC-DPS2011-1021; [11] Andreev et al., 2010, Sol. Syst. Res., 44, 438-443; [12] Lainey et al., EPSC-DPS2011-952; [13] Marty et al., PSS, 57, 350-363; [14] Thuillot et al., EPSC-DPS2011-1833; [15] Oberst et al., 2011, submitted to Experimental Astronomy.

MASS DISTRIBUTION INSIDE PHOBOS: A KEY OBSERVATIONAL CONSTRAINT FOR THE ORIGIN OF PHOBOS.

A. Rivoldini[1], P. Rosenblatt[1], N. Rambaux[2,3], and V. Dehant[1]. *[1]Royal Observatory of Belgium, Brussels, Belgium; [2] Université Pierre et Marie Curie, Paris, France; [3]Institut de Mécanique Céleste et de Calcul des Ephémérides/Observatoire de Paris, Paris, France; Contact: rosenb@oma.be*

Introduction:

The origin of the Martian moons, Phobos and Deimos, is still an open issue. It has been proposed that they formed away from Mars and then captured by Mars gravitational attraction [1] or that they formed *in-situ* from a disk of debris in Mars' orbit [2]. The capture scenario has, however, major difficulties to account for the current near-circular and near-equatorial orbit of Phobos [1]. Previous works of tidal orbital evolution have shown the critical role of the tidal dissipation inside a satellite to make the capture possible, i.e. Phobos' interior might have high dissipative properties [3], which would be closer to those of icy material than to those of rocky material [4]. Among the recent observations made by the Mars Express spacecraft, those concerning the internal structure of Phobos are particularly pertinent for assessing the scenario of origin [4]. Indeed, the density of Phobos, 1.87 +/- 0.02 g/cm^3 [4], is lower than the density of presumed material analogs, suggesting that the interior of this small moon can contain light elements like porosity or water-ice. The former supports *in-situ* formation while the latter favorizes an asteroid capture scenario [4,5]. Therefore, the assessment of the porosity/water-ice content inside Phobos is a key measurement relevant to the open question about its origin [6].

In this study, we develop models of mass distribution inside Phobos, and use the measured libration of amplitude and density of Phobos to constrain the mass distribution within. We explore the possible internal mass distributions, considering three kinds of material inside Phobos: rock, porous-rock and water-ice. We compute the principal moments of inertia, related to the second-order gravity field coefficients, C_{20} and C_{22} and libration amplitude of Phobos, for each of these possible internal mass distributions. Then, we select the distributions that fit the measured libration of amplitude and the density of Phobos within their error bars. For those distributions, we find values of the gravity field coefficients which depart from the expected value of a homogeneous mass distribution for a large amount of porosity and a low amount of water-ice. In turn, precise measurements of both gravity field coefficients and rotation variations of Phobos may provide new constraints on the origin of this small moon of Mars.

Models of mass distribution inside Phobos:

The proportion and repartition of water ice and rock porosity cannot be determined from the average density alone. Another datum, like the libration amplitude (-1.24 +/- 0.15 degrees [7]), which depends on the principal moments of inertia of Phobos (thus on its internal mass distribution), is likely to provide further constraints. In order to constrain Phobos' interior structure, we have discretized its volume by a set of cubes (2626), each having an identical volume of 1300mx1300mx1300m. The cubes are made of one of three different materials: water ice (940 kg/m^3), porous-rock and non-porous rock. For a given porosity and non-porous rock density the number of cubes of each material is determined from the bulk density of Phobos. Our model contains a parameter that controls the size of clusters of identical material within the volume of Phobos. We have calculated the probability density functions for the three principal moments of inertia and for the libration amplitude taking various degrees of porosity, fractions of water ice and rocky material density into account.

Results:

Our results show that the most likely models with a homogeneous matter distribution have libration amplitudes that deviate from the estimated libration amplitude, suggesting a Phobos interior mass distribution that deviates from homogeneous distribution. In order for the models to fit the observed libration amplitude the smoothing parameter values have to be chosen such that clusters of material of intermediate size are obtained. Models with rocky material density lower than about 2.1 g/cm^3 do not fit the libration amplitude whatever the porosity/water ice content and the smoothing parameter values. However, the precision on the observed libration does not allow for a tight constraint on the porosity/water ice content inside Phobos. From our models we have also computed the C_{20} gravity field coefficient. The predicted C_{20} values depart more and more from the value expected for a homogeneous mass distribution when more and more porosity (up to 40%), and equivalently less and less water-ice content (down to a few percent of the mass of Phobos), are considered. In turn, it shows that a precise measurement of Phobos' gravity field could provide additional constraints on its interior and origin.

Summary and perspectives:

A precision of a few percent on the gravity field and the rotation measurements of Phobos are needed to tightly constrain its interior structure. Such precise measurements are challenging but might be obtained from the Phobos-Grunt spacecraft [8], due to launch in October-November 2011 (arrival date to Phobos in early 2013). The Phobos-Grunt spacecraft will indeed orbit Mars at close distance to Phobos (45-55 km), offering the opportunity to measure the gravity field of Phobos and then will stay at Phobos' surface, offering the opportunity to measure the fine variations of the spin rate and orientation of the rotation axis of Phobos. Our models of Phobos' interior will be useful for interpreting these future data. For instance, they can be used for modeling of the rotation of Phobos [9] which will be constrained by the Phobos-Grunt observations [10].

References: [1] Burns J.A., in Mars, Univ. Arizona Press, pp. 1283-1301, 1992; [2] Peale S.J., in treatise of geophysics, vol. 10, Elsevier, 465-508, 2007; [3] Mignard F., Mon. Not. R. astr. Soc., 194, pp. 365-379, 1981; [4] Andert T.P. et al., GRL 37, L09202, 2010. [5] Rosenblatt P. submitted to A&A Rev.; [6] Rosenblatt P. et al., this meeting; [7] Willner et al., Earth Planet. Sci. Lett., 294, pp. 541-546, 2010: [8] Rosenblatt P. et al., 1st Moscow Solar System Symposium, Abstract-29, 2010; [9] Rambaux et al., EPSC-DPS2011-818; [10] Le Maistre et al., EPSC-DPS2011-1021.

PHOTOMETRIC AND RADIOMETRIC PROPERTIES OF PHOBOS REGOLITH FROM DATA GATHERED BY THE PHOBOS MISSION

L. V. Ksanfomality, *Space Research Institute (IKI), Moscow. Contact: ksanf@iki.rssi.ru*

In the paper the reflectance (spectrophotometric) and thermal (radiometric) properties of Phobos' regolith are reviewed. The study is based on data gathered in 1989 by means of the KRFM spectrophotometer installed onboard the Phobos spacecraft. According to the program of the Phobos mission, it had been assumed that the spacecraft would approach the Martian satellite to a distance of roughly 50 m and drift at this altitude above the surface for 20 min. The spectrophotometer and radiometer would have to carry out the measurements with a resolution, respectively, of 26 and 50 cm on the surface of Phobos. Unfortunately, 10 days prior to this approach, the spacecraft was lost, and this portion of the program was not carried out. The two tracks investigated prior to the loss of the spacecraft did, however, provide a large volume of data. The analysis of these data suggest certain extremely interesting properties of fine-grained material, or regolith, on Phobos, established mainly in the spectrophotometric experiment. Improved spectrophotometry of Phobos in the 300-600 nm band, complemented with data on albedo in the shorter wavelengths of the ultraviolet and near infrared bands are presented. On the basis of the surface properties, Phobos would appear to possess an unambiguously nonhomogeneous composition, which suggests a complex history of development. Judging from the spectrophotometric properties of Phobos regolith discovered in the experiment, its true reflectance properties do not agree very well with the properties of carbonaceous chondrites or yield clear cut analogies to other meteorite materials. The significant inhomogeneity of the properties of regolith seen in the 315-600 nm band is associated with particular topographic features. Two series of spectrophotometric and thermal (radiometric) measurements that were carried out by the Phobos spacecraft are presented.

2MS3-MM-10

THE PHOBOS GRAVITATIONAL FIELD MODELED ON THE BASIS OF ITS TOPOGRAPHY.

D. V. Uchaev[1], J. Oberst[2, 3], V. A. Malinnikov[1], K. Willner[3], Dm. V. Uchaev[1], I. S. Prutov[1], [1]*Moscow State University of Geodesy and Cartography, MIIGAiK Gorokhovsky pereulok 4, 105064 Moscow, Russia,* [2]*German Aerospace Center, Rutherfordstrasse 2, 12489 Berlin, Germany,* [3]*Technical University Berlin, Department for Geodesy and Geoinformation Science, Straße des 17. Juni 135, 10623 Berlin, Germany. Contact: d-Uchaev@yandex.ru*

Introduction:

With the increasing data volume available for Phobos, more and more details of this unique natural satellite have been unveiled. However, the knowledge of its gravity field still remains limited, with even GM suffering from large uncertainties [1, 2]. Since knowledge of Phobos' gravity field is not only important for the study of its inner structure, but also crucial for the navigation of spacecraft, it is highly useful to have working models for the gravity field. As for many other small bodies in the solar system, a common way to develop Phobos' gravity model is to use its shape. Fortunately, useful working models for the gravity field may be derived from shape models. For a homogeneous body, the spherical harmonic coefficients of its gravity field can be derived analytically from its shape [3]. With the assumption of homogeneous density, analytical approach can be applied to get spherical harmonic coefficients as well as gridded potential field model. In this work, model for the gravity field of Phobos have been developed on based shape model.

The shape model: Various previous models exist to describe the shape of Phobos (Turner, 1978 [4], Thomas, 1989 [5], Duxbury et al, 1991 [6], Simonelli et al. [7], 1993, Willner et al., 2008 [8]). The expansion model used in the literature is based on 755 control points and is developed up to degree and order 17 (Figure 1) [8]. Quality of the expansion model has been estimated by computing the remaining differences between observed radii of the control points and modeled radii in the respective directions. Residuals naturally decrease with increasing degree and order determination. However, visual control of the resulting shape model indicated that the modeled shape departs from the observations in images when developed the expansion model to a degree and order higher than 17. On the one hand the degradation is caused by a few control points were observed on some areas especially near North and South Poles and larger craters. On the other hand the determination of coefficients in an expansion over spherical functions leads to very large overdetermined ill-conditioned linear systems of the form $A\mathbf{x}=\mathbf{b}$. Coefficient matrix of these systems either might be singular or very ill-conditioned. Therefore, solving such systems by classical direct and iterative methods (example, by least square method) might lead to strange solutions or fail. Moreover, in such systems, a small perturbation in problem data might significantly change the solution. If a linear system is ill-conditioned, a quite effective procedure to find a reasonably good solution, is the Tikhonov regularization, which solves the following minimization problem rather than classical least square problem:

$$\min_x \left(\|A\mathbf{x}-\mathbf{b}\|^2 + \alpha\|\mathbf{x}\|^2 \right), \qquad (1)$$

where α is a regularization parameter ($\alpha>0$).

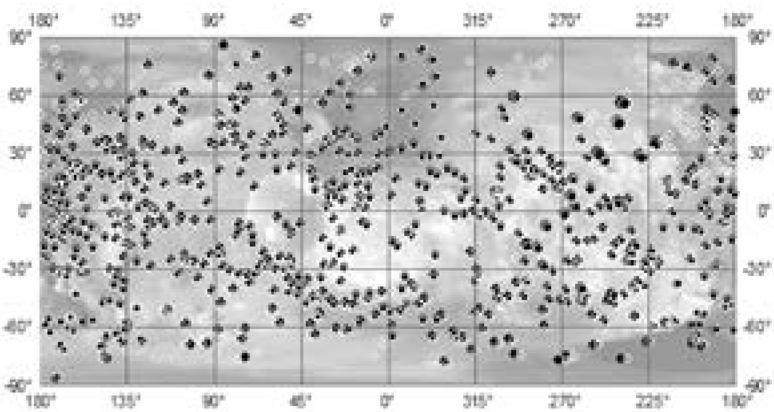

Fig. 1. Control points (white circles) of the using network in comparison with the Willner control point network (black circles) [6].

Tikhonov regularization is the most commonly used method of regularization of ill-posed problems (because of non-existence or non-uniqueness of solution) [9]. It is worth mentioning that when $\alpha=0$, the solution of might have large norm $\|A\mathbf{x}-\mathbf{b}\|^2$ due to ill-conditioned or singular coefficient matrix A. However for suitable small positive α it is not the case.

Thus Tikhonov regularization improves the conditioning of the problem and enabling a numerical solution of ill-conditioned linear system. An explicit solution, denoted by $\hat{\mathbf{x}}$, is given by:

$$\hat{\mathbf{x}} = (\alpha E + A^{\mathrm{T}} A)^{-1} A^{\mathrm{T}} \mathbf{b}.$$

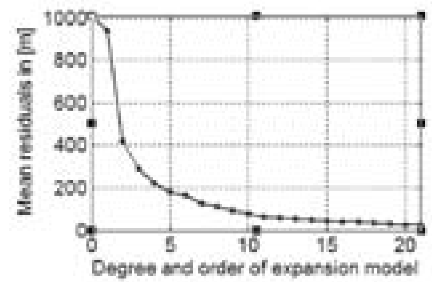

Fig. 2. Mean residuals of control points to the spherical harmonic function model.

When $\alpha=0$ this solution reduces to the unregularized least squares solution provided that $(A^{\mathrm{T}}A)^{-1}$ exists.

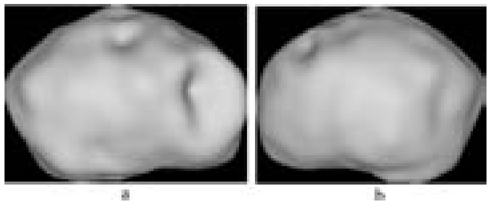

Fig. 3. Panels (a) and (b) show Phobos' leading and trailing side, respec-tively, as modeled with the degree and order 18 spherical harmonic function model. 794 control points were used to compute the coefficients of the expansion model.

We used the Tikhonov regularization method for determination of coefficients in an expansion over spherical functions of degree and order 18. The 3D-coordinates of the 794 control points which were determined, using mainly the last data from HRSC (High Resolution Stereo Camera), SRC (Super Resolution Channel) on board ESA's Mars Express mission and Viking Orbiter images were used as initial input data set (Figure 1). Though a higher degree and order model resulted in further reduction of the residuals (Figure 2), the large spacing of control points in some areas caused again artifacts in the model. The developed spherical harmonic function model represents the shape of Phobos with good detail (Figure 3). Developed shape model motivated us to undertake a new effort of updating previous gravity field models.

The gravity field: The gravity field of a celestial body can be expressed using spherical harmonic coefficients as

$$U(r,\theta,\lambda) = \frac{GM}{r}\sum_{l=0}^{\infty}\left(\frac{R}{r}\right)^{l}\sum_{m=0}^{l}[C_l^m \cos m\lambda + S_l^m \sin m\lambda]P_l^m(\cos\theta),$$

where G is gravitational constant; M is mass of body; R is the radius of an origin-centered sphere enclosing the body; C_l^m and S_l^m are coefficients in an expansion of gravitational potential, U, at range r on body; subscripts l and m of the coefficients indicate the degree and order, respectively, of the spherical functions; $0\le\lambda\le2\pi$; $0\le\theta\le\pi$; P_l^m are the associated Legendre polynomials.

In the case of Phobos, by assuming a homogeneous density, according to [3], C_l^m and S_l^m can be derived by integration over the shape

$$C_l^m = \frac{1}{(l+3)(2l+1)VR^l}\int_0^{\pi}\int_0^{2\pi} R^{l+3}\cdot P_l^m(\cos\theta)\cdot\cos m\lambda\cdot\sin\theta\cdot d\lambda d\theta,$$

$$S_l^m = \frac{1}{(l+3)(2l+1)VR^l}\int_0^{\pi}\int_0^{2\pi} R^{l+3}\cdot P_l^m(\cos\theta)\cdot\sin m\lambda\cdot\sin\theta\cdot d\lambda d\theta,$$

where V is volume of body.

In this work, model for the gravity field of Phobos have been developed using spherical harmonic function model of shape of Phobos to degree and order 18 (Figure 4).

Conclusion and Outlook: It is shown that the harmonic coefficients determined by developed the shape model can readily be used to calculate the gravitational potential on a sphere outside Phobos and can be applied to trajectory analysis of spacecraft near or approaching Phobos. Using in this work shape model is currently the best available for Phobos. However, more close range observations of Phobos through the SRC, HRSC can be densified the control network. This could subsequently lead to a spherical expansion model of higher degree and order, as more control points are determined. The determined spherical harmonic function model can also contribute to Phobos-Grunt and future mission to Phobos.

Acknowledgement: This research was funded by the Ministry of Education of the Russian Federation (MEGA-GRANT, Project name: "Geodesy, cartography and the study of planets and satellites", contract № 11.G34.31.0021).

References: [1] Shi X., Willner K., Oberst J. (2011) Working models for the gravity field and dynamical environment of Phobos. Second International Conference on the Exploration of Phobos and Deimos, 14–16 March 2011, Moffett Field, USA, 11-005. [2] Shi X., Willner K., Oberst J. (2011) Working Models for the Gravity Field of Phobos. (2010) Vol. 5, EPSC2010-221. [3] Balmino G. (1994) Celestial Mechanics and Dynamical Astronomy, 60, 331–364. [4] Turner R. J. (1978) A model of PHOBOS. Icarus 33, 116–140. [5] Thomas P.C. (1989). The shapes of small satellites. Icarus 77, 248–274. [5] Duxbury T. C. (1991) An analytic model for the PHOBOS surface. Planet. Space Sci. 39, 355–376. [6] Simonelli D. P. et al. (1993) The generation and use of numerical shape models for irregular Solar System objects. Icarus 103, 49–61. [7] Willner K. et al. (2010) Phobos control point network, rotation, and shape. Earth and Planetary Science Letters, 294, 541-546. [8] Tikhonov A. N., Arsenin V. Y. (1977) Solutions of Ill-Posed Problems, Winston, New York.

DEVELOPMENT OF A GLOBAL CRATER CATALOG OF PHOBOS, AND GIS-ANALYSIS OF THE DISTRIBUTION OF CRATERS

I.P.Karachevtseva[1], J.Oberst[1,2], K.B.Shingareva[1], A.A.Konopikhin[1], E.V.Cherepanova[1], M.Wählisch[2], K.Willner[2] *[1]Moscow State University of Geodesy and Cartography (MIIGAiK), Moscow, Russian Federation, [2]German Aerospace Center (DLR), Institute of Planetary Research, Berlin, Germany*. *Contact: i_karachevtseva@coslab.ru*

Introduction: At MIIGAiK we are developing a geographic information system (GIS) Phobos using the results of a survey by the European “Mars Express” (MEX), including HSRC and SRC images. The data were previously photogrammetrically processed, including orthorectification, based on the new global DTM [4]. Using these data provided by DLR we created a Global Crater Catalog of Phobos. The Global catalog and the DTM have been used for GIS-analyses of the surface body: measurements of statistic parameters of features and calculating surface parameters such as topographic roughness, size-frequency distribution and spatial density of craters. Our GIS mapping technology developing for celestial bodies can be used for cartography support of the future mission Phobos-Grunt.

Methodology: At present moment, the information system Phobos is developed as a personal geodatabase, because the amount of Phobos data is still small. To create the system, the global image mosaic, global DTM and high resolution MEX images data obtained both on the basis of past and recent surveys were converted and loaded into ArcGIS. The geodatabase now consists of many vector and raster layers and can be used for overlaying analyses at considerable level of detail. Using these data and instrument CraterTools [3] have been provided semi-automatic digitizing of Phobos craters as a GIS layer. CraterTools calculates a best-fit circle based on a user input of three points on the crater. Measurements are automatically corrected for the data frame map projection to provide accurate crater diameter and coordinate values.

Global distribution of Phobos craters: In total, we mapped about 5000 craters (Fig 1). All craters, regardless of degradation state, were included in the catalog if they are clearly visible in the high- resolution images. The global catalog of Phobos craters consists of their diameters and also their depths which were obtained from the DTM, as well as the value of ratio depth/diameter. Using these data we calculate size-frequency distribution (Fig 2), and spatial density of craters (Fig 3), which show the varying degree of cratering on Phobos. The distribution of craters shows (Fig. 4) that most craters are concentrated in the Sub-Mars region, the smallest are found in the polar regions (in the image, all values are normalized to unit area). Craters on Phobos are prevalent in size from 50 to 100 m. The number of large craters (D> 1 km) in different areas of Phobos is about the same, but at the South Pole approximately 2 times smaller. The ratio of crater depth to diameter within the entire territory of Phobos is 0.2, and for large craters (D> 1 km), it is 0.3.

GIS-analyses of surface roughness: The Phobos surface is rough to the resolution limit of the DTM, we calculate surface roughness using the global DTM and 5 difference techniques: 1) Area ratio; 2) Standard deviation of slope (STD Slope, Fig 5-1); 3) Vector roughness measurement (VRM, Fig 5-2); 4) Standard deviation of elevation and 5) Standard deviation of profile curvature. Area ratio operated independently of scale, providing consistent results across spatial resolutions. VRM incorporates the heterogeneity of both slope and aspect by measuring the dispersion of vectors orthogonal to the terrain surface. The VRM values are low both in flat and in steep areas, but values are high in areas that are both steep and rugged. STD elevation correctly identified breaks of slope and was good at detecting regional relief. STD Slope correctly identified both smooth sloping areas and breaks of slope, providing the best results for geomorphological analysis. Standard deviation of profile curvature identified the breaks of slope, although not as strongly as STD Slope, and it is sensitive to errors of the DTM [2].

Geoanalysis of landing sites of the Phobos-Grunt mission: Additionally, we performed geoanalysis of landing sites of the Phobos-Grunt mission for area as was recently proposed [1], [5]. This region is limited from 240°W to 210°W longitude and from 10°N to 30°N latitude. We used MEX image h7915_0009.nd2 whose resolution is up to 4 m/pixel. In the study region, an area of 21 km^2 allocated about 160 craters with a diameter from 23 m to 770 m (1 crater with diameter about 1.4 km located on the edge of the area and far from proposed spacecraft descent-and-approach paths).

Using GIS tools we calculate some parameters of the landing site territory, including spatial density (Fig.7) and size-frequency distribution (Fig.8), which show that craters are probably the most dangerous obstacles for landing, though these are less frequent in the area, which agrees with the results of [1]. The ratio of crater depth to diameter for the study area is 0.07-0.45. The vertical profile of the area shows that the elevation is about 800 m to the distance 3.2 km (Fig.9).

Conclusions: We present the results of development a Global crater catalog of Phobos, which now consists of about 5000 entries with diameters from 20 m to 8.1 km. Geostatistical analysis of Phobos surface have been made using automatic GIS function, including analysis one of the landing site of the Phobos-Grunt mission which showed good agreement comparing with the results of the earlier geomorphological analysis [1]. Our proposed GIS mapping technology can be used for the cartographic support of the Russian project Phobos- Grunt. **A** Global crater catalog of Phobos was constructed using individual MEX images with resolutions from 4 m/pxl to 12 m/pxl, which, unfortunately, were incomplete, and taken at varying solar illumination [4]. Although it is difficult to produce uniform measurements across the entire surface area of the Phobos with the available data, we decided to do this for a first global assessment of the population of craters, because even small-scale features are clearly visible in the high-resolution images. For a more accurate assessment of global distribution, we will study in more detail the coverage and accuracy of the data.

Acknowledgement: This research was funded by the Russian Government (MEGAGRANT, Project name:
“Geodesy, cartography and the study of planets and satellites”, contract № 11.G34.31.0021).

References: [1] Bazilevskij A.T., Shingaryova T.V. (2010) *Astronom. Vestnik, T. 44. № 1,* P. 41–47. (In
Russian). [2] Grohmann C.H et al. (2010) *Geoscience and Remote Sensing, IEEE Transactions on, vol.PP, no
99,pp.1-14.* [3] Kneissl T et al. (2010) *41st LPSC,* [#1638] [4] Wählisch M. et al. (2010) *EPSL 294*, P. 547–553. [5] Willner K. et al. (2010) *The first Moscow Solar System Symposium.*

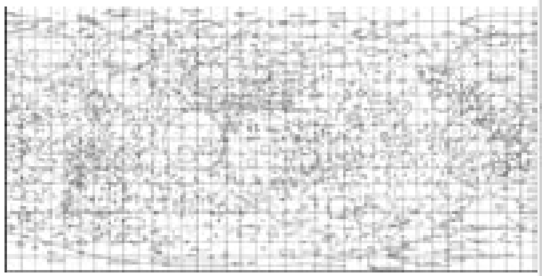

Fig. 1. Global crater catalog of Phobos

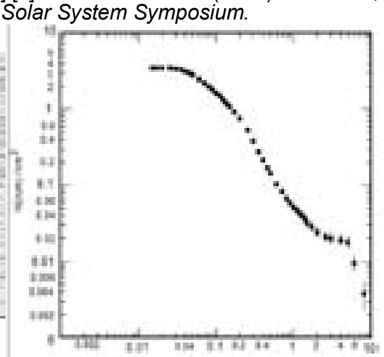

Fig. 2. Global size-frequency distribution of Phobos craters

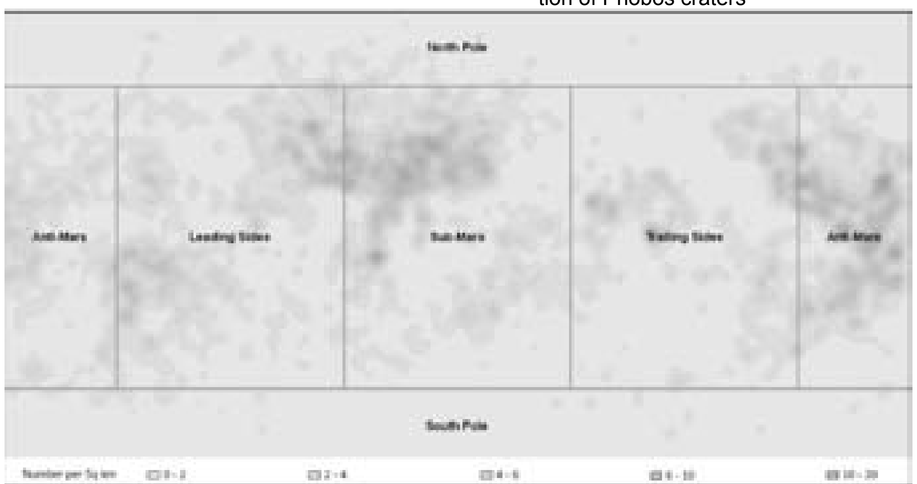

Fig. 3. Global spatial density distribution of Phobos craters

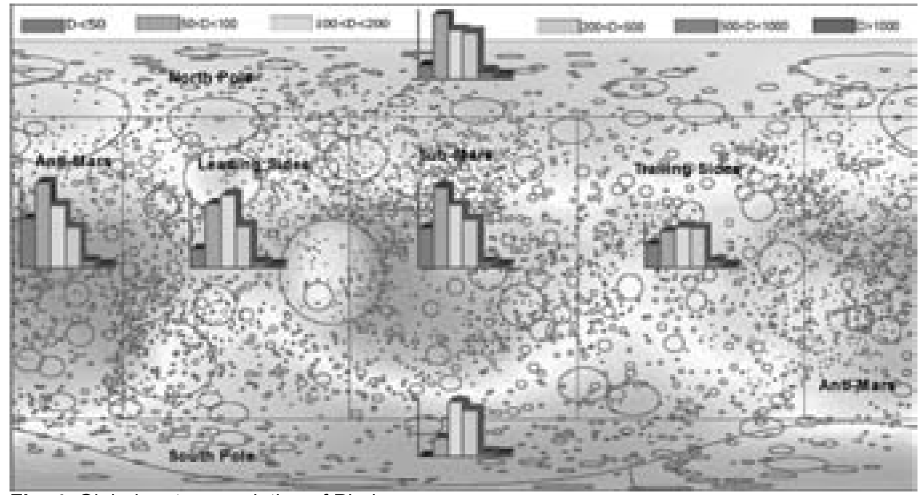

Fig. 4. Global crater population of Phobos

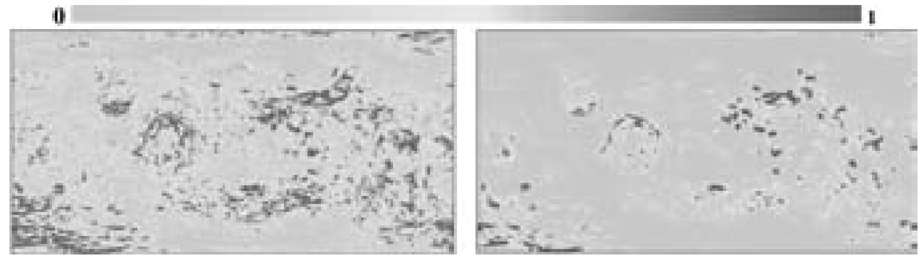

Fig. 5. Global roughness measurement of Phobos
Fig. 5-1. Standard deviation of slope (STD Slope) **Fig. 5-2.** Vector roughness measurement (VRM)

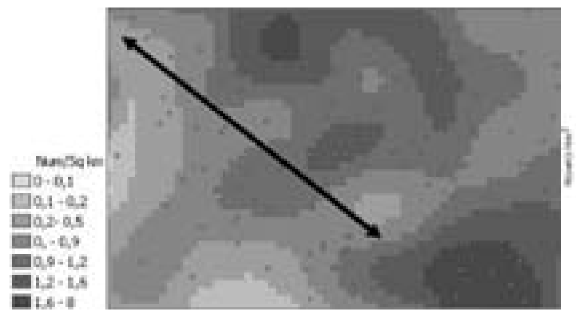

Fig.7. Spatial crater density for one of the proposed landing sites (#3, [1]), calculating using diameter as weight. White points are centroids of the craters

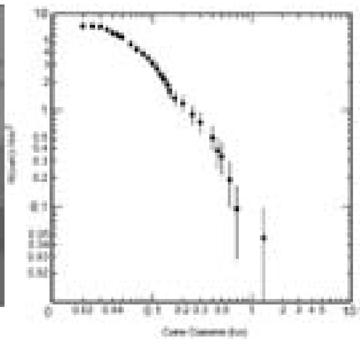

Fig.8. Size-frequency distribution of landing site 3 craters

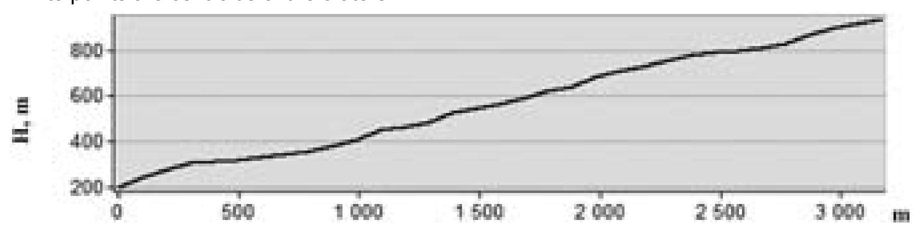

Fig.9. Vertical profile of landing site 3 (along direction as shown by the arrow at Fig. 7)

For a color version ofthis abstract, please download from: http://coslab.ru/files/articles/2M S3 Karachevtseva Catalog Crater Phobos.pdf

PRINCIPALS OF VOLATILE COMPONENTS MEASUREMENTS IN THE GAP EXPERIMENT ONBORD THE PHOBOS-GRUNT MISSION AND BEYOND.

M.V.Gerasimov and the GAP team, *Space Research Institute of the RAS, Moscow, Russia. Contact: mgerasim@mx.iki.rssi.ru*

Introduction: Gas-analytic experiment is aimed on the comprehensive investigation of volatiles inventory of the Phobos surface material. This information is valuable for understanding of origin and differentiation of the Phobos. Chemical composition and abundance of volatile components in different types of meteorites is genetically connected with conditions of origin of primordial materials in different regions of the solar nebular. Such primordial materials are widely presented by chondritic meteorites. Incorporation of volatile elements into forming meteorites in the nebular is the most sensitive to environmental conditions providing compositional difference of volatiles pattern in different types of meteorites. Information about the composition of the Phobos volatiles can give valuable information about the region of its origin in the Solar nebular and its relationship to Mars or any type of meteorites.

Information about isotopic ratios of key volatile elements (C, H, O, N, noble gases, …) is also of great importance for discrimination between different models of the Phobos origin.

Tasks of the Gas-Analytic Package: GAP consists of three individual instruments: 1) Thermal Differential Analyzer (TDA); 2) Gas Chromatograph (KhMS-1F); and 3) Mass-Spectrometer (MAL-1F).

The main tasks of the Gas-Analytic Package (GAP) are:

Detailed investigation of chemical composition and abundances of volatile compounds (H_2O, CO_2, N_2, H_2, noble gases, organics, etc.) in the solid surface material of the Phobos at the landing place;

Investigation of forms of incorporation of volatile components into the solid surface material;

Investigation of organic components in the surface material;

Measurement of isotopic composition of CHON elements ($^{13}C/^{12}C$, D/H, $^{17}O/^{16}O$, $^{18}O/^{16}O$, $^{15}N/^{14}N$) and noble gases;

To constrain the mineralogical composition of the Pobos soil (with emphasis on the volatile-bearing minerals) on the basis of thermal and gas evolving experiments with the use of data from other experiments.

Principals of volatile components measurement: GAP receives a portion of soil from the Sample Acquisition Device of the manipulator. This portion is loaded into the SOil Preparation SYStem (SOPSYS) of the TDA instrument. SOPSYS provides milling of soil stones down to sub millimeter size and prepare a dose of the sample for load and sealing into pyrolytic cell (PC). PC perform programmed heating of the sample up to 1000ºC to do thermal analysis of the sample and to provides the release of volatiles into gaseous phase. Released gases are transported to the gas chromatograph by a flow of carrier gas (helium). Gases in time of pyrolysis are analyzed in KhMS-1F using tunable diode laser absorption spectrometer (TDLAS) to measure H_2O and CO_2 molecules and isotopic ratios $^{13}C/^{12}C$, D/H, $^{17}O/^{16}O$, $^{18}O/^{16}O$ in them. Afterwards gases are trapped in two absorption traps: one for permanent gases and another for high boiling components. Collected gases are analyzed than on two chromatographic capillary columns: one for analysis of permanent gases; and the second for analysis of high boiling components. Separated gases are transferred to mass spectrometer for mass spectrometric analysis.

Paper considers in detail the principals of analysis of components of a complex gas mixture using GAP.

Cooperation: Main partners of the Gas Analytic Package team are:
IKI RAS (Russia),
GEOKHI RAS (Russia),
LATMOS and LISA, University of Paris (France),
CNRS-GSMA, University of Reims (France),
Max Planck Ins. for Solar System Res. (Germany)
Polytechnic University of Hong Kong (China)

THE GAS CHROMATOGRAPH OF GAP, THE GAS ANALYTICAL PACKAGE ABOARD PHOBOS-GRUNT MISSION: IN SITU ANALYSIS OF THE SURFACE OF PHOBOS

M. Cabane[1], C. Szopa[1], P. Coll[2], D. Coscia[1], J.P. Goutail[1], J.J. Correia[1], A. Galic[1], A. Gaboriaud[3], M.V. Gerasimov[4] (4), I.I. Vinogradov[4], A.G. Sapgir[4], A.V. Kalyuzhnyi[4], A.V. Stepanov[4], A.Yu.Titov[4], Yu.V. Lebedev[4], M.M. Gerasimov[4], the GAP team, *[1]LATMOS, UPMC-UVSQ-CNRS, 4 Place Jussieu, 75005 Paris, France; [2]LISA, CNRS-Univ. Paris 7 and 12, Créteil, France; [3]CNES, Toulouse, France; [4]IKI, Moscow, Russia. Contact : michel.cabane@latmos.ipsl.fr*

Abstract: Despite observations done with different space probes, the origin of Phobos still remains unclear. The two main scenarios preferred today are: 1. Phobos would have been created from material ejected by an impact on Mars that reaccreted in Martian orbit [1]; 2. Phobos would be an asteroid (chondrite type) that was captured from the main belt by the Mars gravity [2]. Therefore, exploring the surface of Phobos could allow either to study martian material, or to have a first close view of the surface of a chondrite. Moreover, the Phobos surface should have accumulated, through the geological times, materials coming from the interplanetary space. The analysis of the Phobos surface could reveal the nature of such materials, and hence, provide information on the delivery of such materials to planetary surfaces from the interplanetary medium.

In order to collect pieces of information on the satellite of Mars, the Phobos-Grunt mission is currently developed by the Russian space agency, and the spaceprobe should be launched by the end of 2011 to reach Phobos within two years [3]. The primary objective of the mission is to return samples from the surface of Phobos to Earth for careful study of their physical, mineralogical and chemical properties in laboratory. However, the uncertainty on the fate of the collected samples during the return journey makes uncertain their characterization on Earth (e.g. volatiles conservation). For this reason, the use of *in-situ* measurements is a key point to obtain ground truth data that will give a first insight of the properties of the material collected at the surface of the satellite, and that will be used as a reference to estimate a potential evolution of the material returned to Earth.

The scientific payload of the Phobos-Grunt mission includes the Gas Analytical Package (GAP) devoted to the chemical analysis of the collected samples. It is composed of a gas chromatograph (GC), a mass spectrometer (MS), a tunable diode laser absorption spectroscope (TDLAS) and a thermal differential analyzer (TDA). The main goal of this experiment is the characterization of the chemical composition of volatile species contained in the samples, or coming from their thermal decomposition up to 1000°C.

The gas chromatograph, coupled with the mass spectrometer, is devoted to separate the analyzed volatiles, allowing their strict identification and quantitation. The main chemical targets of this instrument are: 1. volatile species coming from absorbed or frozen components present in the near subsurface of the satellite (e.g. water); 2. Structural gases contained in some minerals (e.g. SO_2 for sulfates); 3. Organic species that could have been originated during the Phobos formation and evolution and/or brought from the outside (e.g. by interplanetary dust particles, for example). In order to be capable to separate all these species, GAP-GC is composed of two analytical channels devoted to two specific classes of products. The first channel will allow the analysis of small molecules (typically with up to 4 atoms), mainly inorganics, whereas the second channel will focus on organics.

This communication aims at presenting a detailed description of this instrumentation, and to show its analytical capabilities to provide an accurate view of the chemical composition of the surface of Phobos.

References: [1] R.A. Craddock : Are Phobos and Deimos the result of a giant impact ?, Icarus 211(2) 1150-1161 (2010)..

[2] A.S. Rivkin, R. H. Brown, et al. : Near-Infrared Spectrophotometry of Phobos and Deimos, Icarus 156(1): 64-75 (2002).

[3] L.M. Zelenyi, A.V. Zakharov : Phobos-Grunt project: Devices for scientific studies, Solar System Research, 44(5) 359-361 (2011)

NEAR INFRARED DIODE LASER SPECTROSCOPY OF C2H2, H2O, CO2 AND THEIR ISOTOPOLOGUES AND THE APPLICATION TO A TUNABLE DIODE LASER SPECTROMETER (TDLAS) FOR THE MARTIAN PHOBOS-GRUNT SPACE MISSION

G. Durry[1] , J.S. Li[1], I. Vinogradov[3], A. Titov[3], L. Joly[1], J. Cousin[1], T. Decarpenterie[1], N. Amarouche[2], X. Liu[1], B. Parvitte[1], O. Korablev[3], M. Gerasimov[3], V. Zéninari[1] , *[1]Université de Reims Champagne-Ardenne, Moulin de la Housse, BP 1039,51687 Reims, Cedex 2, France; [2]Division Technique de l'Institut National des Sciences de l'Univers, 92195 Meudon Cédex, France; [3]Space Research Institute, Moscow, Russia. Contact: georges.durry@univ-reims.fr*

Abstract: A near-infrared tunable diode laser spectrometer called TDLAS has been developed that combines telecommunication-type as well as new-generation antimonide laser diodes to measure C_2H_2, H_2O, CO_2 and their isotopologues in the near infrared. This sensor is devoted to the in situ analysis of the soil volatiles of the Martian satellite PHOBOS, within the framework of the Russian space mission PHOBOS-GRUNT. We report accurate spectroscopic measurements of C_2H_2 and ${}_{13}C_{12}CH_2$ near 1.533 µm, of H_2O and CO_2 at 2.682 µm and of the isotopologues ${}_{13}C_{16}O_2$ and ${}_{16}O_{12}C_{18}O$ near 2.041 µm and $H_{2\ 17}O$, $H_{2\ 18}O$ and HDO near 2.642 µm. The achieved line strengths are thoroughly compared to data from molecular databases or from former experimental determinations. We also present moments of design and early calibration data of the TDLAS spectrometer, which has been integrated into the Gas Analytic Package apparatus and installed on-board of the PHOBOS-GRUNT mission spacecraft.

THE MINIATURIZED MOESSBAUER SPECTROMETER MIMOS II FOR THE PHOBOS-SOIL MISSION.

G. Klingelhoefer[1], D. Rodionov[1,2], M. Blumers[1], B. Bernhardt[3], E. Evlanov[2], J. Girones[1], J. Maul[1], I. Fleischer[1], O. Prilutskii[2], A. Shlyk[2], C. d'Uston[4], *[1]Institut für Anorganische und Analytische Chemie, Universität Mainz, Germany (Staudinger Weg 9, Mainz, Germany, 55122), [2]Space Research Institute IKI, (117997, 84/32 Profsoyuznaya Str, Moscow, Russia), [3]VonHoerner&Sulger GmbH, Germany,. [4]Space Research Center (CESR), Toulouse, France. Contact:klingel@mail.uni-mainz.de*

Introduction:

Moessbauer spectroscopy (MS) is a powerful tool for the mineralogical analysis of Fe-bearing materials due to the unique abilities of the resonance absorption or emission of γ-quanta emitted by particular radioactive isotopes (in our case, 57Fe) and interacting with the corresponding crystal lattices, where the nucleus-recoil energy loss is compensated.

The Miniaturized Moessbauer spectrometer MIMOS II has already been working on the surface of Mars for more than 7 years as part of the NASA Mars Exploration Rovers mission [1-4]. The improved version of the instrument is a component of the scientific payload of the Phobos-Soil mission [5]. The scientific objectives of the instrument are the following: to identify the iron-bearing phases, to determine the quantitative distribution of iron among these phases, and to determine the distribution of iron among its oxidation states.

General design of the instrument:

The MIMOS II instrument consists of two units connected with a cable: the sensorhead (Fig.1) and the electronics board. The sensorhead contains an electromechanical oscillator, two Co-57 sources of γ-radiation (the main source (300 mCi) and the calibration source (10 mCi), used for the measurement of a calibration sample in transmission geometry, a collimator, a radiation-protection system, five detectors (Si-PIN) and their preamplifiers, and the main (linear) amplifiers (Fig.2). MIMOS II operates in the backscatter geometry, which allows to avoid any preliminary preparation of the sample.

Fig. 1. MIMOS II Sensorhead installed on robotic arm.

Most functions of the instrument and the capabilities of the data processing (including the acquiring and separate storage of the spectra obtained at different temperatures) are fulfilled with the internal microprocessor, memory, and embedded firmware. MIMOS II is an independent instrument: it can autonomously operate for a long time. The total power consumption is about 2 W. The sensorhead (in flight configuration) is about 450 g in mass and its size is 50x50x90 mm. The electronics is about 100 g in mass and it's size is 160x100x20mm.

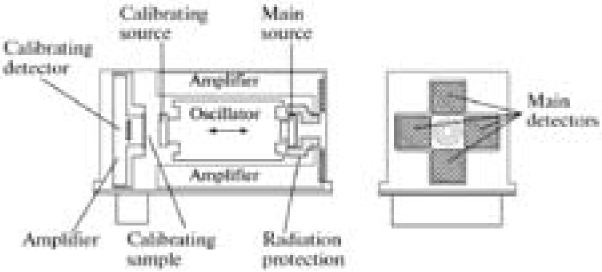

Fig. 2. The principle scheme of MIMOS II Sensorhead

The MIMOS II Sensorhead was designed at Mainz University (support of German Space Agency under contract 50 QM 0703 is acknowledged). The electronics board was designed in collaboration of Mainz University, VonHoerner&Sulger GmbH and Space Research Institute (IKI). The MIMOS II has successfully passed all preflight tests.

Current activity:

One of the main obstacles in operating of MIMOS II is the use of radioactive sources. Preparation for the installation of Co-57 sources at Baykonur at the end of October 2011 is currently underway.

Also, during the next year, a number of calibration measurements of Phobos soil analogues are planned. For that purpose the experimental setup is being prepared at IKI. An exact copy of the flight sensorhead will be used in conjunction with specially designed electronics (manifactured by VonHoerner&Sulger GmbH, Germany).

Scientific output:

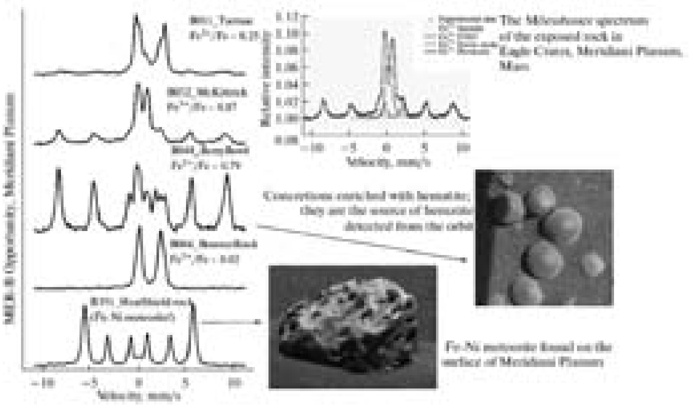

Fig. 3. The examples of the Moessbauer spectra obtained at Meridiani Planum by the Opportunity rover of the MER mission.

During the MER mission, a substantial number of Moessbauer spectra (several hundred) of different samples from the surface of Mars were acquired. An example is presented in Fig. 3. to illustrate possible scientific output of MIMOS II instrument.

References:

[1] Klingelhoefer et al, Science, 2004, vol. 306, [2] Morris et al, Science, 2004, vol. 305, [3] Morris et al, JGR, 2006a, vol. 111, [4] Morris et al, JGR, 2006b, vol. 111, [5] Rodionov et al, Solar System Research, 2010, Vol. 44, No. 5, pp. 362–370

SUBSURFACE RADAR SOUNDING OF THE PHOBOS GROUND

N.A.Armand, V.M.Smirnov, V.N.Marchuk, O.V.Yushkova, V.N.Sekistov[1], V.V.Abramov, A.S.Bazhanov[2] [1]*Institute of Radioengineering and Electronics of RAS, Moscow, Russia;* [2]*Special Design Bureau of IRE RUS, Fryazino, Russia. Contact: marchuk@ms.ire.rssi.ru*

The purposes and problems of experiments with device LWR:

The basic purpose of experiment is revealing of deep structure of a Phobos, research of a relief and a roughness of the Phobos surface, an estimation of dielectric properties of a ground on different depths along a line of spacecraft flying.

The long-wave planetary radar (LWR) is the radar complex intended for sounding of the Phobos ground by a method of pulse radio sounding on frequency of 150 MHz by duration 26.6 ns (four periods of carrier frequency) that corresponds to a frequency bandwidth of 50 MHz. The chosen frequency range will allow to carry out sounding of the Phobos ground, at the accepted model, to depths from units to hundreds meters with resolution about 2 m.

In contrast to traditional georadar LWR has the big range of working distances, caused by necessity to work both from orbit KA, and from the Phobos surface. Device operating modes provide formation of a signal or in the form of the single impulse consisting from four periods of a radio frequency - a simple signal, or in the form of pseudo-casual sequence of radio-frequency pulses – complicated phase code manipulated signal. Parameters and types of radiated signals are defined by problem statement on sounding of structure of a ground and technical possibilities of spacecraft (SC).

Planned experiments:

It is supposed to make following experiments with device LWR in mission “Phobos-Soil”.

1. Survey sounding of the Phobos surface at being SC in a quasisynchronous orbit (a mode 1 (low informative) - 4 sessions for 3 hours), (fig. 1)
2. Detailed sounding of the chosen sites of a surface at being SC in a quasisynchronous orbit (a mode 2 (highly informative) - 6 sessions for 5 minutes), (fig. 2).
3. Sounding at SC landing (in a range of heights from 30 km to 1 km (a mode 3) – 1 session of 10 minutes), (fig. 3).
4. Sounding at SC landing (in a range of heights from 1 km to 100 m (a mode 4) – 1 session of 10 minutes), (fig. 3).
5. On the Phobos surface it is supposed to provide 4 sessions approximately on one minute in each of four modes (fig. 4). (The given type of experiment is carried out facultatively, that it is in the presence of free energy).

Operating time in each mode and the planned volume of the information presented in table 1.

Table 1. LWR information in various modes.

Locality	Mode	Measurement volume, byte	Operating time for a session, min	Quantity of measurements for a session	Quantity of session in the mission	Full volume for mission, Mb
Quasi synchronous orbit	1	57024	180	120	4	26.1
Quasi synchronous orbit	2	16896	5	600	6	58.0
Landing (Up to 10 km)	3	4224	10	1200	1	4.8
Landing (below 10 km)	4	2112	10	1200	1	2.4
On Phobos surface	1,2,3,4	≈20064	1	10	4	0.8
Total:						92.1

2MS³-PhS-05

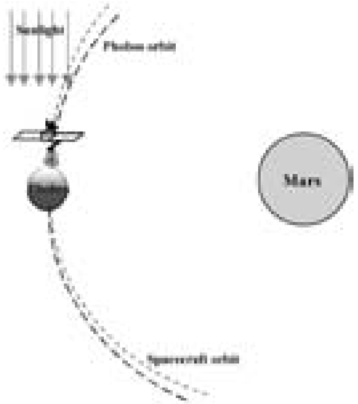

Fig. 1. The scheme of carrying out of experiments in a quasisynchronous orbit.

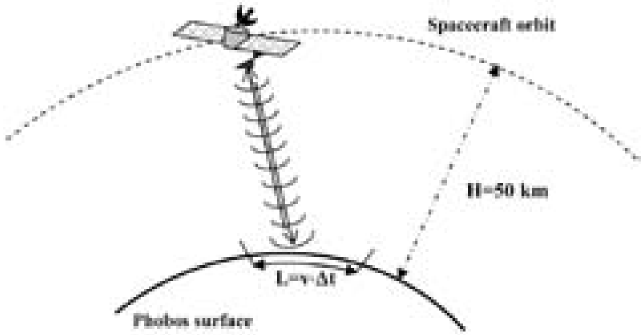

Fig. 2. The scheme of carrying out of experiment in a quasisynchronous orbit in a mode 2.

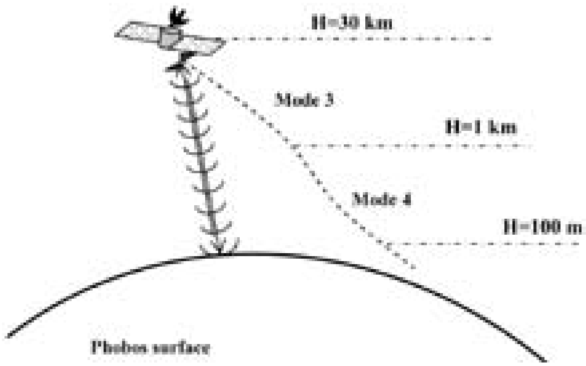

Fig. 3. The scheme of carrying out of experiments in modes 3 and 4 at spacecraft landing.

Probing impulse characteristics:

Carrier frequency of a signal:

Value of carrier frequency (or the central frequency of a signal spectrum) of the subsurface sounding radar is defined by the compromise between several mutually inconsistent requirements. Most important of them are the following:

- Specific absorption, i.e. signal attenuation on unit of a way in ground Γ=54,6Im $\sqrt{\varepsilon}/\lambda$(dB/m) in inverse proportion to length of a wave. Hence, at research of absorbing environments it is necessary to increase length of a wave.

- Conditions of a radio impulse formation by transmitter cascades and by the radar antenna impose certain restrictions on the relation of spectrum signal bandwidth to value of carrier frequency $\Delta f/f_0$. As appears from experience of working out of a traditional georadar this relation usually is $\Delta f/f_0<0.5$. Conditions of radar placing and radar work on spacecraft is limited with the size and weight of the antenna and, hence, with the used wavelength of a radio signal. Overall dimensions of antenna are, as a rule, one of the basic limiting factors of practical application of land-based and satellite-based georadars.

Kind of probing impulses:

On fig. 4a the probing impulse consisting of four periods of frequency f_0=150 MHz is shown, on fig. 4b the power spectrum of this impulse is resulted. The width of a spectrum on level 0.5 is ~45 MHz. Side lobe of a spectrum can be reduced using corresponding hardware filters at signal formation. Such impulses can be applied at a stage of spacecraft landing on the Phobos near to a surface or at work on the surface. However energy of single impulses hasn't enough at sounding of the Phobos surface from an orbit and at the initial stages of a landing.

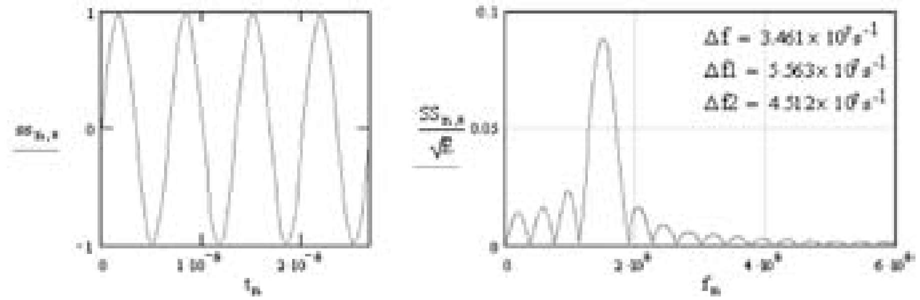

a) b)

Fig. 4. A shape of probing signal and its spectrum

The common decision applied in a radar-location it is using of the complicated signals, allowing to realize high resolution at small pulse power of the radar transmitter. Application of matched filtering method during its processing allows to raise a signal/noise ratio proportionally to base of a signal equal to product of signal bandwidth on its duration T: $B=\Delta f \times T>>1$, while for a simple signal (a single impulse) $B\cong 1$. On the Phobos surface and near to it can be applied both a simple signal in the form of single radio impulses, and a complicated signal to achievement of the maximum depths of sounding.

The condition of use of signals both with base $B\cong 1$, and with base B>>1 defines a choice of structure of a complex signal in a kind phase code manipulated (PCM) binary sequence of the maximum duration (it still name M-sequence or pseudo-casual sequence). Advantage of M-sequences is simplicity and convenience of formation by generators on registers of shift with linear feedback. The length of M-sequences is equal $N=2^n-1$, where N – quantity of pulses with τ duration, and n – the number of cascades in the generator on the shift register. At optimum processing of the accepted signals there is the correlation function, peak duration is equal to τ. Thus, the relation of the maximum value of a lateral petal of correlation function to a maximum is equal $N^{-1/2}$. The spectrum of the PCM-sequence consisting of 2047 radio impulses presented on fig. 5. The spectrum is strongly irregularity, but its width is comparable with width of an individual element – a radio impulse

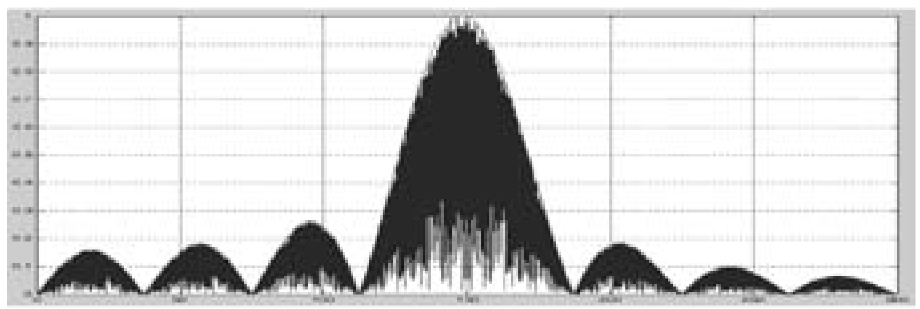

Fif.5. Spectrum of LWR signal, consisting of 2047 pulses of PCM sequence.

Signal processing simulation:

LWR signals processing simulation for the purpose of definition of algorithm stability to additive noise is carried out. PCM sequence reflection from the multilayered reflecting environment within the limits of approach of a flat wave was modeled. On fig. 6a the pulse response of the three-layer reflecting environment model is resulted. On fig. 6b the signal reflected from the modeling environment after correlation processing is shown, at level of noise in 6 times exceeding signal level. Apparently, from fig. 6b the pulse characteristic at such processing is restored practically without distortions.

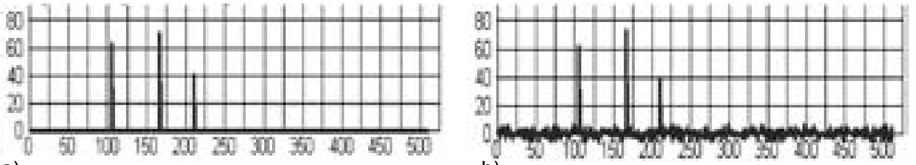

a) b)

Fig.6. Model of reflecting medium (a) and the result of signal processing (b).

Device LWR structure:

LWR mode is presented on fig. 7 (for a scale on a background the laptop is placed). DPR device consists of the antenna and electronic block. Total weight of the device is 3.5 kg, average power consumption is about 6 W. One antenna is used both to transmit and receive signal in mode with division on time, therefore there is a restriction on the minimum range of sounding (a dead zone), caused by time of switching from a mode of transmitter to a reception mode. For the big heights, existence of such dead zone does not represent problems, for sounding from a surface it will lead to that depth of sounding will begin approximately with 8-16 meters.

Fig. 7. General view of LWR.

TIMM: ECHELLE-SPECTROMETER TO STUDY THE ATMOSPHERE OF MARS

O. Korablev[1], F. Montmessin[2], A. Trokhimovsky[1], A.A. Fedorova[1], A.V. Kiselev[1], J.L. Bertaux[2], J.P. Goutail[2], D.A. Belyaev[1], A.V. Stepanov[3,1], A.Yu. Titov[4], Yu.K. Kalinnikov[5], O.N. Andreev[1], O.E. Kozlov[1], A. Venkstern[1], *[1]Space research Institute (IKI), Moscow, [2]LATMOS, Guyancourt, France, [3]Physical faculty, Moscow State University, [4]Special Design Office of IKI, Tarusa, Kaluga reg, [5]VNI-IFTRI, Mendeleevo, Moscow reg.*

Echelle-spectrometer TIMM for Phobos-Grunt is dedicated to studies of the martian atmosphere analyzing the spectrum of solar light passed through the atmosphere on the limb of the planet. The main science goals of the instrument on Mars are to detect methane, measure the D/H ratio in water, and to study the vertical structure of the aerosol. The spectral range of the spectrometer is 2300-4100 nm, spectral resolving power $\lambda/\Delta\lambda$ >25 000, the field of view is 1.5x21 arc min. The spectrum is measured in narrow intervals corresponding to echelle diffraction orders; during one cycle up to 8 spectral intervals can be measured. Four photometric channels from UV to near IR spectral range serve to study the vertical distribution of the aerosol. The mass of the instrument is 2.8 kg, power consumption is below 12 W. The science goals, technical description and some ground testing results of the experiment will be presented.

GEOLOGY OF PHOBOS-GRUNT LANDING SITES: A VIEW FROM THE MEX HRSC IMAGES.

C. A. Lorenz[1], J. Oberst[2,3], M. Wahlish[3], K. Willner[2], G. Neukum[4] , A. Basilevsky[1],
[1]Vernadsky Institute, Moscow, Russia,; [2]TU Berlin Germany, 3DLR Berlin, Germany. [4]Free University Berlin, Germany. Contact: c-lorenz@yandex.ru

Introduction: Geology of the PHOBOS-GRUNT potential landing sites were characterized through the analysis of high-resolution images of Phobos taken by the HRSC and SRC cameras on-board of MARS-EXPRESS spacecraft. Three approaches are being used in this study: 1) photogrammetric analysis of the images resulted in Phobos DTM models and topographic maps, 2) morphological analysis resulted in geological maps, and 3) the analysis of surface colors aiming to deduce from it indications on the surface material compositional differences.

Data and Results: The study area covers a “square” with coordinates of its corners: 30°S 180°W - 30°N 245°W. The major landforms in this area are craters and grooves. Based on their morphologic prominence four classes of craters are recognized – the fresh, degraded, rimless ones, and possible ancient impact depressions. For the relatively young large craters additional structure elements like ejecta blankets and avalanches inside the craters can be mapped.

Two of the craters show indication of the layered target suggesting at least two layers of different physical-mechanical properties. The high resolution images allow to estimate thickness of regolith layers by the craters’ structure and their relationships with the grooves. Based on the observed grooves’ intersections several age populations of these features are suggested..

Within the study area, three general types of the terrains are recognized probably being of different stages of resurfacing (from older to younger): 1) densely cratered and grooved terrain; 2) less cratered terrain with smoothed groves; 3) homogeneous blanket-like terrain covering the older cratered and grooved surfaces. We propose that these terrain types were formed by overlying ejecta from several sequential large impact events. The officially approved landing area of Phobos-Grunt mission is localized inside the terrain №3, while the ellipse of the new-considered landing site is within the border area of terrains №2 and №3.

Conclusions: Geological interpretation of Phobos surface morphology allow to estimate and compare the characteristics of regolith within the landing site areas, and is the base for ongoing analysis of the HRSC color images.

EXPERIMENT BIOPHOBOS IN THE CONTEXT OF CURRENT TASKS OF ASTROBIOLOGY

E.A. Vorobyova[1,3], A.K. Pavlov[2], V.S. Soina[3], M.A. Vdovina[2], and B.H. Lomasov[2],
[1]IKI RAS, 117997 Profsoyuznaya str. 84/32,Moscow, RF; [2]Phys.-Techn. Inst. RAS, Polytechnicheskaya str., 26, S.-Petersburg, RF; [3]Lomonosov Moscow State University, 119192 Leninskiye Gory1-12, Moscow,RF. Contact:esautin@yandex.ru

Astrobiology today becomes one of the main problems in studies of the Solar System. The scientific interest to the mechanisms of cell resistance, the duration of cell viability and the role of stress in the evolutionary process is growing. Novadays, the very evolution of life can be theoretically presented as "evolution of revived life", i.e. as evolution of ready bioforms when the adaptive processes in new environment involve "turning on" genes brought to Earth by the alien as well as the original creative planetary processes.

Transpermia (panspermia) hypothesis allows to constract theoretical models implying the interplanetary exchange by the original living matter or using the idea of potential "archetypical" viability (contamination) of the Solar System bodies, first of all rocky planets, moons of planets, meteorites, and comets. Assuming the possibility of forming biospheres by planets or moons, we can represent the Solar System as a set of "resting" or "active" living systems.

Currently, astrobiology is designed primarily to assess the potential of extraterrestrial environments as well as deep space in terms of maintaining known principles of life to predict the possible extraterrestrial pathways of evolution. Indeed, known stability of microorganisms may seem redundant to terrestrial conditions and needs an explanation. It is based on genetically determined mechanisms of transition of cells into the resting state, the interaction of microbial cells with geological substrates and mechanisms of cell resuscitation. These basic processes provide the extension life limits, and it is important to go beyond the planet to determine the boundaries. Carried out on a low earth orbit astrobiological experiments require further studies with varying orbits and conditions, increasing time of exposure living organisms in space. The experimental areas requiring development include: understanding the effects of space radiation on microbes and their interactions with rocks; more experiments exposing microbes to space to try and understand how specific or combined stressors in space influence cells and microbe-mineral interactions; experiments on modified environments and atmospheric compositions in planetary simulation facilities; development of micro-arrays and other bioinformatic tools/techniques for studying microbes and their responses to space conditions; terrestrial testing instruments for potential application to extraterrestrial environments.

The Phobos Sample Return project demonstrates how multi-purpose space mission outside Earth magnetosphere could be used for astrobiological tasks. Biological experiment does not limit astrobiological significance of the whole project. Any data of planetary research are valuable in characterizing the putative environment. Low-cost biological experiment "BioPhobos" will enable to get extremely significant information, particularly to study resistance and survivability of great variety of earth organisms in deep space environment during an interplanetary transit (transpermia), to assess the effects of prolonged exposure of cosmic factors on the interaction of microorganisms and geological substrate, to investigate transformation of native microbial communities, to analyze soil sample from Phobos (presumably, a matrix material of the Solar System with the inclusion of martian matter) including search for biosignatures (panspermia, transpermia), and to determine the requirements for interplanetary transport of extraterrestrial samples. The experiment will provide new information to adjust the quarantine measures for future projects. In parallel with the space experiment provides laboratory testing of samples. It was confirmed that microbial cultures which were kept dry in laboratory for two years at 20-22^{O}C remain viable. At present the experimental results are processed after exposure of some cultures of microorganisms and soil sample to ionizing radiation at doses corresponding to those that will be obtained on the trajectory of an interplanetary flight of the spacecraft "Phobos-Grunt". Soil microbial communities as well as pure cultures were resistant to the treatment.

2MS3-PhS-09

THE CHOMIK INSTRUMENT FOR PHOBOS-GRUNT MISSION – FUNCTIONAL TEST AND CALIBRATION DATA.

K. Seweryn[1], S. N. Aleksashkin[3], M. Banaszkiewicz[1], A. Cichocki[1], M. Ciesielska[1], M. Dobrowolski[1], J. Gurgurewicz[1,4], J. Grygorczuk[1], B. Kędziora[1], J. Krasowski[1], O. E. Kozlov[2], T.O. Kozlova[2], T. Kuciński[1], M. Królikowska[1], M. Morawski[1], H. Rickman[1], K. Skocki[1], E. Słaby[4] T. Szewczyk[1], R. Wawrzaszek[1], Ł. Wiśniewski[1], A.V. Zakharov[2], *[1] Space Research Centre, Polish Academy of Sciences, 18a Bartycka St., 00-716, Warsaw, Poland, contact: kseweryn@cbk.waw.pl, [2]Russian Space Research Institute, Russian Academy of Sciences, 84/32 Profsoyuznaya St., 117997, Moscow, Russia, [3]Lavochkin Association, 24 Leningrad Hwy, Khimki-2, 141400, Moscow Region, Russia, [4] Institute of Geological Sciences, Polish Academy of Sciences, Twarda 51/55 00-818, Warsaw, Poland*

Introduction:

A unique geological penetrator CHOMIK dedicated for the Phobos-Grunt space mission was designed and manufactured at the Space Research Centre Polish Academy of Sciences (SRC PAS) in Warsaw. In June 2011 the flight model was integrated with the manipulator arm designed at the Space Research Institute Russian Academy of Sciences (IKI RAN) and installed on the Phobos-Grunt lander.

One of the most important goals of the mission is to collect a soil sample from Phobos, Mars' moon, and deliver it to Earth. The sample will be collected from the surface of the satellite by the Polish penetrator and deposited in a container that is going to land in 2014 in Kazakhstan encased in the Russian re-entry capsule. The CHOMIK instrument is one of three instruments on the lander designated to collect sample from Phobos' soil, especially designed for sampling the stony surface. Apart from sampling, the penetrator will perform thermal and mechanical measurements of Phobos' regolith. All these goals play an important role in the future exploration plans of the space bodies.

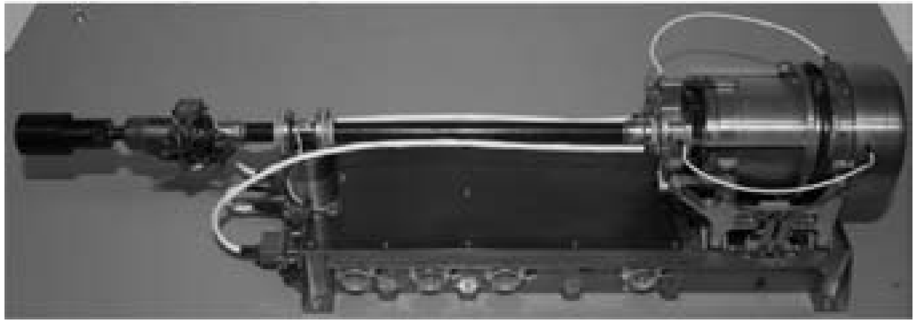

Fig. 1. Flight model of the CHOMIK penetrator.

Measurements of thermophysical and mechanical properties of planetary surface allow to determine many important parameters for scientists working in different fields of research. For example effective heat conductivity or thermal inertia of the regolith can help with better understanding of processes occurring in the body interior. Chemical and mineralogical composition gives us a chance to better understand the origin and evolution of the moons. Mechanical properties of the surface are one of the key factors for civil engineers developing future bases on the space bodies.

Functional tests and calibration data:

The series of functional tests were conducted at SRC PAS, IKI RAN and Lavochkin Association (LA) to check the performance of the CHOMIK device wrt to the task that will be performed on the Phobos' surface. The following tests were completed:

- Sampling performance in Earth and zero gravity conditions (SRC PAS).
- Sampling progress with different materials (starting from sand like materials to stony materials) (SRC PAS).
- Calibration of the thermal conductivity sensor (LA).
- Complex functional test after CHOMIK integration with manipulator arm (IKI RAN).

On the figure below, the CHOMIK qualification model integrated with manipulator arm is presented.

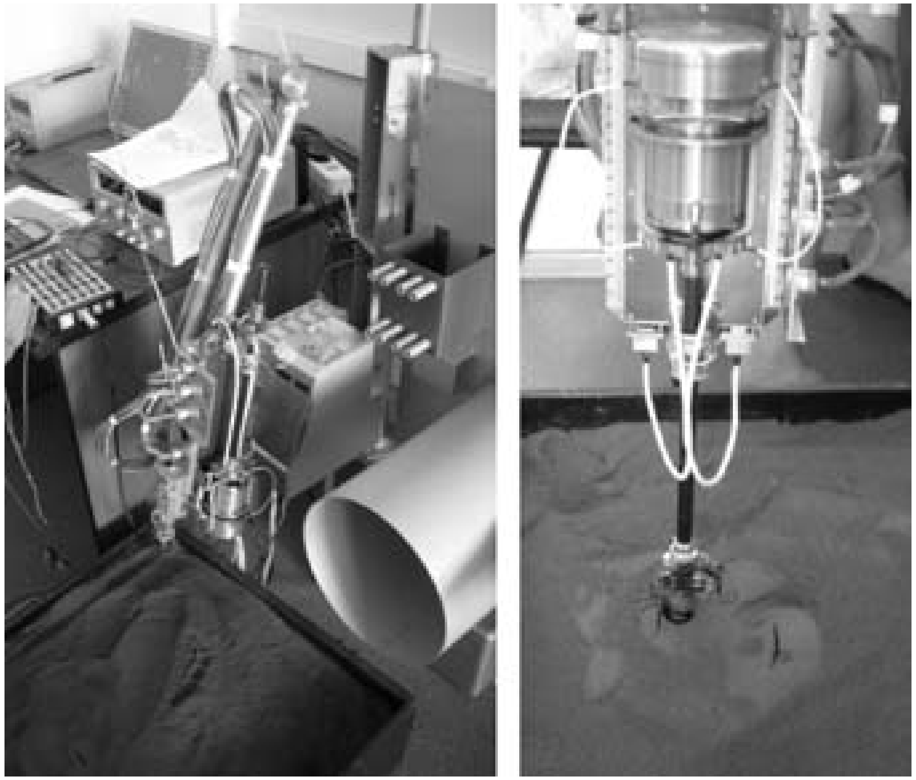

Fig. 2. Sampling scenario: the CHOMIK QM integrated with the manipulator arm in the starting position (left) and during sampling in the Phobos' analogue (right).

The results from the functional test and the calibration data will be presented in the paper.

Acknowledgments: The paper was supported by national grant project 791/N-ROSJA/2010/0

RADIO SCIENCE EXPERIMENTS OF JOINT OBSERVATION OF YH-1 AND PHOBOS-GRUNT.

J. Ping[1], J. LI[1], H. Yan[1], S. Zhang[1], N. Jian[1], X. Shi[1], M Wang[1], Q. Meng[2], Z. Wang[3], *[1]Nandan Rd.80, Shanghai Astronomical Observatory, CAS, Shanghai, China; [2] South-East University, Nanjing, China; [3] Xinjiang Astronomical Observatory, CAS, Urumqi, China. Contact:pjs@shao.ac.cn*

Introduction:

Since the beginning of the new century, Mars exploration has attracted the huge attention from space communities. A new race and cooperation in lunar and planetary exploration has started. Being a beginner in this area, China has launched her 1st lunar orbiter Chang'E-1 successfully, and has got many new scientific results from this exploration. Beyond this, a joint Russian-Chinese Martian mission, Yinghuo-1 (YH-1) & Phobobs-Grunt (FGSC), has been developed and promoted solidly[1].

In this joint mission, the Chinese Mars Probe YH-1 is a small satellite focused on investigating the Martian space environment and the solar wind-Mars interaction. YH-1 and Phobos-Grunt will forms a two-point measurement configuration in the Martian space environment. Equipped with similar plasma detecting payload on two spacecraft would give some coordinated exploration around Mars. The two S/Cs will also carry out satellite-to-satellite radio link, so as to study the Martian ionosphere by using radio occultation links at UHF. It will also test the deep space navigation techniques. For this mission, the open-loop radio tracking methods like DOR/DOD and 1-way Doppler, are developed and applied to determine the s/c orbit and position. Some general characteristics for YH-1 are read as:

- Total mass of YH-1, 110kg
- Power supply 150W (average)，and instant 180W
- Data down link: 0.9m in diameter, HGA，directly to earth, 80bps---8kbps
- X-band Receiver and transmitter onboard s/c for communication.
- 3-axis stabilized, deployable solar panel.

The main scientific objectives of YH-1 are read as:

- Martian space environmental structure, plasma distribution and characteristic in the regions;
- Solar wind-atmosphere coupling and energy deposition processes, and Martian ions escaping processes and possible mechanisms；
- Martian and Phobos surface imaging;
- Regional gravity field of the Mars.

Using the Delta-VLBI and SBI observation, many possible scientific results are expected to be reached from the radio science experiments of VLBI tracking of the joint mission. These objectives are estimated as:

- To define more exactly Sun system's parameters (Astronomical constant, orbital parameters of Mars and Phobos);
- To evaluate the rotation/liberation of Phobos and to obtain mass distribution inside Phobos;
- To define more exactly limits of variation of universal gravitational constant (GM) for Mars and Phobos;
- To define more exactly geometrical tie of dynamical coordinate system having original in Sun system mass centre of with coordinate system based on quasar angular coordinate measurements;
- To explore the Martian atmospheric characteristics by means of radio occultation method [2].

To accomplish above joint tracking and experiments between China and Russia, a resolution of time scale and reference frame is coordinated and recommended to be adopted for manufacture, launch, telemetry, control and scientific application of YH-1 spacecraft in Mars exploration project. This resolution also provides the definitions of some concerned time scales and reference frames in the project, with the values of certain constants. The transformations between the different time scales are also provided [3].

Reference: [1]http://www.russianspaceweb.com/phobos_grunt.html; Proposal of Using VLBI for YH-1 Tracking and Orbit Determination, 2007.04, Shanghai Astronomical Observatory, in Chinese.
[2] Zhang Sujun, et al., Physics 2009 in Chinese;
[3]Jinling Li, Jianguo Yan , YH-1 Mars Exploration Project Resolutions on Time Scales and Reference Systems (Proposal), Shanghai Astronomical Observatory, CAS; Beijing Aerospace Control Center,March, 2009

INTERPLANETARY MATTER ON THE MOON.

V.V.Shevchenko, *Sternberg State Astronomical Institute, 119992 Moscow, Universitetsky prosp. 13, Russia. Contact: vladislav_shevch@mail.ru*

Introduction:

Hydrogen has been inferred to occur in enhanced concentrations within permanently shadowed regions and, hence, the coldest areas of the lunar poles. Neutron flux measurements of the Moon's south polar region from the Lunar Exploration Neutron Detector (LEND) on the Lunar Reconnaissance Orbiter (LRO) spacecraft were used for hydrogen mapping of the lunar south pole area. The final value corresponds to a water (as ice) content of ~4% by weight (Mitrofanov et al., 2010), which is in good agreement with independent estimates of the water content associated with the LCROSS Centaur impact site (Colaprete A. et al., 2010). The maximum total water vapor and water ice within the instrument field of view was 155 kilograms. Given the estimated total excavated mass of regolith that reached sunlight, and hence was observable, the concentration of water ice in the regolith at the LCROSS impact site is estimated to be 5.6 % by mass. In addition to water, spectral bands of a number of other volatile compounds were observed, including light hydrocarbons, sulfur-bearing species, and carbon dioxide (H_2S/H_2O, NH_3/H_2O, SO_2/H_2O, and CO/H_2O). Of interest is the indication from this preliminary analyses that some volatiles other than water are considerably more abundant (some by orders of magnitude) than the ratios found in comets, in the interstellar medium, or predicted from gas-gas reactions in the protoplanetary disk.

Comet impacts on the Moon:

The most convincing model for the "swirls" (lunar albedo and magnetic anomalies, Fig. 1) origin seems to be lunar surface contact with the gas/dust coma of comets passing by or falling onto the Moon (Shevchenko, 1999). It's possible to show that the most probable scenario for origin of the water ice polar deposits is the falls of young comets onto the Moon during comet showers. Characterized by their low average density and large nuclei as well as in the considerable mass of the matter they brought even several falls of such young comets could provide for the revealed ice concentration on the lunar pole.

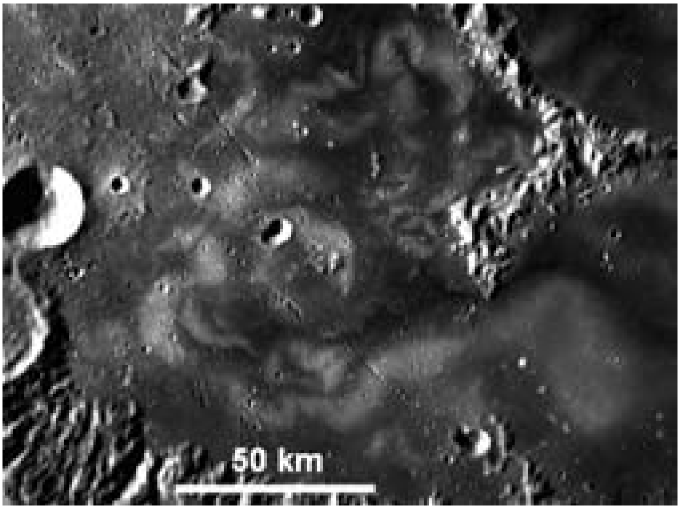

Fig. 1. Swirls in Mare Ingenii region. Image from LROC (http://wms.lroc.asu.edu/lroc).

In particular the comet Hale-Bopp has become a sufficiently convincing confirmation of the existence of the bodies with gigantic nuclei. Thus its parameters can serve as the first interaction data for the quantitative assessment of the lunar ice with a comet origin. The lowest limit of the nucleus substance density can be less than 0.1 g/cm^3 if this comet nucleus rotation period is 11.47 hours (Meech, 1997). The fall of a body with a density of 0.1 g/cm^3 and an impact velocity of 40 km/s (these parameters are similar to those of the Hale-Bopp comet) results in a collision with the same physical parameters as a solid body with a density of 1.0 g/cm^3 and a collision velocity of 10.5 km/s does (O'Keef & Ahrens, 1982). According to the model elaborated by Yakovlev et al. (1987) the initial temperature of the vapour collision formed cloud will be about 6300°C. The most probable thermal velocity of the atoms will be about 5.5 km/s. This means that the dissipating part of the cloud mass will be 0.9 of its total mass taking into account the parabolic velocity for the Moon of 2.4 km/s. Nucleus diameter of the Hale-Bopp comet was estimated to be about 40 km. Consequently after a similar body with a density of 0.1 g/cm^3 falls on the lunar surface a vapour cloud with a mass of about 3.4x10^{18}g is formed. The water melting, surface, and crush-up energies are neglected. According to the above given assessment the mass of the volatile compounds which stay in the lunar environment will be 3.4x10^{17}g. Assuming that these substances, distributed equally above the lunar surface, will further cool and deposit in the regolith upper layer, the assessed mass will be about 10^{10} g per a square kilometer. It is obvious that the subsequent preservation of the deposit is only possible in cold traps located near to the poles. Thus for the given assessments of the total area for both the southern and northern poles where the neutron spectrometer of the Lunar Prospector fixed the ice presence (3700 km^2), the calculated mass of the volatile deposits of comet origin can be up to 3.7x10^{13} g for each giant comet fall. If common mass of lunar polar ices is about 3 x10^{15}g it is needed about 300 falls of new giant comet to form such amount of deposits.

Whence the comet came into inner part of Solar System:

The Hale-Bopp comet is a similar potential impactor. In that time Szab´o et al. (2011) detected comet Hale–Bopp at 30.7 AU, which is the most distant detection of a comet so far. It's position between Kuiper Belt and Oort Cloud. Oort Cloud comets are currently believed to have formed in the Sun's protoplanetary disk and to have been ejected to large heliocentric orbits by the giant planets. Detailed models of this process fail to reproduce all of the available observational constraints, however. In particular, the Oort Cloud appears to be substantially more populous than the models predict. **Levison** et al. (2010) presented numerical simulations that show that the Sun captured comets from other stars while it was in its birth cluster. The results imply that a substantial fraction of the Oort Cloud comets, perhaps exceeding 90%, are from the protoplanetary disks of other stars!

Conclusions: We know that other stars have circumstellar clouds of dust or icy bodies that may be analogous to the Kuiper Belt in the Solar System. So, we can propose that a particles of a dust may be brought on the Moon by giant comet from other star system.

Acknowledgments: Author is grateful to NASA LEND Science Team, I.G.Mitrofanov, PI, and NASA LCROSS Science Team, Colaprete A., PI.

References: *Шевченко В.В.* О кометном происхождении лунного льда // Астрон. вестн. 1999. Т. 33. № 5. С. 456 – 465.
*Як*овлев О.И., Маркова О.М., Манзон Б.М. Роль процессов испарения и диссипации в образовании Луны // Геохимия. 1987. № 4. С. 467-481.
Colaprete A. et al. Detection of water in the LCROSS ejecta plume // Science. 2010. V. 330 P. 463-468.
Levison H.F., Duncan M.J., Brasser R., Kaufmann D.E. Capture of the Sun's Oort Cloud fromstars in its birth cluster // *Science.* Published Online June 10, 2010.
Meech K.J. Physical properties of cometary nuclei // Preprint IfA-97-38. 1997. 16 p.
Mitrofanov I. G. et al. Hydrogen mapping of the lunar south pole using the LRO Neutron Detector Experiment LEND // Science. 2010. V. 330 P. 483-486.
O'Keef J.D., Ahrens T.J. Cometary and meteorite swarm impact on planetary surfaces // J. Geophys. Res. 1982. V. 87. No. B8. P. 6668 - 6680.
Shevchenko V.V. On the Cometary Origin of Lunar Polar Ice. Lunar and Planet. Sci. XXX. 1999. # 1317.
Szab´o Gy.M., S´arneczky K., Kiss L.L. Frozen to death? – Detection of comet Hale-Bopp at 30.7 AU // Astronomy & Astrophysics manuscript no. hb, April 25, 2011.

CURRENT EVENTS ON THE MOON.

V.V.Shevchenko[1,2], P.C.Pinet[1], S.Chevrel[1], Y.Daydou[1], Y.Lu[2], T.P.Skobeleva[2], O.I.Kvaratskhelia[3], C.Rosemberg[1]. *[1]UMR 5562 "Dynamique Terrestre et Planetaire"/CNRS/UPS, Observatoire Midi-Pyrenees, Toulouse, 31400 France; [2]Sternberg Astronomical Institute, Moscow University, Moscow, 119992, Russia, [3]Abastumany Astrophysical Observatory, Georgian Academy of Sciences, Georgia. Contact: vladislav_shevch@mail.ru*

Introduction:

We know from practices of geology that rock material slides along a plane of structural weakness such as a bedding plane. Although they are most common on steep slopes, they can even occur on slopes of 15°. We can see such slopes from 10° to 20° on the Moon. On the Earth millions of tons of rock may plunge down slope at speeds greater than 160 km per hour in what is often the most catastrophic form of mass wasting. On Mars, similar slope failures are possibly caused by erosion from "running" water. However, the lunar triggering mechanism of the down slope movement of the material remains unclear. It's needed to study many questions regarding the stability of natural lunar slopes else. Moreover, it's needed to note that resent studies show that new computer models simulating the creation of gullies on the surface of Mars suggest that they are in fact created by the flow of dry debris (i.e. landslides) and not by the flow of water (Kolb et al., 2010).

Spectral analyses of the crater Reiner:

Processes of the space weathering on the Moon affect the optical properties of an exposed lunar soil. The main spectral/optical effects of space weathering are a reduction of reflectance, attenuation of the 1-μm ferrous absorption band, and a red-sloped continuum creation. Lucey et al. (2000) proposed to estimate the maturity of lunar soils from Clementine UVVIS data using a method which decorrelates the effects of variations in Fe^{2+} concentration from the effects of soil maturity. The method calculates optical maturity defined as parameter OMAT. Pinet et al. (2000) used the method to analyses the "Reiner-γ – Reiner" region on the basis of Clementine spectral image data. Crater Reiner is located in western Oceanus Procellarum. Diameter of the crater is 30 km, its depth is 2.4 km and its central peak height is about 700 m. Topographic data is showing that general slope of the western part of the inner walls is about 20°. There is a terrace on the western wall slope. Slope of the eastern crater inner wall is in range 17° – 18°. Diagram, depicted plots Lucey's parameters (Fe content in weight % versus maturity index OMAT), was constructed. The spatial distribution associated to the color scale coded boxes (1 to 4) displayed in Fig. 1. It reveals the presence of extremely immature soils (coded in color box 4) at the hundred meters scale in the crater Reiner area. Also the soil iron content in the regions is higher (up to 16%) than in the surrounding mare background soils (about 11- 12%). Immature soils (coded in green, box 3) occupy most areas of the inner wall slopes of the crater. Extremely immature materials (coded in light grey, box 4) are observed in the north-north-western part of the inner walls.

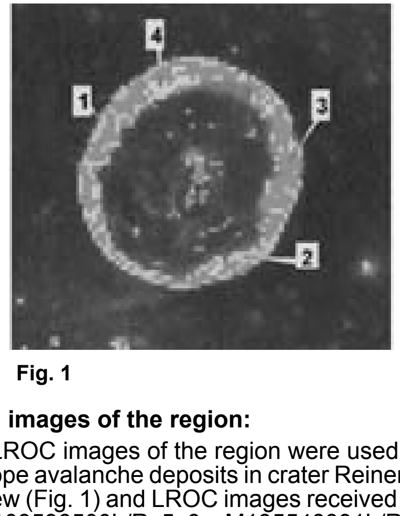

Fig. 1

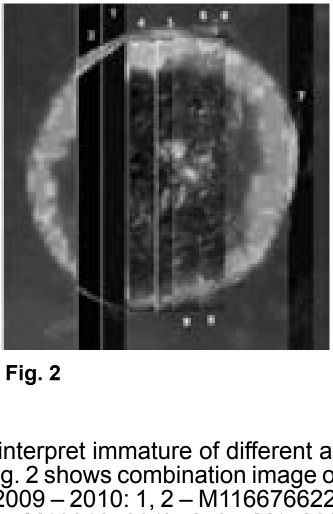

Fig. 2

LROC images of the region:

Nine LROC images of the region were used to interpret immature of different areas of the slope avalanche deposits in crater Reiner. Fig. 2 shows combination image of spectral view (Fig. 1) and LROC images received in 2009 – 2010: 1, 2 – M116676622L/R; 3, 4 – M109596500L/R; 5, 6 – M135548391L/R; 7 – M133187091L; 8, 9 – M142625106L (http://wms.lroc.asu.edu/lroc/). Evidence of avalanching and of other down slope movement of material is clearly visible on the inner walls of the crater now. In general, freshly exposed lunar material is brighter than undisturbed materials nearby. The brightness of the avalanche scars is a numerous bright avalanche deposits on the steep crater walls, apparently originating at outcrop ledges near the top of the wall. On the western wall, most avalanches stop in a moat at the base of the wall (near terraces). On the eastern wall, avalanches extend out onto the irregular, inward-sloping floor. Extremely immature soils coded in color box 4 reveal near part of northern slope of the crater Reiner wall. The local OMAT estimates points out at the occurrence of slope instability processes. Also, we note that the iron content estimates of these slope soils reach locally maximal values of 16% and more, with a systematic increase of Fe content with regolith depth in the investigated region. Using similar Clementine data for other lunar regions of mare and highland types, we obtain a scale of conformity between OMAT, Is/FeO (by Morris, 1978) and spectropolarimetric maturity indexes (Shevchenko et al., 2003). The maturity index values ranging from box 2 to box 4 correspond to exposure age from 6 to 0.5 million years. Avalanching appears to be a major means of the current erosion on steep lunar slopes. Many features of the surface structures occur where the wall is bowed outward and probably represent slump deposits where portions of the crater wall have collapsed into the crater. Soil inner friction angle is not more than 20^{o} for upper layer matter. Bulk density of the surface soil is about 1.5 g/cm3 in the case. The age of the observed lunar slope degradation is very young (Shevchenko et al., 2011).

Anomalous avalanche deposits in crater Burg:

Fig. 3 shows two fragments of crater Burg inner wall slope. The left fragment is part of image M113778346L/R (http://wms.lroc.asu.edu/lroc), the right fragment is part of image from “Chang’e 2” (http://moon.bao.ac.cn). The last image was obtained by China’s “Chang’e 2” lunar probe on 23 October 2010 (Credit: China Lunar Exploration Program). The resolution of the image is near 7 m.

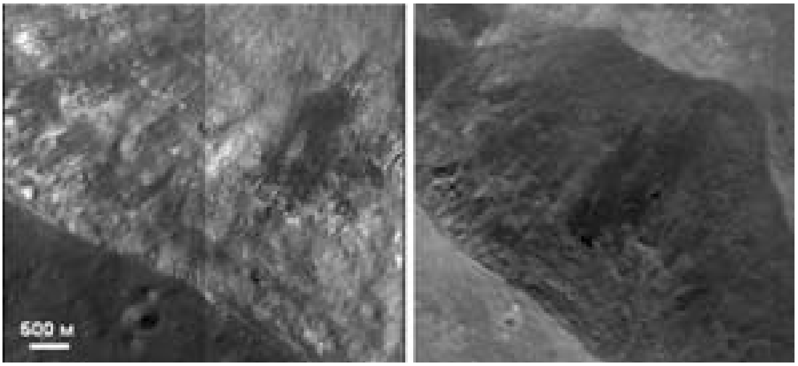

Fig. 3

The presence of very young dark details and immature soils on the inner wall slopes of the crater Burg suggests recent intensive slope processes. The most immature soils covered inner walls of this crater demonstrate that the origin age may be equal to the exposure age of the surface layer on inner wall. Calculated exposure age of the dark feature shows that it be as less as 10^{2} years or less. It’s possible the process is present.

Acknowledgments: We are grateful to NASA LROC Science Team, M.S.Robinson, PI, and China Lunar Exploration Program, and also Yong-Chun Zheng.

References: *Kolb K.J., Pelletier J.D., McEwen A.S.* Modeling the formation of bright slope deposits associated with gullies in Hale Crater, Mars: Implications for recent liquid water//Icarus. 2010. V. 205. P. 113–137.

Lucey P. G., Blewett D. T., Taylor G. J., Hawke B. R. Imaging of lunar surface maturity // J. Geophys. Res. 2000. V. 105. P. 20.377 –20.386.

Morris R.V. In situ reworking (gardening) of the lunar surface: Evidence from the Apollo cores // Proc. Lunar Sci. Conf. – IX, 1978. P. 1801 – 1811.

Pinet P.C., Shevchenko V.V., Shevrel S.D. et al. Local and regional lunar regolith characteristics at Reiner Gamma formation: optical and spectroscopic propertits from Clementine and Earth-based data // J. Geophys. Res. 2000.V.105 (E4). P.9457-9475.

Shevchenko V. V., Skobeleva T. P., Kvaratskhelia O. I. A spectropolarimetric maturity index of lunar soil // Solar System Res. 2003. V. 37. No. 3. P. 178–197.

Shevchenko V.V., Pinet P.C., Chevrel S., Daydou Y., Lu Yangxiaoyi, Skobeleva T.P., Kvaratskhelia O.I., Rosemberg C. The current avalanche deposits in lunar crater Reiner . LRO data // LPS-38. 2011. # 1161.

LUNAR SCIENTIFIC FRONTIERS AND GOALS FOR FUTURE EXPLORATION: INSIGHTS FROM RECENT SPACECRAFT RESULTS.

James W. Head, *Department of Geological Sciences, Brown University, Providence, RI 02912. Contact: james_head@brown.edu.*

Lessons From Lunar Exploration: Ten things we have learned about the Moon from past and recent missions and analyses have set the stage for our thinking about the early evolution of the Earth and other planetary bodies and provided an important set of goals for future human and robotic exploration: 1) The Moon formed from the impact of a Mars-sized object into early Earth: How does this process, and its immediate aftermath, set the Moon on an evolutionary path that is the same as, or different than, other planetary bodies? 2) The early Moon was characterized by a global-scale magma ocean: Near-global melting caused by accretional energy produced an anorthositic highland crust, a “primary crust”. Is the evolution of the lunar “primary crust” unique? How do primary crusts on planets with different compositions and interior structures form and evolve? 3) The Moon initially differentiated into chemical layers, including a crust and mantle, which set the stage for further evolution. What is the nature of late-stage crustal differentation processes and how do they contribute to the character of lower planetary crusts? 4) The chemical and thermal nature of these stratified layers may have led to net negative buoyancy, large-scale overturn, and significant vertical mixing. Is this predicted early overturn unique to the Moon or applicable to other planets? 5) The Moon is stratified into mechanical layers; the lithosphere, the outer thermal boundary layer, thickened and became less heterogeneous with time. What controlled the initial thickness, variability and rates of thickening on the Moon and other planets? 6) Tectonically, the Moon is a one-plate planet, characterized by a globally continuous lithosphere; how does the evolution of the global state of stress in the lithosphere, recorded in the sequence of tectonic features, and the thickness of the lithosphere with time, as recorded in its flexural response to loads and in the gravity field, vary from body to body? 7) Lunar volcanism records processes of mantle melting in space and time, and the volcanic record reflects the general thermal evolution of the Moon, including the state and magnitude of stress in the lithosphere. The unique ability to link lunar samples to specific deposits significantly enhances our understanding of these processes: for example, recent results implicate water in the formation of volatile-rich pyroclastic eruptions. How does the volcanic record of the planets differ? 8) The Moon is a fundamental laboratory for the study of impact cratering processes, particularly at the complex crater to multi-ring basin scale. The ability to combine studies of lunar impact breccias and melts with crater and basin deposits considerably enhances this understanding. How can this understandig be applied to other planets? 9) The Moon is a template for the record of the distribution and history of impactors in the inner solar system. The lunar cratering record, in conjunction with the unique chronology afforded by returned and dated samples, can inform us about a) the reality of a Late Heavy Bombardment, b) the changing size-frequency distribution of impactor populations with time, and c) the potential non-linear nature of the bombardment record in the last half of solar system history. 10) Volatiles play a more important role in lunar evolution than previously thought: Recent reports of detection of water and water-related species: a) as coatings on surface minerals, b) in buried near-polar deposits, and c) in mantle derived melts, all provide exciting insight into a range of water-related processes during different time in lunar history, including accretion, differentiation, cometary impact, and interaction with the solar wind.

Role of the Moon in Future Planetary Exploration: In what context does this integrated comparative planetology perspective place the Moon? Some see the Moon as a *cornerstone*: this metaphor implies that the Moon is of extreme importance because all other stones will be set in reference to it, thus determining the position of the entire structure. The Moon as a *keystone* implies a central cohesive source of support and stability for ideas about the formation and evolution of planets. Still others see the Moon as a *Blarney stone*: those who have “kissed the stone” have been imparted with an excessive skill in flattery about the Moon. It can be argued that the lessons from comparative planetology place the Moon where it belongs, as one member of a family of Solar System objects, each of which provides insight into fundamental lessons of planetary evolution. As such, an appropriate metaphor for the Moon might be a *touchstone*, which refers to any physical or intellectual measure by which the validity or merit of a concept can be tested.

The Renaissance of Lunar Exploration and What it Means for the Future: At the advent of the atomic age, Albert Einstein is reported to have said: “Everything has changed but our way of thinking”, a thought that might be applied to our current understanding of the Moon and its role in solar system exploration. ESA, Japan, China, India and the United States have launched comprehensive missions to the Moon, and each has plans for continuing lunar exploration. The onslaught of new data is monumental, and the data are just barely starting to be ingested, digested and analyzed. Nonetheless, the future is clear. We are on the verge of a renaissance in our study and understanding of the Moon. We have acquiring extremely high spatial and spectral resolution data across a wide wavelength range. This has changed everything, and fundamental changes in our way of thinking will surely follow: The distribution of rocks from the lunar sample collection can now be mapped globally. New minerals and rock types are being discovered. The provenance of recognized rock types can be studied and established using new very high spatial and spectral resolution data. The mineralogy and context of individual large boulders and clusters of boulders can be mapped, and then placed in their geological contexts. Models of crustal stratigraphy can be tested and depth of sampling of craters can be assessed. Refined models of crustal stratigraphy and evolution can be constructed. New avenues of communications are being opened between planetary scientists utilizing approaches such as mineralogy, petrology, geochemistry, geology, spectroscopy, geophysics, etc. The lunar renaissance is propelled not just by the new data, but by the fundamental foundation and interpretative context provided by information collected by dozens of previous missions, and analyzed in sophisticated laboratories on Earth. These data have provided a basic framework that is unequalled on any planetary body other than the Earth.

Lessons for Future Lunar Exploration: The basic framework of the lunar renaissance will crisply define the questions to be addressed by a range of new lunar robotic missions including geophyscical networks, sample return, and integrative rover missions. When humans inevitably return to explore the Moon in the coming decades, the lunar renaissance will have provided both compelling reasons for human exploration and detailed locations at which humans can optimize their exploration skills.

THE LUNAR SOUTH POLE-AITKEN BASIN AS A TECTONIC EQUIVALENT OF THE INDIAN GEOID MINIMUM.

G. G. Kochemasov, *Institute of ore deposits geology, petrography, mineralogy and geochemistry (IGEM) RAS; 35 Staromonetny, 119017 Moscow, Russia. Contact: kochem.36@mail.ru*

Earth and its satellite both are well studied topographically and gravimetrically. It turned out that at both bodies there are solitary unique planetary scale objects origin of which puzzles scientists. Geophysicists know about existence of an unique depression in the geoid form on the Indian Ocean deep –112 m but its origin is mysterious. According to prevailing since some time the plate tectonics the basin of the Indian Ocean was formed as a result of moving apart lithosphere blocks around a triple junction of the middle-ocean ridges. Such interpretation of the present tectonics contradicts to a real disposition of different ages planetary geologic blocks around the Indian minimum [1] and does not explain its profound nature. The minimum occurs at the axe “b” of three main Earth’s moments of inertia and thus is a fundamental part of its rotation figure [2].

Lunar Basins and Marea, as it is known, are traditionally considered as traces of impacts of giant cosmic bodies during an earlier bombardment (3 to 4 b. y. ago). Even their regular symmetric disposition on the surface is neglected [3]. However, serious difficulties recently arise in concordance of their supposed ages with ages of “impact” breccias and relations between them. But the supporters of impacts stand firm on their opinion and do not accept alternatives. The South Polar-Aitken basin is considered as the largest impact basin in the Solar system; its depth is about 8 km with the total lunar relief range about 16 km.

The comparative wave planetology [3-4 & others] could help in solution of the question. It turns out that both considered planetary structures occupy analogous positions in a wave structure of their bodies (Fig. 1-3). They are deeply subsided sectors (πR-structures) on their respective uplifted continental highland segments-hemispheres (2πR-structures) [5]. Such their regular arrangement on two globes makes dubious their interpretation according to the hypotheses of plate tectonics and impacts [5, 6].

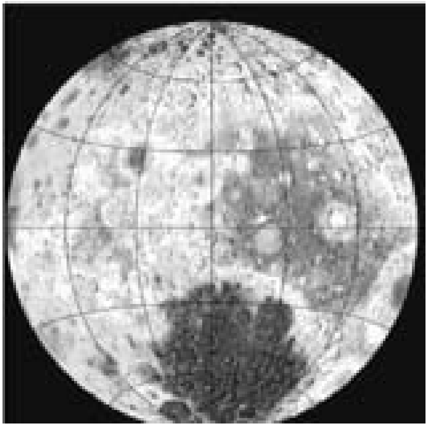

Fig. 1. Lunar geoid. Center-down (black) – SPA basin (moontopogeoidusgs_farside.jpg).

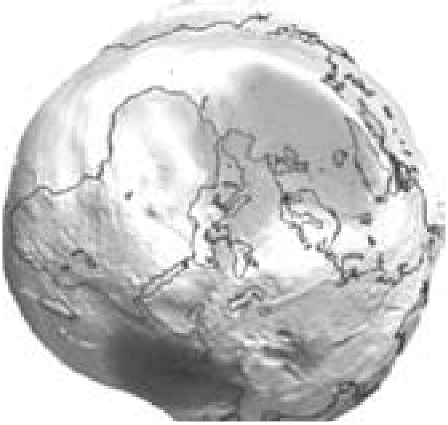

Fig. 2. Earth’s geoid. Center-down (black) – Indian minimum (832e4f812d1e_.jpg).

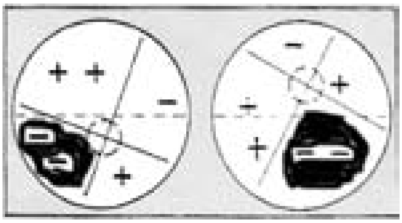

Fig. 3. Schemes of different levels (+, ++, -, --) tectonic sectors on continental segments-hemispheres of the Moon (left) and Earth. The sectors are grouped around the Mare Orientale and the Pamirs-Hindukush mountain massif. Black – the most subsided sectors: SPA basin and Indian geoid minimum.

Similarity of the lunar and Earth's deepest geoid minima (the SPA Basin and the Indian Ocean basin) is proven by their even shapes and relative sizes, similar tectonic settings and dense mantles (Fig. 1-3) [5-7]. To these decisive factors one ought to add some similarity of the inner structures. Thus, very characteristic pointed sectoral projection of the Hindustan peninsula has an analogy in the SPA Basin (Fig. 4-5) in form of the pointed relatively less dense projection in limits of the round geoid anomaly. To the west and east of the projection the geoid anomaly increases, as well as on a spacious territory to the south. Such internal structure corresponds to the subsided crust blocks around the Hindustan: the Arabian Sea, Bengal Bay and Indian Ocean. Such analogy is explained by an interference of lithosphere waves making a tectonic pattern of both planetary bodies [4 –7 & others]. Tectonic sectoring by this way is shown in a geometric model (Fig. 6). The ascertain of "relationship" of two largest geoid anomalies in the Earth-Moon system might be considered as an "blow" at once at two dubious planetary tectonic hypotheses – steady delusions (plate tectonics and early giant impacts). A future planetology must diminish role of random impacts in favor of regular wave structures.

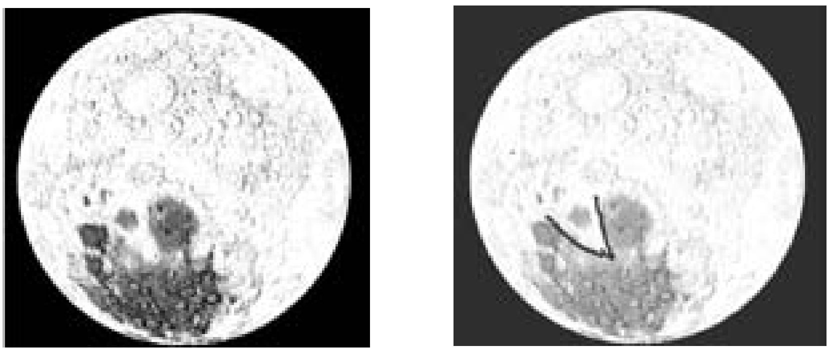

Fig. 4-5. Detailed and contrast enhanced lunar SPA geoid minimum displaying a sectoral "peninsula" surrounded by "seas".

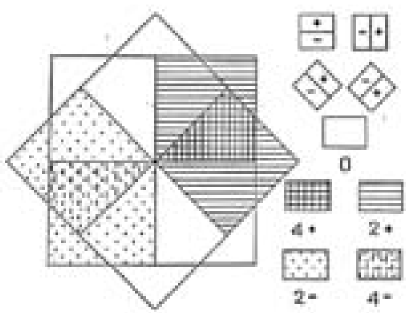

Fig. 6. Flat geometric model of four waves interference. Segmentation (dichotomy) and sectoring. One needs mentally to wrap up it around a globe.

References: [1] Kochemasov G.G. (2009) Geometric tectonic regularities in the Eastern hemisphere of Earth // MatGeoS'09. Geosciences from Earth to Space. 2nd workshop on mathematical geosciences, 07 to 08 December 2009, Freiberg, Germany. **[2]** Liu, H.S., Chao, B.F., 1991. The Earth's equatorial principal axes and moments of inertia. Geophys. Jour. Intern.,v. 106, no. 3, p. 699-702. **[3]** Kochemasov G.G. (1997) The wave planetology against the impact and plate tectonics ones // Regularities and symmetry in the Earth's structure. Proceedings of the I-III scientific seminars TRINITI RAS-MSU, 1994-1996. ROST, Moscow, 1997, 151 pp. (5-17) (In Russian). **[4]** Kochemasov G.G. (1998) Sectoral tectonics of the Earth's eastern hemisphere and its crucial role in localization of giant ore deposits, prominent rift systems and large flood basalt provinces // Global Tectonics and Metallogeny, V. 6, # 3 & 4, 1998, 195-197. **[5]** Kochemasov G.G. (1998) The Moon: Earth-type sectoral tectonics, relief and relevant chemical features // Abstracts of the papers submitted to the 3rd international conference on Exploration and utilization of the Moon, Oct. 11-14, 1998, Moscow, Russia (Eds.: E.M. Galimov, V.B. Polyakov, Yu.I. Sidorov), p. 29. **[6]** Kochemasov G.G. (2010) Well known outstanding geoid and relief depressions as regular wave woven features on Earth (Indian geoid minimum), Moon (SPA basin), Phobos (Stickney crater), and Miranda (an ovoid) // EGU Congress, Vienna 2010, Abstract # EGU2010-A-4044. **[7]** Kochemasov G.G. (2010) Two deepest geoid minima on Earth (Indian) and the Moon (South Pole-Aitken basin) are deemed having different origins but surprisingly similar by their tectonic positions //: "Planet Earth" system: 300 anniversary of the M.V. Lomonosov birthday. 1711-2011. Monograph.- Moscow: LENAND, 2010.-480 pp. (p. 394-396) (In Russian).

SHARING LUNAR EXPLORATION WITH THE WORLD: EXAMPLES FROM THE MOON MINERALOGY MAPPER/CHANDRAYAAN-1 E/PO PROGRAM.

C.J. Runyon[1], C. Hall[1], E. Joyner[1], K. Boyce[2], K. Garver[2]; *[1]Geology, College of Charleston, Charleston, SC 29403, runyonc@cofc.edu, [2]Montana State University, Bozeman, MT. Contact: kgarver@montana.edu*

Introduction:

In the 1960s and 70s, Lunar exploration stimulated many to pursue science and engineering careers. Now, with the human element so far removed from space exploration, students must rely on textbooks, TV's, and computers to build their understanding of our Moon. With the growing need for a scientifically trained workforce, lunar exploration still has an important role to play in encouraging students to pursue science, technology engineering and/or math (STEM) careers. Many of NASA's lunar educational materials are static and out-of-date. They do not effectively address 21st Century Skills, or cross curricula, essentials for today's learning environment. Here, we present a three-part model for developing opportunities in lunar science education professional development that is replicable and sustainable and integrates NASA mission-derived data (e.g., Moon Mineralogy Mapper (M^3)/Chandrayaan-1) into science and fine art curriucula. The M^3 Education / Public Outreach (E/PO) program is helping to convert STEM to STEAM (science, technology engineering, arts and mathematics)

Moon Mineralogy Mapper / Chandrayaan-1:

Moon Mineralogy Mapper (M^3) was one of eleven instruments oboard India's Chandrayaan-1 (Ch-1) spacecraft launched on October 22, 2008. M^3 , a high spatial and spectral resolution spectrometer, mapped the compositional variation of the Moon's surface[1]. Analyses of the M^3 mineralogy maps revealed the presence of water and spinel on the lunar surface, generating a renewed vigor and excitement among the science team and lunar community. These discoveries also help make M^3 an ideal focus for STEAM-based educational materials and programs.

Fig1. Chandrayaan-1 launch.(J.Boardman).

M^3 Education & Public Outreach.

The M^3 Education and Public Outreach (E/PO) team takes advantage of the power of lunar exploration to design engaging outreach and educational products. These products present the ongoing story of exploration and discovery.

M^3 E/PO activities and resources engage students in learning how the Moon and planetary surfaces form, and help them to understand how scientists and engineers explore remote worlds. For example, wit the M3 resources and activities students and citizens may answer such questions as:

Why go to the Moon? What are the new discoveries? How is the Moon similar to/different from the Earth? What is the benefit (to me) of lunar exploration?

These activites also bring to the general public an awareness of NASA's mission and vision1 using of a variety of media platforms.[2]

The M^3 E/PO program promotes STEM literacy using the excitement of the success of Chandrayaan-1 and the discoveries of M^3**.**[3,4] The outreach material highlights M^3's science, engineering, and technology and is developed are around three unifying themes: 1) *Geology of the Earth-Moon System***,** 2) *Properties of Lunar Materials*, and 3) *Science & Technology of Lunar Resources.* M^3 EPO activities and programs designed within the themes are inquiry-rich, meet the National Standards in science, math and engineering, and have been reviewed by teachers for content and useability.

M³ Educator Guide: I) With the return of high resolution/high spatial data from M³/ Chandrayaan-1, we can now better explore and understand the compositional variations on the lunar surface. Data and analysis techniques from the imaging spectrometer are incorporated into the M3 Educator's Guide: *Seeing the Moon in a New Light*. The guide includes an array of activities and lessons to help educators and students understand how NASA is currently exploring the Moon. The guide integrates NASA maps and data into the interactive lessons, bringing the excitement of scientific exploration and discovery into the classroom.

This guide includes eight new activites developed for M³-sponsored Geology of the Moon workshops and on-line course. Written for upper middle school – high school, the activities examine spectroscopy, lunar geology, surface morphology and composition. Students use an ALTA hand-held spectrometer to identify and map compositional variation on the moon's surface. From these measurements, the students discover that the Moon is similar to, yet different from, the Earth and terrestrial planets.

On-line Learning Resources: Utilizing the M³ Educator's Guide as well as educational activities from more current NASA lunar missions, we offer two sustained professional development opportunities for educators to explore the Moon through interactive and creative strategies. 1) *Geology of the Moon*, an online course offered through Montana State University's National Teacher Enhancement Network, is a 3-credit graduate course. 2) *Fly Me to the Moon*, offered through the College of Charleston's Office of Professional Development in Education, is a two-hour graduate credit course. Through these courses, teachers explore NASA's historic and current lunar missions. We incorporate interactive ways for educators to explore and communicate their ideas through a series of scaffolded webquests. Educators work through inquiry-oriented lessons to gather information and data directly through the Internet. The webquests allow students to freely explore, motivating them to investigate open-ended questions and enhance their self-learning process.

Fig. 2. M³ science/mission site

Web sites - Background information on the Chandrayaan-1 mission and M³ and instrument are available via the world wide web, as are the latest science updates, 3D image cube releases, E/PO resources, and activities.

Three connected M³ specific web sites share the different aspects of the team's activities. These include a more technical mission / instrument specific site (http://m3.jpl.nasa.gov : Fig. 2); a science blog that shares the latest and greatest imagery and comments from the science team; and the E/PO web site designed for use by educators and a more general audience (http://m3.cofc.edu Fig. 3).

From the Moon Exhibits: To address more diverse audiences, a unique partnership among the College of Charleston's School of Science and Math and the School of the Arts will showcase lunar observations and analyses. *From the Moon: Mapping and Exploration* will open in November, 2011. *From the Moon: Mysteries and Myths* exhibit at the Halsey Gallery of Art in Charleston, SC will open in Fall, 2013. Patrons will explore one-of-a-kind artifacts, as well as early observations from Galileo to M³ and current observations from ongoing NASA lunar missions. Both exhibits will be paired with tactile activities, lesson plans and professional development opportunities.

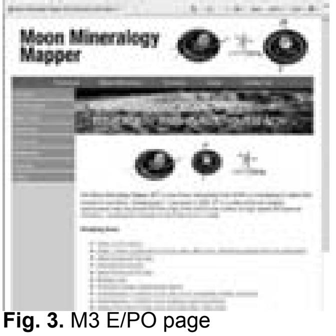

Fig. 3. M3 E/PO page

M³ Educator Tool Kits – Included in the kits are activities and resources related to the current Chandrayaan-1 mission, the M3 instrument, spectroscopy, lunar history and more. The kits were created for use in workshops and classrooms. Formal and informal educators have used these tool kits since the Summer of 2008. By generating the M3 activities and resources such that they support one or more of the three themes, they may be useful for future mission EPO programs such as Lunar Reconnaissance Orbiter (LRO), LADDIE, the NLSI and more.

Acknowledgment: We are honored to be part of ISRO's Chandrayaan-1 mission and thank the NASA Discovery Program and Science Mission Directorate for supporting the development and implementation of the M3 E/PO program.

References: [1] Pieters et al. (2009) Science, vol 326, pp 568-572;[2] Pieters et al (2007) LPSXXXVIII #1295;[3] NASA Headquarters; [4] Runyon et al (2007) LPSXXXVIII #1812.

COMPOSITION OF THE LOWER CRUST OF THE MOON IDENTIFIED AT BASIN RINGS.

C. M. Pieters[1], J. W. Head[1], D. Dhingra[1], P. Isaacson[1], R. Klima[2], N. Petro[3], L. A. Taylor[4] , *[1]Brown University, Providence, RI USA, [2]JHU/APL, [3]NASA Goddard Space Flight Center, [4]University of Tennessee, Knoxville, TN. Contact: Carle_Pieters@brown.edu*

Introduction:

In contrast to the extensively mixed lunar mega-regolith [e.g., 1], materials exposed along the inner ring of several impact basins exhibit compositionally distinct mineral lithologies. We interpret these rock-types to be deep-seated materials brought to the surface and exposed by the basin forming event. An initial survey of such materials using data from the Moon Mineralogy Mapper (M3) reveals compositions expected from the lunar samples (anorthosite, norites, troctolites), as well as new and unusual lithologies (pink spinel anorthosite, pyroxenite, and perhaps dunite). A simple magma ocean model is consistent with remote observations and samples from the upper crust, but is inadequate to describe our observations of the lower crust. We are beginning to glimpse the actual complexity of lunar lower crust evolution.

The Oriental Example:

The diversity of compositions in and around the Orientale Basin was noted with the first return of high-spectral and high-spatial resolution data from M3 [2]. Overall, the region is highly feldspathic, but massive crystalline anorthosite was detected for the first time along the Inner Rook Mountains (IRM) based on a diagnostic 1300 nm absorption feature due to small amounts of Fe+2 in the plagioclase structure. This lithology is found in direct association with the featureless form of shocked plagioclase detected earlier and well known to lunar astronomers [3]. With the high spatial resolution available to modern sensors such as M3 and those on Kaguya, the crystalline form of anorthosite was found to be widespread [4]. Example spectra are seen in Figure 1.

A remarkable observation at Orientale, however, is that the entire IRM is shown to be composed of crystalline and shocked anorthosite. This extensive unit was uplifted and exposed from depth by the impact event [e.g., 5, 6]. The scale of Orientale and its location on the western limb leave little doubt that the IRM anorthosite represents massive exposures of magma ocean products of the primary upper crust.

Moscoviense and Nectaris Basins:

The Moscoviense and Nectaris Basins both also occur in regions of highly feldspathic crustal material. The inner ring of Moscoviense on the farside contains widely dispersed km-scale regions of three distinct lithologies embedded in the feldspathic matrix [7]. The mafic mineral content is exceptionally high in all, and two could approach pyroxenite and harzburgite in composition. The third is a new rock-type identified on the Moon that is dominated by Mg-rich spinel with no other mafic minerals detectable (<5 % pyroxene, olivine). All these exposures along the inner ring are old and appear undisturbed since basin formation. They are effectively undetectable in panchromatic image data and are only recognized by their distinctive composition identified spectroscopically. A possible schematic cross section of the pre-basin region is shown in Figure 2.

A second exposure of the new Mg-spinel rock type was discovered in association with the Nectaris Basin on the nearside [8]. In this case Nectaris ring material was excavated and exposed in the central peaks of the large crater Theophilius (D=100 km). A spectrum of the Mg-spinel-rich lithology is included in Figure 1. Coordination with high spatial resolution imagery demonstrates that the Mg-spinel lithology is in direct contact with outcrops of shocked plagioclase.

Other Basins:

Analyses are under way for the South Pole-Aitken Basin (SPA) and superimposed basins Schrödinger and Apollo. Due to their location and size, each has a story to tell. Although SPA contains excellent exposures of highly noritic materials, it is also one of the few non-mare areas that contain regions with high-Ca pyroxene as the dominant mafic mineral. Example spectra that identify these components are shown in Figure 1. The Schrödinger Basin provides an important window into these deep-seated lithologies. Preliminary analyses show prominent exposures of plagioclase as well as olivine [e.g. 9].

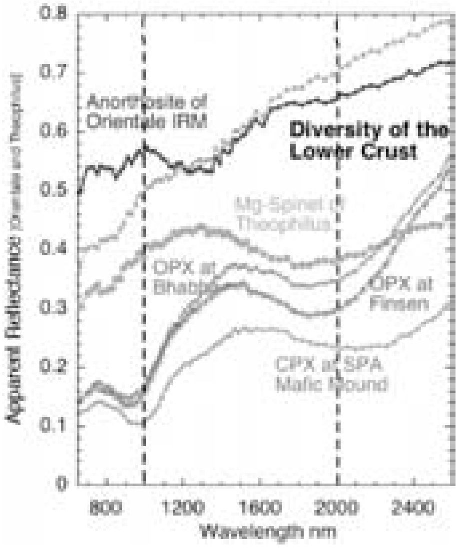

Fig. 1. Apparent Reflectance of basin materials. Deep-seated lithologies exposed include both crystal-line and shocked Anorthosite across Orientale IRM, Mg-spinel at Theophilus (Nectaris), Low-Ca pyroxene at the central peaks of SPA craters Bhabha and Finsen, and Fe-and Ca-rich pyroxene at SPA Mafic Mound. The reflectance scale for Orientale and Theophilus spectra is twice that of the SPA spectra. Vertical lines are provided at 1000 and 2000 nm for ease of comparison.

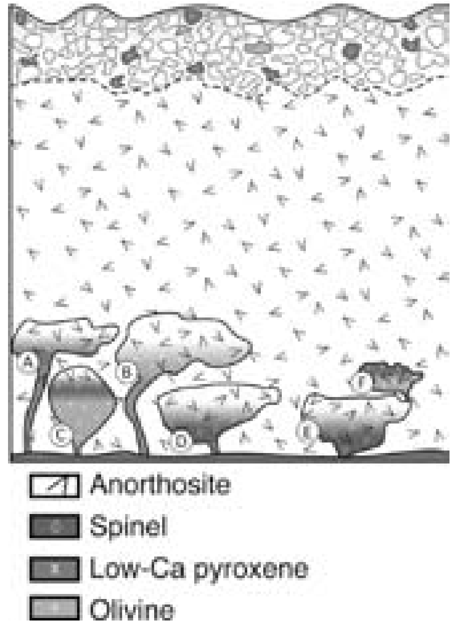

Fig. 2. Possible schematic cross section for the crust exposed at Moscoviense Basin (after [7]). The mixed megaregolith [1] is at the top. In this example the diverse lithogies of the lower crust are portrayed as plutonic intrusions that may have interacted with an anorthositic upper crust.

References: [1] Petro, N. E. and Pieters, C. M. (2008) The Lunar-Wide Effects of Basin Ejecta Distribution on the Early Megaregolith, Meteoritics and Planetary Science, v. 43(8), p. 1517-1529.

[2] Pieters, C. M., et al. (2009) Mineralogy of the Lunar Crust in Spatial Context: First Results from the Moon Mineralogy Mapper (M3), 40th Lunar and Planetary Science Conference, Abstract #2052.

[3] Hawke, B. R., C. A. Peterson, D. T. Blewett, D. B. J. Bussey, P. G. Lucey, G. J. Taylor, and P. D. Spudis (2003), Distribution and modes of occurrence of lunar anorthosite, J. Geophys. Res., 108, 5050, doi:10.1029/ 2002JE001890.

[4] Ohtake, M., et al. (2009) The global distribution of pure anorthosite on the Moon, Nature 461, 236-240, | doi:10.1038/nature08317

[5] Head, J. W. (2010), Transition from complex craters to multi-ringed basins on terrestrial planetary bodies: Scale-dependent role of the expanding melt cavity and progressive interaction with the displaced zone, Geophys. Res. Lett., 37, L02203, doi:10.1029/2009 GL0 41790.

[6] Head, J. W. C. M. Pieters, J. Whitten, et al., (2011) Orientale Multi-Ring Impact Basin: New Insights into Crustal Structure and Depth of Sampling from Chandrayaan-1 Moon Mineralogy Mapper (M3) Spectroscopy Data, J. Geophys Res. In submission.

[7] Pieters, C. M., et al. (2011), Mg-spinel lithology: A new rock type on the lunar farside, J. Geophys. Res., 116, E00G08, doi:10.1029/2010JE003727.

[8] Dhingra, D., C. M. Pieters, J. Boardman, J. W. Head III, P. J. Isaacson, and L. A. Taylor (2011), Compositional diversity at Theophilus crater: Understanding the geological context of Mg-spinel bearing central peaks, Geophys. Res. Lett., 38, L11201, doi:10.1029/2011GL047314.

[9] Yamamoto, S., R. Nakamura, T. Matsunaga, Y. Ogawa, Y. Ishihara, T. Morota, N. Hirata, M. Ohtake, T. Hiroi, Y. Yokota, and J. Haruyama (2010), Possible mantle origin of olivine around lunar impact basins detected by SELENE, Nature Geoscience, doi:10.1038/ngeo897

SOLAR WIND INTERACTION WITH THE LUNAR SURFACE: SARA/CHANDRAYAAN-1 RESULTS.

P. Wurz[1], A. Schaufelberger[1], S. Barabash[2], M. Wieser[2], C. Lue[2], Y. Futaana[2], M. Holmström[2], A. Bhardwaj[3], M. B. Dhanya[3], R. Sridharan[3], and K. Asamura[4],
[1]Physikalisches Institut, University of Bern, Sidlerstrasse 5, 3012 Bern, Switzerland; [2]Swedish Institute of Space Physics, Kiruna, SE-981 28, Sweden, [3]Space Physics Laboratory, Vikram Sarabhai Space Center, 695022 Trivandrum, India, [4]Institute of Space and Astronautical Science, 3-1-1 Yoshinodai, Sagamihara, Kanagawa 229-8510, Japan. Contact: peter.wurz@space.unibe.ch

Introduction:

The Moon has neither a strong, global magnetic field, nor a dense atmosphere, thus the solar wind ions directly interact with the lunar surface, actually with the lunar regolith, which is a layer of loose, heterogeneous material of small grain size (Clark et al., 2002). It has been tacitly assumed that the solar wind plasma is almost completely absorbed in the surface material (e.g. Crider and Vondrak, 2002; Schmitt et al., 2000; Feldman et al., 2000; Behrisch and Wittmaack, 1991). However, in 2008 ion sensors onboard the SELENE spacecraft in lunar orbit detected backscattered solar wind ions and found that 0.1–1% of the solar wind protons flowing towards the lunar surface backscatter from the Moon as ions (Saito et al., 2008). Moreover, neutralised solar wind protons, i.e., energetic hydrogen atoms, at the level of 10% to 20% were observed by the IBEX spacecraft (McComas et al., 2009) far away from the Moon, and in lunar orbit by the SARA instrument on Chandrayaan-1 (Wieser et al., 2009). In the following we will report on the Chandrayaan-1 observations of backscattered solar wind, both in the form as ions and neutral energetic atoms.

Backscattered solar wind ions:

The first observation of backscattering of solar wind ions was reported by Saito et al. (2008) where the authors found that the backscattered ion fraction is in the range of 0.1–1% of the impinging solar wind protons. Using SARA/Chandrayaan-1 data, a global study of the solar wind ion backscattering was performed (Lue et al., 2011) where the average fraction of backscattered ions was also in the range of 0.1 – 1%. However, a strong correlation of the flux of backscattered ions with the magnetic anomalies was found, where the fraction of reflected ions typically is 10% and for the strongest magnetic anomalies it can be as much as 50% over these large scale regions. Figure 1 shows the resulting map of fluxes of backscattered solar wind protons. Contours of the modelled magnetic field data (Purucker, 2008) are overlaid in Figure 1. Clearly, the strong correlation between the crustal magnetic fields and the backscattered ion flux is seen, even at weak magnetic field strengths at the level of 3 nT at 30 km altitude and small-scale (< 100 km) magnetic structures. The large anomaly cluster at the Imbrium Antipode (IA) is clearly seen, as well as the Serenitatis Antipode (SA), Crisium Antipode (CA) and several smaller magnetic anomalies (Lue et al., 2011).

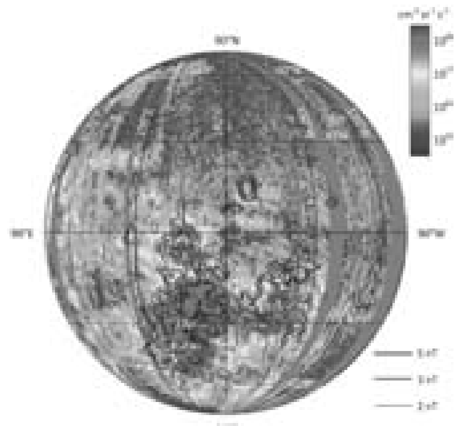

Fig. 1. Map of observed backscattered protons in the energy range of 0.2 – 1.7 keV. The peak differential flux of protons is traced linearly to the surface of the Moon and binned to 1° x 1° resolution, without interpolation or smoothing. Black contours show modelled 2 nT, 3 nT and 5 nT magnetic field strength at 30 km altitude (Purucker, 2008).

Ion backscattering from the regolith surface is small, 0.1 – 1%, as can been seen in the areas without crustal magnetic field. However, the strong correlation of the backscattered ion flux with the crustal magnetic field suggest that in these areas the solar wind ions are actually reflected above the surface, and not from the regolith. The solar wind ion deflection from a wide area implies that the magnetic anomalies act as a magnetosphere-like obstacle to the solar wind, causing the ion reflection, reducing solar wind ion flux to the underlying surfaces, and affecting the upstream solar wind. The ion deflections detected over weak magnetic structures (< 3 nT at 30 km altitude) and small-scale (< 100 km) magnetic anomalies, might be explained by charge separation and the resulting electric potential.

Backscattered neutralised solar wind:

Backscattered neutralised solar wind, also referred to as lunar energetic neutral atoms (ENAs), has to have had contact with the lunar surface to become neutralised. From laboratory studies it is known that ions with solar wind energies interacting with solid surfaces are almost completely neutralised, e.g. by resonant or Auger neutralisation, before being absorbed or scattered (e.g. Niehus et al., 1993). After the initial observation of backscattered neutralised solar wind by SARA (Wieser et al., 2009) maps of these ENAs have been compiled. Already in the first images of lunar ENAs the effect of the shielding of the surface by magnetic anomalies against the solar wind ions could be observed (Wieser et al. 2010) where a reduction in the lunar ENA flux from the surface above the strong magnetic anomaly at the Crisium Antipode (CA) near the Gerasimovich crater was observed.

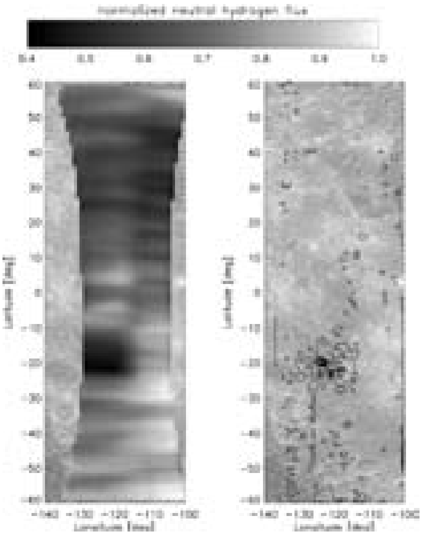

Fig. 2. Map of normalised flux of lunar ENAs near Gerasimovich crater for an energy range of 130 – 290 eV (left panel) and contours of the magnetic field at 30 km altitude from lunar prospector with contours ranging from 3 to 30 nT (right panel).

Figure 2, left panel, shows a new map of lunar ENAs from an area near the Gerasimovich crater on the far side of the Moon observed with SARA / Chandrayaan-1 from an altitude of 200 km comprising the data of 8 orbits. The ENA emission function derived from SARA data has been applied to calibrate this image (Schaufelberger et al., 2011). Figure 2, right panel, shows the magnetic field data for this area (Richmond and Hood, 2008). Good correlation between the magnetic anomaly and the ENA image is observed, where high magnetic field strengths correlate with low fluxes of lunar ENAs. The lunar ENA flux is reduced to about half its value compared to undisturbed locations far away from the magnetic anomaly. This observation shows that the magnetic field of this anomaly is able to reduce the solar wind ion flux to the lunar surface, which goes together with the increased ion flux observed for magnetic anomalies.

References: Barabash, S., A. Bhardwaj, M. Wieser, R. Sridharan, T. Kurian, S. Varier, E. Vijayakumar, V. Abhirami, K.V. Raghavendra, S.V. Mohankumar, M.B. Dhanya, S. Thampi, A. Kazushi, H. Andersson, F. Yoshifumi, M. Holmström, R. Lundin, J. Svensson, S. Karlsson, D. Piazza, and P. Wurz, Current Science 96 (2009) 526–532.

Clark, B.E., Hapke, B., Pieters, C., and D. Britt, in Asteriods III, W.F. Bottke Jr., Cellino, A., P. Paolicchi, R.P. Binzel, (Eds.), University of Arizona Press, Tucson, (2002) pp. 585–599.

D.H. Crider, and R.R. Vondrak, Adv. Space Res. 30 (8), (2002) 1869–1874.

Feldman, W.C., D.J. Lawrence, R.C. Elphic, B.L. Barraclough, S. Maurice, I. Genetay, and A.B. Binder, Jou. Geophys. Res. 105 (E2), (2000) 4175–4196.

Lue, C., Y. Futaana, S. Barabash, M. Wieser, M. Holmström, A. Bhardwaj, M.B. Dhanya, and P. Wurz, Jou. Geophys. Res. 38, (2011) L03202, doi:10.1029/2010GL046215.

McComas, D.J., F. Allegrini, P. Bochsler, P. Frisch, H.O. Funsten, M. Gruntman, P.H. Janzen, H. Kucharek, E. Möbius, D.B. Reisenfeld, and N.A. Schwadron, Geophys. Res. Lett. 36, (2009) L12104

Niehus, H., W. Heiland, and E. Taglauer, Surf. Sci. Rep. 17, (1993) 213–303.

Purucker, M.E., Icarus, 197 (2008), 19–23, doi:10.1016/j.icarus.2008.03.016.

Richmond, N.C., and L.L. Hood, Jou. Geophys. Res., 113, (2008) E02010, doi:10.1029/2007JE002933.

Saito, Y., S. Yokota, T. Tanaka, K. Asamura, M. N. Nishino, M. Fujimoto, H. Tsunakawa, H. Shibuya, M. Matsushima, H. Shimizu, F. Takahashi, T. Mukai, and T. Terasawa, Geophys. Res. Lett., 35, (2008), L24205, doi:10.1029/2008GL036077.

Schaufelberger, A., P. Wurz, S. Barabash, M. Wieser, Y. Futaana, M. Holmström, A. Bhardwaj, M.B. Dhanya, R. Sridharan, and K. Asamura, Geophys. Res. Lett. (2011) submitted.

Schmitt, H.H., G.L. Kulcinski, J.F. Santarius, J. Ding, M.J. Malecki, and M.J. Zalewski, in: Proceedings of Space 2000: the Seventh International Conference and Exposition of Engineering, Construction, Operations, and Business in Space, February 27–March 2, Albuquerque, NM, USA, (2000) pp. 653–660, doi:10.1061/40479(204)79.

Vondrak, R.R., in: Proceedings of the second Conference on Lunar Bases and Space Activities, NASA Johnson Space Center, September 1992, vol. 1, pp. 337–345 (SEE N93-17414 05-91), 1992lbsa.conf.337V.

Wieser, M., S. Barabash, F. Yoshifumi, M. Holmström, A. Bhardwaj, R. Sridharan, M.B. Dhanya, P. Wurz, A. Schaufelberger, and K. Asamura, Planet. Space Science, 57 (2009) 2132–2134; Corrigendum: Planetary and Space Science 59 (2011) 798–799.

M. Wieser, S. Barabash, Y. Futaana, M. Holmström, A. Bhardwaj, R. Sridharan, M.B. Dhanya, A. Schaufelberger, P. Wurz, and K. Asamura, Geophys. Res. Lett., 37 (2010) L05103, doi:10.1029/2009GL041721.

A color version of this abstract can be found at: http://space.unibe.ch/staff/wurz/2MS3_abstract.pdf

INTERIOR STRUCTURE AND PHYSICAL LIBRATIONS OF THE THREE-LAYER MOON.

A. V. Gusev, *Kazan federal university, 18, Kremlevskaya str, Kazan, Russia. Contact: Alexander.Gusev @mail.ru*

Introduction. Substantial information about the Moon can be obtained through supervision of physical libration, as well as by way of theoretical modeling of the latter. The beginning of a new millennium has been marked by publication of a number of papers containing reviews of relevant results and problems ([1] Gusev et al., 2008; [2] Williams et al., 2001). Studies of celestial objects' rotation allow understanding of their complex internal structure, especially when other (geophysical) methods are inapplicable.

Evidences of existence of a lunar core and preliminary estimations of its parameters:

- *The structure of the gravity field:* the present determination of the is consistent with an iron core with a radius of 220 to 450 km or a Fe-FeS core with a radius 330-590 km (Konopliv, 1998, Williams, 2001).
- *Analyses of lunar rotational dissipation,* obtained by LLR has shown, that the core radius could be as much as 352 km if iron and 374 km for the Fe-FeS eutectic composition.
- *The magnetometric measurements* give an independent conformation of the metal core with a radius from 250 up to 430 km.
- *An interpretation of the polar momentum* when combined with compositional, thermal, and density models of the lunar crust and mantle (Dickey et al., 1994; Kuskov, Kronrod, 2001), can allow some useful inferences to be drown about the mass and size of the core.
- *The remnant magnetization of lunar rocks* is itself an argument in favor of the field being generated by a dynamo process in a liquid iron core at this early period of the lunar evolution (Runcorn, 1996, Stegman et al., 2003).
- *The seismic detection of the two-layer lunar core* was obtained after reanalyzed Apollo lunar siemograms ([3]Weber et al., 2011).

Fig. 1.

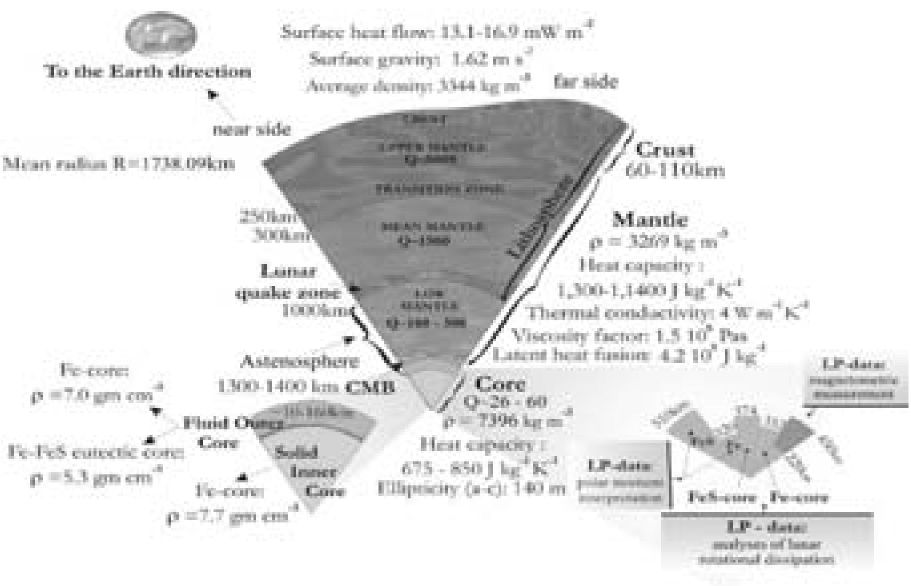

Fig. 2. Two-layer lunar core

Physical libration of two - layer model of the Moon.

The *Chandler Wobble* (CW) is a motion of the rotation axis of the Moon around its dynamical figure axis due to the bulges of the lunar body. For the completely solid Moon the CW has long period 74.6 year in a frame tied to the Moon and is prograde. This

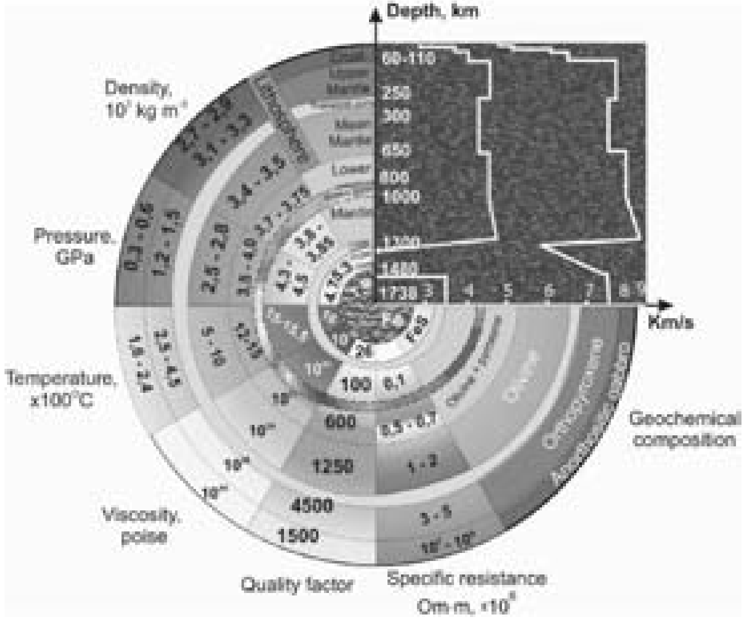

Fig. 3. Cross-section of the Moon

Fig. 4.

Fig. 5.

mode was detected from LLR observation as 3”×8” (69×28 м) elliptical component in the oscillation (Newhall and Williams, 1997).

The *Free Core Nutation* (FCN) represents a differential rotation of the liquid core relatively the rotation of the mantle. This mode does exist only if a core is liquid. It has a quasi-diurnal period in a frame connect to the Moon and *is* retrograde.

Physical libration of three - layer model of the Moon.

For a moon with a solid inner core and a liquid outer core, there are **four rotational normal** modes. This numbers is reduced to two for a planet without inner core, and to one for a planet without liquid core:

The *Chandler Wobble* (CW), which is a motion of the rotation axis of the Moon around its dynamical figure axis due to the bulges of the Lunar body.

The *Free Core Nutation* (FCN), which represents a differential rotation of the liquid core relatively the rotation of the mantle.

The *Free Inner Core Nutation* (FICN), which represents a differential rotation of the rigid inner core relatively the rotation of the mantle.

The *Inner Core Wobble* (ICW), which represents a differential rotation of the figure axis of the lunar inner core with respect to the rotation axis of the Moon.

Modeling the free periods of the Moon.

The dependence on the core’s radius *is very weak* for both periods (P_{CW} and P_{FCN}), when the radius is set to vary within the range of 300 to 600 km, the periods are changed by less than 1 %.

Both periods Pcw and P_{FCN} depend *very weakly* on the core’s density. Only for radii greater than 400 km, the difference in density is observed. The difference in the periods between the eutectic composition with the density 5.5 gm/cm³ and the pure iron core (7 gm/cm³) is vey small. The FCN-period *is very sensitive to the core’s ellipticity.* This property can be used to impose an additional constraint on the core’s parameters, if the expected observation data allows detecting the FCN-mode in the polar motion. The expected amplitudes of the free core’s libration lie within the range of 1-3 milliarcseconds.

Resilts of modelling:

1. Both periods (Pcw and P_{FCN}) depend very slowly on the density. Only for the radius great than 400 km the impact of density is remarkable: the difference in periods for

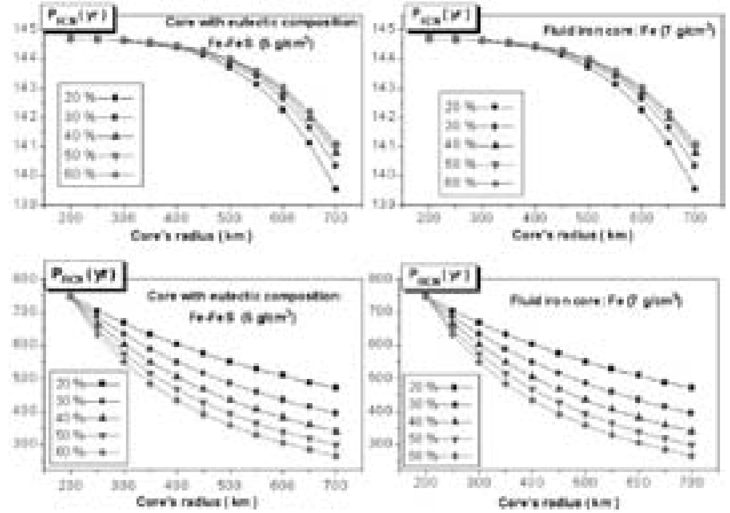

Fig. 6.

eutectic composition with a density 5.5 gm/cm³ with the pure iron core (7 gm/cm³) is less than 0.04%.

2. Significant dependence on the core’s ellipticity takes place for P_{FCN}: for the core, whose dynamical figure is similar to those of mantle (e_c=5.17×10^{-4}) the FCN-period is about 144 years, and the decreasing of the ellipticity only on 3% (5.0×10^{-4}) increases the period up to 149 years, i.e. on 3.5% too. Therewith the correlation with the radius of a core is very weak. The FCN-period for the ellipticity given by LLR-analyses (4×10^{-4}) is about 186 years. At the same time the Pcw is weakly depends on the ellipticity and more essentially – on the core’s radius.

3. The CW-period does not feel the dissipation: this is an internal process for the whole Moon and it should not have an effect for these oscillations. But for the FCN the strong correlation with the dissipation is observed for core’s radiuses Rc less than 400 km. This fact is very interesting indicator of internal processes, which may be derived from observations.

4. In comparison with two-layer model for FCN and CW the three-layer model contributes no more 1% in the values of period for both kind of FOC.

5. Total tendency of behavior of two new periods is preliminary revealed: a) the FICN-period decreases both with the core’s radius and with the thick of fluid shell; b) conversely, the ICW-period increases with the core’s radius and with the thick of fluid shell. The magnitudes of periods for FICN and ICW were obtained for the first time.

Planet	$\frac{A}{A_m}$	Ω 1 rev. per planetary day	Free librations periods		References
Earth	1.12	$\frac{1}{24h}$	P_{CW}	433 d	Lambert, 2006; Herring et al. 2002; Getino et al., 1997- 2001; Ferrandiz, Barkin, 2000
			P_{FCN}	430.23d	
			P_{FICN}	445–737 d	
			P_{ICW}	896 – 5764 d	
Mars	1.02 - 1.08	$\frac{1}{23h}$	P_{CW}	190 –208 d	Van Hoolst et al, 2000; Dehant et al., 2003 Defraigne et al., 2003
			P_{FCN}	230–280 d	
			P_{FICN}	360 –680 d	
			P_{ICW}	440 – 1150 d	
Moon	1.000065	$\frac{1}{27d}$	P_{CW}	74-75 yr	Eckardt, 1981;Williams, 2001
			P_{FCN}	144 – 186 yr	Petrova, Gusev,1999, Barkin, 2004
			P_{FICN}	515 – 634 yr	Gusev, Petrova, 2004-2009
			P_{ICW}	100 – 108 yr	
Mercury	1.68	$\frac{1}{59d}$	P_{CW}	562 – 1033 yr	Peale, 2005
				964yr	Rambaux, Bois, 2004;
				1013 -1017 yr 501 – 571	Barkin, 2004; Gusev, Petrova, 2005 –2008
			P_{FCN}	472–538 yr	
Venus	1.084	$\frac{1}{243d}$	P_{CW}	45630–47240 yr	Gusev, Petrova, 2005- 2008
			P_{FCN}	44280–45840 yr	

Lunar Navigation Almanac

The *Lunar navigational almanac* is necessary for realization of any observations from the surface of the Moon. The almanac should contain precise and detailed information about position of stars, Sun, planets, transition from the lunar time to the universal time and inversely, program for sending of signals of time. The lunar navigation at the observations from a lunar surface requires the high-accurate theory of the lunar rotation.

Time:

- Transition from the lunar time to the universal time and inverse
- The program of sending of signals of time
- The mean longitude of the ascending node
- The physical libration in the longitude, presented in time
- Correction for irregularity of the true tropical time

Stars:

- The visible selenoequatorial coordinates of the brightest star
- The maps of polar regions of the sky; visible places of the polar stars
- The altitudes and azimuths of the polar stars
- Selection of navigational stars

Earth:

- The selenographical coordinates
- The sunrise-, sunset-moments
- The passage of the Earth's surface points through the observable terminator

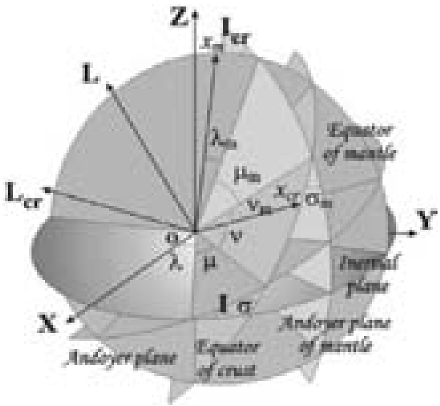

Fig. 7.

Conclusions

We discuss geophysical parameters, geometrical and dynamic compression of liquid core and elastic mantel of the multilayered Moon. The research results include the survey of internal structure of the Moon, tabulated values of geophysical parameters and geophysical profile of the Moon, including liquid lunar core. The given characteristics are important for the evaluation of free librations of a multi - layers of the Moon – Chandler Wobble (CW), Free Core Nutation (FCN), Inner Core Wobble (ICW), Free Inner Core Nutation (FICN) ([1] Gusev et al., 2008).The emphasis was put on the evidences of lunar core existence and on the necessity to take this fact into account in the lunar libration theory.

The periods of free librations were evaluated. The model of the two-layer Moon gives several normal rotational modes - Chandler Wobble and Free Core Nutation. They can play an important role in the determination of the core's parameters: radius, density and geochemical composition.

We offer model physical libration of the two-layer Moon in which dynamic connection between various inside layers was considered. In particular, it was shown, how interaction of a liquid core and a viscoelastic mantle of the Moon influences frequencies and amplitudes physical librations. Amplitudes and frequencies physical libration depending on geophysical parameters of model - the size, a thickness and density of a mantle and the lunar core was calculated.

Conception of the Lunar navigational almanac on the basis of SELENE-2 data for the ILOM-project was discussed. In view of the Lunar mission SELENE-2 (Japan) with geodetic experiments on board and with an optical telescope on the lunar pole, a contribution of the theory of lunar rotation was considered.

References: [1] Williams J.G., Boggs D., Yoder Ch., Ratcliff J., Dickey J.: 2001. Lunar rotational dissipation in solid body and molten core. J. Geoph.Res., v.106, No E11, p.27, 933-27, 968.
[2] Gusev A., Petrova N., 2008. Rotation, Physical libration and Interior of the Moon, Kazan Univ. Press, 212pp
[3] Weber R.C. et al., 2011. Seismic Detection of the Lunar Core, Science, v.331, p.309-312,

SIGNIFICANT RESULTS FROM CHANDRAYAAN-1 MISSION

J. N. Goswami, *Physical Research Laboratory, Ahmedabad – 380009, India*

Chandrayaan-1, India's first planetary exploration mission, conducted remote sensing observations of the lunar surface and sub-surface regions for close to one year. The mission made the discovery of water molecule and hydroxyl on lunar surface and provided new data on lunar surface and sub-surface composition based on reflectance spectroscopy, X-ray fluorescence spectrometry and Radar observation. The mission also probed the tenuous lunar exosphere and identified lunar mini-magnetosphere as well as possible site for future human habitation. These and other important results from this mission will be presented.

REGIONS OF WATER-RICH PERMAFROST ON THE MOON: RESULTS FROM LEND IN LRO

I.G.Mitrofanov on behalf of LEND instrument team, *Space Research Institute (IKI), Moscow. Contact: imitrofa@space.ru*

First results of lunar neutron mapping are presented for two years of LRO mapping stage on the orbit around Moon. It is shown that lunar poles have local Neutron Suppression Regions (NSRs) with enhanced content of hydrogen, presumably in the form of water ice, which do not coincide with the permanent shadow regions. The most interesting NSRs are discussed at Shoemaker-Malapert and Cabeus craters at south pole and at Peary-Whipple craters at north pole.

EPITHERMAL FLUX DEPRESSION AND PSR IN SHOEMAKER CRATER

V.V.Shevchenko[1], I.G.Mitrofanov[2], E.A.Kozlova[1], A. A. Shangaraev[1], and the LEND Science Team. *[1]Sternberg State Astronomical Institute, 119992, Moscow, Russia; [2]Space Research Institute, RAS, Moscow, 117997, Russia. Contact: vladislav_shevch@mail.ru*

Introduction:

Unique capability of LEND to measure epithermal neutron albedo with high spatial resolution allow to create maps with resolution up to 10 km of this type of neutrons albedo for circumpolar areas (Mitrofanov et al., 2011). Analysis of these maps for both poles shows existence of areas with relatively strong suppression of epithermal neutron flux (named as Neutron Suppressed Regions or NSRs), which are interpreted as areas with high concentration of hydrogen in regolith. The most unique property of NSRs is that their boundaries may located outside of or may not correlate at all with a positions of Permanently Shadowed Regions (PSRs). Currently available neutron data from LEND allowed to identify several local areas around both lunar poles, which might have rather high content of water ice about several weight percents within ~ 1 meter layer of sub-surface.

"Cold traps" and PSRs:

So, neutron spectrometer LEND aboard the LRO spacecraft has detected an excess of hydrogen not only in the PSRs but outside them (Mitrofanov et al., 2010). One possible explanation of this may be that not only PSR can play role of "cold traps". The existence of volatiles in the "cold traps" is determined by the temperatures in these traps which are dependant on insolation of given area. So PSR may not be a "cold trap" if it is heated by an illuminated area. "Cold traps" may also not be PSR if they are illuminated by the Sun either when the Sun illuminates them over a short period of time or at a low elevation angle of the Sun above the Moon's horizon. We investigated the distribution of the temperature and illumination in the South Pole region of the Moon with data obtained by LRO (LOLA) spacecraft (http://wwwpds.wustl.edu/). The boundaries of the "cold traps" are about T < 110 K (this is an upper temperature limit for long-term presence of water ice (Vasavada et al., 1999). The total area of PSR in the South Pole region of the Moon is more than 600 sq. km. The total area of "cold traps" exceeds this value and is more than 800 sq. km (Kozlova et al., 2011). Such craters as Shoemaker, Faustini, Shackleton, Haworth and Sverdrup were called as the most likely candidates for the role of "cold traps" for volatiles in the South Pole region of the Moon.

PSR in Shoemaker crater:

Well-seen NSR with area about 1500 km^2 was detected within crater Shoemaker. Its boundary coincides very well with the contour of PSR in the bottom of this crater. In this case the surface of NSR is permanently cold, and there are perfect conditions for permanent storage of frozen water in the regolith.

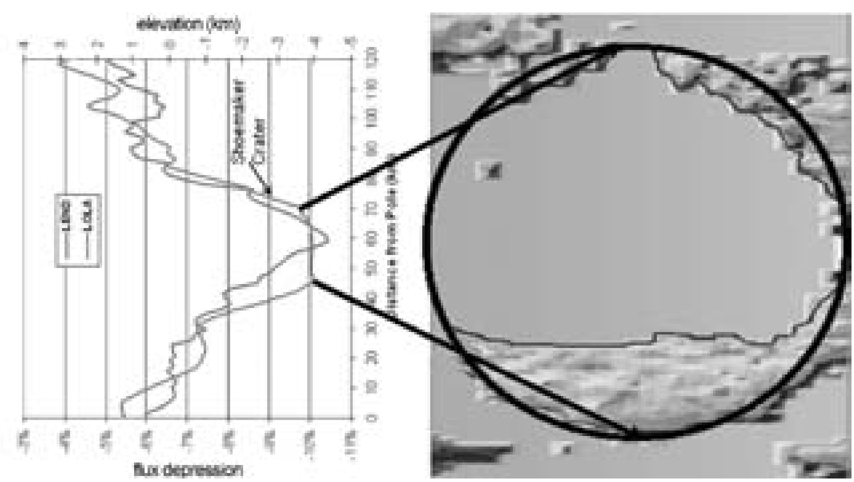

Fig. 1

Left part of Fig. 1 shows epithermal flux depression and PSR in Shoemaker crater from LEND and LOLA data. Model of distribution of the maximum temperatures in crater Shoemaker represents on the right part of the figure. The considerable part of the crater is occupied with “cold trap” for water ice. The maximum temperatures don’t exceed 110 K in the area. According to the model, temperatures in this area don’t exceed 70 K. Substantial increase of temperatures is observed around a southern slope of crater only. The thermal wave in this area gets to depth of 0,7 m, and full attenuation of a daily thermal wave is observed on depth of 4,5 m. For a case of “dry” regolith, despite considerable temperatures around a southern slope on a surface, sub-surface temperatures decrease quickly enough and already on depths more than 0,2 m don’t exceed 150 K. Thus even in this part of a crater water ice can exist in the presence of a shielding layer of the “dry” regolith easily extinguishing temperature fluctuations.

Features of the soil upper layer:

At speed of formation of a layer of regolith equal 1 cm for 50 million years (Killen et al., 1997), for formation of a shielding layer by thickness of 0,2 m it is necessary on the average 1 billion years. We estimated the maturity of lunar soils near crater Shoemaker from Clementine UVVIS data using a method which decorrelates the effects of variations in Fe^{2+} concentration from the effects of soil maturity. The method calculates optical maturity defined as parameter OMAT (Pinet et al., 2000). Fig. 2 shows distribution of the OMAT values for soils near crater Shoemaker.

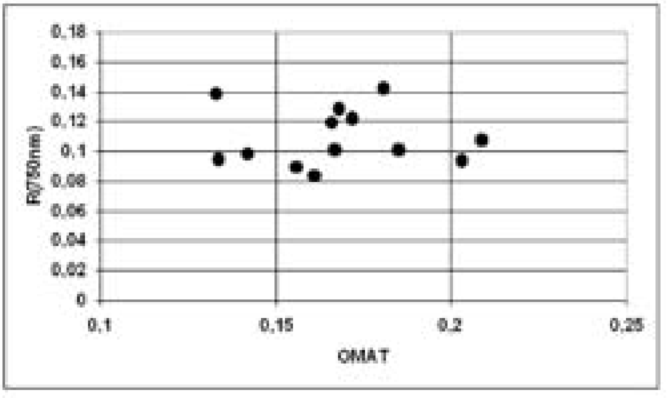

Fig. 2

Using similar Clementine data for other lunar regions of mare and highland types, we obtained a scale of conformity between OMAT, spectropolarimetric maturity indexes and exposure age of surface soil (Shevchenko et al., 2003). The maturity index values ranging from 0,15 to 0,20 correspond to exposure age from 0,2 to 0.4 billion years.

Conclusions: It’s possible that a shielding layer in crater Shoemaker has a thickness up to 1 meter.

References: Killen R.M., Benkhoff J., Morgan T.H. Mercury’s polar caps and the generation of an OH exosphere // Icarus 1997. V.125. p.195-211.
Kozlova E A., Lazarev E. N., Shangaraev A. A. “Cold traps” and PSR near South Pole of the Moon // LPS-42. 2011. # 2039.
Mitrofanov I. G. et al. Hydrogen mapping of the lunar south pole using the LRO Neutron Detector Experiment LEND // Science. 2010. V. 330 P. 483-486.
Mitrofanov I. G. et al. Neutron suppression regions at lunar poles, as local areas of water-rich permafrost // LPS-42. 2011. # 1787.
Pinet P.C., Shevchenko V.V. et al. Local and regional lunar regolith characteristics at Reiner Gamma formation: optical and spectroscopic propertits from Clementine and Earth-based data // J. Geophys. Res. 2000.V.105 (E4). P.9457-9475.
Shevchenko V. V. et al. A spectropolarimetric maturity index of lunar soil // Solar System Res. 2003. V. 37. No. 3. P. 178–197.
Vasavada A.R., Paige D.A. and S.E. Wood. Near-Surface Temperatures on Mercury and the Moon and the Stability of Polar Ice Deposits // Icarus 1999. V. 141. p. 179-193.

IMMATURE LUNAR FORMATIONS AND PALAEOREGOLITH DEPOSITS AS SOURCES OF INFORMATION ABOUT THE HISTORY OF THE SOLAR SYSTEM.

M. P. Sinitsyn[1], [1]*Sternberg Astronomical Institute Moscow State University; Universitetsky pr.,13, Moscow 119992 Address, Russia. Contact: msinitsyn.sai@gmail.com*

Introduction:

It is well known that among the inner planets of the Solar system, only Mercury and the Moon are atmospherless bodies. This means that they are exposed to a wide range of external radiation. The rays, which leave traces in the lunar regolith can be divided into the following main components: galactic cosmic rays (GCR), solar cosmic rays (SCR) and solar wind (SW). As a consequence we expect that the lunar regolith contains information about the external radiation for the period of exposure. Each of these three types of radiation leaves traces in the form of tracks of protons and alpha particles. Moreover, these tracks are at different depths: SW penetrates to a depth of several microns; SCR – a few inches; GCR – a few meters. In addition, the regolith layer thickness of 1 meter builds up in about 1 billion years.

Thus, making the vertical column of the lunar soil up to 4 meters may receive information about changing the content of external radiation in the history of lunar evolution. Unfortunately, in the process of meteorite bombardment (gardening) of regolith on the Moon thickness of 3-5 meters is largely homogenous. The column of regolith, delivered the spacecraft Apollo-12 demonstrated this. It consists of much of the mixed soil, which exposed a few times and then immersed as a result of gardening Thus, to restore the history of the solar evolution and history of sun's rotation around the galactic center is very important to obtain a layer of the regolith, which was exposed only once in a certain historical period (palaeoregolith). So it is important to find a place where there is access to the palaeoregolith deposits. But now there is an opportunity to explore the surface layers, where gardening of the last 20-200 million years ago did not have time to play a significant role. Such places are apparently melts formed during impact processes.

Lunar immature impact formations: On the lunar surface there are a number of immature formations whose age is suitable to study the vertical cores of soil. Investigation of shock process shows that even when the meteoroid is not very large, but flying at speeds of about 30 km/sec as a result of the shock process is formed melt.

Fig.1. The area of the crater Proclus (LROC camera). Age of the crater is estimated at 20 million years. He is one of the extremely immature formations. Impact melt is visible at the bottom of the crater.

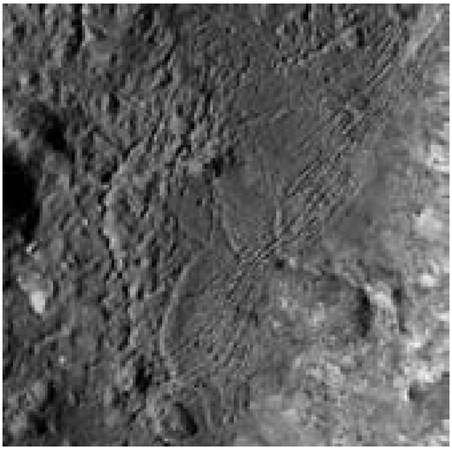

Fig.2 The characteristic form of impact melt on the crater Necho (LROC camera), located on the far side of the Moon.

Figure 2 shows the typical image of impact melt. For immature impact craters can be attributed, for example, the following well-known formations: Proclus (Fig.1), Aristarchus, Plinius, Tycho and some other are up to age 200 million years. This limit due to the fact that the melt will not have time to undergo a large extent the process of mixing.

The potential scientific results from the study of impact melts and palaeoregolith: In the study of GCR in the long-term scales (> 1 billion years) is possible to trace the rate of star formation in the Galaxy [1]. Traces of the SCR on time scales up to 4 billion years have important information about the early evolution of the Sun. Study the changes of the SW will provide an opportunity to confirm and adjust models of the evolution of the Sun as a main-sequence stars. Information obtained at shorter time intervals, especially reflecting the past 200 million years, can be an opportunity to trace the movement of the Sun through the spiral arms of the Galaxy and supernova explosions in the vicinity of the Sun [1]. Information received from all external radiation on the short and long time scales can be very useful for modeling the evolution of life on Earth.

Because with very high information content of the palaeoregolith deposits and impact melt we consider it important finding and cataloging of these objects to the sampling of them in the future space missions.

References: [1] Crawford, I. A. et al, 2010, Earth Moon Planets, 107, 75-85.

PHASE FUNCTION OF LUNAR COLOR RATIO.

Yu. I. Velikodsky[1], Ya. S. Volvach[2], V. V. Korokhin[1], Yu. G. Shkuratov[1], V. G. Kaydash[1], N. V. Opanasenko[1], M. M. Muminov[3], B. B. Kahharov[3], [1]*Institute of Astronomy, Kharkiv National University, 35 Sumskaya Street, Kharkiv, 61022, Ukraine;* [2]*Faculty of Physics, Kharkiv National University, 4 Svobody Square, Kharkiv, 61077, Ukraine;* [3]*Andijan-Namangan Scientific Center of Uzbekistan Academy of Sciences, 38 Cho'lpon Street, Andijan city, 170020, Uzbekistan. Contact: dslpp@astron.kharkov.ua*

Introduction: The dependence of a color ratio of the lunar surface on phase angle α is poorly studied. The ratio, which is defined as $C(\lambda_1/\lambda_2)=A(\lambda_1)/A(\lambda_2)$, where *A* is the radiance factor (apparent albedo), λ is the wavelength ($\lambda_1>\lambda_2$), is believed to increase monotonically in the visible spectral range with increasing α in the range 0–90° by 10–15% [1,2]. From the ground based colorimetry [3] it has been found that at α < 40–50° the color ratio *C*(603/472 nm) for lunar highlands grows with α faster than that of the mare regions. For α > 50° a reverse dependence is observed.

Laboratory measurements of lunar regolith samples, which are more accurate than telescope observations, have shown that a minimum of the *C*(α) curve can be observed at α ~ 10–15° [4–6]. Figure 1 shows phase curves of color ratio *C*(620/430 nm) for two lunar samples delivered by the Soviet probes *Luna-16* and *Luna-20*. The behavior of the samples is quite different. The samples of some other materials demonstrate the same [6]. Hapke et al. [7] also has found this minimum for eight lunar samples at α ≈ 4º.

Using data by Lane and Irvine [8], Korokhin et al. [9] have shown that the phase curve of the color ratio of the Moon in the range 359–1064 nm reveals a maximum at α near 50º and may probably have a minimum near 10º. On the other hand, data processing of *Clementine* UVVis data has shown a monotonic behavior of *C*(α) at small α [10,11] for *C*(750/415 nm) and *C*(950/750 nm). The same has been found recently with SELENE measurements [12] for NIR color ratios from *C*(999/753 nm) to *C*(1676/753 nm).

The controversial information on the minimum of *C*(α) at small α requires further consideration. The existence of such a colorimetric opposition effect can be considered as evidence of the coherent backscattering enhancement effect that predicts more prominent opposition peak of the lunar regolith in red light where the regolith is brighter [6,7].

In this work we present new independent investigation of phase curve of color ratio, which is based on new absolute measurements of lunar albedo and color. This study is an update of [15] (small α were added).

Observational data: In 2006 we carried out a two-month series of quasi-simultaneous imaging photometric observations of the Moon and Sun at Maidanak Observatory (Uzbekistan) [13]. During 42 observational dates we have acquired about 20,000 images of these objects in 3 spectral bands ("R": 603 nm, "G": 529 nm, and "B": 472 nm) in a wide range of phase angles (1.6–168°) and zenith distances.

At present time, we have computed radiance factor maps in spectral bands "R" and "B" at α in the range 1.7–73° with a resolution of 2 km near the lunar disk center. Using the radiance factor distributions, we have obtained 26 maps of lunar color ratio *C*(603/472 nm). An example of such a map at α=16° is shown in Fig. 2.

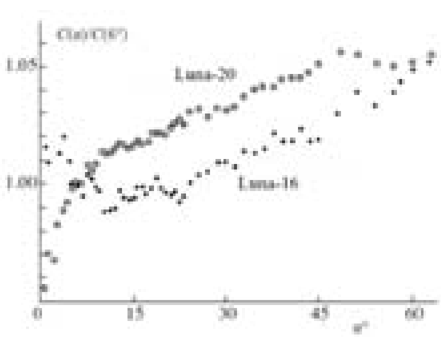

Fig. 1. Phase curves of color ratio C(620/430 nm) for two lunar samples [6].

Fig. 2. Map of color ratio C(603/472 nm) at α=16°.

Phase function of color ratio: Using the maps of color ratio, we have plotted phase curves for two lunar areas (Fig. 3) and for the "average" lunar nearside (Fig. 4). The curves can be approximated by an empirical function

$$C(\alpha) = C_0 \frac{1 + ae^{-b\alpha}}{1 + ce^{-d\alpha}},$$

where C_0, a, b, c, and d are free parameters. This approximation significantly reduces the residual sum of squares at a significance level of 1% in comparison with a second-order parabolic function (the best polynomial fit; the function has no minimum; see Fig. 4). The approximation shows (Fig. 3–4) that the phase curve of color ratio may have a minimum at $\alpha \approx 6$–12º. A trend at large phase angles is not reliable due to large data scattering.

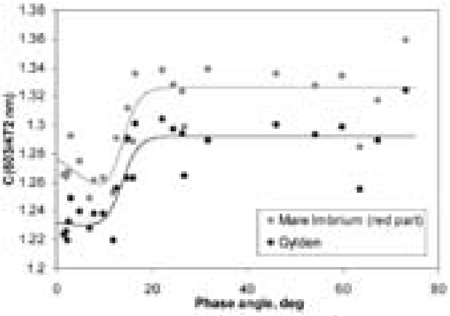

Fig. 3. Phase curves of color ratio C(603/472 nm) for mare (a red part of Mare Imbrium) and highland (Gylden) sites.

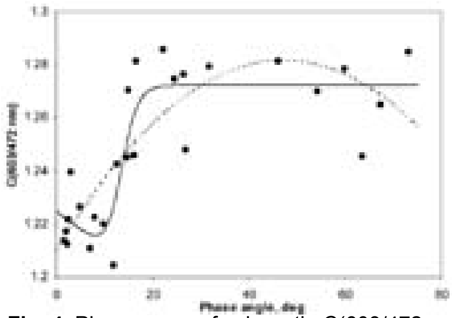

Fig. 4. Phase curve of color ratio C(603/472 nm) averaged over lunar disk.

We note that lunar maria have more pronounced minimum than highlands. This indicates that maria have a narrower opposition peak of brightness in orange light in comparison with blue light. Highlands have less noticeable spectral difference of the peak width.

We also have studied this effect computing phase curves of different color ratio using the ROLO model of integral albedo [14] (Fig. 5). We have found a minimum of C(549/475 nm) at $\alpha \approx 5$º. There is a hint of the minimum for C(665/475 nm) and no minimum for the ratios C(745/475 nm) and C(475/355 nm).

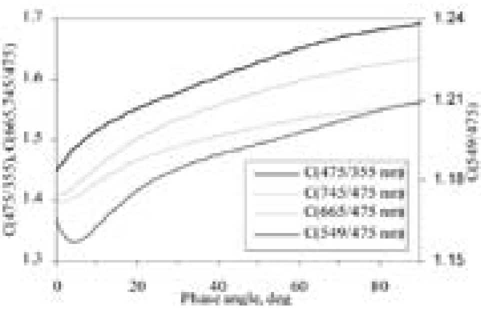

Fig. 5. Ratio of pairs of ROLO's model phase curves of disk-equivalent albedo [14].

Interpretation: Analyzing the results of lunar measurements listed in Introduction together with ours, we may conclude that the minimum of color-ratio phase curves near $\alpha \approx 5$–10º is not observed regularly. It just can appear in specific spectral range (green–blue light). This does not support the hypothesis about the manifestation of the coherent backscattering enhancement effect of the Moon in the visible spectral range [7]. Figure 1 shows that the minimum is observed for the sample of *Luna-16* that is darker than that of *Luna-20*. This also contradicts to the coherent backscatter effect. Thus, we deduce that the behavior of color ratio near small phase angles is rather defined by single scattering indicatrices of regolith particles at different wavelengths.

References: [1] McCord T. B. et al. (1969) *JGR, 74. 12,* 3131. [2] Mikhail J. S. (1970) *Moon 2,* 167. [3] Kaydash V. G. et al. (2010) *Sol. Syst. Res. 44(4)*, 267. [4] O'Leary B., Briggs B. (1973) *JGR, 78(5),* 792. [5] Akimov L. A. et al. (1979) *LPS X,* 9. [6] Shkuratov Y. et al. (1996) *Sol. Syst. Res, 30(1),* 76. [7] Hapke B. et al. (1998) *Icarus 133*, 89. [8] Lane A., Irvine W. (1970) *Astron. J. 78(3)*, 267. [9] Korokhin V. et al. (2007) *Sol. Syst. Res., 41(1),* 19. [10] Shkuratov Y. et al. (1999) *Icarus 141*, 132. [11] Buratti B. et al. (1996) *Icarus 124*, 490. [12] Yokota Y. et al. (2009) *LPS XL,* 2525. [13] Velikodsky Yu. I. et al., (2011) *Icarus 214*, 30. [14] Kieffer H. H., Stone T. (2005) *Astron. J. 129*, 2887. [15] Velikodsky Yu. I. et al., (2011) *LPS XLII,* 2060.

PHASE-RATIO AND COLOR-RATIO IMAGERY OF LUNAR CRATER CAUCHY.

V. G. Kaydash, Y. G. Shkuratov, *Astronomical Institute of Kharkov V.N. Karazin National University, Sumskaya 35, Kharkov 61022, Ukraine. Contact: vgkaydash@gmail.com*

Introduction: The lunar surface reflectance (albedo) is affected by the composition and structure of the lunar surface. While the composition can be characterized with color-ratio imagery, the structure might be described with phase function parameters of the lunar surface [1]. The phase function A(α) is a dependence of the albedo on the phase angle α; it is mainly dominated by the shadow-hiding effect and multiple scattering in the upper mm-cm regolith layer [1-3]. Ratio of albedo images acquired at different α (phase ratio) is a measure of phase function slope, similar to color ratio that is a quotient of albedo images acquired at different wavelengths C(λ1/λ2)=A(λ1)/A(λ2). A direct correlation between the slope parameter A(α1)/A(α2), α1 > α2, and A(α1) is usually observed for the Moon; significant deviations from this rule may indicate anomalies in the regolith structure [2,4,5]. Photometric anomaly with smaller A(α1)/A(α2), α1 > α2, indicates higher surface roughness. The phase-ratio method has been applied to search for regions supposed to be fresh shallow regolith disturbances caused by impacts of meteoroid swarms [4]. Phase-ratio imagery also revealed the landing sites of the Apollo-14, -15, and -17 missions as structure anomalies of approximately 170x120 m size, caused by engine jets of the landing modules [5]. In this study we apply phase-ratio technique to identify the slope processes in craters using LROC NAC / LRO data [6] for the crater Cauchy.

Phase-ratio imagery of Cauchy: We map a phase ratio of a portion of the northern rim, wall, and floor of the 14-km sized crater Cauchy (38.6º E, 9.6º N) in the eastern part of Mare Tranquillitatis. To obtain phase ratios, we use calibrated NAC LROC images, M144375369RC (α=65º) and M144368584R[L]C (α»29º), acquired at the 0.5 m/pix spatial resolution [6]. We coregistered these images using the rubber-sheet method [e.g., 5]. It is important that the images have close illumination condition. Left panel in Fig. 1 shows a reflectance image of Cauchy; the rim is seen at the upper edge, and the floor is below. Pixel numbers are calibrated in radiance, μW/cm2·sr·nm; the proper scale bar is shown in Fig. 1. Brightness variations visible in the scene are a manifestation of albedo, local illumination, and surface roughness; whereas, phase ratio image (right panel in Fig. 1) mainly presents the surface roughness that is in particular formed by debris and boulders (in size under resolution) collected in small topographic lows, terraces etc. We note that features of slope processes clearly seen in phase ratios are often hardly distinguished in reflectance images. Visual comparison of reflectance and phase-ratio A(65º)/A(29º) images immediately reveals no direct correlation between these two distributions. Thus, the phase-ratio is largely free of the albedo variations, showing mainly the variations of the phase-function slope. All darker tone patches correspond here to steeper phase functions. We interpret the areas of lower A(65º)/A(29º) as increased surface roughness that is naturally produced by accumulating of debris, boulders, and rock fragments with sizes up to image resolution (~0.5 m) during the slope processes disturbing the structure of upper regolith layers. The reason of the slope processes can be meteorite bombardments triggering landslides and taluses on the crater wall. We can identify other higher roughness objects in the phase-ratio image (e.g., lobate flows and streams in thalwegs). In many cases details seen in both images reveal different shapes. To estimate the relative age of these flows, we studied maturity degree of their regolith.

Color-ratio imagery (maturity degree variations): Global spectral survey provided by the Multiband Imager (MI) camera onboard the spacecraft SELENE allowed multispectral lunar imaging with a spatial resolution of 20 m/pixel [7]. We used images of MI/SELENE to produce the color ratio C(0.95/0.75 μm) that is a measure of depth of the 1 μm spectral band in lunar minerals. Maturity degree of the lunar surface can be estimated by this spectral ratio because the immature regolith is characterized by lower C(0.95/0.75 μm) [8,9]. Figure 2 presents the color-ratio distribution obtained with MI/SELENE data for Cauchy at α=15º. The outlined part of the image corresponds to the area displayed in Fig. 1. Comparison of the phase-ratio and color-ratio images reveals good coincidence of rougher areas with regions of low C(0.95/0.75 μm). Thus, slope processes in craters, producing resurfacing of their walls, expose immature materials.

Conclusion: Thus, the phase-ratio imagery allows the remote sensing determination of roughness variations of the lunar surface. The phase-ratio method can be used to search for disturbances of structure, e.g., to detect areas of eroded surface, fresh slumps, accumulated material on crater's walls, terraces, and floors. The distribution of maturity degree estimated using the color ratio C(0.95/0.75 μm) shows close correlation with the photometric anomalies, pointing out that relatively recent slope processes in the crater walls are possible. The combination of phase-ratio and color-ratio imagery could be important to study asteroids and moons of planets.

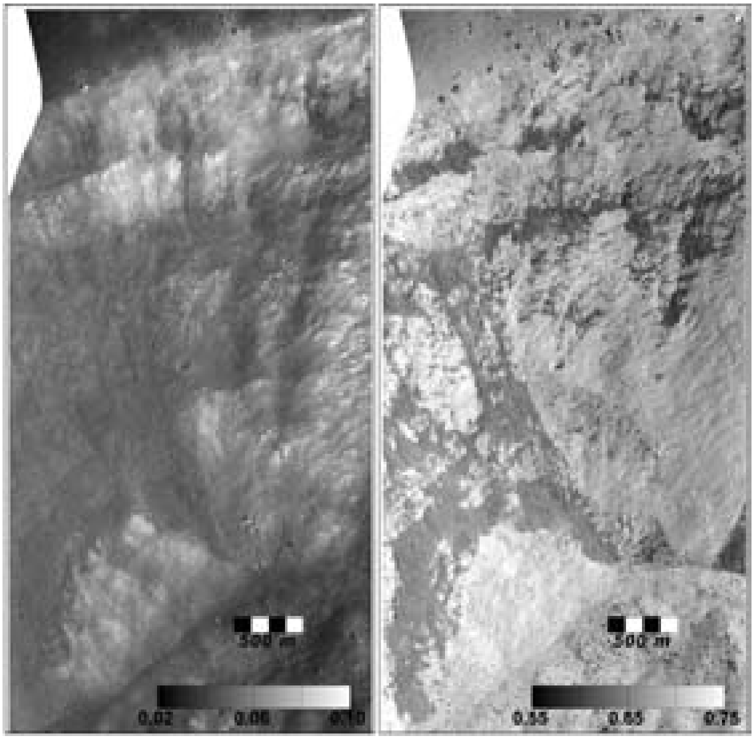

Fig. 1. Left: A fragment of the LROC NAC image presenting a part of the northern rim, wall, and floor of Cauchy. Phase angle for the image is 65º. Right: Distribution of phase ratio A(65º)/A(29º) for the same scene. North is up. Original resolution is 0.5 m/pix.

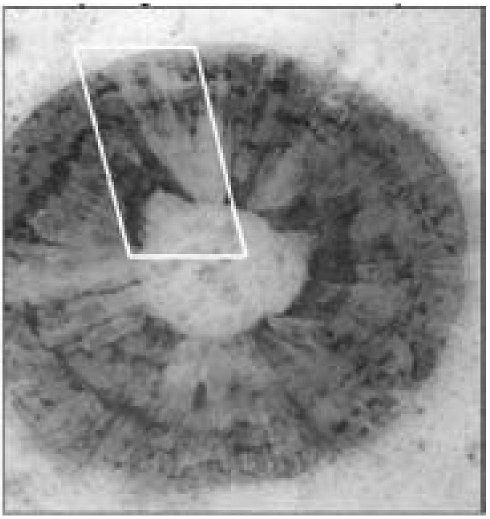

Fig. 2. Spectral ratio C(0.95/0.75 μm) for the crater Cauchy from MI/SELENE data; phase angle is 15º. Darker tones correspond to lower values of the ratio. Outlined part corresponds to the area shown in Fig. 1. Resolution is 20 m/pix.

References: [1] Hapke B. (1993) Theory of Reflectance and Emittance Spectroscopy. Cambridge Univ. Press. [2] Shkuratov Yu. et al. (1994) Icarus. 109, 168-190. [3] Shkuratov Yu. et al. (2005) Icarus, 173, 3–15. [4] Shkuratov Yu. et al. (2010) Icarus, 208, 20–30. [5] Kaydash V. et al. (2011) Icarus, 211, 89-96. [6] Robinson M. et al. (2010) Space Sci. Rev., 150, 81–124. [7] Ohtake M. et al. (2010) Space Sci. Rev., 154, 57-77. [8] Lucey P. et al. (2000) J. Geophys. Res., 105, 20377–20386. [9] Pieters C. et al. (2006) Icarus.184, 83–101.

RADAR COMPLEX IN THE PROJECT "MOON-GLOB": MONO- AND BISTATIC- RADIO LOCATION OF MOON

V.M. Smirnov[1], A.G. Pavelyev[1], V.N. Marchuk[1], S.S. Matyugov[1], O.V. Yushkova[1], O.I. Yakovlev[1], V.V. Abramov[2], Yu.F. Kvulinskiy[2], *[1]Kotel'nikov Institute of Radio Engineering and Electronics of RAS, Fryazino Branch, Russia; [2] Special Design Bureau IRE RAS, Fryazino, Russia. Contact:* **o.v.y@mail.ru**

Introduction:

Studying of the Moon is an intensively developing direction in space research. Start of the "Moon-Glob" Russian program was announced in 2007.

The practical importance of research of the Moon consists in the expansion of knowledge of formation and development of the Solar system planets; the studying an opportunity of investigation of lunar minerals for practical usage; a choice of the disposition places for the future expeditions. Water (a water ice) which is a source of oxygen and hydrogen for manned expeditions and fuel for traffic is necessary for maintenance of an inhabitancy on Moon bases. For this reason, the search of water in subsurface layer of the Moon is a priority problem in lunar researches. One of the possible methods of its search it is the radar location from an orbiting spacecraft.

Scientific tasks:

In frame of the "Moon-Glob" project it is planned to place into the lunar orbit a flying module with multi-purpose radar complex (RLC-L) for remote sensing with the goal:

- research of deep structure of the Moon ground;
- detection and identifications of the large lunar subsurface structures;
- estimation of dielectric permeability of a lunar ground;
- localization of places with the increased conductivity;
- research of large-scale roughnesses of lunar surface;
- registration of the electromagnetic emission in circumlunar space.

Hardware:

Designed radar complex RLC-L consists of two subsurface sounding radars: Radar-20 and Radar-200. The main characteristics of locators are given in Table 1 and Table 2, respectively.

Table 1. Radar-20 technical characteristics

• Range of accepted frequencies on the minus 3 dB level	17.5 up to 22.5 MHz;
• Bandwidth of intermediate frequency in an active location mode on the minus 3 dB level	5 KHz up to 5 MHz;
• Bandwidth of intermediate frequency in a bistatic location mode on the minus 3 dB level	300 KHz;
• radiated power, not less than	30 W;
• radiated signal	pulse, chirp signal;
• Duration of a radiated impulse	250 μs;
• Duration of registration of the accepted signal	350 μs
• Repetition frequency, not less than	1 Hz;
• Range of radiated frequencies on the minus 1 dB level	17 up to 23 MHz;
• Average power consumption, no more	20 W;

Table 2. Radar-200 technical characteristics

• Range of accepted frequencies on the minus 3 dB level	175 up to 225 MHz;
• Bandwidth of intermediate frequency on the minus 3 dB level	5 KHz up to 5 MHz;
• radiated power, not less than	30 W;
• radiated signal	pulse, chirp signal;
• Duration of a radiated impulse	250 μs;
• Duration of registration of the accepted signal	350 μs
• Repetition frequency, not less	1 Hz;
• Range of radiated frequencies on the minus 1 dB level	170 up to 230 MHz;
• Average power consumption, no more than	20 W;

Operational modes:

The work of RLC-L radar complex is planned in three modes:

1-st mode - active monostatic location from a spacecraft board,

2-nd mode - bistatic radio location with use of a radio emission of the ground transmitter, 3-rd mode - registration of electromagnetic radiation in circumlunar space.

Mode 1: it is intended for work of the Radar-20 and Radar-200 from heights of 100-150 km. For an active location, it is planned to use a chirp modulation signal. Sounding in a range from 17.5 up to 22.5 MHz (the Radar-20) will allow determining structure of layers in the Moon ground up to depths of about some kilometers (with the vertical resolution not worse than 25 m). In a range 175 - 225 MHz (Radar-200) it is supposed to investigate heterogeneity of surface and vertical distribution of the radio-physical characteristics in the top layers up to ten meters depth. For analysis of reflections from surface with different spatial resolution, the Radar-20 and Radar-200 are functioning alternately with minimally possible time of switching between them. The received reflected signals will be collected in the onboard memory of the Radar-20 and Radar-200, and then transmitted to the Earth. The geometry of experiment is presented on Figure 1.

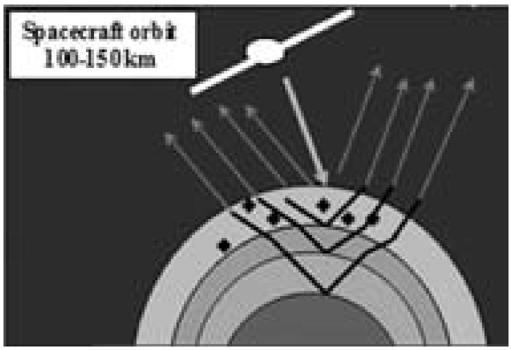

Fig.1. Remote sensing of the lunar soil in active location mode.

Mode 2: - In this mode, at the 100-150 km altitudes the radar RLK-L receives the signal emitted by an Earth-based transmitter at one of the frequencies in the range of 17-23 MHz. In Figure 2, the geometry of experiment in this mode is presented.

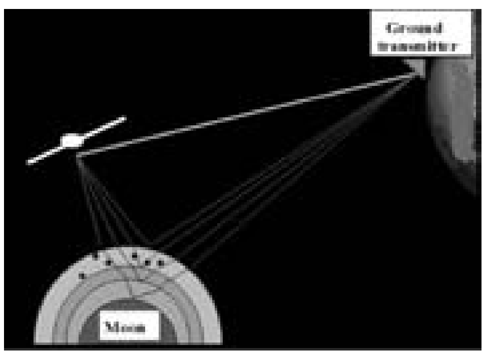

Fig. 2. Remote sensing of the lunar soil in the bistatic location mode.

Mode 3: Mode 3 is applied for detection of an electromagnetic emission produced by cosmic sources. Measurements will be executed by reception system of RLC-L radar complex.

RLC-L complex is developed in cooperation by Kotel’nikov Institute of Radio Engineering and Electronics of the Russian Academy of Science and Special Design Bureau IRE RAS.

The work is executed in part at financial support of the RAS programs «Plasma processes in solar system» and «Radio-electronic methods for researches of environment».

COMPOSITION OF THE LUNAR CRUST FROM LABORATORY AND REMOTE VNIR SPECTROSCOPY.

P.J. Isaacson[1], C. M. Pieters[1], R, L. Klima[2], N.E. Petro[3] and the M3 Team, *[1]Brown University, Providence, RI USA; [2]JHU/APL, Laurel, MD, USA, [3]NASA GSFC, Greenbelt, MD, USA. Contact: Peter_Isaacson@Brown.edu*

Introduction:

The Moon is an important solar system body for geologic study, as it preserves a record of critical and fundamental processes in the formation and evolution of rocky solar system bodies. The Moon's crust in particular harbors a preserved record of these processes in the diversity and spatial association of lithologies. The relative abundance and spatial association (geologic context) of key crustal rock-forming minerals thus provide important constraints on the wide variety of processes responsible for the formation of the lunar crust. As many of these processes are thought to be active on all rocky solar system bodies to some degree, the accessible, preserved record in the lunar crust makes the continued geologic study of the Moon a priority.

Returned samples from the Apollo and Luna programs as well as lunar meteorite samples offer direct insights into lunar geology. However, these collections are spatially limited and lack geologic context in the case of meteorite samples, which limits their utility for forming "big picture" assessments of lunar geology. Orbital remote sensing, particularly with visible to near-infrared (VNIR) spectroscopy, offers the capability to assess lunar mineralogy from a global perspective. VNIR spectroscopy is sensitive to the relative abundances of key lunar rock-forming minerals, as these minerals exhibit diagnostic absorption features across VNIR wavelengths caused by transition metal cations in distorted crystal lattice sites [e.g., 1]. Furthermore, this technique offers the potential for discovery of new minerals not present in the sample collection [e.g., 2, 3]. In the present work, we conduct a global study of lunar crustal mineralogy and compositional structure with Moon Mineralogy Mapper (M3) VNIR imaging spectroscopy data, and present interpretations based on fundamental constraints from laboratory investigations.

Lunar mineral VNIR spectroscopy:

Orbital VNIR spectroscopy offers compositional data at relatively high spatial resolution. However, interpretation of the returned VNIR spectra is fundamentally tied to the results of laboratory investigations of returned samples and analogue materials or mixtures (ground truth). Analogue materials and synthetic mixtures provide important constraints for interpretation of remote spectra, but there is no substitute for the complexities and unique compositional attributes of real planetary samples. The relative abundance of lunar samples (relative to samples of other planetary bodies), in particular the abundance of returned samples from known locations, provides relatively strong ground truth for investigations of lunar geology with orbital VNIR spectroscopy. Examples of such ground truth data are shown in Figure 1, which illustrates laboratory VNIR reflectance spectra of returned lunar samples and lunar meteorites.

VNIR spectra of major lunar minerals (e.g. olivine, pyroxene) are sensitive to mineral composition (Mg/Fe content for olivine, Mg/Fe/Ca content for pyroxene) in addition to mineral composition [4-9]. Mineral composition is an additional and powerful clue to constraining formation processes responsible for a particular lithology or suite of lithologies. This capability is illustrated by Figure 2, which shows trends in the diagnostic olivine absorption features with changing olivine composite (Mg/Fe content). The combined capabilities of analyzing mineralogy in spatial context and evaluating mineral composition concurrently with mineralogy are powerful tools for investigation of global lunar geology, and are unique capabilities of VNIR imaging spectrometers such as M3 [e.g., 10, 11].

Compositional Survey of the Lunar Crust through M3 imaging spectroscopy: The NASA Moon Mineralogy Mapper (M^3) is a VNIR imaging spectrometer that orbited the Moon on the ISRO Chandrayaan-1 spacecraft. It covers the wavelength range from ~650 to ~3000 nm at high spatial and spectral resolution, and acquires reflectance spectroscopy data in an imaging context [12]. The spectral sampling of M^3 ranges from 20–40 nm in the instrument's reduced resolution mode (which comprises the bulk of the acquired data), allowing analyses that require high spectral resolution and full coverage across VNIR wavelengths. The present study leverages these capabilities to conduct a compositional survey of the lunar crust through analysis of imaging spectroscopy data collected from relatively immature craters with central peaks. Central peaks merit study for a variety of reasons, including the fact that they expose material from depths related to their size, allowing investigation of compositional trends both laterally and vertically if craters are sampled across the globe. Immature craters also have rugged topography that tends to inhibit the development of a thick regolith layer; such a regolith layer would have adverse implications for investigation of mineralogy and mineral composition with VNIR spectroscopy. This approach has been employed previously as a means to investigate lunar crustal structure, although previous studies were limited by the available data [e.g., 13, 14]. We build on these previous studies by incorporating the capabilities of new datasets such as M3. We have assembled mosaics of M3 imaging spectroscopy data covering a range of lunar central peak craters (the locations are illustrated in Figure 3), and are evaluating the data with a technique that quantifies the diagnostic mineral absorption features in spatial context. The most recent results of this ongoing investigation will be presented.

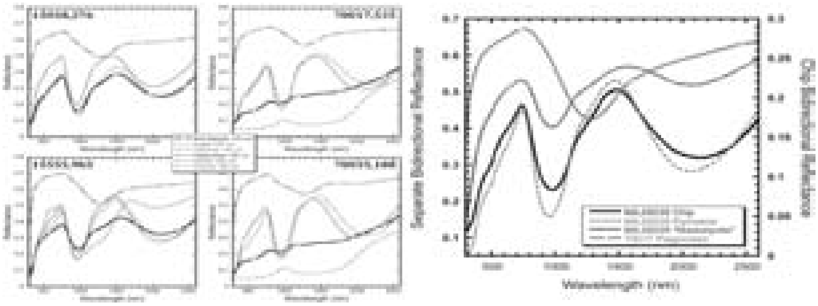

Fig. 1: Laboratory VNIR reflectance spectra. (L) Spectra from [15] of lunar samples used for ground truth and interpretation of remote reflectance spectra. Black lines are basalts; colored lines are mineral separates from the basalts. Low-Ti samples are on the left and ilmenite-rich high-Ti samples are on the right. Note the dramatic effect of ilmenite on reflectance spectra illustrated by the differences between the low-Ti and high-Ti basalt spectra. (R) Spectra of lunar basaltic meteorite MIL05035. Black line is the bulk sample (measured from a chip); red and blue are separates from the chip. Green is a plagioclase separate spectrum from the left figure.

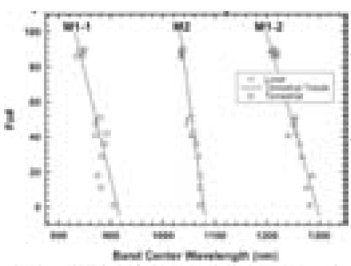

Fig. 2: Trends in the three principal olivine absorptions near 1000 nm with changing olivine composition from [9]. The three principal absorptions (labeled with the Fe2+-bearing cation site responsible for the absorption) shift to longer wavelengths with increasing Fe content; this shift can be used to determine olivine composition through VNIR spectroscopy.

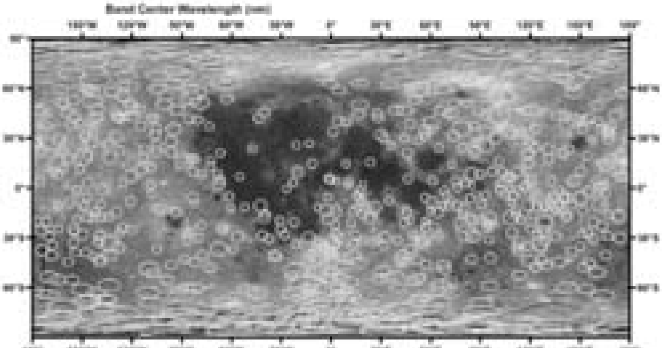

Fig. 3: Locations of M3 imaging spectroscopy data mosaics created for analysis of central peak craters. The basemap is Clementine 750 nm albedo mosaic, simple cylindrical projection, ULCN 2005 coordinate system.

References: [1] Burns, R.G. (1993) Mineralogical applications of crystal field theory. [2] Pieters, C.M. et al. (2011) JGR, 116, 10.1029/2010JE003727. [3] Dhingra, D. et al. (2011) Geophys. Res. Lett., 38, L11201, 10.1029/2011gl047314. [4] Klima, R.L. et al. (2008) MAPS, 43, 1591-1604, 10.1111/j.1945-5100.2008.tb00631.x. [5] Adams, J.B. (1974) JGR, 79, 4829-4836, 10.1029/JB079i032p04829. [6] Hazen, R.M. et al. (1978) PLPSC, 9, 2919-2934. [7] Cloutis, E.A. and Gaffey, M.J. (1991) JGR, 96, 22809-22826, 10.1029/91JE02512. [8] Sunshine, J.M. and Pieters, C.M. (1998) JGR, 103, 1367513688, 10.1029/98JE01217. [9] Isaacson, P.J. and Pieters, C.M. (2010) Icarus, 210, 8-13, 10.1016/j.icarus.2010.06.004. [10] Klima, R.L. et al. (2011) JGR, 116, E00G06, 10.1029/2010JE003719. [11] Isaacson, P.J. et al. (2011) JGR, 116, 10.1029/2010JE003731. [12] Pieters, C.M. et al. (2009) Current Science, 96, 500-505. [13] Tompkins, S. and Pieters, C.M. (1999) MAPS, 34, 25-41. [14] Cahill, J.T.S. et al. (2009) JGR, 114, 10.1029/2008je003282. [15] Isaacson, P.J. et al. (2011) MAPS, 46, 228-251, 10.1111/j.1945-5100.2010.01148.x.

SOLAR BURSTS AND SEISMIC RESPONS OF LUNAR LITHOSPHERE

Oleg B. Khavroshkin, Vladislav V. Tsyplakov, *Schmidt Institute of Physics of the Earth, RAS Moscow, Russia. Contact: khavole@ifz.ru*

Abstract: Development of researches of lunar exoseismicity on the basis of Nakamura Catalogue has resulted in understanding of the importance of the solar activity contribution in seismic fields of lunar lithosphere. The analizing of modulation processes on the Moon by statistical methods find that the periodicity seismic wave field contain a long-wave part of own pulsations of the Sun.

Acting of burst activity and optic - acoustic effects (γ - and X-rays-pulse components of flash) on seismic fields of the Moon is investigated. Both components that is wave (**γ,** X-rays and optic radiation) and corpuscular, at enough powerful burst (or one of its component) are accompanied by the seismic acoustic response of lunar lithosphere. The found out interaction allows to proceed to research structure of burst under its seismic acoustic response and has fundamental value. On the other hand, new features of structure of a wave field in a time vicinity of the moment of influence of burst that is displayed in seismogramm durations (duration is considered as the period of wave which acted on process of the day surface) and as a result of the analysis of their histograms are revealed. Features consist in the following. Before the burst the wave field of lunar lithosphere contains a significant component on the periods of waves concerning to a spectrum of own solar oscillations. After shock of burst on a lunar surface this component almost disappears and appears only through some tens hours. Probably similar features of a waves field of the Moon can display dynamics of the waves processes on the Sun.

DEEP FAULTS OF THE MOON AND MULTIPLE REFLECTED WAVES

Oleg B. Khavroshkin, Vladislav V. Tsyplakov, *Schmidt Institute of Physics of the Earth, RAS Moscow, Russia. Contact: khavole@ifz.ru*

Abstract: Existed seismic waves on the lunar lithosphere are of two kinds. First kind is well-known types and other has a seismic acoustic nature. Second type is usually dominated and complicates interpretation wave fields. The characteristics of such a seismic acoustic signals are similar to the same signals on the Earth according to their property are well known. Deformation of lunar lithosphere by seismic waves and elastic processes of a wide frequency range is accompanied by radiation and modulation of high-frequency seismic acoustic waves of emission type. Deep faults of the lunar lithosphere promote formation from powerful impact sources of multiple waves such as type PKiKP, and also PcP etc. which were found out with use of various statistical methods of the analysis including the kepstrum. Temporal characteristics of modulated processes for example own oscillations of the Moon and multiple reflected waves are an authentic material for research of an internal structure of the Moon. It is desirable to choose places of landing of lunar stations in view of registration of multiple reflected waves.

CONSTRAINING THE COMPOSITION AND THERMAL STATE OF THE MOON FROM INVERSION OF SEISMIC MODELS

O.L. Kuskov, V.A. Kronrod, E.V. Kronrod, *Vernadsky Institute of Geochemistry and Analytical Chemistry Russian Academy of Sciences, Moscow, Russia. Contact: ol_kuskov@mail.ru*

Abstract: In spite of the fact that a lot of works have been concerned with the thermal history of the Moon, the temperature of the lunar interior remains one of the most speculative and uncertain physical parameters. Knowledge of chemical composition and thermal regime is essential for the correct interpretation of seismic data and for our understanding of the origin and internal structure of the Moon. The internal structure of the Moon depends strongly on its composition and thermal regime. However, geochemical studies of returned lunar samples do not give direct information about the composition and physical properties of the mantle. Seismic models and surface heat-flow measurements provide only indirect information about the composition and temperature of the Moon. In situ heat flow measurements were carried out during the Apollo 15 and 17 missions. According to these measurements, heat-flow estimates were from only two rather special locations (at the Hadley Rille and Taurus Littrow), and values of 21 and 16 mW/m^2 have been obtained. Despite over the last 10 years extensive progress has been made in understanding of the seismic structure of the Moon, one of the most difficult factors to determine is the present temperature of the lunar interior. We invert the Apollo lunar seismic data set, together with geochemical models, for the thermal state of the Moon. Based on self-consistent thermodynamic approach, we calculate a family of selenotherms and discuss the temperature distribution models in the upper and lower mantle obtained from *P*- and *S*-wave velocities and geochemical constraints. For the computation of phase equilibrium relations, we have used a method of minimization of the Gibbs free energy combined with a Mie-Grüneisen equation of state. Our forward calculation of phase equilibria, seismic velocities and density, and inverse calculation of temperature include anharmonic and anelastic parameters as well as mineral reaction effects, including phase proportions and chemical compositions of coexisting phases. The chemical and mineral compositions in the upper and lower mantle and a probable law of temperature distribution in the entire lunar mantle are suggested. The seismically derived temperatures allow us to constrain the thermal structure of the lunar mantle and estimate the mantle heat flow value. The general temperature distribution in the entire lunar mantle (at 50-1000 km depth) inferred from the seismic profiles, showing a considerable scatter, can be described by the following strongly approximate expression: $T(^{o}C) = 351 + 1718[1 - \exp(-0.00082 \times H)]$ (Kuskov, Kronrod, 2009). Our temperature models are much colder than temperatures found by Keihm and Langseth (1977). Their heat flow and thorium abundance measurements lead to upper mantle gradients in the range of 1.8-3.2 K/km and temperatures at 300 km in the range 800-1300^{o}C. Assuming temperature gradient of ~1.1 K/km and thermal conductivity of the upper mantle of 3.3 W/m K, we get the upper mantle heat flow value of 3.6 mW/m^2, which is not consistent with heat fluxes in the range of 7-13 mW/m^2 at depth of 300 km found by Keihm and Langseth (1977). Our results show that these heat-flow estimates are too high by a factor of two to three. The results of our inversion procedure indicate that upper and lower mantle compositions are strikingly different. General increase in seismic velocities from the upper to lower mantle is consistent with a change in bulk composition from a dominantly pyroxenite upper mantle depleted in Al and Ca (~2 wt% CaO and Al_2O_3) to a dominantly fertile lower mantle enriched in Al and Ca (~4-6 wt% CaO and Al_2O_3) with larger amounts of olivine, garnet and clinopyroxene. A pyrolitic model cannot be regarded as a geophysical-petrological basis for the entire mantle of the Moon. The solution of the inverse problem yields a strong independent tool, which can reduce the uncertainty of seismic data and discriminate between the observational models.

References: Keihm, S.J., Langseth, M.G., 1977. Proc. Lunar Sci. Conf. 8, 499-514.
Kuskov, O. L., Kronrod, V. A., 2009. Izv. Phys. Solid Earth 45, 753–768.

2MS³-LS-17

SOURCE CUTOFF FREQUENCY ESTIMATIONS FOR A NUMBER OF IMPACTS DETECTED BY THE APOLLO SEISMOMETERS.

T. Gudkova[1], **P. Lognonné**[2], **J. Gagnepain-Beyneix**[2], **V. Soloviev**[1], *[1]Schmidt Institute of Physics of the Earth, B.Gruzinskaya 10, Moscow 123995, Russia; [2]Institut de Physique du Globe de Paris, 4 av. De Neptune 94100 Saint-Maur des Fossés, France. Contact: gudkova@ifz.ru*

Introduction: Meteoroid impacts on the Moon are interesting and important sources for seismic experiments that might be deployed in the next decade. Most of these impacts are weak enough (typical meteorite impacts on the Moon range in mass from a fraction of kilogram to several tons) and they are detected by less than three seismic stations. Monitoring light flashes generated during the impact provides new opportunities for modeling the arrival times of seismic waves from these events. The increase of the meteoroid recordings are needed to make inversions for very shallow regolith structure on the Moon and investigate the 3D structure of the lunar crust. A model for the seismic source associated with an impact was considered in [1, 2]. The recordings of the meteoroid impacts are well explained by this model, which accounts the ejecta and the effects of attenuation. The duration of the impact process leads to relatively low (about 1s) corner frequency.

Source function: Let us consider the source excitation process for an impact where an impactor is instantaneously absorbed by the surface without ejecta generation. The seismic force can be modeled as a point force

$$\mathbf{F_0}(t,\mathbf{x})=m\mathbf{v}\ d\ (t)\ d\ (\mathbf{x}-\mathbf{x}_s) \qquad (1)$$

where m is the mass, **v** is the velocity vector (v being the velocity amplitude. We assume a simple model for the seismic source function, namely, a time-dependent force acting downward on the surface of the planet during the impact, which takes into account the fact that part of the seismic force could be associated with ejecta material [2]. Let the seismicforce function be in the form

$$f(t,\mathbf{x})=m\mathbf{v}\delta(\mathbf{x}-\mathbf{x}_s)\ g(t)=\mathbf{F_0}(t,\mathbf{x})\times g(t),\ g(t)=1+\cos\omega_l t \text{ for } -\pi/\omega_l<t<\pi/\omega_l,\ g(t)=0 \text{ otherwise.} \qquad (2)$$

We define the seismic amplification parameter as $S=I/mv$, I is the seismic impulse, defined as an intergral of the equivalent force $f(t)$, $\tau=2\pi/\omega_l$ to denote the time-duration of the excitation process. The Fourier transform of $g(t)$ is proportional to ω^{-3} for angular frequencies higher than the cutoff angular frequency ω_l. That is why we expect the seismic acceleration spectrum, which varies as ω^3 at low frequency for an impact, to be flat after the cutoff frequency and even to decrease due to additional effects such as attenuation.

The amplitude of the spectrum recorded at a given epicentral distance D can be approximated as

$$\hat{s}(\omega)=B\omega^3\exp\left(-\frac{\omega t_{prop}}{2Q}\right)\quad g(\omega) \qquad (3)$$

where B is a constant depending on the source impulse and epicentral distance.

This source model was tested for artificial impacts and three large meteoroids impacts in [1, 2]. The results with the seismic force in the form of (1) assuming the source function to be a delta function are not satisfactory.

Source cutoff frequency estimations: For our analysis we have selected 40 impacts well enough recorded on vertical component by the most of the stations. We note that many of the impacts under consideration occur on the nearside of the Moon, and limited seismic recordings of impacts (impacts on farside) were made at large epicentral distances from the nearside Apollo network (Figure1).

We have determined, by a least squares fit of the logarithmic amplitudes, the best values for Q, t and B in Eq. (3) by a grid search. We get a good fit to the data and a very high quality factor. Figure 2 shows the results for the best values for the impacts on 19710523 and 19770628 (Q>20000; t = 0.45 and 1.3 sec, respectively). The impact 19710523 takes place far a way from the stations on the highlands, while 19710523 being near the stations on the soil. As seen from the Figure 2, source function (2) approximates well enough both impacts: the impact at short distance and the impact at long distance.

The time duration process/momentum transfer distributions for the events are shown in Figure 3. We propose that the difference between the source cutoff frequency for the impacts with the same momentum transfer are caused by the excitation processes due to the location (subsurface composition) and incident angle. Some uncertainties exist due to factors that include instabilities of the amplitudes of seismic signals and shape of the spectrum associated with propagation effects, variations in the upper mantle attenuation beneath different sites. The response is calculated for idealized structure, as the local geophysical conditions were not taken into account. But the tendency is seen the larger an impact is, the lower is its cutoff frequency for the impacts falling in the same area. The cutoff frequency is lower for the impacts falling on rock in comparison with the cutoff frequency for the impacts falling on soil.

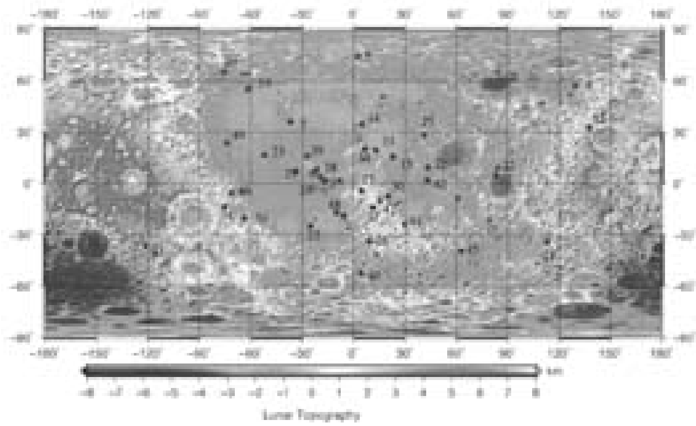

Fig. 1. Location of the impacts under consideration.

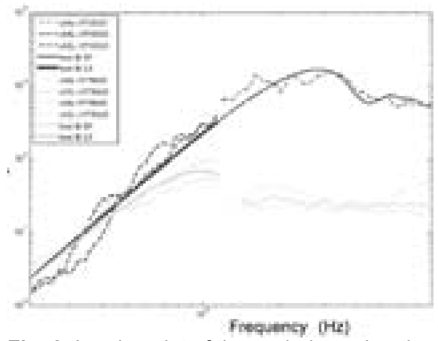

Fig. 2. Log-log plot of the scaled acceleration spectral density for two meteoroids impacts: 19710523, recorded on LP and SP vertical components at station 14, and on LP vertical component at station 12; and 19770628, recorded on LP vertical component at stations 12 and 15, and on SP vertical components at stations 14 and 16. The solid lines are the theoretical scaled acceleration spectral densities calculated for simulated events with the assumed source function in the form of (2). In addition to the seismic impulse scaling, the attenuation effect has been corrected by multiplying the spectrum by exp(ωt_{prop}/2Q), where Q is the quality factor found by the least squares inversion.

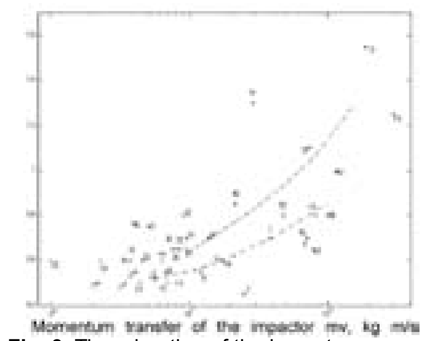

Fig. 3. Time duration of the impact process as function of the momentum transfer of the meteoroids. Dashed line is approximation for the impacts on the rock material, and the dot-dashed line is for the soil.

Conclusion: The estimate of source cutoff frequency for a number of impacts detected by the Apollo seismometers was done in order to find the dispersion of parameters depending on the location (subsurface composition) and the amplitudes of the seismic signals. The recordings of the meteoroid impacts are well explained by the model of the seismic impulse (2) due to the impactor, resulting ejecta and the effects of attenuation. The target material which vary a great deal between nearside and farside of the Moon acts the efficiency of the impact.

Acknowledgements: This work was supported by Programme National de Planetologie from INSU and by the French Space Agency (R&T program) and Grant No. 09-02-00128 from the Russian Fund for Fundamental Research.

References: [1] Lognonné, Ph., Le Feuvre, M., Johnson, C.L., and Weber, R.C. : Moon meteoritic seismic hum : steady state prediction. JGR, Vol. 114, E12003, 2009. [2] T.V.Gudkova, Ph. Lognonné, and J. Gagnepain-Beyneix : Large impacts detected by the Apollo seismometers: impactor mass and source cutoff frequency estimations, Icarus, 211, 1049-1065, 2011.

STUDIES OF FORMER SOVIET AND MODERN LUNAR CO-ORDINATE SYSTEMS USING SOVIET SPACECRAFT ON THE LUNAR SURFACE

I. Nadezhdina[1], A. Konopikhin[1], J. Oberst[1,2], A. Zubarev[1], [1]*Moscow State University of Geodesy and Cartography (MIIGAiK), Gorokhovsky pereulok 4, 105064, Moscow, Russia,* [2]*German Aerospace Center, Institute of Planetary Research, Rutherfordstaße 2, 12489 Berlin, Germany. Contact: i_nadejdina@coslab.ru*

Introduction: The Moon enjoyed an extensive early exploration program by Soviet and NASA spacecraft. Spacecraft development, but also spacecraft navigation and mission support were solved by each country rather independently.

Today, there is great interest in studying the early Soviet technology for navigating in deep space and to study the accuracy of the Soviet lunar co-ordinate systems that were used in the middle of the 20th century (the USSR $_{\text{(20th century)}}$).

Recently, seven Soviet landers have been identified on the Lunar surface in high-resolution images obtained by the LRO (Lunar Reconnaissance Orbiter) spacecraft. The coordinates of the landers in the modern ME (Mean Earth / Polar Axis) coordinate systems were accurately established.

We have compared these modern coordinates with the previously published and predicted co-ordinates in the USSR $_{\text{(20th century)}}$ system and have studied relationships between the two sets.

Our preliminary findings are that the planar co-ordinates (latitude and longitude) of the USSR $_{\text{(20th century)}}$ system agree with the co-ordinates in the ME system within errors in the range of 0.1 - 0.12 ° (3.0 – 3.5 km at the equator). Absolute heights (radius vector) in the USSR $_{\text{(20th century)}}$ system differ by up to 2.8 km from the values obtained by the Lunar Orbiter Laser Altimeter (LOLA). Both coordinate sets can be transformed to one another by simple common shift and rotations, with 50% (to be confirmed) of coordinate errors remaining.

We conclude that differences between the previously published and true coordinates of the Soviet landers are due to systematic lateral and rotational offsets of the coordinate systems that were used, lack of knowledge regarding absolute Lunar heights, as well as random ballistic errors.

Details of the analysis will be presented at the meeting.

GIS-ANALYSES OF THE LUNOKHOD-1 LANDING SITE USING LROC IMAGES AND HIGH RESOLUTION DEM

I. P. Karachevtseva[1], O. Peters[2], J. Oberst[1,2], A. A. Konopichin[1], K.B. Shingareva[1], F. Scholten[2], M. Wählisch[2], I. Haase[3], J. Plescia[4], M. Robinson[5], [1]*Moscow State University of Geodesy and Cartography (MIIGAiK);* [2]*German Aerospace Center (DLR);* [3]*Technical University Berlin, Germany;* [4]*Johns Hopkins University, Applied Physics Laboratory, USA;* [2]*Arizona State University, USA. Contact: i_karachevtseva@coslab.ru*

Introduction: MIIGAiK is developing an automated GIS-oriented mapping technology for studies of planetary surfaces. Here we present the new results of the Luna-17 Landing Site large-scale mapping. In our study we used the high resolution orthoimages and DEM, which were previously obtained at DLR from the photogrammetric processing of LRO (Lunar Reconnaissance Orbiter) NAC (Narrow Angle Camera) stereo images (07350_M150749234, 07351_M150756018) with spatial resolutions of 0.5 m/pixel. Both data sets were used for landing site area and Lunokhod-1 traverse GIS analyses. The work carried out may prepare us for searching and assessing future landing sites of the LUNA-GLOB and LUNA-RESOURCE missions.

Lunokhod-1 area mapping and geoanalyses: We have studied the Lunokhod-1 area using large-scale maps. For analysis of surface morphology and e.g. for measurements of sizes of craters along the Lunokhod track, a DTM (derived by F. Scholten, DLR) was used. To improve the identification of the traverse (obtained by J. Plescia, Johns Hopkins University Applied Physics Laboratory), we used topographic plans (large-scale maps whose resolution varied from 1 to 2.5 m per 1 cm) derived from stereo-photogrammetry processing of the Lunokhod-1 surface image data [2]. We identified about 99% of the Lunokhod's traverse, which is approx. 9.5 km long, as measured in the GIS (Fig.1). About 1% segments of the traverse (150 m) could not be identified as these parts of the traverse was in shadow in the image we used. Integrating all types of data as described above we digitized craters in the Lunokhod traverse area and created a crater catalog as geodatabase in ArcGIS which now consists about 45 000 crater objects and includes their diameter and depth, obtained from the DTM. Using this information we calculated various parameters of the Lunokhod-1 area (about 8.75 sq. km), including spatial density for craters with diameter more 10 m entire all area of the Luna-17 Landing Site (Fig. 2), size-frequency distribution for all craters at the Lunokhod-1 traverse area (Fig.3). We calculated crater relative depths for the study area (ratio of crater depth to diameter: min=0,006; max=0,036, mean=0,06) and also slopes, roughness that demonstrated possibilities of high-resolution elevation data (that corresponds to the scale of 1:5000, 50 m per 1 cm) for distinguish local scale geomorphic units.

Lunokhod-1 surface image data: In addition to identifying the Lunokhod-1 track, we also used topographic plans, that had accuracy in the positions and heights of of 10 cm and 4 cm [2], respectively, for testing the possibility of using the LRO NAC data for large-scale mapping of purposed future lunar landing sites. Results of GIS measurements showed good agreement with the results of the large-scale mapping derived from Lunokhod-1 surface image data. For example, the difference between crater depths from lunar old topographic plans and new GIS measurements is from 20 cm to 1 m (Fig. 4). Slopes measured on topographic plan N3 have a value between 16° and 23° [2], which also shows good agreement with measurements in GIS (Fig 5). From the other side, these results attest to the very high quality work that had been done 40 years ago during Soviet lunar missions.

Conclusions: GIS mapping of the landing site Lunokhod-1 has been carried out using semi-automatic function for the crater detection and measurements from high resolution orthoimages and DTM. We show that these data can be used for large-scale mapping and studies of candidate landing sites for future lunar missions, for example LUNA-GLOB and LUNA-RESOURCE missions. `The purpose of our future work is computation of archived Lunokhod panoramas [2], [3,] [4] and assignment of these panoramas to their respective rover position along the track.

Acknowledgement: This research was partly funded by the Russian Government (MEGA-GRANT, Project name: "Geodesy, cartography and exploration of planets and satellites", contract № 11.G34.31.0021).

Reference: [1] Abdrakhimov A.M. et al. (2011) Luna 17 / Lunokhod 1 and Luna 21 / Lunokhod 2 landing sites as seen by the Lunokhod and LRO cameras. 42nd LPSC (#2220). [2] Barsukov V.L. et. al. (1978) Peredvijnaya laboratoriya na Lune Lunokhod-1, Volume 2. Nauka. (in Russian). [3] Vinogradov A.P. et. al. (1977) Peredvijnaya laboratoriya na Lune Lunokhod-1, Volume 1. Nauka. (in Russian). [4] http://www.planetology.ru/panoramas/

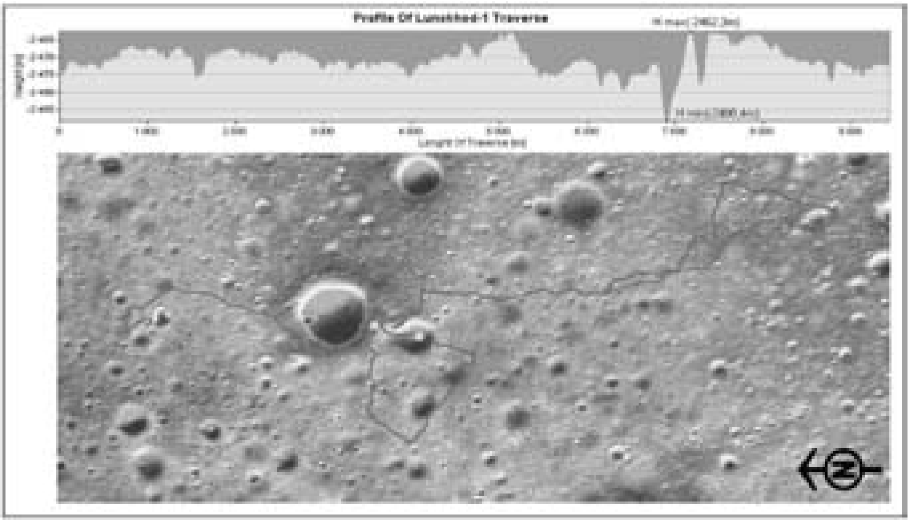

Fig.1. Lunokhod-1 traverse, digitized in GIS

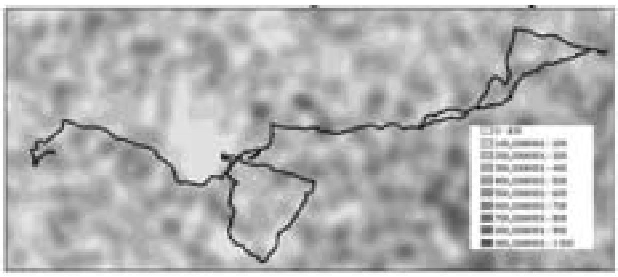

Fig.2. Lunokhod-1 area map of the spatial density of craters (Diam>10 m)

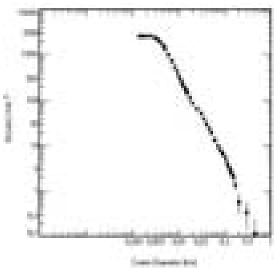

Fig.3. Size-frequency distribution for all craters at the Lunokhod-1 traverse area

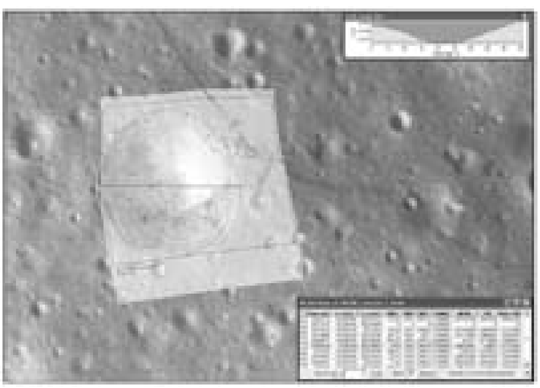

Fig.4. Lunokhod-1 surface large scale map and GIS-measurements

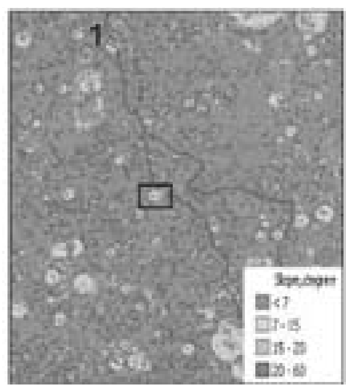

Fig.5. Slope map of Lunokhod-1 area

For a color version of this abstract, please download from:
http://coslab.ru/files/articles/2M-S3_Karachevtseva_GIS_Lunokhod-1.pdf

SCIENCE INVESTIGATIONS ON THE LUNA-GLOB ORBITER

A.A. Petrukovich[1], L.M.Zelenyi[1], I.G.Mitrofanov[1], O.I.Korablev[1], *[1]Space Research Institute (IKI), Moscow. Contact: apetruko@iki.rssi.ru, lzelenyi@iki.rssi.ru, imitrofa@space.ru*

Luna-glob mission of Russian space agency includes an orbiter to be deployed at the circum-lunar orbit simulataneously with the lander. The orbiter includes a science instrumentation package for surface, plasma, and exosphere investigations. The report presents scientific rationale of the mission.

SCIENCE INVESTIGATIONS ON LANDERS OF LUNA-RESOURCE AND LUNA-GLOB MISSIONS

V.I.Tretyakov, *Space Research Institute (IKI), Moscow*

Scientific payload will be presented landers of Luna-Resource and Luna-Glob missions, which was selected in accordance to two main goals of these mission: studies of lunar polar volatiles and studies of polar exosphere. The plan of surface operations will be discussed. Criteria for landing site selection will be considered and potential landing sites will be introduced for these missions.

CHANDRAYAAN-2 MISSION: THE ORBITER AND ROVER PAYLOADS

J. N. Goswami, *Physical Research Laboratory, Ahmedabad – 380009, India*

Chandrayaan-2 mission to moon will have a Orbiter-Lander-Rover configuration and is a joint Indo-Russian effort in planetary exploration. India will provide the Orbiter and the Rover, along with a set of scientific instruments in them as well as the Launch vehicle. Russia will provide the Lander having a suit of instruments to probe lunar surface and interior for geochemical and geophysical characteristics. This talk will provide an outline of the payloads to be carried in the Orbiter and Rover that are being developed in India.

LANDING DYNAMICS ON THE MOON IN “LUNA-GLOB” PROJECT

Yu.G. Sikharulidze[1], B.I. Zhukov[1], A.GTuchin[1], Yu.K. Zaiko[2], V.P. Fedotov[2], V.N. Likhachov[2], A.I. Sheikhet[2], *[1]KIAM RAN, [2]Lavochkin design center*

Annotation:

Current Russian lunar program includes two missions with landing of the spacecrafts in the polar regions of the Moon: “Luna-Resurs” (South pole) and “Luna-Glob” (North pole). It is necessary to provide a high landing accuracy in the given place for the scientific investigations. So, the terminal guidance algorithm is developed for the “Luna-Glob” lander.

Total descent trajectory includes tree phases. The first phase starts in de-orbit point (near the pericenter of the prelanding orbit) and terminates by the vertical descent with given velocity and altitude. The second phase is a vertical descent trajectory above the given landing point. The phase is terminates at altitude of a few ten meters and velocity of a few meters per second. The engine with thrust of 4120 N is used during both phases for deceleration and correction of trajectory. The third phase is also vertical and terminates by the soft landing. At last phase the engine with thrust of 1177 N is used for precise deceleration.

Developed terminal guidance algorithm is used at all phases with adaptation to the real deceleration conditions. For this purpose the phantom acceleration measurements (due to engine only) are used. The algorithm is based on the numerical prediction of the remained trajectory in the two-point boundary problem (so called the numerical prediction-corrector NPC).

Allowable initial conditions and boundary conditions between phases are investigated. The total optimization of trajectory from de-orbit point till landing provides the minimal propellant consumption. There are also the mathematical simulation results with estimation of the required propellant and preliminary estimation of the landing accuracy.

RADIOSCIENCE EXPERIMENTS WITH "MOON-GLOB" ORBITER RECEIVER AND BEACONS ON MOON'S LANDERS

A.S. Kosov[1], O.N. Andreev[1], V.M. Aniskovich[1], I.A. Babushkin[1], S.V. Fedorov[1], L.I. Gurvits[3], R.S. Kalandadze[1], V.V. Korogod[1], S.M. Maleev[1], V.G. Nechaev[1], S.V. Pogrebenko[3], V.S. Roshkov[1], D.P. Skulachev[1], I.A Strukov[1], Y. Sun[5], V.K. Sysoev[2], S.G. Turyshev[4], V.A. Zotov[1], *[1]Space Research Institute RAS, 84/32 Profsouznaya, 117997, Russia; [2]Lavochkin Science Production Association, Chimky, Moscow Region, 24, Leningradskaya St., 141400, Russia; [3]Joint Institute for VLBI in Europe, Dwingeloo, The Netherlands; [4]JPL, 4800 Oak Grove Drive, 91109-8099 Pasadena California Dwingeloo, USA; [5]Center for Space Science and Applied Research, Chinese Academy of Sciences, No.1 Nanertiao Zhongguancun, P.O.BOX:8701 Beijing 100080, China. Contact: akosov@iki.rssi.ru*

Abstract: The Radioscience Experiments will be performed with two Moon's Beacons on Landers and Receiver on "Moon-Glob" Orbiter. The experiments chart is shown on Fig.1 below.

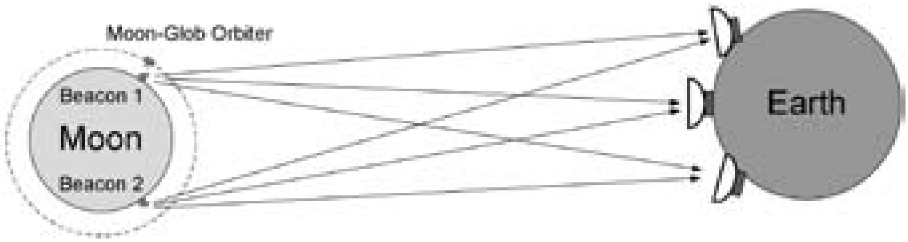

Fig.1. The experiments chart.

The main feature of the instruments is very high frequency stability and very narrow spectrum line width of the beacons signals and the orbiter's receiver local oscillator signal. Such performance is due to OCXO 8607 frequency standard used in beacons and orbiter's receiver. The stability of the standard is shown below:

- 3-30 sec, better than $8 \cdot 10^{-14}$;
- 1-300 sec, better than $1 \cdot 10^{-13}$;
- 0.1-10000 sec, better than $1 \cdot 10^{-12}$;
- 24 h, better than $5 \cdot 10^{-12}$;
- year, better than $2 \cdot 10^{-9}$;

The beacons will irradiate signal at two frequency bands: 8.4 GHz and 32 GHz. The 8.4 GHz signals will be directed to the Earth and together with VLBI ground based network will be used for celestial mechanics experiments and navigation goal. It will be possible to measure the beacon's positions with accuracy about 1 cm and to register Moon's libration.

The 32 GHz band will be used for orbiter navigation goal and gravitation field investigation. The Ka band signal will be directed to zenith and will be received by orbiter's receiver. Investigation of Nonuniformity of Lunar Gravitation field (experiment INGL) will be performed in vicinity of landing regions with accuracy 3-5 mGal. The spatial resolution will be about 20 km. The experiment is based on precise Doppler shift measurement. So the velocity and the acceleration will be recorded.

It is planned to make beacons as long life instruments with life time no less than 5 years. On first stage the beacons will be powered from solar batteries, and after that from nuclear power source.

2MS³-LM-05a

MICROWAVE INVESTIGATION OF LUNAR REGOLITH

D. P. Skulachev, *Space Research Institute (IKI), Moscow, Russia. Contact: dskulach@mx.iki.rssi.ru*

Introduction:

Lunar regolith is a pretty good dielectric, and microwaves penetrate it to a certain depth. Microwave investigation may use an active (radar) and a passive (radiometric) methods. Microwave energy, radiated by radar penetrates in regolith, some of it reflects from inner inhomogenities. Reflected signal can then may be received and analyzed. Radiometer does not radiate any microwave power but simply receives natural Planck thermal radiation that comes from the regolith depth.

These two methods differ from each other. Radar may find dielectric inhomogenities but is not sensitive to temperature. Microwave radiometer may measure temperature, but is low sensitive to dielectric inhomogenities.

Microwave radiometer measurements of lunar regolith were performed many times, both from the Earth and from lunar orbiter. Last investigation from lunar orbiter ChangE-1 [1] determined regolith temperature, depth, and permittivity.

Water ice dielectric constant is close to it of lunar regolith. Therefore, if we are interested in water ice presence in regolith, radar looks useless. Most likely, ice inclusion in regolith has the same temperature as surrounded substance, so microwave radiometer looks useless too. In this case we are forced to seek some indirect method of investigation.

ChangE-1 data [2] show a considerable variation in regolith temperature during lunar day (lunation). The variation is due to the Sun thermal effect. The regolith heats up in the daytime and cools down at night. An extent and rate of temperature change depends on thermal properties of regolith. If the presence of ice leads to changing in regolith thermal properties, we have a chance to detect this effect. Unfortunately, modern data shows very small amount of hydrogen in lunar regolith (less than 1000 ppm), so we have to seek a mechanism that strongly changes thermal conductivity from even small amount of ice.

Lunar regolith thermal conductivity:

Samples of lunar regolith were supplied by Luna and Apollo missions. These samples show that regolith consists on small grains with irregular shapes. Under a microscope regolith looks like as in Fig.1 [3].

Fig.1.

Lunar regolith exists in a vacuum, so the bulk of thermal conductivity is determined by physical contacts of nearby grains. The area of every contact is extremely small, so a regolith thermal conductivity is very low. Contact area depends on the external pressure, and regolith thermal conductivity increases with depth.

A value of the contact area may be greatly increased even a very small of a linking agent, which can be, for example, a water ice. This effect is well known: thermal conductivity of powder increases rapidly in the event of moisture or freezing.

Lunar ice lifetime:

Due to the fact the lunar ice exists in a vacuum, it appears that ice must be quickly evaporate. However, the low temperature can significantly increase ice lifetime. Article [4] shows that at temperatures around 100 K the evaporation time of ice reaches millions and billions of years.

Method:

Information on the thermal properties of regolith can be extracted from measurements of regolith temperature during lunation at different depths. We plan to use for this purpose microwave radiometer onboard “Luna-Glob” lunar lander.

Microwave penetration into regolith depends on the frequency. Therefore, if we carry out long-term radiometer measurements at different frequencies, we can determine the dependence of regolith temperature on the depth and time. It is possible to derive the regolith thermal conductivity from these data and make judgment about the presence of ice.

The Instrument:

For this experiment we plan to use three-channel microwave radiometer PAT (**P**l**A**anck **T**hermometer). The radiometer is shown in Fig.2.

Fig.2.

PAT operates in three frequency bands: 9, 12, 17 GHz. It sensitivity is about 0.1 K. The radiometer has two small horn antennas. One antenna is directed at the nadir, the other is directed opposite, at the zenith. During the measurement the radiometer determines difference between sky temperature and temperature of the regolith directly under the device. Calibration of the radiometer is made by comparing the temperature of sky and the temperature of microwave internal load.

The radiometer mass is about 600 g, power consumption is about 1 W.

Measurements will be performed within 3 minutes permanently, repeating them every 12 hours. We plan to carry out this periodically measurements for two lunations, and then repeating the measurements after six and ten months.

References: [1] Wang Zhenzhan, Li Yun, Jiang Jingshan (2010). A estimation of the lunar surface temperature, dielectric constant, regolith thickness and Helium-3 content retrieved from brightness temperature by CE-1 microwave sounder . 41-st Lunar and Planetary Science Conference, 1124
[2] Li Yun, Wang ZhenZhan, Jiang JingShan (2010). Simulations on the influence of lunar surface temperature profiles on CE-1 lunar microwave sounder brightness temperature . Science China. Earth Sciences, v.53, No.9, p.1379
[3] E. Robens, A. Dabrowski, et al. (2008). Investigation of surface properties of lunar regolith – Part IV, Annales Universitatis Mariae Curie-Skladowska, Lubin – Plonia. Vol. LXIII, 13, Sectio AA, p.144
[4] F.P. Fanale, J.R. Salvail (1989). Loss of water from Fobos, Geophys. Res. Lett., V. 16, No. 4, p. 287-290

SELECTION OF LANDING SITES FOR THE LUNA-GLOB AND LUNA RESOURCE MISSIONS

A.T. Basilevsky[1], A.M. Abdrakhimov[1], M.A. Ivanov[1], E.N. Guseva[1], J.W. Head[2], J.L. Dickson[2], D. Smith[3], M. Zuber[4], D.B.J. Bussey[5], C.D. Neish[5], *[1]Vernadsky Institute, Moscow, 119991, Russia, [1] Brown University, Providence, RI 02912, USA, [3]Goddard Space Flight Center, Greenbelt, MD 20771, USA, [4]MIT, Cambridge, MA 02139, USA, [5]The John Hopkins University Applied Physics Lab, Laurel, MD 20723. Contact: atbas@geokhi.ru*

Abstract: The talk will describe the results of selection of potential landing sites for the Luna-Glob and Luna-Resource missions to the Moon. Based on analysis of LOLA altimetry data, LROC WAC and NAC images and MiNi RF survey we are mapping now the relatively smooth areas within the southern (70-85^o S, 0-60^o E) and northern (70-85^o N, 20 W-60^o E) polar regions. Figure 1 shows a preliminary version of the map of relatively smooth areas for the southern region.

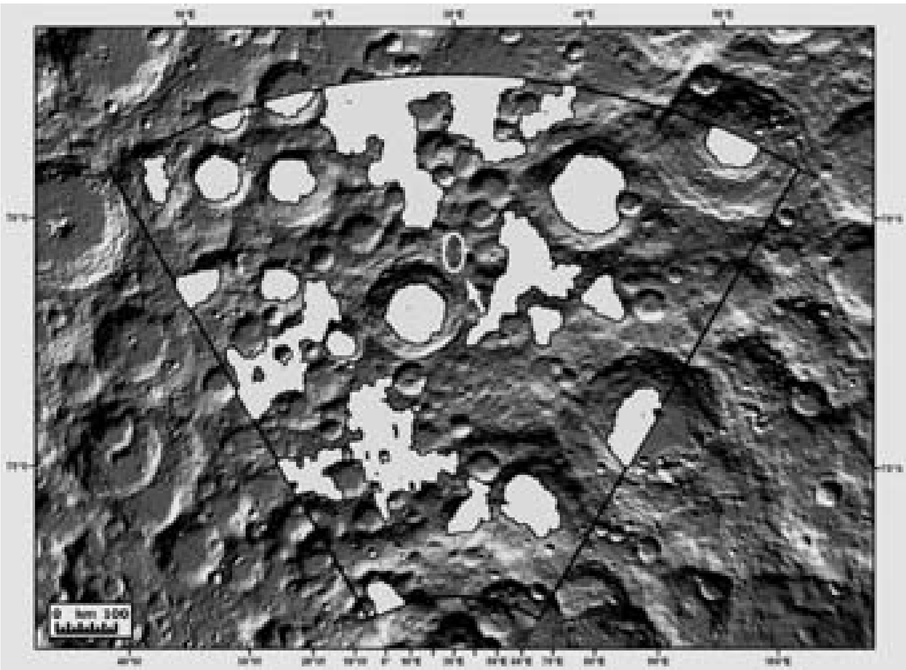

Fig. 1. The map of relatively smooth areas (very light gray) for the southern polar region of the moon to be used for selection of potential landing sites. The size of landing ellipse is 30 x 15 km. Its example is shown in the upper center of the map.

Then jointly with Space Research Institute RAS and Shteinberg Institute of Moscow State University within these smooth areas the subareas with low neutron flux (high hydrogen content) and simultaneously with acceptable visibility from Earth and reasonably good Sun illumination conditions will be selected as potential landing sites.

LANDING SITE FOR LUNA MISSION IN SOUTH POLE – AITKEN BASIN

V.V.Shevchenko[1], S.G.Pugacheva[1], *[1]Sternberg Astronomical Institute, Moscow University, Moscow, 119992, Russia. Contact: vladislav_shevch@mail.ru*

Introduction:

The nature and origin of a unique formation, which is still conditionally called the South Pole – Aitken basin, remain one of the most important problems in recent studies of the Moon. The basin, which apparently belongs to the pre-Imbrian Period, is the largest ring formation not only on the lunar surface but also in the entire Solar System. Not only the basin dimensions on the absolute scale but also the fact that the basin diameter almost coincides with the lunar diameter are of interest. A similar relationship is not observed on other silicate or icy bodies in the Solar System. It was preliminarily estimated that this structure originated about 4 Ga ago (Petro and Pieters, 2002).

Sizes of the South Pole – Aitken basin:

The hypsometric map shown in Fig. 1 makes it possible to study the generalized structure of the SPA basin relief. The basin outer ring is traced based on the system of highlands in the northwestern, northern, northeastern and eastern zones of the ring structure. Fig. 2 presents the generalized topographic profile of the considered hemisphere along the 180o meridian (1). The spherical reference surface is shown by segment (2). The maximal altitude of the outer ring crest in its northern zone is marked by (a). The deepest part of the basin inner depression is denoted by (b). The vertical and horizontal scales of the profile are identical. The basin profile constructed for the first time based on the spherical reference surface demonstrates the real “depth – diameter” ratio for the basin.

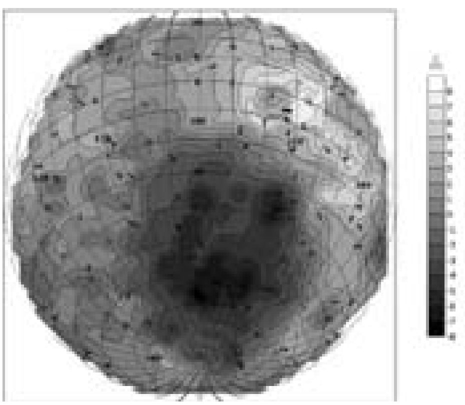

Fig. 1

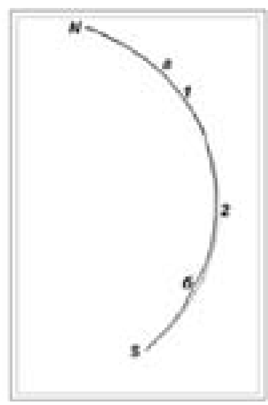

Fig. 2

In spite of the fact that the general height difference in the SPA basin exceeds 16 km, the primary depth penetration of this structure is relatively insignificant, taking into account that the formation diameter is huge. The basin structure has substantially changed as a result of the intense impact transformation of the surface during several billion years; however, this transformation did not delete certain traces of the initial basin formation. Since the inner depression of the SPA basin was not filled with lava, this formation is the only ancient lunar structure for which the primary excavation depth is close to the currently observed depth and does not require special reconstruction.

A uniquely small “depth – diameter” ratio for the SPA basin is confirmed by comparing with similar characteristics of the largest ring formations on the Moon. In (Wieczorek and Phillips, 1999), which became the final work for the cycle of studies of these researchers in this direction, it was indicated that the “depth-diameter” ratio for the SPA basin is an order of magnitude as small as the value determined by extrapolating a similar dependence for ring structures larger than 200 km when comparing with the diameter of the depression that originated during the excavation stage.

A comparison of the considered characteristics on the absolute scale of magnitudes quite definitely indicates that the SPA basin structure is unique, and the “depth-diameter” ratio does not result in the dependence typical of other basins observed on the Moon. Fig. 3 demonstrates the dependence of the reconstructed excavation depth on the diameter of the corresponding depression from the data presented in (Wieczorek and Phillips, 1999) for the formations of 200-500 km in diameter (1). The SPA basin, for which the depression diameter during the excavation stage was taken equal to 2099 km at an excavation depth of 17.6 km, occupies position (2) on the diagram. According to our version, the excavation depth and the diameter of the corresponding depression can be taken equal to 14 and 2575 km, respectively, based on the hypsometric map shown in Fig. 1 and the profiles presented in Fig. 2. In this case the SPA basin will occupy position (3) on the diagram demonstrated in Fig. 3.

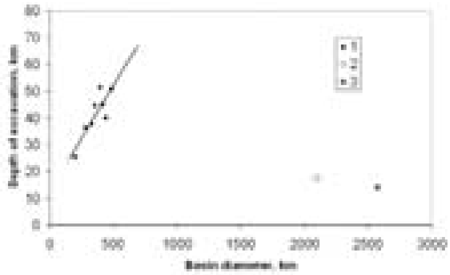

Fig. 3

Fig. 4

In spite of a certain difference in positions (2) and (3) due to differences in the outer ring diameter accepted in either case, it is quite evident that the SPA formation does not correspond to the general tendency for large lunar ring formations with respect to the above parameters and is characterized by an anomalously shallow depth at a considerable diameter.

What is impactor:

As a result of an analysis of the global lunar topography, Byrne (2006) also found that the SPA basin rings differ from the centrally symmetrical configuration and are shifted in the north-south direction. The results reported in work (Shevchenko et al., 2007) comprehensively confirm that such a model of the basin structure is real since a systematic clearly defined shift of the centers of individual rings southeastward from the outer ring center was revealed based on an independent analysis of the hypsometric characteristics and on the specific distribution of iron and thorium (Fig. 4). The shift direction of the secondary ring centers obtained in the work makes an angle of about 75^{o} with the lunar equatorial plane (or the ecliptic plane, which is the same in a first approximation). On the assumption that this shift resulted from an oblique impact of an impactor that produced the SPA basin, it is not improbable that this direction can be interpreted as a trace of the impactor trajectory immediately before the contact with the lunar surface. These assumptions completely agree with the main results obtained by Garrick-Bethell & Zuber (2009). Without going into details of impact process simulation, we can refer to two probable assumptions. A hypothetical impactor followed a trajectory (or orbit) oriented almost normally to the ecliptic plane (1). A decrease in the “depth-diameter” ratio in impact structures results from a decrease in an impactor matter density. So, we can assume that impactor that produced the SPA basin excavation depression had also a low density (2). Proceeding from these two statements, we can make the hypothetical conclusion that the unique features of the SPA basin nature can be caused by the unusual basin formation as a result of the impact of a comet-type body. The predominance of the Kuiper Belt objects or gigantic comet bodies from the Oort Cloud among the main types of impactors during the assumed period of the SPA basin origination is justified in many publications (Schmitt, 2001 etc.).

Conclusions: Lunar robotic missions to the South Pole - Aitken basin are proposed as the best means of addressing major problems concerning the early impact history of the inner Solar System, the nature of very large impact events, and the early differentiation of rocky planets.

References: *Byrne C.J.* The near side megabasin of the Moon // Lunar and Planet. Sci. XXXVII. 2006. #1930.

Garrick-Bethell I., Zuber M.T. Elliptical structure of the lunar South Pole-Aitken basin // Icarus. 2009. V. 204. P. 399–408

Petro N.E., Pieters C.M. Reconstructing the stratigraphy of the ancient South Pole – Aitken basin interior // The Moon beyong 2002: next steps in lunar science and exploration. № 1. 2002. P. 47.

Schmitt H.H. Source and implications of large lunar basin-forming objects // Lunar and Planet. Sci. XXXI. 2001. # 1821.

Shevchenko V.V., Chikmachev V.I., Pugacheva S.G. Structure of the lunar South Pole – Aitken basin // Solar System Res.. 2007. V. 41. № 6. P. 483—499.

Wieczorek M.A., Phillip R.J. Lunar multiring basins and the cratering process // Icarus. 1999. V.139. P. 246-259.

EXPERIMENTAL STUDIES OF LUNAR EXOSPHERE

O.I. Korablev[1], A.A. Petrukovich[1], E. Quémerais[2], V.I. Gnedykh[1], K.I.Marchenkov[1], [1]*Space research Institute (IKI), Moscow,* [2]*LATMOS, Guyancourt, France*

Studies of lunar rarified atmosphere, or exosphere are encouraged by its direct coupling o the surface, possible clues which it could provide for evolutionary processes, and comparisons with exospheres of other airless celestial bodies. First definitely revealed by Apollo investigations followed by remarkable discovery of sodium and potassium the atmosphere has been then mostly studied by ground-based and HST observations in the UV-visible spectral ranges. Dedicated observations from the orbit around the moon are only planned within the frame of NASA Lunar Atmosphere And Dust Environment Explorer (LADEE) orbiter to be launched in 2012. In the meanwhile, in the frame of Bepi Colombo ESA mission to Mercury, PHEBUS UV spectrometer is devoted to the characterization of Mercury's exosphere composition and dynamics and surface–exosphere connections. PHEBUS (Probing of Hermean exosphere by ultraviolet spectroscopy) is a double spectrometer for the Extreme Ultraviolet range (55–155 nm) and the Far Ultraviolet range (145–315nm) This French-led instrument is implemented in a cooperative scheme involving Japan (detectors), Russia (scanner) and Italy (ground calibration). On board of Russian Luna-Globe orbiter LEVUS instrument is an adapted version of PHEBUS spare model addressing the following main scientific objectives relative to Moon's exosphere: determination of its composition and the vertical structure; characterization of the exospheric dynamics: day to night circulation, transport between regions; study of surface release processes; identification and characterization of the sources of exospheric constituents; detection and characterization of ionized species and their relation with the neutral atmosphere; space and time monitoring of exosphere/magnetosphere exchange and transport processes; study and quantification of escape, global scale source/sink balance and geochemical cycles.

We will discuss the methods of characterization of the lunar exosphere with an emphasis on neutral component and will describe the LEVUS experiment in somewhat more detail.

FARSIDE EXPLORER: UNIQUE SCIENCE FROM A MISSION TO THE FAR SIDE OF THE MOON.

M. A. Wieczorek[1], R. F. Garcia[2], D. Mimoun[3], [1]*Institut de Physique du Globe de Paris, France;* [2]*Université de Toulouse, UPS-OMP, IRAP, Toulouse, France;* [3]*Université de Toulouse, ISAE, France. Contact: wieczor@ipgp.fr*

Introduction: The farside hemisphere of the Moon is a unique place in the Solar System for a large range of scientific investigations. Being shielded from terrestrial radio-frequency interference, the farside of the Moon is the most radio-quiet environment in near-Earth space. The farside hemisphere faithfully records the primary differentiation of the Moon and hosts the largest recognized impact basin in the Solar System. From the Earth-Moon L2 Lagrange point, the farside hemisphere of the Moon is ideal for continuous monitoring of meteoroid impacts with the lunar surface.

Farside Explorer aims to place two robotic landers on the farside hemisphere of the Moon and to put an instrumented relay satellite into a halo orbit about the Earth-Moon L2 Lagrange point. During the course of its 4-year nominal mission, Farside Explorer would conduct three broad scientific investigations.

First, from the vantage point of the lunar surface, **Farside Explorer would make the first extensive radio astronomy measurements in the most radio-quiet region of near-Earth space**. It would perform the first sky mapping at low frequencies and make pathfinder measurements of the red-shifted neutral hydrogen line that originates from before the formation of the first stars. Low-frequency radio bursts from our Sun would be quantified, as would auroral emissions from the giant planets in our Solar System, pulsars, and the interaction of ultra-high energy cosmic rays with the lunar surface. The Farside Explorer radio astronomy experiment would be a pathfinder technology demonstration for a future radio array on the farside lunar surface.

Second, from the same landers, **Farside Explorer would make precise geophysical measurements of the Moon's interior and measure the composition of its surface.** From seismological, heat flow, and electromagnetic sounding measurements, these data would determine the bulk composition of the Moon, the thickness of its crust, the size and composition of its core, and the temperature profile of its interior. The surface geochemical data would provide critical ground truth measurements for the interpretation of orbital remote-sensing data sets, and would help decipher the origin of two of the Moon's most prominent geologic provinces: the giant South Pole-Aitken basin and the primordial farside highlands.

Third, from the vantage point of the relay satellite, **Farside Explorer would quantify near-Earth impact hazards by continuously monitoring the farside of the Moon for meteoroid impacts.** Unspoiled by Earthshine and an intervening atmosphere, this experiment would measure (by the detection of impact flashes) the Earth-Moon impact flux, the size-frequency distribution of impactors in near-Earth space, and spatial and temporal variations in the lunar impact rate during the lunar night. The measured impact times and locations would be used as known seismic sources for the seismology experiment.

Farside Explorer is an innovative mission that involves the development of soft-landing capabilities on airless bodies and that benefits from existing state-of-the-art geophysical and astronomical instrumentation in Europe. The scientific objectives of Farside Explorer are supported jointly by the radio astronomy and lunar science communities, and directly address all four of the top-level scientific objectives of ESA's Cosmic Vision program. Farside Explorer would participate in the internationally renewed exploration of Earth's nearest celestial neighbor.

Relationship of Farside Explorer science themes to the lander and orbiter payload. Lunar science and impact hazard objectives are addressed by synergistic measurements from the surface and orbit.

SOUNDING OF THE INTERIOR STRUCTURE OF GALILEAN SATELLITE IO USING THE PARAMETERS OF THE THEORY OF FIGURE AND GRAVITATIONAL FIELD IN THE SECOND APPROXIMATION.

V. N. Zharkov, T.V. Gudkova, *Schmidt Institute of Physics of the Earth, B.Gruzinskaya 10, Moscow 123995, Russia. Contact: zharkov@ifz.ru*

Introduction: For the theory of Io's figure to be consistent with currently available observational data, it must include effects of the second order in smallness. In the first approximation, the ratio of the moments J_2 and C_{22}: J_2=10/3C_{22}. The parameters of the gravitational field for the Galilean satellites determined in the Galileo space mission have shown that this relation holds with a high accuracy. If the Galilean satellites of Jupiter are in a state close to hydrostatic equilibrium, then data on their figures and gravitational fields allow us to impose a constraint on the density distribution in the interiors of these bodies and, thereby, to make progress in modeling their internal structure [1]. To show the effects of the second approximation, two three-layer trial models of Io are used [2]. They differ by the size and density of the core Io1 (the core density ρ_c=5150 kg/m^3: Fe-FeS eutectic) and Io3 (ρ_c=4600 kg/m^3: FeS with an admixture of nickel), while having the same thickness and density of the crust (50-km crust , ρ_{crust}=2700 kg/m^3), and the mantle density difference is only 20 kg/m^3.

Figure theory: The equilibrium figure of the satellite is an equipotential surface of the sum of three potentials: $U = W_t + Q + V = const$, the tidal potencial $W_t = \frac{GM}{R}\sum_{n=2}^{\infty}\left(\frac{r}{R}\right)^n P_n(\cos Z)$, the centrifugal potencial

$Q = \frac{\omega^2 r^2}{3}\left[1 - P_2(\cos\theta)\right] = \frac{GM}{3R}\left(\frac{r}{R}\right)^2\left[1 - P_2(\cos\theta)\right]$ (the angular rotation velocity of the satellite ω is equal to the angular velocity of a synchronous satellite around the planet, and according to Kepler's third law, ω^2=GM/R^3 for synchronous satellites), and the potencial from mass distribution inside the satellite $V(r,u,\varphi)$.

In the figure theory we pass from the actual radius κ to the effective radius s defined as the radius of a sphere of equivalent volume (r,u,φ)à(s,u,φ):

$$r = s\left[1 + \sum_{n=0}^{\infty} s_{2n}P_{2n}(t)\right] = s(1 + s_0 + s_2P_2(t) + s_{22}P_2^2(t)\cos 2\phi + s_{31}P_3^1(t)\cos\phi +$$

$$s_{33}P_3^3(t)\cos 3\phi + s_4P_4(t) + s_{42}P_4^2(t)\cos 2\phi + s_{44}P_4^2(t)\cos 4\phi)$$

The figure theory is constructed by expanding the expressions for the potencials in powers of a small parameter $\alpha = 3\pi / G\rho_0\tau^2$, where ρ_0, τ are the average density and rotation period of Io, respectively.

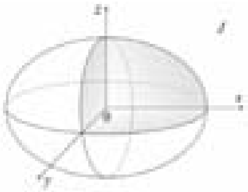

Fig. 1. To zeroth approximation the equilibrium figure of a body has the form of a sphere with the mean radius s_1. In the first approximation the sphere transforms to a triaxial ellipsoid (normal figure) with the equatorial semiaxes *a*, *b* and the polar semiaxis *c*. In the second approximation equilibrium figure is deviated from a triaxial ellipsoid.

We have estimated the contribution from the effects of the second approximation to the lengths of the semiaxes *a*, *b*, and *c* for the equilibrium figure of Io: 55, 9, and -4 m, respectively.

Dualism in the figure theory: The values of the figure functions at *x* = 1 are called the figure parameters. Figure parameters specify the shape of the figure of an equilibrium satellite. The values s_{nm}(s) at the surface of the body determine the J_n and C_{nm} coefficients (gravitational moments) in the expansion of the external gravity field. If the satellite is in hydrostatic equilibrium, then the coefficients in the expansion of its external gravitational field in terms of spherical functions can be determined by measuring its figure parameters. The reverse is also true.

Results: To calculate the figure parameters s_4, s_{42} and s_{44} and consequently gravitational moments J_4, C_{42} and C_{44} , three integro-differential equations [3] for trial model density distributions were first solved numerically and, as a result, all second order corrections were obtained. Figure functions $\overline{s}_2(s)$, $\overline{s}_{22}(s)$ and $\overline{s}_{31}(s)$, $\overline{s}_{33}(s)$ are proportional to the Love functions $h_2(s)$ and $h_3(s)$, respectively. The figure 2 shows that the outer regions of Io's interiors influence more the Love number $h_3(s)$, then $h_2(s)$. It is seen more clearly in Fig. 3. If we write the formulas for the gravitational moments in the form $J_n = \int_0^1 \delta(x) d\left[x^{n+3} f_n(x)\right] = \int_0^1 \chi_n dx$.

The zeroth gravitational moment J_0 is the mass of the planet, which is unity in dimensionless variables. The functions $\chi_n(x)/J_n$ (n= 0, 2, 4) for a trial model of Io are plotted in Fig. 3. These functions have a simple physical meaning: they are the relative densities of the gravitational moment J_n, and the quantity $(\chi_n(x)/J_n)dx$ gives the relative contribution from the region of the planetary body in the interval $[x, x+\Delta x]$ to J_n. The graphs of the functions $\chi_n(x)/J_n$ show the contributions of various zones in the planetary interior. Thus, it is evident from Fig.3, that the mantle of Io contributes significantly to the values of the gravitational moments J_2 and J_4, whereas the region of the core is of less importance. That is why the gravitational moments for Io 1 and Io3 models, calculated in the second approximation, differ in the third decimal digit. These models have the same crust thickness and density, while the mantle density for the Io1 model is being only 20 kg/m³ higher than for the Io3 model.

An important parameter of the silicate reservoir is the magnesium number Mg#, the ratio of the number of magnesium atoms to the sum of the numbers of magnesium and iron atoms (occasionally, this ratio multiplied by 100 is used). Theoretically, such an important parameter as the mantle silicate iron content (Fe#=1-Mg#) in the model Io3 is equal to 0.265. This value is a factor of two and half higher than the value for mantle silicates in the Earth. The high iron content in the Io3 model leads to high mantle density. Therefore, one can assume, that if the accuracy of the gravity field determination for Io is significantly improved, the effects of the second approximation will put restrictions on the value of average mantle density of Io.

Note how strongly the parameters depend on small variations in the mantle density of the satellite at constant crust thickness and density. To quantitatively estimate this effect, let us form two logarithmic derivatives based on the Io models: $\delta k_2/ k_2$=1.324 $\delta\rho_m/ \rho_m$, $\delta m_c/m_c$=-12.23 $\delta\rho_m/\rho_m$, where ρ_m is the density of the mantle, and / m_c is the core mass. We see that small variations in the number k_2 change greatly the core mass.

Conclusion: The analysis of the effects of the second approximation on the figure parameters and gravitational moments of the satellite Io has been done. The considered models mainly differ in the core density and the core size. It turns out that the account of the second order values decrease gravitational moments J_2 and C_{22} by 2 units in the third decimal digit. The effects of third and forth harmonics are determined mostly by outer layers of Io. To reveal the difference in density distribution, the gravitational moments J_4, C_{42} and C_{44} should be determined to accuracy with three or four decimal digits. Then the mantle density could be known with good precision.

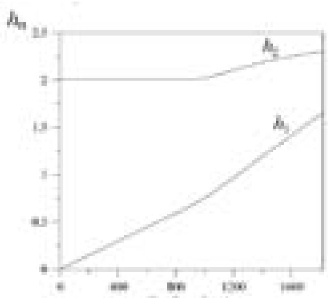

Fig. 2. Love numbers h_2 and h_3 along the planetary radius.

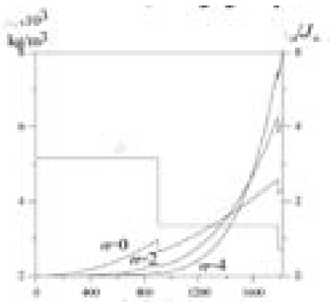

Fig.3. Functions of the relative density of the gravitational moments $\chi_n(s)/J_n$ (n=0, 2,4) and density distribution r(s) for a trial model of Io.

Acknowledgements: This research was made possible partly by Grant No. 09-02-00128 from the Russian Fund for Fundamental Research.

References: [1] Zharkov, V.N. A theory of the equilibrium figure and gravitational field of the Galilean satellite Io: the second approximation, Astronomy lettes, 30, 496-507. [2] Zharkov, V.N., Karamursov, B.S., Models, figures and gravitational moments of Jupiter's satellites Io and Europa. Astronomy Letters. 32. 495-505,2006. [3]Zharkov,V.N.,Gudkova,T.V.Models, figures, and gravitational moments of Jupiter's satellite Io:effects of second approximation, PSS, 58,1381-1390, 2010.

MODEL OF SPATIAL DISTRIBUTION OF RELATIVISTIC ELECTRON FLUXES IN VICINITY OF JUPITER'S MOON EUROPA

M. V. Podzolko[1], I. V. Getselev[1], Yu. I. Gubar[1], I. S. Veselovsky[1, 2], *[1]Skobeltsyn Institute of Nuclear Physics, Lomonosov Moscow State University, Moscow 119991, Russia; [2]Space Research Institute (IKI), Russian Academy of Sciences, Moscow 117997, Russia. Contact: 404@newmail.ru*

Currently projects of sending research space vehicles to Jupiter's moon Europa in the next decade are being developed. Such mission will be connected with high radiation risks, because Europa's orbit is located inside the region of highly-intensive energetic particle fluxes of powerful Jupiter's radiation belts. In particular the main radiation impact for the spacecraft electronic components behind the shielding of >1 g/cm^2 Al will originate from the fluxes of relativistic electrons with energies up to tens of MeV (Fig. 1).

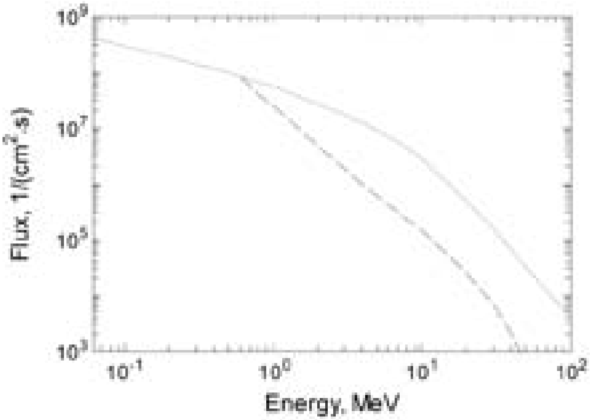

Fig. 1. Integral fluxes of electrons (solid line) and protons (dashed line) of Jupiter's radiation belts in Europa's orbit.

However, near Europa part of the flux will be shaded by the moon. Moreover, this reduction of the fluxes is sufficiently nonuniform and differs for various particle energies and pitch-angles and for the surface and the low-altitude orbit. This is caused by several factors:

– relation between particles longitudinal drift speed relative to Europa and their bounce-period;

– Larmor motion of the particles near the surface;

– difference of Europa's orbital plane from Jupiter's geomagnetic equator plane;

– certain disturbance of magnetic and electric fields in vicinity of Europa;

– interaction of particles with the moon's tenuous atmosphere;

– diffusion of particles;

– and the last but not least, thickness and configuration of spacecraft's shielding.

These factors were taken as the input parameters for the model of spatial distribution of relativistic electron fluxes near Europa and on its surface, which is currently being developed by the authors. We plan to consecutively "switch on" these factors, complicating the model step-by-step and estimating qualitative and quantitative contribution of each of them.

Distributions of fluxes of relativistic electrons of various energies on Europa's surface and at 100 km altitude have been computed taking into account several of the mentioned above factors (Fig. 2, 3). Comparison with the results received by other researches has been made.

The results of our modeling can be used for choosing the optimal landing site and the low-altitude spacecraft orbit around Europa.

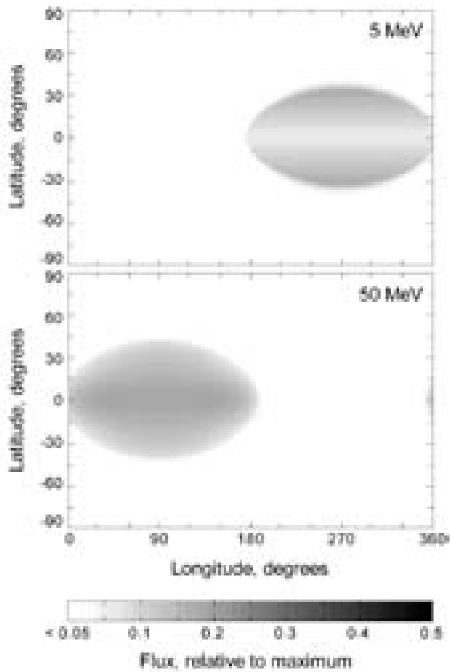

Fig. 2. Distribution of differential fluxes of electrons with energies 5 and 50 MeV on Europa's surface taking into account their guiding center motion in Jupiter's magnetosphere and Larmor motion near Europa.

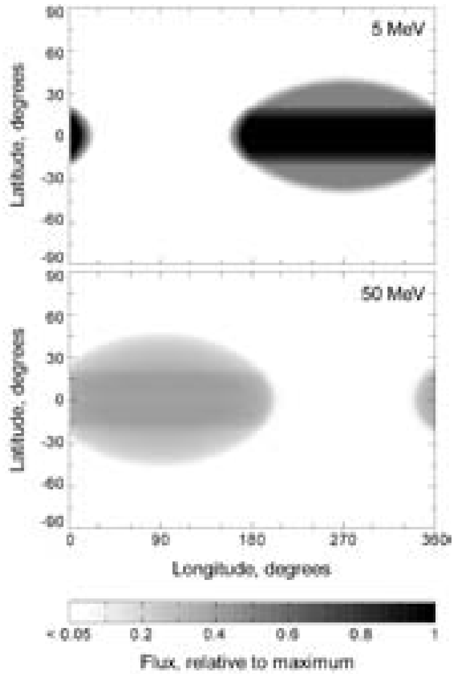

Fig. 3. Distribution of differential fluxes of electrons with energies 5 and 50 MeV at 100 km altitude taking into account their guiding center motion in Jupiter's magnetosphere and Larmor motion near Europa.

References: Podzolko M. V., Getselev I. V., Gubar Yu. I., Veselovsky I. S., Radiation conditions of a mission to Jupiter and Europa, Solar System Res, 43 (2), 116–120, 2009.
Podzolko M. V., Getselev I. V., Gubar Yu. I., Veselovsky I. S., Charged particles on the Earth–Jupiter–Europa spacecraft trajectory, Adv Space Res, 48 (4), 651–660, 2011.

CALLISTO – MAGNETOSPHERE INTERACTIONS: HYBRID SIMULATIONS AND COMPARISON WITH THE MOON

S. B. Barabash, M. Holmström, *Swedish Institute of Space Physics, Box 812, 98128, Kiruna, Sweden. Contact: stas@irf.se*

Abstract: The simulations of the Callisto–magnetosphere interaction is important (1) to investigate the fundamental interaction of a non-magnetized, airless object with a sub-Alfvenic and sub-sonic plasma flow, (2) to understand contributions from the plasma currents to the magnetic field perturbations recorded by Galileo and related to the subsurface ocean, (3) to model the plasma environment at this moon in preparation for coming Jupiter system missions. The airless non-magnetic Callisto is just a factor of 1.4 larger than the Moon. The typical gyroradius is a factor of 0.2 – 1 of the Callisto radius. The hot plasma magnetospheric electrons are magnetized. The Alvfenic Max number is in the range 0.4 – 4 (for the Moon 5 – 15) and the ion sonic number (cold plasma with a beta around the unit) is around 3 (for the Moon 6.0). Therefore, global hybrid models (particle ions, fluid mass-less electrons) simulating the Moon–solar wind interaction may be applied to investigate the Callisto–magnetospheric interactions when the plasma flow super Alfvenic (Callisto above the magnetic equator) provided the near–Earth solar wind parameters are replaced by the ones corresponding to the Jovian conditions. We conducted runs of such a model assuming the “solar wind” ions have the mass/charge equal to 16, the temperature 45 eV, the density 0.5 /cc, and the magnetic field equals to the magnetospheric field. In these initial simulations we assumed the obstacle (Callisto) to be fully non-conductive to simplify the boundary conditions. The first runs demonstrate that the model used is capable of handling satisfactory the plasma conditions around this satellite. The interaction patterns remind those obtained in the lunar simulations. We also discus the implication of the latest findings related to the Moon – solar wind interaction to the Callisto – magnetosphere interactions, namely,the reflection and neutralization of the impinging ions by the obstacle’s surface.

SURFACE MATERIALS ON EUROPA: CONSIDERATIONS FOR LANDING SITE SELECTION.

J. B. Dalton[1], L. M. Prockter[2], M. A. Ivanov[3], [1]*Jet Propulsion Laboratory, California Institute of Technology, MS 183-301, 4800 Oak Grove Drive, Pasadena CA 91109, USA;* [2]*Applied Physics Laboratory, Johns Hopkins University, 11100 Johns Hopkins Road, Laurel, MD 20723, USA;* [3]*Laboratory of Comparative Planetology, V. I. Vernadsky Institute of Geochemistry and Analytical Chemistry, RAS, Russia. Contact: dalton@jpl.nasa.gov*

Introduction:

The possibility of a landed mission to Europa presents a number of important scientific opportunities and technological challenges. The unique environment at the surface of Europa must be taken into account in order to maximize the potential science return and engineering success. The present surface has resulted from the interplay of both endogenic and exogenic processes, including aqueous geochemistry, transport phenomena, magnetospheric charged particle impacts, and radiolytic chemistry. Mission design must consider the orbital dynamics and magnetospheric influences both for safety of the spacecraft and for meaningful scientific inquiry (Ivanov *et al*. 2011). Knowledge of the surface topography and composition is essential for mission safety and selection of scientifically interesting landing sites.

Orbital Considerations:

While Europa orbits Jupiter once every ~3.6 days, Jupiter has a rotational period of slightly less than ten hours. Consequently the trailing hemisphere of Europa is bathed in charged particles trapped in the co-rotating Jovian magnetic field. These include electrons, protons, and ions such as sodium, potassium, oxygen and sulfur (Paranicas *et al.* 2009). Ions are implanted into the surface ice, and the deposited energy drives radiolytic chemistry. The total radiation dose peaks near the trailing hemisphere apex at 270° W longitude. Although equatorial locations on the antijovian hemisphere are desirable from the standpoint of spacecraft trajectory design, the leading hemisphere (0-180° W) presents a reduced risk to the spacecraft and instruments from radiation as well as the opportunity to sample more pristine, less processed endogenic material. The quadrant where the leading and antijovian hemispheres intersect (90-180° W) thus represents a balance between these considerations.

Morphological Considerations:

The highest-resolution imagery from the Galileo mission tends to be from the trailing hemisphere. This selection effect arises from characteristics of trajectory design. However there is sufficient imagery to evaluate a number of sites exposed to lower radiation levels than near the trailing apex. Locations of smooth surface topography represent the lowest risk to the spacecraft, and in some cases may be associated with cryovolcanic activity that has brought materials to the surface from the interior. The morphology and gentle topography (Schenk, 2009) of the grey dilational “pull-apart” bands place them among the most promising candidates.

Compositional Considerations:

An important goal of a Europa mission is to investigate the composition of the putative ocean. Materials deposited at the surface provide a window to this interior composition. Known surface materials include water, carbon dioxide and sulfur dioxide ices, hydrated sulfuric acid, and a number of magnesium and sodium sulfate hydrates and brines (Dalton, 2007; Shirley *et al.* 2010). Estimates of surface composition derived from remote sensing spectroscopy allow evaluation of sites that may contain endogenically-derived materials. Access to the near subsurface may sample organic or other materials that have not been as strongly processed by radiation; selecting a site of low total radiation dose can also serve to limit such influences.

Conclusion:

Further assessment of potential landing sites must take into account numerous orbital, morphological and compositional considerations. Risk reduction and scientific imperative lead to significant constraints on landing site selection. Current knowledge of geomorphology, composition and the space environment suggest that endogenically-emplaced surface deposits in equatorial portions of the antijovian quadrant of the leading hemisphere may provide a balance between safety and high scientific value. Similar constraints will also apply to Ganymede, where the possibility of ocean-derived surface material in a reduced radiation environment represents another target of high scientific value.

2MS³-GM-04

References: Ivanov, M.A., Prockter, L.M., and Dalton, B., Landforms of Europa and selection of landing sites, Adv. Space Res. 48:661-677, 2011.
Dalton, J.B., Linear mixture modeling of Europa’s non-ice material based upon cryogenic laboratory spectroscopy, *GRL* **34**:L21205, 2007
Paranicas, C., J.F. Cooper, H.B. Garrett, R.E. Johnson, and S.J. Sturner, Europa’s radiation environment and its effects on surface, in Pappalardo, R.T., W.B. McKinnon, and K. Khurana, Eds., *Europa*, U. of Arizona, 529-544, 2009.
Schenk, P.M., Slope characteristics of Europa: constraints for landers and radar sounding, *GRL* **36**:L15204, 2009.
Shirley, J.H., J.B. Dalton, L.M. Prockter, and L.W. Kamp, Europa’s ridged plains and smooth low albedo plains: Dis- tinctive compositions and gradients at the leading side-trailing side boundary, *Icarus* **210**:358-384, 2010.

THE OCEANS OF EUROPA AND GANYMEDE. AQUEOUS SOLUTIONS UNDER PRESSURE AS POTENTIAL HABITATS.

O. Prieto-Ballesteros[1], V. Muñoz-Iglesias[1], and L. Jimenez-Bonales[1, 2]. *[1]Centro de Astrobiología-INTA-CSIC, Ctra. Ajalvir km. 4, Spain. 2Departamento de Química Física I, Facultad de Química. Universidad Complutense de Madrid, Spain. Contact: prietobo@cab.inta-csic.es*

Europa and Ganymede are both satellites of Jupiter which may harbor global liquid water reservoirs under their icy crusts. It is assumed that both oceans are salt-rich, because there are evidences that 1) salt materials at the surface have endogenic origin, and 2) the detected magnetic signature may be related to the internal dynamics of this layer. Geophysical models show that Europa's ocean may be at some tens of kilometers to the surface and in contact to the rocky mantle, while the Ganymede's is deeper than 150 km and sandwiched between different phases of water ice [1]. These differences in the internal structure determine the physical-chemical conditions at the ocean and their habitability.

Direct access to study the oceans of these moons is not feasible in the near future. However, the analysis of the salty endogenic materials at the surface and its cryomagmatic evolution may give some clues about the environmental characteristics of their liquid reservoir sources. At this moment, rough remote sensing data about the chemical composition and the distribution of these material are available. The future mission to the Jupiter system, which is being planned by ESA (JUICE) [2], will be a closer approach to the surfaces from the orbits of the moons. Besides, new lander missions are expected for the next decades, which will contribute to reveal more about the oceans and their habitability by detailed in situ measurements of the surface and the sub-surface.

Meanwhile, laboratory simulations may help to understand how endogenic materials at the surface evolves from the source to the current state as temperature and pressure decreases. We are experimentally studying the geochemical equilibria of some salty and acid solutions under pressure in order to characterize some parameters concerning the habitability of the original aqueous solutions. There are some theoretical models about the equilibria of these solutions at low temperature and different pressures that show how the precipitation sequences of minerals at subzero temperatures should be [3, 4, 5]. Gases like CO_2 are included in our experiments. Gas dissolution and fractional crystallization in aqueous salt-rich cryomagmas are being simulated inside a high pressure chamber. Changes in the physical-chemical parameters of the cryomagma and crystallization of minerals are followed "in situ" by Raman spectroscopy. As an example: the salting-out process has been detected and recorded during the kinetic studies by spectroscopy of the cryomagma evolution. Implications of this result to Europa and Ganymede activity are the fractional crystallization of the original aqueous solutions and the mobilization of more buoyant cryomagmas [6].

Acknowledgements: This work is supported by MALTA-Consolider (CSD2007-00045) and QUIMAPRES (S2009/PPQ-1551) projects.

References: [1] Showman and Malhotra (1999). Science 286, 77-84
[2] Dougherty M. K. et al. (2011) EPSC-DPS2011-1343
[3]Zolotov M.Y. and Shock E. L. (2001). J. Geophys. Res. 106, 332815-32827
[4]Marion, G. M. (2002). Geochim. And Cosmochim. Acta 66, 2499-2516
[5]Marion G. M. et al. (2005). Geochim and Cosmochim Acta 69, 259-274
[6] Muñoz-Iglesias V. et al. (in press). Spectroscopy Letters

THE ROLE OF THE MAGNETODISK IN THE JUPITER'S MAGNETOSPHERE

Igor I. Alexeev, *Scobeltsyn Institute of Nuclear Physics, Lomonosov Moscow State University, Leninskie Gory, 119992, Moscow, Russia*

In the middle and outer Jovian magnetosphere the equatorial plasma disk serve as main source of the magnetospheric magnetic field. As demonstrated by Galileo magnetometer data at the radial distances of 45 - 27 R_J, B_r from the equatorial current sheet far exceeds the B_r from Jupiter's internal field (*Khurana*, 2001). The azimuthal current also considerably depresses the north-south component of the field. To make plasma disk corotate with the planet Alphenic current system generated in the Jupiter magnetosphere. This current system included field-alinged current flowing out of the Jovian ionosphere to equatorial plane at the inner edge of the plasma disk, radial outflowing current in the equatorial plane, the return field aligned current at the outer edge of the current disk, and closure longitudinal ionospheric Pedersen current. As estimated by *Khurana*, 2001 the total strength of the Alphenic currents can be about 100 MA. The magnetic moment of the azimuthal current in the plasma disk is more than 3 times bigger compare to the planetary dipole. As results the dipole field at subsolar magnetopause is about 10% from measured field and the size of the Jovian magnetosphere about two times bigger than purely dipole magnetosphere. Detail discussion of the influence of the magnetodisk on the cold magnetospheric plasma acceleration and the Joule heating of the upper Jovian atmosphere are presented. These processes play key role to made Jupiter mostly bright radio sourse in the Solar System and transfer of the energy balance in the Jupiter magnetosphere such way that the Jupiter surface temperature is more higher than give the just Solar irradiance absorption.

2MS³-GM-poster

EFFECTS OF SECOND APPROXIMATION OF THE FIGURE THEORY FOR JUPITER'S SATELLITE IO.

V. N. Zharkov, T.V. Gudkova, *Schmidt Institute of Physics of the Earth, B.Gruzinskaya 10, Moscow 123995, Russia. Contact: zharkov@ifz.ru*

Introduction: All Galilean satellites are in synchronous rotation; their orbits are nearly circular and lie in the equatorial plane of Jupiter. Io is the large satellite closest to Jupiter. Therefore, the influence of Jupiter's tidal potential on the equilibrium figure and gravitational field of Io is appreciably stronger than it is on the remaining large satellites. For the theory of Io's figure to be consistent with currently available observational data, it must include effects of the second order in smallness. In the first approximation, the ratio of the moments J_2 and C_{22}: J_2=10/3C_{22}. The parameters of the gravitational field for the Galilean satellites determined in the Galileo space mission have shown that relation holds with a high accuracy. Consequently, these bodies have equilibrium figures. For Io, J_2 and C_{22} are given to the fourth decimal place. This main relation that is used to judge whether Io has an equilibrium figure was derived in the first approximation. Therefore, the following question arises: With what accuracy is this theoretical ratio valid? To answer this question, we must construct a theory in the next (second) approximation by including the terms of order α^2 (α is the small parameter of theory of figure, defined as $\alpha=3\pi/(G\rho_0\tau^2)$, where ρ_0 and τ are the average density and rotation period of Io, respectively. This is the main goal of our analysis.

Results: The method for solving the equations of the figure theory is described in detail in [1]. A computer code was developed to calculate figures functions $s_4(s)$, $s_{42}(s)$ and $s_{44}(s)$ for the Io models. Tables 1 and 2 give results of numerical solutions of figure equations for the Io1 and Io3 models [2] at s=s_1 (for visual perception tables list the normalized figure parameters $\overline{s}_2$, $\overline{s}_{22}$, $\overline{s}_{31}$, $\overline{s}_{33}$, $\overline{s}_4$, $\overline{s}_{42}$ and $\overline{s}_{44}$ and gravitational moments $\overline{J}_2$, $\overline{C}_{22}$, $\overline{C}_{31}$, $\overline{C}_{33}$, $\overline{J}_4$, $\overline{C}_{42}$, and $\overline{C}_{44}$). As seen from Table 1, including the second order terms in $\overline{J}_2$ and $\overline{C}_{22}$ decreases the values by two units in the third decimal digit. To make clear insight into the problem, we plot figure functions $\overline{s}_2(s)$, $\overline{s}_{22}(s)$, (Fig. 1a) and $\overline{s}_4(s)$, $\overline{s}_{42}(s)$, $\overline{s}_{44}(s)$ (Fig. 1b).

Figure functions $\overline{s}_2(s)$, $\overline{s}_{22}(s)$ and $\overline{s}_{31}(s)$, $\overline{s}_{33}(s)$ are proportional to the Love function $h_2(s)$ and $h_3(s)$, respectively. The outer regions of Io's interiors influence more the Love number $h_3(s)$, then $h_2(s)$. The same fact is seen, when comparing the figure function $\overline{s}_2(s)$, $\overline{s}_{22}(s)$ (Fig. 1a) and figure functions $\overline{s}_4(s)$, $\overline{s}_{42}(s)$, $\overline{s}_{44}(s)$ (Fig. 1b). In that way, functions of the second approximation $\overline{s}_4(s)$, $\overline{s}_{42}(s)$, $\overline{s}_{44}(s)$ sound the density distribution of the external zones to a greater extent than functions of the first approximation $\overline{s}_2(s)$, $\overline{s}_{22}(s)$.

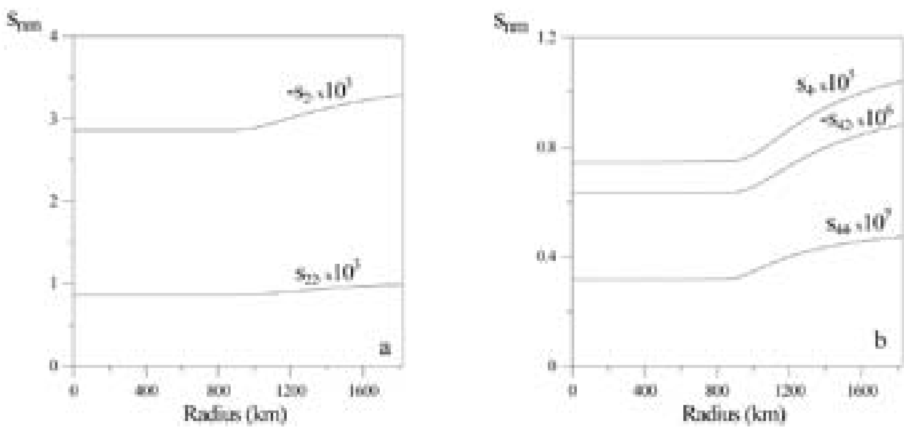

Fig. 1. The distribution of the parameters of the equilibrium figure of Io $s_2(s)$, $s_{22}(s)$ (a) and $s_4(s)$, $s_{42}(s)$, $s_{44}(s)$ (b) along the planetary radius. The functions $s_2(s)$, $s_{22}(s)$ and $s_4(s)$, $s_{42}(s)$, $s_{44}(s)$ are not normalized.

Parameters	Model values
$-\overline{s}_2$, 10^{-3}	1.4709
$\overline{s}_{22}$, 10^{-3}	1.5287
$-\overline{J}_2$, 10^{-6}	832.25
$\overline{C}_{22}$, 10^{-6}	864.90
$-\Delta\overline{s}_2$, 10^{-3}	0.0017
$\Delta\overline{s}_{22}$, 10^{-3}	0.0022
$-\Delta\overline{J}_2$, 10^{-6}	1.6993
$\Delta\overline{C}_{22}$, 10^{-6}	2.2378

Table 1. Normalized figure parameters $\overline{s}_n$ and gravitational coefficients $\overline{J}_n$ and $\overline{C}_{nm}$ (the first order) and the second order corrections for the model Io1.

Parameters	Io1	Io2
$-\overline{s}_{31}$, 10^{-6}	2.8404	2.8334
$\overline{s}_{33}$, 10^{-6}	3.6670	3.6579
$\overline{s}_4$, 10^{-6}	3.4666	3.4498
$-\overline{s}_{42}$, 10^{-6}	3.9415	3.9223
$\overline{s}_{44}$, 10^{-6}	2.2472	2.2190
$-\overline{C}_{31}$, 10^{-6}	1.1266	1.1196
$\overline{C}_{33}$, 10^{-6}	1.4545	1.4454
$-\overline{J}_4$, 10^{-6}	3.0926	3.0952
$-\overline{C}_{42}$, 10^{-6}	3.5163	3.5014
$\overline{C}_{44}$, 10^{-6}	1.9096	1.9008

Table 2. Normalized figure parameters $\overline{s}_n$ and gravitational coefficients $\overline{J}_n$ and $\overline{C}_{nm}$ (the second order) for the models Io1 and Io3.

Conclusion: The effects of the second approximation on the figure parameters and gravitational moments of the satellite Io have been considered. It turns out that the account of the second order values decrease gravitational moments J_2 and C_{22} by 2 units in the third decimal digit. To calculate the figure parameters s_4, s_{42} and s_{44} and consequently gravitational moments J_4, C_{42} and C_{44}, three integro-differential equations [3] for trial model density distributions were first solved numerically and, as a result, all second order corrections were obtained.

Acknowledgements: This research was made possible partly by Grant No. 09-02-00128 from the Russian Fund for Fundamental Research.

References: [1] Zharkov,V.N.,Trubitsyn,V.P.,Physics of Planetary interiors.Pachart Publishing House, Tucson, 1978. [2] Zharkov, V.N., Karamursov, B.S., Models, figures and gravitational moments of Jupiter's satellites Io and Europa. Astronomy Letters. 32. 495-505,2006. [3]Zharkov, V.N.,Gudkova,T.V.Models, figures, and gravitational moments of Jupiter's satellite Io:effects of second approximation, PSS, 58,1381-1390, 2010.

MODELS, FIGURES, AND GRAVITATIONAL MOMENTS OF JUPITER'S SATELLITE EUROPA. EFFECTS OF SECOND APPROXIMATION.

V. N. Zharkov, T.V. Gudkova, *Schmidt Institute of Physics of the Earth, B.Gruzinskaya 10, Moscow 123995, Russia. Contact: zharkov@ifz.ru*

Introduction: If the Galilean satellites of Jupiter are in a state close to hydrostatic equilibrium, then data on their figures and gravitational fields allow us to impose a constraint on the density distribution in the interiors of these bodies and, thereby, to make progress in modeling their internal structure. The effects of the equilibrium figure theory to within terms of the second order in a small parameter α (defined as $\alpha=3\pi/(G\rho_0\tau^2)$, where ρ_0 and τ are the average density and rotation period of a satellite) on figure parameters and gravitational moments of the satellite Europa have been considered. As the effects of third and forth harmonics are determined mostly by outer layers of Europa, to distinguish between model mantle density, the gravitational moments J_4, C_{42} and C_{44} should be determined to accuracy with four decimal digits. The most important question to be answered by modeling the internal structure of the Galilean satellites is that of the condensate composition at the formation epoch of Jupiter's system.

Models: The gravitational moments (J_2 and C_{22})Europa were first determined as a result of the successful Galileo space mission and then refined in the review [1] (Table 1). To show the effects of the second approximation, two three-layer trial models of Europa [2] and a model from [3] are used. The considered models of the Europa's interiors [2] differ by the size and density of the core: E1 (the core density ρ_c=5200 kg/m³: Fe-FeS eutectic) and E3 (ρ_c=4600 kg/m³: FeS with an admixture of nickel), while having the same thickness and density of the crust, and the mantle density difference is only 10 kg/m³. In models E1 and E3 the outer layer that consists of crystal and liquid water is 123 km thick and its mass is 7.6 weight %. The model EH [3] has a smaller Fe-FeS core and higher silicate mantle density. The theory set out in [4] allows all three principal, nondimensional moments of inertia normalized to ms_1^2 to be calculated for the constructed models (see Table 2). According to the data in Table 2, the difference between the polar moments of inertia calculated without using the Radau-Darvin formular is 4.40x10⁻⁴ (E1), 4.35x10⁻⁴ (E3) and 5.36x10⁻⁴ (EH). The same differences for Io are a factor of 3 larger, which roughly corresponds to the ratio of the small parameters for the satellites (about 3.4). Note how strongly the parameters depend on small variations in the mantle density of the satellite at constant crust thickness and density. To quantitatively estimate this effect, let us form two logarithmic derivatives based on the Europa models: $\delta k_2/k_2$=1.322 $\delta\rho_m/\rho_m$, $\delta m_c/m_c$='-13.2 $\delta\rho_m/\rho_m$, where ρ_m is the density of the mantle, and / m_c is the core mass. We see that small variations in the number k_2 change greatly the core mass.

Table 1. Observational data and model parameters for Europa

Parameter	Europa
Orbital radius R,	670.9
10^3 km	3.551
Period τ ,days	1565.0 ± 8.0
s_1, km	480.0
m_0, 10^{20} kg	2989 ± 46
ρ_0, kg m⁻³	1.31
g_0, m s⁻²	0.502
a, 10⁻³	0.346 ± 0.005
$C/m_0s_1{}^2$	435.5 ± 8.2
J_2, 10⁻⁶	131.5 ± 2.5
C_{22}, 10⁻⁶	

Table 2. Parameters of the three-layer models for Europa (s_1=1565 km, ρ_0=2989 kg/m³, ρ_1, ρ_2, ρ_3 – core, mantle and crust density; S_c and S_m - core and mantle radius, respectively; m_c - core mass).

Parameter	E1 [2]	E3 [2]	EH [3]
ρ_1, g cm³	5.2	4.6	5.15
ρ_2, g cm³	3.31	3.30	3.563
ρ_3, g cm³	1.05	1.05	1.0
S_c km	701.5	806.7	566.0
S_m, km	1442.23	1442.23	1420.0
k_2	1.044	1.050	1.043
m_c, wt %	15.67	21.07	8.15
$\bar{A}$	0.3458	0.3467	0.3458
$\bar{B}$	0.3461	0.3470	0.3461
$\bar{C}$	0.3464	0.3473	0.3464
$\bar{C}_{RD}$	0.3460	0.3468	0.3458
$\bar{I}$	0.3461	0.3470	0.3461
$(\bar{C}-\bar{C}_{RD})$, 10⁻⁴	4.4064	4.3576	5.3592

Results: Three integro-differential equations [5] for trial model density distributions were first solved numerically. Figure 1 shows functions $s_2(s)$, $s_{22}(s)$ and $s_4(s)$, $s_{42}(s)$, $s_{44}(s)$. Figure functions $s_2(s)$, $s_{22}(s)$, and $s_{31}(s)$, $s_{33}(s)$ are proportional to the Love function $h_2(s)$ and $h_3(s)$, respectively (Fig. 2). The outer regions of Europa's interiors influence more the Love number $h_3(s)$, then $h_2(s)$. The same fact is seen, when comparing the figure function $s_2(s)$, $s_{22}(s)$ and $s_4(s)$, $s_{42}(s)$, $s_{44}(s)$. In that way, functions of the second approximation $s_4(s)$, $s_{42}(s)$, $s_{44}(s)$ sound the density distribution of the external zones to a greater extent than functions of the first approximation $s_2(s)$, $s_{22}(s)$. It is seen more clearly in Fig. 3. The graphs of the functions $\chi_n(x)/J_n$ show the contributions of various zones in the planetary interior [6].

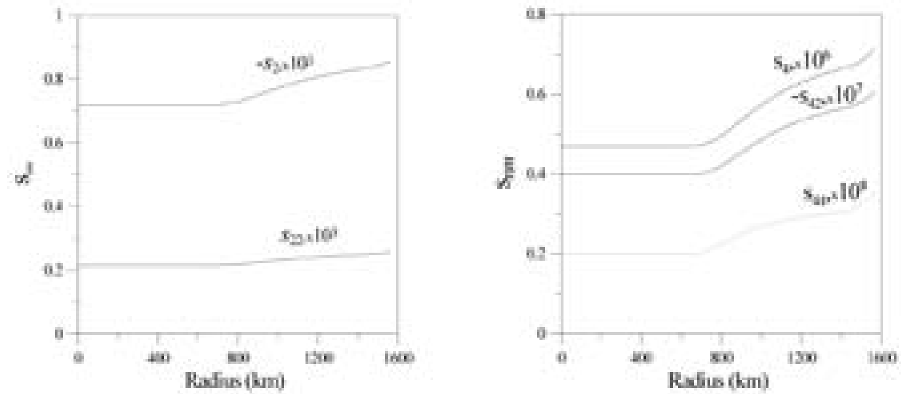

Fig. 1. The distribution of the parameters of the equilibrium figure of Europa $s_2(s)$, $s_{22}(s)$ (a) and $s_4(s)$, $s_{42}(s)$, $s_{44}(s)$ (b) along the planetary radius. The functions $s_2(s)$, $s_{22}(s)$ and $s_4(s)$, $s_{42}(s)$, $s_{44}(s)$ are not normalized.

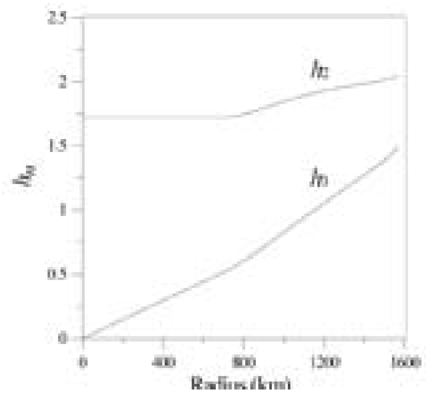

Fig. 2. Love numbers h_2 and h_3 along the planetary radius.

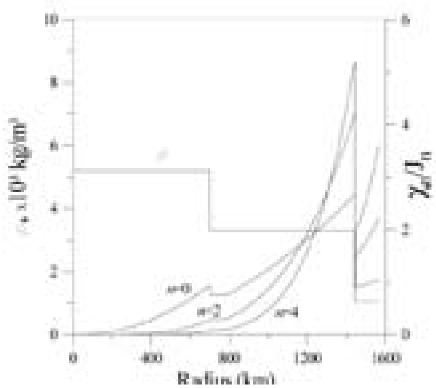

Fig.3. Functions of the relative density of the gravitational moments $\chi_n(s)/J_n$ (n=0, 2,4) and density distribution r(s) for a trial model of Europa.

Conclusion: To calculate the figure parameters s_4, s_{42} and s_{44} and consequently gravitational moments J_4, C_{42} and C_{44}, three integro-differential equations [5] for trial model density distributions were solved numerically and, as a result, all second order corrections were obtained. It turns out that the account of the second order values decrease gravitational moments J_2 and C_{22} by 2units in the forth decimal digit. Including the corrections of second order changes the a, b, and c semiaxes by 5 m, 1 m, and -10 cm, respectively.

Acknowledgements: This research was made possible partly by Grant No. 09-02-00128 from the Russian Fund for Fundamental Research.

References: [1] Schubert, G. et al. (2004) Jupiter: The planet, satellites, and magnetosphere, Ed. By F.Bagenal, T.Dowling, W.McKinnon (Cambridge Univ.Press, Cambridge), p.281-306. [2] Zharkov, V.N., Karamursov, B.S., Models, figures and gravitational moments of Jupiter's satellites Io and Europa. Astronomy Letters. 32. 495-505,2006. [3] Hussman H., Sohl F., Oberst J. Measuring tidal deformations at Europa's surface. J.Adv.Space.Res, doi:10.1016/j.asr.2010.06.001. [4] Zharkov, V.N. A theory of the equilibrium figure and gravitational field of the Galilean satellite Io: the second approximation, Astronomy lettes, 30, 496-507, 2004. [5]Zharkov,V.N.,Gudkova,T.V. Models, figures, and gravitational moments of Jupiter's satellite Io:effects of second approximation, PSS, 58,1381-1390, 2010. [6] Zharkov,V.N.,Gudkova,T.V. Sounding of the interior structure of Galilean satellite Io using the parameters of the theory of figure and gravitational field in the second approximation. The second Moscow Solar System Symposium 2M-S³, 2011.

2MS³-GM-poster

LAPLACE – EUROPA LANDER MISSION ARCHITECTURE

M.B. Martynov, I.V. Lomakin, A.A. Simonov, *Lavochkin Association, Leningradskoye Highway 24, Khimki 141400, Moscow Region, Russia*

Since 2007 the Russian Academy of Science and Roscosmos are heading an assessment study of a Russian mission to the Jupiter system emphasizing a surface element, Europa Lander. The mission, dedicated mostly to studies of the Europa ocean and exobiological aspects (Zelenyi et al., Adv. Space Res 48, 615–628, 2011) includes the soft lander (total mass of 1210 kg), and a small telecommunication and science orbiter (395 kg), launched by the Proton-class rocket. Mission design relies on radioisotope energy sources and solar-powered electrojet propulsion during the cruise. Present status of the mission development will be presented and potential cooperation options with ESA JUICE mission will be discussed.

SCIENCE INVESTIGATIONS IN THE FRAMEWORK OF EXPEDITION TO EUROPA

L.M. Zelenyi[1], O.I. Korablev[1], E.A. Vorobyova[2], M.V. Gerasimov[1], M.B. Matynov[3], A.V. Zakharov[1], *[1]Space research Institute (IKI), Moscow, [2]Soil science faculty, Moscow State University, [3]Lavochkin Association, Khimki, Moscow Region*

Science investigations and model payloads for Laplace – Europa Lander Russian mission will be discussed. These will include methods to characterize the geophysical and geochemical context on the surface of Europa, approaches to assess the habitability of the ocean, and experiments which could be conducted from the orbiter and during the cruise. The key requirements vis-à-vis the mission will be summarized, and the points where the international cooperation is necessary will be identified.

SCIENCE INVESTIGATIONS AND PAYLOAD FOR THE JPL EUROPA LANDER MISSION

K.P. Hand[1], J.R. Casani[1], J.A. Dooley[1], A.T. Klesh[1], N.J. Strange[1], T.P. McElrath[1], S. Campagnola[1], H.J. Eisen[1], J.O. Eliott[1], D. MacPherson[1], G.T. Chen[1], M.A. Jones[1], M.R. Grover[1], E.D. Skulsky[1], G. Singh[1], E.J. Jorgenson[1], M. Dinicola[1], E.H. Kopf[1], N.B. Alhambra[1], D.M. Hansen[1], J.M. Ratliff[1], D. Hohreiter[1], I. Jun[1], C.J. Phillipsv, G. Birur[1], J.C. Gallon[1], B.K. Okerlund[1], J.M. Weiss[1], C.S. Guernsey[1], E.M. Slimko[1], S. Eremenko[1], T.P. Rivellini[1], and J.A. Spry[1], [1]*Jet Propulsion Laboratory, California Institute of Technology, 4800 Oak Grove Drive, Pasadena, CA, 91109, USA; Contact: nathan.strange@jpl.nasa.gov*

Introduction:

The Jet Propulsion Laboratory, California Institute of Technology, conducted a mission design study focused on delivering a redundant two-lander mission to the surface of Europa. A mission focused on surface science permits a short lifetime for the prime mission (7 days) and thus enables a low total radiation dose mission to Europa. Lowering the radiation dose retires much of the risk and cost threats associated with Europa missions. Here we describe the science investigations and accompanying payload studied as part of this effort. The science payload allocation for each lander is approximately 40 kilograms.

The goal of this mission is to explore Europa to investigate its habitability. Our study of life on Earth has revealed three critical components that comprise a habitable environment and our current understanding of Europa indicates that it may harbor all three. These “keystones” for habitability are liquid water, a suite of essential elements, and chemical or radiation energy to power life. Europa, with its global liquid water ocean, likely in contact with a rocky seafloor, may be habitable today and it may have been habitable for much of the history of the solar system. Europa is thus the premier target in our search for evidence of both past and contemporary habitability. The discovery and exploration of a world that hosts extant, i.e., living, life permits investigations that could revolutionize our understanding of chemistry, biology, the origin of life, and the broader context of whether or not we are alone in the Universe. This mission provides the first steps toward that goal.

To investigate the habitability of Europa the following specific objectives are targeted:

1. Characterize the chemistry of the non-ice material on Europa’s surface, especially as relates to habitability and biosignatures.
2. Measure tectonic activity within the ice shell over a europan day to determine if Europa is geologically active in the modern epoch.
3. Assess the regional and local geology to advance our understanding of the relationship of Europa’s ocean with the overlying ice shell.

These objectives map directly to critical questions identified for the exploration of Planetary Habitats by the Vision and Voyages for Planetary Science (2013–2022) report:

1. What were the primordial sources of organic matter and where does organic synthesis continue today?
2. Beyond Earth, are there today, elsewhere in the solar system habitats with necessary conditions, organic matter, water, energy, and nutrients to sustain life, and do organisms live there now?

The science investigations of this mission can be broadly characterized to address Astrobiology, Geophysics, and Geology. The combination of these three themes enables focused science that advances our understanding of Europa at local, regional, and global scales.

The landed science payload selected to achieve the mission goals and objectives is identical for both landers. Three sets of stereo cameras provide a panoramic view of the surface, a mass spectrometer performs analysis of the surface composition, and two seismometers—one on the lander pallet and one deployed to make direct contact with the surface—monitor for activity in the ice shell over two diurnal cycles. With added payload capacity an infrared or Raman spectrometer and a magnetometer would be included.

SYSTEM DESCRIPTION OF A EUROPA ORBITER/ LANDER MISSION.

John R Casani[1], Kevin Hand[1], Duncan MacPherson[1], John O. Elliott[1], Howard Eisen[1], Jennifer Dooley[1], Tim McElrath[1], Nathan Strannge[1], Eli D. Skulsky[1], Jeff Weiss[1], John Gallon[1], Nelson Ahambra[1], Ted Kopf[1], Martin Ratliff[1], Dave Hansen[1], Danielle Hohreiter[1], Chuck Phillips[1], Gaj Birur[1], Brian Okerlund[1], Carl Guernsey[1], Rob Grover[1], Eric Slimko[1], Alexander Eremenko[1], Andy Spry[1], Tommaso Revellini[1], Andrew Klesch[1], *[1]Jet Propulsion Laboratory, 4800 Oak Grove Drive, Pasadena, California, Contact: jrcasani@jpl.nasa.gov*

The exploration of Europa remains one of the highest priorities in the international science community. While most of the studies over the last decades have focused on Orbiter missions (sometimes including a modest lander payload), a team at JPL has recently completed a study investigating the feasibility and science value of a Europa mission which focuses on delivering a pair of landers, each equipped with a comprehensive instrument suite and capable of communication directly with Earth. The Landers would be delivered by an independent Orbiter/Cruise Stage that would remain in Europa orbit after lander separation to perform a limited-duration (up to four weeks) orbital mission using its own science instrument suite.

By placing the primary emphasis the Europa lander phase of the mission and proceeding as directly as possible to the Europan surface, this mission concept is able to return significant and unique science while avoiding the issues associated with the extremely high radiation dose experienced by a long term orbiter. This paper provides an overview of the Europa Lander mission concept with a focus on flight system design, including both the Lander and the Cruise/Orbiter Stage elements of the mission. Major system engineering trades are discussed as well as resulting subsystem and system design features that highlight the robustness and cost-effectiveness of this mission concept.

2MS^3-EL-05

RADIATION ENVIRONMENT ESTIMATES FOR EUROPA LANDER MISSION

M. V. Podzolko[1], I. V. Getselev[1], Yu. I. Gubar[1], I. S. Veselovsky[1, 2], A. A. Sukhanov[2],
[1] Skobeltsyn Institute of Nuclear Physics, Lomonosov Moscow State University, Moscow 119991, Russia; [2] Space Research Institute (IKI), Russian Academy of Sciences, Moscow 117997, Russia. Contact: 404@newmail.ru

In the current research the radiation environment for the future space mission to Jupiter and its moon Europa is studied, which is necessary to for estimating the radiation influence on spacecraft components and planning the mission.

The highest radiation influence during the mission the spacecraft will experience during its flight in Jupiter's near-planetary space. Charged particles trapped by strong magnetic field of the planet form the powerful radiation belts (Fig. 1). And, unlike the Earth's Moon, the orbits of Jupiter's large satellites Io, Europa and Ganymede are located inside Jupiter's radiation belts. In Europa's orbit the dose behind 2 g/cm^2 Al shield will be majorly contributed by relativistic electrons and amount up to almost 1 Mrad during 2 months (Fig. 2, upper plot). Thus the radiation hazard for Europa lander mission is very high.

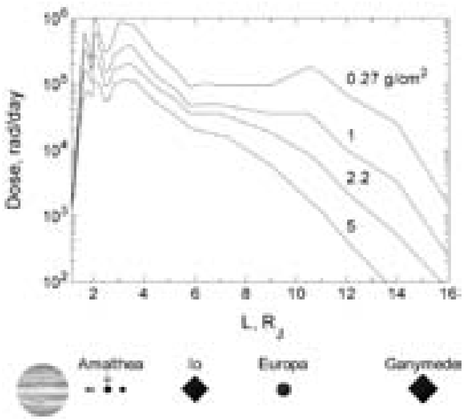

Fig. 1. Equatorial profiles of radiation doses behind 0.27, 1, 2.2 and 5 g/cm^2 Al shielding in Jupiter's radiation belt. Below, the location of Jupiter's satellites is shown.

However, near Europa part of the flux is shaded by the moon. This reduction of the fluxes is sufficiently nonuniform and differs for various particle energies and pitch-angles and for the surface and the low-altitude orbit. This is caused by several factors: complexity of particle trajectories near Europa and in Jupiter's magnetosphere in general, difference of Europa's orbital plane from Jupiter's geomagnetic equator plane, certain disturbance of magnetic and electric fields in vicinity of Europa, and tenuous atmosphere of the moon. We have computed distribution of the fluxes of charged particles of various energies and radiation doses under different shielding on Europa's surfaces and at 100 km altitude taking into account several of the mentioned above factors (Fig. 2, lower plot).

On the basis of our computations we conclude, that the most hazardous region for the mission on Europa's surface with regard to radiation conditions is the trailing side of the moon along its orbital motion. But the maximum doses there behind 2–5 g/cm^2 are 4–5 times lower, than in the low-altitude orbit around Europa, and further decrease from middle latitudes to equator. The safer regions are the leading side of the moon and the high-latitude regions: within the considered approximation the doses there appear to be by ≈1 degree of magnitude lower, than the maximum values without taking into account the influence of the moon. The orbiter in a 100 km circular orbit around Europa will encounter higher radiation impact than the lander. Yet by choosing the polar orbit for it radiation dose can be lowered to about 1/4 of the maximum value without Europa.

Also the considerable radiation dose will be absorbed during the gravity assists in the system of Jupiter. Generally, gravity assists will consist of 1st fly-by and entering the highly-elliptical orbit around Jupiter, then several gravity assists using Jupiter's large satellites, and the final approach to Europa. Our computations have shown, that the optimal 1st Jupiter's fly-by with regard to minimizing both the power consumption and radiation hazard should have the pericenter "under the radiation belts" (r_p < 1.5–1.8

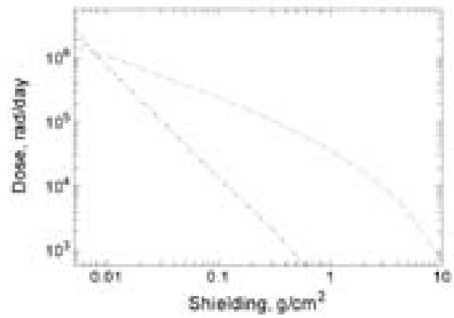

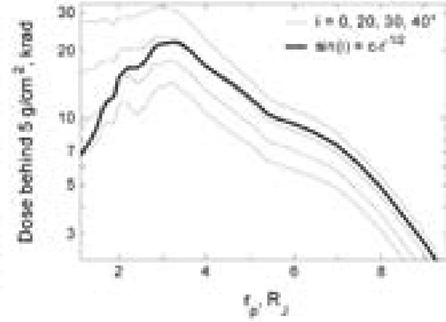

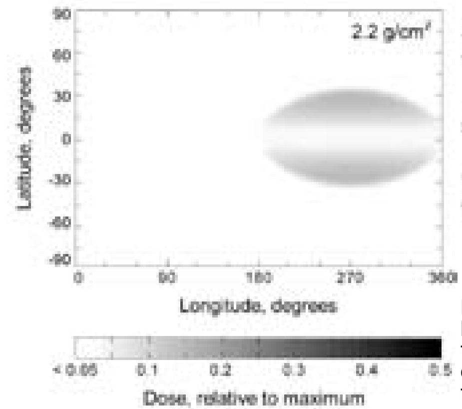

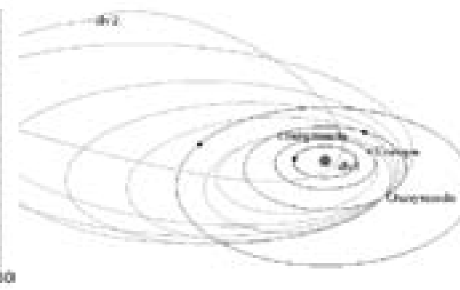

Fig. 2. Upper plot – radiation doses behind different shield from electrons (upper curve) and protons (lower curve) in Europa's orbit. Lower plot – distribution of the doses behind 2.2 g/cm^2 Al on Europa's surface.

Fig. 3. Upper plot – dependency of the dose behind 5 g/cm^2 during the 1st Jupiter fly-by from the pericenter radius for several given values of orbit inclination (thin curves) and for approximation of real dependence of the inclination from pericenter radius (bold curve). Lower plot – example of the optimal strategy of gravity assists in the system of Jupiter.

Jupiter radii) and inclination ≈40° (Fig. 3, upper plot). (Yet more advanced strategy is to use the gravity of one of Jupiter's large moons, e.g. Io, during 1st fly-by, but it is the question of possibility to provide the sufficient navigation accuracy). On the 2nd stage the optimal trajectory will consist of the several gravity assists using Ganymede. The orbit of this large Jovian moon is located near the outer boundary of planet's radiation belts, the dose rates there are ≈100 times lower, than near Europa (Fig. 1). Consequently the last approach to Europa in order to minimize the final impulse with the engines should have the apocenter near Ganymede and the pericenter near Europa, but it should be preceded with several intermediate circuits with the pericenter radii >12–13 R_J. An example of such orbit is shown in Fig. 3 (lower plot). The radiation dose in this orbit will amount to ≈50 and 20 krad behind 2.2 and 5 g/sm^2 Al shield correspondingly; the total impulse with the engines is ≈2.5 km/s (in case of single-impulse maneuver of finally entering the low-altitude orbit around Europa).

Additionally estimates of the radiation influence in near-Earth's and interplanetary parts of mission trajectory have been made. It occurs relatively small compared to that in Jupiter's nearplanetary space.

References: Podzolko M. V., Getselev I. V., Gubar Yu. I., Veselovsky I. S., Radiation conditions of a mission to Jupiter and Europa, Solar System Res, 43 (2), 116–120, 2009.
Podzolko M. V., Getselev I. V., Gubar Yu. I., Veselovsky I. S., Charged particles on the Earth–Jupiter–Europa spacecraft trajectory, Adv Space Res, 48 (4), 651–660, 2011.

MISSION DESIGN FOR A LOW-RADIATION EUROPA LANDER

N.J. Strange[1], T.P. McElrath[1], S. Campagnola[1], J.R. Casani[1], H.J. Eisen[1], J.O. Eliott[1], K.P. Hand[1], D. MacPherson[1], J.A. Dooley[1], G.T. Chen[1], A.T. Klesh[1], M.A. Jones[1], M.R. Grover[1], E.D. Skulsky[1], G. Singh[1], E.J. Jorgenson[1], M. Dinicola[1], E.H. Kopf[1], N.B. Alhambra[1], D.M. Hansen[1], J.M. Ratliff[1], D. Hohreiter[1], I. Jun[1], C.J. Phillipsv[1], G. Birur1, J.C. Gallon[1], B.K. Okerlund[1], J.M. Weiss[1], C.S. Guernsey[1] , E.M. Slimko[1], S. Eremenko[1], T.P. Rivellini[1], J.A. Spry[1], [1]Jet Propulsion Laboratory, California Institute of Technology, 4800 Oak Grove Drive, Pasadena, CA, 91109, USA;
Contact: nathan.strange@jpl.nasa.gov

In the summer of 2011, a group at NASA's Jet Propulsion Laboratory undertook a three-week study to develop a mission concept for a Europa lander with an order of magnitude less radiation dose than a Europa orbiter mission. This concept was motivated by the observation that the surface radiation on regions of Europa's leading hemisphere is only 2 krad/day (behind 100 mils of Al with an RDF of 2), compared to 13 krad/day in orbit. This mission would consist of two redundant landers and a cruise stage that enters Europa orbit. We examined options for both a simple cruise stage without science and a cruise stage with focused science. We estimate a mission TID (Total Ionizing Dose) of 150 krad for the landers and 300 krad for a cruise stage with a 14-day orbital mission. This is a very small radiation dose compared to the 2.9 Mrad TID for the Jupiter Europa Mission (JEO) concept.

Both options could launch on a single Delta IV Heavy or Falcon 9 Heavy class launch vehicle. We estimate both the concepts would cost less than $2B (FY15). Two recent technology developments greatly reduce the complexity and risk of this mission: 1) flash LIDAR that enables autonomous hazard avoidance on Europa's rough and largely unknown terrain, and 2) a novel gravity-assist tour design that minimizes the radiation exposure before arriving at Europa.

This presentation will discuss the mission design and architecture for this mission concept. It will focus on the trajectory design, concept of operations, and landing strategy including hazard avoidance. The mission architecture will be discussed in terms of the science opportunities and limitations of this mission concept. Other presentations will discuss the flight system design and science implementation.

SEARCHING FOR LIFE IN EXTREME ENVIRONMENTS RELEVANT TO JOVIAN'S EUROPA: LESSONS FROM SUBGLACIAL ICE STUDIES AT LAKE VOSTOK (EAST ANTARCTICA).

S. A. Bulat[1,2], I. A. Alekhina[1,2], D. Marie[3], J. R. Petit[2], *[1]Petersburg Nuclear Physics Institute, St. Petersburg Gatchina 188300, Russia; [2]Laboratoire Glaciologie et Géophysique Environnement CNRS-UJF, 38402 St. Martin d'Hères Cedex, France; [3]Station Biologique de Roscoff, Place Georges Teissier, 29682 Roscoff Cedex, France. Contact: sergey.bulat@ujf-grenoble.fr*

The objective was to estimate the genuine microbial content of ice samples from refrozen water (accretion ice) from the subglacial Lake Vostok (Antarctica) buried beneath the 4-km thick East Antarctic ice sheet. The samples were extracted by heavy deep ice drilling from 3659 m below the surface. High pressure, a low carbon and chemical content, isolation, complete darkness and the probable excess of oxygen in water for millions of years characterize this extreme environment. A decontamination protocol was first applied to samples selected for the absence of cracks to remove the outer part contaminated by handling and drilling fluid. Preliminary indications showed the accretion ice samples to be almost gas free with low impurity content. Flow cytometry showed the very low unevenly distributed biomass while repeated microscopic observations were unsuccessful.

We used strategies of Ancient DNA research that include establishing contaminant databases and criteria to validate the amplification results. To date, positive results that passed the artifacts and contaminant databases have been obtained for a few of bacterial phylotypes only in accretion ice samples featured by some bedrock sediments (Fig. 1).

Fig. 1. Melt water from 5G2-3608 m deep segment of Lake Vostok accretion ice showing a lot of mostly mica-clay mineral fine-grained sediments (at the bottom of an acrylic container).

The phylotypes included the chemolithoautotrophic thermophile *Hydrogenophilus thermoluteolus* (Beta-*Proteobacteria*), one unclassified uncultured bacterium of OP11 Candidate Division (91% similarity with closest relative) and unknown bacterium related (94% similarity) to lake-river sediment-inhabiting *Ilumatobacter luminis* (*Actinobacteria*). Combined with geochemical and geophysical considerations, our results suggest the presence of a deep biosphere, possibly thriving within some active faults of the bedrock encircling the subglacial lake, where the temperature is as high as 50^{o} C and in situ hydrogen is probably present.

Our approach indicates that the search for life in the subglacial Lake Vostok is constrained by a high probability of forward-contamination. Our strategy includes strict decontamination procedures, thorough tracking of contaminants at each step of the analysis and validation of the results along with geophysical and ecological considerations for the lake setting. This may serve to establish a guideline protocol for studying extraterrestrial ice samples.

THEORETICAL AND COMPUTER INVESTIGATION OF CRACK FORMATION ON EUROPE'S SURFACE

E. N. Chumachenko[1], R. R. Nazirov[1], I. V. Logashina,[1] and S. A. Aksenov[1],
[1]Space Research Institute, Russian Academy of Sciences, Profsoyuznaya st. 84/32, Moscow 117997, Russia. Contact: mmkaf@miem.edu.ru

The paper deals with an investigation of relief formation in Europe's surface. Jupiter's satellite Europe relates to large satellites of Solar system's planets. It is close in size to the Moon. The surface of Europe is covered with a layer of water about 100 km thick, the part of which represents, presumably, the ice surface crust of thickness 10-30 km, and the other part is believed to represent a subglacial ocean.

The gravitational effect of Jupiter essentially influences Europe and, along with tectonic processes on Europe itself, promotes existence of a liquid ocean in satellite's depths. As the scientists believe, the degree of warmth of the satellite is higher at the equator, than near the poles. The thicker ice layer at poles tends turning relative to the equator. However, the frozen substance generates a uniform surface of Europe owing to which the entire shell begins to rotate.

It is possible to estimate approximately the scale of tidal forces' effect on the ice structures of Europe. In the day side of a tide the elongation of Europe's body equals about 60 meters. This extension should be compared with the diameter of Europe, which is about 3100 km. Thus, the mean, local surface "expansions" on Jupiter's satellite should be of the order of 2 meters per every 100 km. Taking into account essential heterogeneity of planet's ice cover both in thickness and in density, as well as the tectonic and thermal effects, such surface loadings should, undoubtedly, result in forming the defects in ice structures.

The analysis performed showed that compressing, extending, shearing and bending stresses can influence some arbitrarily separated section of Europe's ice surface. It seems interesting for us to see, what types of defects could arise from such effects.

In this work we examined, how the stresses, initiated by tidal effects, will influence a separately located zone of Europe's ice surface with some extended section thawed over the frontal tectonic stub. For this purpose we separated the rectangular section of surface with rectilinearly located "weakening". We conventionally fixed the left edge and applied loading to the right edge in various directions while moving clockwise. Then we simulated the weakened section taking into account the change of ice cover thickness over a stub and accounting for ice properties variation at various temperatures. In this case, at small relative drop of temperatures in the zones from 1 to 4, the change of thickness will be rather essential there and can vary from 10 to 0.1 kilometers. Simultaneously, for studying the effect of bending loads, we considered the cross-section of the same area of surface. Calculations of a thermal-stressed-strained state were performed by means of the finite-element computation system SPLEN (www.kommek.ru).

The calculations, carried out for the cross-section of a thawed ice structure's area, have shown that, the most dangerous, from the crack formation viewpoint, is the shear stress at loading application angles of ±90º. Analyzing the destruction appearance and propagation zones depending on the type of applied load, one can classify the defects arising on Europe's ice surface. When the inner splitting is formed, the liquid ice is ejected, and a small double furrow is generated. The cracks of similar type, at extending stresses in ice structures, result in generating a highly eroded double furrow. The outer splitting at extending stresses finally leads to formation of an ice knot extending along the whole crack. At compressing stresses such a knot either is not formed at all, or has minimum size and fragmentary shape formed from separate splinters. If the ice plates essentially diverge after splitting, the relief in a crack zone lowers owing to subsequent freezing of an air hole.

We have convinced in the given task, that under different mechanical loading conditions the defects can appear both in the upper, colder ice layer, and in the warmer one. The obtained results well correlate with photo pictures of Europe's surface and allow one to estimate the contribution of a set of acting temperature and mechanical forces into formation of ice structures' defects.

Using locally homogeneous models of thawed ice patches in the distributed field of temperatures, the effect of mechanical gravitation-tidal forces on the formation of surface defects on a Europe was studied. It is shown that fractures and cracks can have various forms depending on the stress-strained state arising in their vicinity. The formation of such defects is caused by the chaotic set of many factors, mechanic and temperature ones predominantly. These processes are essentially similar to tectonic processes on the Earth and demand further investigation.

LASER-INDUCED PLASMA SPECTROSCOPY FOR *IN-SITU* CHEMICAL ANALYSIS FOR LANDER MISSIONS TO ICY MOONS.

S. G. Pavlov[1], S. Schröder[1], E. K. Jessberger[2], H.-W. Hübers[1,3], *[1]Institute of Planetary Research, German Aerospace Center (DLR), Rutherfordstr. 2, 12489 Berlin, Germany; [2]Institut für Planetologie, Westfälische Wilhelms-Universität, Wilhelm-Klemm-St. 10, 48149 Münster, Germany; [3]Institut für Optik und Atomare Physik, Technische Universität Berlin, Hardenbergstr. 36, 10623 Berlin, Germany. Contact: sergeij.pavlov@dlr.de*

Introduction:

Several future space missions to planets, moon and asteroids in solar system consider the landers equipped with laser-induced plasma (breakdown) spectroscopy (LIBS) instruments in the scientific payload. This technique provides quantitatively the microscopic *in-situ* abundances of all major and many trace elements of surfaces of solar system bodies. Since excitation and evolution of the plasma depend on the properties of the investigated material and on environmental conditions, the capability of this spectroscopic method to operate at different pressures, atmospheres as well as for materials with different absorbance must be studied for each individual space mission. We focus on two major parameters affecting laser-induced plasma spectroscopy for exploration of icy moons: transparent icy materials as well as thin atmospheres. We demonstrate the spectroscopy capability for analysis of different frozen salt solutions as well as operation at ultra-high vacuum (below 1 mPa). In both cases we derive the laser power density necessary for creation of a plasma with brightness required for analysing the chemical composition.

LIBS spectrometer and planetary simulation chamber at DLR-Berlin:

A dedicated chamber for simulation of planetary conditions at DLR-Berlin can hold the Martian-like atmosphere or high vacuum conditions [1]. Two infrared Q-switched lasers are used for ablation of material: Nd:YAG laser (Inlite, Continuum) operating at 1064 nm and at 10 Hz, pulse energy up to 230 mJ at 8-10 ns pulse duration and Nd:YLF laser (NeoLASE) operating at 1053 nm and at 10 Hz, pulse energy up to 3 mJ at 3-5 ns pulse duration. A beam spot in the focal plane hitting the sample (target) surface is about 300 µm for the Inlite laser and ≈ 60-80 µm for the NeoLASE laser. The emitted light of the laser-induced plasma is collected into the 50 µm entrance slit of an echelle spectrometer (LTB Aryelle Butterfly) covering the wavelength range of 280–900 nm with a spectral resolution of around 10^4. A time-gated ICCD camera (Andor) at the exit of the spectrometer records the spectrally dispersed plasma emission signal. Each individual measurement is an acquisition of a signal induced by a particular number of sequent laser shots. For the described measurements the laser beam is focused at a new position for each series of measurements. Identification of the spectral lines usually is performed by the LTB built-in spectrometer software by comparison with the NIST spectral database [2].

LIBS on frozen salt solutions:

Excitation of laser-induced plasmas in transparent materials is challenging. As shown in many previous studies [3], laser-induced breakdown spectroscopy typically requires power densities exceeding 10 MW/mm^2 during a few nanosecond laser pulse and the entire energy is usually absorbed on the sample surface. High-concentrated water salt solutions and brines are considered as the most probable candidates to preserve liquid water at least temporally down to very low temperatures and at high sublimation rates. They are of special interest in the search for extraterrestrial life and, therefore, stimulate the analysis of salts by various techniques including LIBS [4,5]. For our laboratory experiments various salt solutions were prepared with different concentrations. To reduce the inclusion of air in the icy samples, we degassed them before freezing in a copper container. As the atmosphere in the simulation chamber we had air at a pressure of ≈ 1 Pa or a Martian atmosphere-like gas mixture at ≈ 700 Pa [6]. The measurements were performed at temperatures of ≈ 240 K by cooling with liquid nitrogen and controlled heating. The delay time and the integration time of the ICCD camera have been optimized to obtain good signal-to-noise ratios, while at the same time not losing signals from fast recombining ions. The typical signal-to-noise ratios rose up to 150 for the maximum available laser power, with density of about 80 MW/mm^2. The spectra of several frozen salt solutions were qualitatively investigated focusing on the major and minor element abundances. As usual, the alkali metal and alkaline earth metal elements, oxygen and hydrogen were clearly detectable in the LIBS spectra and thus allowed the distinction between different frozen solutions. Sulphur and chlorine, having weak emission lines in the used spectral range, were difficult to detect. These experiments demonstrate the capability of LIBS for the detection and identification of different frozen salt solutions under Martian-like conditions.

LIBS at ultrahigh vacuum:

At low pressures ≤ 1 mPa the excited plasmas have small plumes and expand very rapidly, which limits both the LIBS signal intensity and the available acquisition time [3]. At a few mPa air pressure one requires relatively powerful laser sources to create a detectable LIBS plasma [3,4,7-9]. We have investigated laser-induced plasma spectra obtained with a miniaturized low-energy (2.7 mJ) laser (NeoLASE) developed for future planetary missions. The measurements were performed at room temperature. We used several basaltic rock and sediment standards that were first crushed to powder and then pressed into pellets. Our results demonstrate that even an infrared laser excitation energy of only ~1 mJ is sufficient to detect atomic emission lines of elements with relative abundances above 10^{-3} (0.1 wt%). Despite a significant decrease of signal-to-noise ratio for most of atomic lines (an exception are the widely broadened lines of H) and a significant decrease of the number of observed atomic transitions, most elements in the investigated materials clearly can be identified in the LIBS spectra at < 1 mPa and with a laser power densities of $\approx$ 40 MW/mm^2. Moreover, some atomic doublet and triplet transitions that are unresolved at ambient pressures (100 kPa), become resolved and are identified below 1 mPa. Thus we have unambiguously demonstrated the feasibility of miniaturized laser-induced breakdown spectrometry – the mass of the complete instrument is only about 1 kg – for space missions to solar bodies with absent or thin atmospheres.

Acknowledgements: This work was partly supported by the Helmholtz-Gemeinschaft Deutscher Forschungszentren (HGF) Alliance “Planetary Evolution and Life”.

References: [1] H.-W. Hübers, S. G. Pavlov, R. Preusker, I. Rauschenbach, and E. K. Jessberger, Trace element detection by laser-induced breakdown spectroscopy under simulated Martian conditions, EMSLIBS2007 Conference 10th-13th Sept. 2007, Cité des Sciences et de l’Industrie, Paris, France, Abstract # P030, 2007.
[2] Yu. Ralchenko, A. E. Kramida, J. Reader, and NIST ASD Team. NIST on-line Atomic Spectra Database. National Institute of Standards and Technology, Gaithersburg, MD, 2010.
[3] A. K. Knight, N. L. Scherbarth, D. A. Cremers and M. J. Ferris, Characterization of laser-induced breakdown spectroscopy (LIBS) for applications to space exploration. Appl. Spectrosc. **54**, 331–340, 2000.
[4] Z. A. Arp, D. A. Cremers, R. C. Wiens, D. M. Wayne, B. Sallé and S. Maurice, Analysis of water ice and water ice/soil mixtures using Laser-Induced Breakdown Spectroscopy: Application to Mars polar exploration, Appl. Spectrosc. 58, 897-909, 2004.
[5] V. Lazic, I. Rauschenbach, S. Jovicevic, E. K. Jessberger, R. Fantoni and M. Di Fino, Laser induced breakdown spectroscopy of soils, rocks and ice at subzero temperatures in simulated Martian conditions, Spectrochim. Acta B 62, 1546–1556, 2007.
[6] S. Schröder, S. Pavlov, H.-W. Hübers, I. Rauschenbach, E. K. Jessberger, Analysis of frozen sulfate and chloride salt solutions using laser-induced breakdown spectroscopy under Martian conditions, LPSC XXXXII, Abstract#1165, 2010.
[7] R. D. Harris, D. A. Cremers, C. Khoo and K. Benelli, LIBS-based detection of geological samples at low pressures (<0.0001 Torr) for Moon and asteroid exploration. LPSC XXXVI, Abstract#1796, 2005.
[8] K. Ishibashi, S. Ohno, S. Kameda, K. Wada, H. Senshu, M. Kobayashi, T. Arai, N. Namiki, T. Matsui, Y. Cho, and S. Sugita, Laser-induced breakdown spectroscopy measurement under low pressure simulating vacuum conditions, EPSC2010, 19-24 Sept. 2010, Rome, Italy, Abstract#EPSC2010-453.
[9] J. Lasue, R. C. Wiens, S. M. Clegg, D. T. Vaniman, K. H. Joy, S. Humphries, Applicability of LIBS on the Moon: Elemental analysis of lunar simulants in vacuum. LPSC XXXXII, Abstract#1165, 2011.
[10] I. Rauschenbach, E. K. Jessberger, S. G. Pavlov, H.-W. Hübers, Miniaturized LIBS for the in-situ analysis of the Martian surface: Calibration and quantification. Spectrochim. Acta B 65, 758–768, 2010.